MICROWAVE POLARIMETRIC BACKSCATTERING FROM NATURAL ROUGH SURFACES

Yisok Oh

December, 1993

MICROWAVE POLARIMETRIC BACKSCATTERING FROM NATURAL ROUGH SURFACES

by

Yisok Oh

A dissertation submitted in partial fulfillment
of the requirements for the degree of
Doctor of Philosophy
(Electrical Engineering)
in The University of Michigan
1993

Doctoral Committee:

Assistant Professor Kamal Sarabandi, Co-Chairman
Professor Fawwaz T. Ulaby, Co-Chairman
Professor Sushil K. Atreya
Professor Anthony W. England
Assistant Professor Brian E. Gilchrist

To my wife, EuiJung Yee, for her patience and constant support; to my son, Saroonter, who already grew up to be a fourth grade student; and to my parents who inspired me to pursue the doctoral degree.

ACKNOWLEDGEMENTS

I would like to express my gratitude to the members of my committee and to the Radiation Laboratory for supporting my research. Special thanks are due to Professor Kamal Sarabandi and Professor Fawwaz T. Ulaby for their constant advices, encouragements, and generous financial support throughout the course of this work. I consider myself very fortunate to have these professors as my advisors for my doctoral work.

I would also like to thank the following friends and colleagues for their help, friendship and encouragement during my graduate studies: Roger DeRoo, Richard Austin, Jim Ahne, Raid Khalil, Adib Nashashibi, Jim Stiles, John Kendra, Leo Kempel, Dr. Leland Pierce, and Craig Dobson.

Finally, none of this would have been possible without the constant love, patience, and sacrifice of my wife, EuiJung Yee, and my son, Saroonter.

TABLE OF CONTENTS

LIST OF FIGURES

LIST OF TABLES

LIST OF APPENDICES

Appendix

CHAPTER I

INTRODUCTION

1.1 Motivations and Objectives

Recently, spaceborne remote sensing of the Earth has become an important source of information in monitoring the Earth's environment. Depending on the application, sensors operating in different parts of electromagnetic spectrum have been designed. The sensors in optical, thermal infrared, millimeter, and microwave frequencies have been commonly used to retrieve information about different target types on the Earth's surface by virtue of their spectral properties. Propagation properties of electromagnetic waves at microwave frequencies offer the following advantages over optical sensors: (1) microwave sensors are capable of penetrating clouds and precipitations, (2) microwave sensors may have their own source of illumination so that they are independent of the Sun and thus the desired incidence angle, frequency, and polarization can be chosen, and (3) the microwave signals can penetrate to some extent into various types of the surface cover such as vegetation, and thus provide some information about the subsurface targets.

Among other applications, microwave remote sensing of soil moisture has been of primary concern to hydrologists since many atmospheric and environmental processes are closely linked to the spatial distribution of soil moisture. Application of

both passive and active sensors in microwave remote sensing of soil moisture have been attempted [Schmugge et al., 1986 ; Dobson and Ulaby, 1986a], however only active sensors are capable of producing estimates of soil moisture within fine spatial resolution from a spaceborne platform. Radar backscatter from terrain is influenced by two sets of parameters: 1) physical parameters such as complex dielectric constant of the scatterers and the surface topography, and 2) the radar parameters such as frequency, incidence angle, and polarization. For bare soil surfaces, the dielectric constant is strongly dependent upon the liquid water content, and the effects of other soil parameters like soil type (particle size distribution) on the dielectric constant of the soil medium are less important, particularly at the lower microwave frequencies [Ulaby, 1974]. Radar backscatter, away from normal incidence, from a bare soil surface is a direct result of the surface irregularity. The strength of the backscattered field and its statistics are complex functions of these surface irregularities relative to the wavelength and the dielectric constant of the soil medium.

Researchers, for a long time, have been trying to develop mathematical models to predict the backscattered characteristics of randomly rough surfaces. At present there exist numerous analytical models each pertaining to specific cases [Ulaby et al., 1982; Tsang et al., 1985; Ishimaru, 1978]. The success of these models when applied to real rough surfaces is very limited, however, because of the over simplifying approximate nature of these models. There are also a large number of experimental data sets, all collected in an attempt to establish the relationship between the radar backscatter and the soil moisture and surface parameters empirically [Bartlivala and Ulaby, 1977; Ulaby et al., 1978; Jackson et al., 1981; Dobson and Ulaby, 1986a and 1986b; Mo et al., 1988; Wang et al., 1986]. However due to the lack of precise ground truth data, accurate calibrations, complete angular and polarization response characterization, or

a sufficient span of the surface parameter, the existing data sets have not been able to contribute much to the understanding of the scattering process. Therefore, no reliable algorithm has yet been developed to retrieve soil moisture and surface roughness parameters from radar data with an accuracy required for hydrologic applications. One of the added complexity in the soil media is the inhomogeneous nature of the soil medium which is the result of nonuniform moisture profile.

The problem of scattering from random surfaces has been investigated only for homogeneous surfaces. Even for this case, theoretical solutions exist only for limiting cases. There are two conventional models dealing with rough surface scattering [Ulaby et al., 1982; Tsang et al., 1985]. One is the small perturbation method (SPM), which has been developed for surfaces whose height variations are small compared to the wavelength and where surface slopes are much smaller than unity. The second is the Kirchhoff approximation (KA), which has been developed for rough surfaces with large radii of curvature. In recent years, there has been a considerable interest in determination of the regions of validity of these two methods as well as the development of a more general theory that can bridge these two limiting scattering models [Brown, 1978; Bahar, 1981; Wineberner and Ishimaru, 1985; Fung and Pan, 1987]. The validity regions of the SPM and KA have been examined previously by comparing the model predictions to the results derived from exact numerical simulation [Chen and Fung, 1988; Broschat et al., 1987; Thorsos, 1988]. Unfortunately, these numerical solutions could only address one-dimensional surface roughness, thus the numerical simulation does not produce depolarization and its prediction for co-polarized components are much different from real surfaces that are two-dimensional. So far, no exact numerical solution for two-dimensional surfaces has been developed due to the limited computer power. Therefore, carefully controlled experiments are necessary to

study the two-dimensional surface of arbitrary surface correlation functions.

The major goal of this thesis is to develop an algorithm for retrieving soil moisture content and surface roughness parameters from radar backscatter data. To accomplish this task, first a polarimetric radar backscattering model is developed that is valid for natural rough surfaces over a wide range of surface conditions at microwave frequencies. Development of the scattering model requires four major steps: (1) acquisition of accurate polarimetric radar backscatter data from bare soil surfaces over a wide range of moisture conditions and surface roughnesses, (2) acquisition of accurate ground truth data for surface roughness and soil moisture using a laser surface profile meter and a dielectric probe, (3) development and enhancement of theoretical and numerical scattering models, (4) development of a hybrid scattering model for bare soil surfaces constructed based on the experimental observations and the theoretical and numerical models. Once the hybrid (semi-empirical) model is developed and tested, development of an inversion algorithm capable of providing accurate estimates of soil moisture contents and surface roughnesses from polarimetric radar backscatter is considered.

1.2 Thesis Overview

In this section, the structure of the thesis is explained and content of each chapter is briefly discussed. Figure 1.1 shows a simplified flow chart of the topics discussed in this thesis. A theoretical basis for this work is reported in Chapters 2 and 4 which is used to verify both numerical simulations as well as experimental observations. The numerical simulations of radar backscattering from random surfaces are introduced in Chapters 3 and 5 and are used to examine the accuracy of the theoretical models and also to guide the development of the semi-empirical scattering model. Chapter

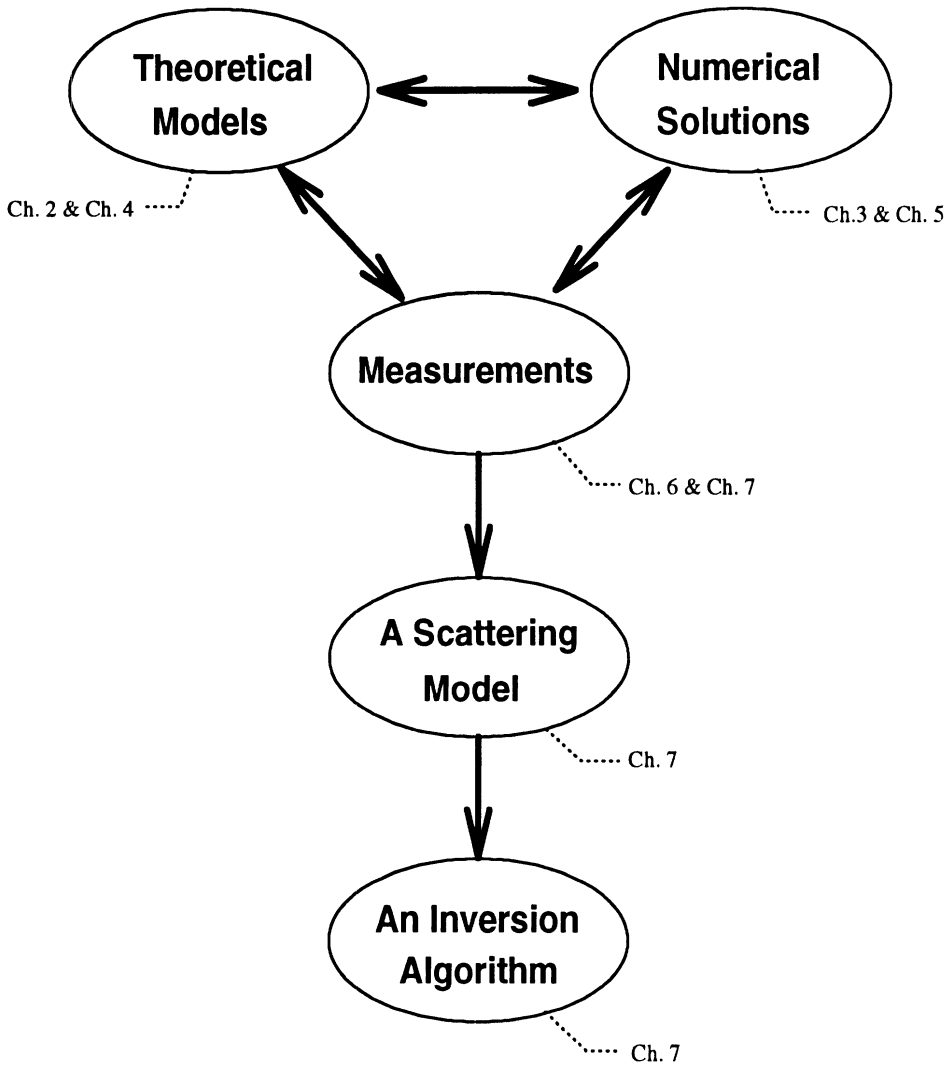

Figure 1.1: Investigation of backscattering from randomly rough surfaces

6 is devoted to the development of an accurate calibration technique for polarimetric measurement of distributed targets. The experimental data acquired using this calibration technique were used to evaluate the existing scattering models. Development of the semi-empirical model and its inversion algorithm is described in Chapter 7. In this chapter the scattering behavior based on the extensive experimental observations and the results derived from the theoretical and the numerical studies are combined to develop the semi-empirical scattering model for the backscattering coefficients, σ°_{vv}, σ°_{hh}, σ°_{hv}. The inversion algorithm can provide an estimate for soil moisture and surface rms height, s, when radar parameters (frequency and incidence angle) are known.

In Chapter 2, classical scattering models are reviewed. In specific, the small perturbation method, the physical optics model and the geometrical optics model are considered.

In Chapter 3, a Monte Carlo method in conjunction with the method of moments is introduced to solve scattering from a one-dimensional conducting surface numerically. To make numerical simulation of random surfaces tractable, finite samples of the random surface must be considered. However, the edges of the finite sample perturb the scattering solution. To suppress the edge contribution a tapered resistive sheet is added to each edge. Using this numerical technique, the phase difference statistics as well as the backscattering coefficients are computed, and the existing scattering models are examined against the numerical calculation.

In Chapter 4, an improved high frequency solution for random surfaces is formulated and evaluated numerically for a one-dimensional surface. Using this formulation, the zeroth- and the first-order classical physical optics approximations are examined.

In Chapter 5, the effect of dielectric inhomogeneity in a soil medium is considered

by developing an efficient numerical technique for one-dimensional inhomogeneous dielectric rough surfaces.

In Chapter 6, an accurate technique for measurement of polarimetric backscatter from distributed targets is introduced. In this technique the polarization distortion matrix of a radar system is completely characterized from the polarimetric response of a sphere over the entire main lobe of the antenna.

In Chapter 7, the experimental procedure and the backscattered data collected from bare soil surfaces with many different roughness and moisture conditions at microwave frequencies are explained. These data are analyzed and compared with the theoretical scattering models. Also they are used to find the dependency of the backscattering coefficients on the radar and the surface parameters. Using the co-polarized and the cross-polarized ratios ($\sigma^{\circ}_{hh}/\sigma^{\circ}_{vv}$, $\sigma^{\circ}_{hv}/\sigma^{\circ}_{vv}$), a semi-empirical scattering model is developed. It is shown that the semi-empirical scattering model provides a very good agreement with independent experimental observations. In this chapter an inversion algorithm for the empirical model is also developed and its performance in estimating the soil moisture and surface roughness parameters is tested.

CHAPTER II

REVIEW OF CLASSICAL MODELS FOR BACKSCATTERING FROM RANDOMLY ROUGH SURFACES

2.1 Introduction

Even though the scattering of electromagnetic waves from a randomly rough surface has been studied for many decades, no exact closed-form solutions have been obtained because of the complexity of the problem. Instead, approximate models are available for a limited range of random surface parameters. The objective of this chapter is to study such approximate analytic models.

In order to study scattering models of random surfaces, it is convenient to treat the rough surface as a particular realization of a random function with given statistical properties. Let $z(x, y)$ be such a random function describing the height distribution of the xy plane. Then, z is a random variable with a probability density function $p(z)$ and a correlation function given as

$$C(\xi) = \langle z(x, y)\, z(x + \xi_x, y + \xi_y) \rangle \,. \tag{2.1}$$

We assume as follows; (1) $z(x, y)$ is stationary in the wider sense. In other word, the probability density function and the correlation function are independent of the coordinate of x and y. (2) The surface is isotropic, which means that the correlation

function depends only on the distance regardless of its direction. (3) $z(x,y)$ is mean-square differentiable with partial derivatives z_x, z_y. This means that there is a function z_x (or z_y) such that

$$\lim_{\Delta x \to 0} = \left\langle \left[\frac{z(x+\Delta x, y) - z(x,y)}{\Delta x} - z_x(x,y) \right]^2 \right\rangle = 0. \tag{2.2}$$

Based on the probability density function and the correlation function, the surface roughness is commonly characterized by two parameters, namely rms height and correlation length [Ulaby et al., 1982]. The rms height s is the standard deviation of the surface height distribution, and the correlation length l is defined as the displacement such that the correlation function is equal to $1/e = 0.367 \cdots$. The rms height m [Ulaby et al., 1982] is also defined as the mean square of the slope distribution which is

$$m = \left\langle z_x^2 \right\rangle^{\frac{1}{2}} = \left\langle z_y^2 \right\rangle^{\frac{1}{2}} = \sqrt{|C''(0)|}, \tag{2.3}$$

where $C''(0)$ is the second derivative of $C(\xi)$ for ξ=0. It is often convenient to use the normalized correlation function (or correlation coefficient function) which is defined as

$$\rho(\xi) = \frac{C(\xi)}{s^2} \tag{2.4}$$

where s is the standard deviation of the probability density function $p(z)$.

Two commonly used classical models are the small perturbation method (SPM) [Rice, 1951] and the Kirchhoff approach (KA) [Beckmann and Spizzichino, 1963]. The SPM can be used for the random surface of which the surface rms height is much smaller than the wavelength and the surface rms slope is relatively small. In SPM, the surface field is expanded in a perturbation series to solve for the scattered field from a random surface. The SPM appears to be exact because this method is using the exact

boundary conditions on the surface, but in practice the infinite series representing the solution converges reasonably quickly only for very slightly rough surfaces.

The KA is applicable to the random surface of which the correlation length is larger than the incident wavelength and the rms height is small enough so that the average radius of curvature is larger than the incident wavelength [Ulaby et al., 1982] where the average radius of curvature R_c is given as

$$R_c = \left[\frac{2}{\pi}\frac{\partial^4 C(0)}{\partial \xi^4}\right]^{-\frac{1}{2}}. \tag{2.5}$$

The KA method employs the so called tangent plane approximation to apply the boundary conditions on the surface. Under the tangent plane approximation, the surface fields at any point of the surface are approximated by the fields that would be present on the tangent plane at that point. However, even with the tangent plane approximation, the scattered field in the Kirchhoff-approximated diffraction integral is still difficult to solve analytically. Therefore, additional assumptions are required to obtain an analytical solution. A commonly used approximation is to expand the integrand of the diffraction integral in terms of the surface slope, keeping only the lower order terms. This additional approximation provides the physical optics (PO) model, which is valid when the surface rms slope is small relative to the wavelength. In the high frequency limit as $k \longrightarrow \infty$, the geometrical optics (GO) model can be obtained using the methods of stationary-phase. The GO model is independent of the frequency, and is valid when the rms height is large relative to the wavelength.

Although the small perturbation method and the Kirchhoff approach are the most common models over the decades for computing the scattering from randomly rough surfaces, many other techniques are introduced recently to extend the validity regions of the two classical models, including the phase perturbation method (PPM) [Winebrenner and Ishimaru, 1985a], the full-wave method (FWM) [Bahar, 1981], and the

integral equation method (IEM) [Fung and Pan, 1987].

The classical models (*i.e.*, SPM, PO, and GO) for two-dimensional dielectric random surfaces are summarized and numerical examples are computed to show the dependency of the backscattering coefficients on the radar and surface parameters in section 2.2 and 2.3.

2.2 Small Perturbation Method

The scattering of electromagnetic waves from a slightly rough surface can be obtained by using the Rayleigh hypothesis to express the reflected and transmitted fields into upward and downward waves, respectively [Rice, 1951]. The surface field amplitudes are then determined from the boundary conditions and the divergence relations, from which the scattered fields can be obtained.

In order to illustrate the Rayleigh hypothesis, let us assume a periodic surface with period L. The scattered fields in $z > B$, where $B \equiv \max z(x,y)$, may be written as

$$\mathbf{E}^s = \sum_{-\infty}^{\infty} \mathbf{A}_{mn} \exp[-ia(mx+ny) - ib(m,n)z] \tag{2.6}$$

where

$$a = \frac{2\pi}{L}, \quad b(m,n) = \begin{cases} \sqrt{k^2 - a^2(M^2+n^2)} & ; \ k^2 > a^2(m^2+n^2) \\ -i\sqrt{a^2(M^2+n^2) - k^2} & ; \ k^2 < a^2(m^2+n^2), \end{cases}$$

and the coefficients $\mathbf{A}_{mn}$ are to be determined. Rayleigh [1945] made the assumption that the series (2.6) with coefficients $\mathbf{A}_{mn}$ was a valid representation for the scattered field not only for $z > B$ but also throughout $z > z(x,y)$. This assumption has come to be known as the *Rayleigh hypothesis*, and it was shown that this hypothesis is valid if $\frac{2\pi}{L}B < 0.448$ in the case of a periodic surface [Millar, 1973].

In this section, the formulation of the SPM is summarized by following closely the derivation in Ch. 12 of [Ulaby et al., 1986]. Considering a plane wave incident upon a two-dimensional dielectric rough surface as shown in Fig. 2.1, the orthonormal coordinate systems are given by $(\hat{v}_i, \hat{h}_i, \hat{k}_i)$ and $(\hat{v}_s, \hat{h}_s, \hat{k}_s)$ with

$$\begin{aligned} \hat{k}_i &= \hat{x}\sin\theta\cos\phi + \hat{y}\sin\theta\sin\phi - \hat{z}\cos\theta \\ \hat{h}_i &= \hat{x}\sin\phi - \hat{y}\cos\phi \\ \hat{v}_i &= \hat{x}\cos\theta\cos\phi + \hat{y}\cos\theta\sin\phi + \hat{z}\sin\theta, \end{aligned} \tag{2.7}$$

$$\begin{aligned} \hat{k}_s &= \hat{x}\sin\theta_s\cos\phi_s + \hat{y}\sin\theta_s\sin\phi_s + \hat{z}\cos\theta_s \\ \hat{h}_s &= \hat{x}\sin\phi_s - \hat{y}\cos\phi_s \\ \hat{v}_s &= -\hat{x}\cos\theta_s\cos\phi_s - \hat{y}\cos\theta_s\sin\phi_s + \hat{z}\sin\theta_s, \end{aligned} \tag{2.8}$$

$$\begin{aligned} \hat{k}_r &= \hat{x}\sin\theta\cos\phi + \hat{y}\sin\theta\sin\phi + \hat{z}\cos\theta \\ \hat{k}_t &= \hat{x}\sin\theta_t\cos\phi_t + \hat{y}\sin\theta_t\sin\phi_t + \hat{z}\cos\theta_t. \end{aligned} \tag{2.9}$$

If we consider only the backscattering direction ($\theta_s = \theta$ and $\phi_s = \pi + \phi$), and set $\phi = 0$ for simplicity, the coordinate system can be simplified as

$$\hat{k}_i = \hat{x}\sin\theta - \hat{z}\cos\theta, \quad \hat{h}_i = -\hat{y}, \quad \hat{v}_i = \hat{x}\cos\theta + \hat{z}\sin\theta, \tag{2.10}$$

$$\hat{k}_s = -\hat{k}_i = -\hat{x}\sin\theta + \hat{z}\cos\theta, \quad \hat{h}_s = \hat{y}, \quad \hat{v}_s = \hat{x}\cos\theta_s + \hat{z}\sin\theta. \tag{2.11}$$

The total field in medium 0 is the sum of the incident, reflected, and scattered fields, where the scattered field in a homogeneous half space may be represented by superimposing plane waves with unknown amplitudes as follows:

$$\mathbf{E}_p = \mathbf{E}_p^s + \mathbf{E}_p^i + \mathbf{E}_p^r, \quad p = v \text{ or } h, \qquad \text{with} \tag{2.12}$$

$$\begin{aligned} \mathbf{E}_p^s &= \tfrac{1}{(2\pi)^2}\int\int_{-\infty}^{\infty} \mathbf{U}^p(k_x, k_y) e^{-ik_x x - ik_y y + ik_z z} dk_x dk_y, \\ \mathbf{E}_p^i &= \hat{p}_i\, e^{ik_0 \hat{k}_i \cdot \mathbf{r}}, \\ \mathbf{E}_p^r &= \hat{p}_r R_p\, e^{ik_0 \hat{k}_r \cdot \mathbf{r}}, \end{aligned} \tag{2.13}$$

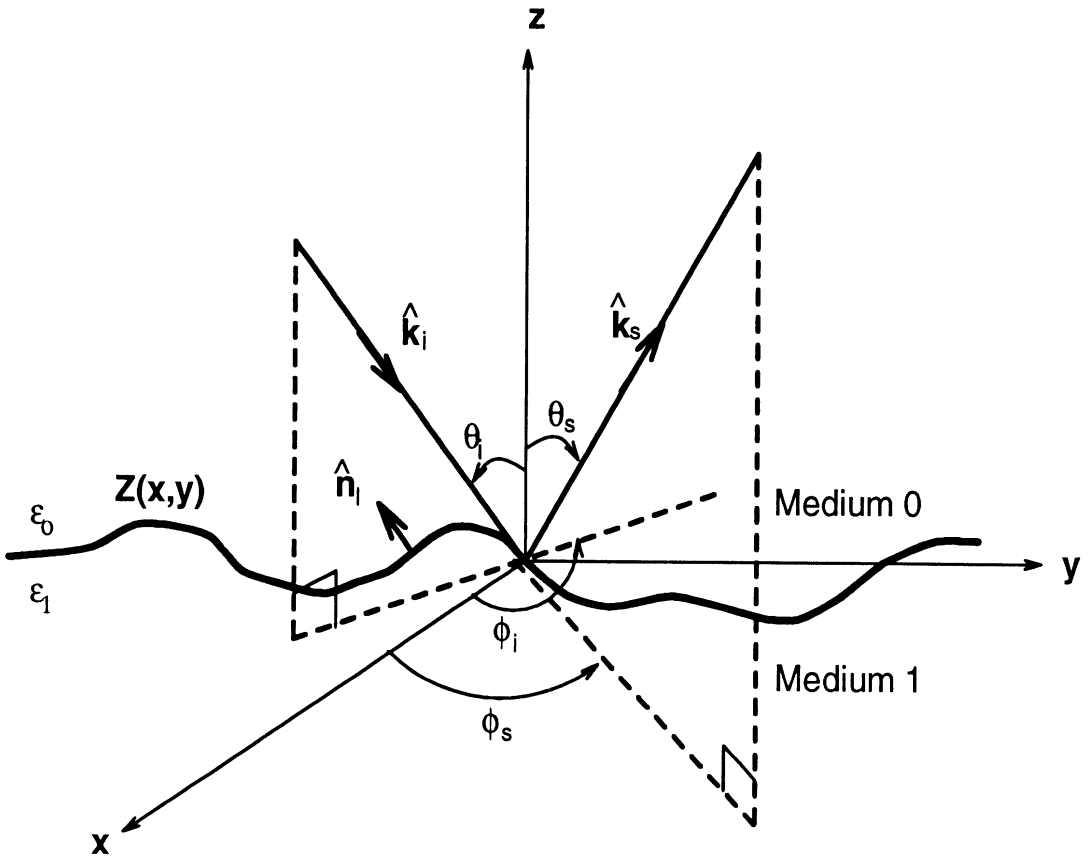

Figure 2.1: Geometry of the scatter problem for a two-dimensional rough surface

where the subscript p stands for v or h which indicates vertically and horizontally polarized incident wave, respectively, R_p is the Fresnel reflection coefficient for p-polarized wave, the $\mathbf{U}^p(k_x, k_y)$ is the unknown to be determined using the boundary conditions, and $k_z = \sqrt{k_0^2 - k_x^2 - k_y^2}$. Similarly, the total field in medium 1 can be given as

$$\mathbf{E}_p^1 = \mathbf{E}_p^{1s} + \mathbf{E}_p^{1t}\,, \quad p = v \text{ or } h, \qquad \text{with} \tag{2.14}$$

$$\begin{aligned} \mathbf{E}_p^{1s} &= \tfrac{1}{(2\pi)^2} \int\int_{-\infty}^{\infty} \mathbf{D}^p(k_x, k_y) e^{-ik_x x - ik_y y - ik_{1z} z} dk_x dk_y, \\ \mathbf{E}_p^{1t} &= \hat{p}_t T_p \, e^{ik_0 \hat{k}_t \cdot \mathbf{r}}, \end{aligned} \tag{2.15}$$

where $T_p = 1 + R_p$ is the Fresnel transmission coefficient for p-polarized wave, and the $\mathbf{D}^p(k_x, k_y)$ is the unknown to be determined. The boundary conditions, $\hat{n} \times (\mathbf{E}_p - \mathbf{E}_p^1) = 0$ and $\hat{n} \times (\mathbf{H}_p - \mathbf{H}_p^1) = 0$, give four equations as follows,

$$\begin{aligned} &\Delta E_y + \tfrac{\partial z}{\partial y} \Delta E_z = 0, \\ &\Delta E_x + \tfrac{\partial z}{\partial x} \Delta E_z = 0, \\ &\tfrac{\partial \Delta E_x}{\partial z} - \tfrac{\partial \Delta E_z}{\partial x} + \tfrac{\partial z}{\partial y} \left(\tfrac{\partial \Delta E_y}{\partial x} - \tfrac{\partial \Delta E_x}{\partial y} \right) = 0, \\ &\tfrac{\partial \Delta E_z}{\partial y} - \tfrac{\partial \Delta E_y}{\partial z} + \tfrac{\partial z}{\partial y} \left(\tfrac{\partial \Delta E_y}{\partial x} - \tfrac{\partial \Delta E_x}{\partial y} \right) = 0, \end{aligned} \tag{2.16}$$

where $\Delta E_x = E_x - E_x^1$, $\Delta E_y = E_y - E_y^1$, and $\Delta E_z = E_z - E_z^1$ on the surface. The divergence relations, $\nabla \cdot \mathbf{E}_p = 0$ and $\nabla \cdot \mathbf{E}_p^1 = 0$, give two more independent equations,

$$\begin{aligned} \tfrac{\partial E_x}{\partial x} + \tfrac{\partial E_y}{\partial y} + \tfrac{\partial E_z}{\partial z} &= 0, \\ \tfrac{\partial E_x^1}{\partial x} + \tfrac{\partial E_y^1}{\partial y} + \tfrac{\partial E_z^1}{\partial z} &= 0, \end{aligned} \tag{2.17}$$

The six relations given by (2.16) and (2.17) permit the six unknown field amplitudes U_x^p, U_y^p, U_z^p, D_x^p, D_y^p, and D_z^p in (2.12)-(2.15) to be determined.

Since we assume $k_z z$ to be a small quantity, we can expand all exponentials involving $k_z z$ in Taylor series,

$$e^{\pm ik_z z(x,y)} = 1 \pm ik_z z(x, y) - \cdots. \tag{2.18}$$

The surface field amplitudes can also be expanded in a perturbation series,

$$\begin{aligned} \mathbf{U}^p(k_x, k_y) &= \mathbf{U}_1^p + \mathbf{U}_2^p + \cdots, \\ \mathbf{D}^p(k_x, k_y) &= \mathbf{D}_1^p + \mathbf{D}_2^p + \cdots. \end{aligned} \tag{2.19}$$

Substituting (2.18) and (2.19) into (2.16) and (2.17) up to the first order in magnitude, we can get six algebraic equations for the six unknown amplitudes, U_{x1}^p, U_{y1}^p, U_{z1}^p, D_{x1}^p, D_{y1}^p, and D_{z1}^p, where subscript 1 indicates the first order solution.

Once we find the six unknown surface field amplitudes, the q-polarized scattered fields can be computed in case of the p-polarized incident fields as

$$E_{qp}^s = \hat{q}_s \cdot \mathbf{E}_p^s, \tag{2.20}$$

where $\hat{q}_s$ is $\hat{h}_s$ or $\hat{v}_s$, and $\mathbf{E}_p^s$ is the scattered field for a p-polarized incident wave.

The backscattered fields are given for backscattering direction in [Ulaby et al., 1986],

$$E_{qp}^s = \frac{1}{(2\pi)^2} \int\int_{-\infty}^{\infty} \left\{-i2k\cos\theta\alpha_{qp} Z(k_x + k\sin\theta, k_y)\right\} e^{-ik_x x - ik_y y + ik_z z} dk_x dk_y, \tag{2.21}$$

where

$$\begin{aligned} \alpha_{hh} &= \frac{-\cos\theta + \sqrt{\epsilon_r - \sin^2\theta}}{\cos\theta + \sqrt{\epsilon_r - \sin^2\theta}}, \\ \alpha_{vv} &= (\epsilon_r - 1)\frac{\sin^2\theta - \epsilon_r(1+\sin^2\theta)}{\left(\epsilon_r\cos\theta + \sqrt{\epsilon_r - \sin^2\theta}\right)^2}, \\ \alpha_{vh} &= \alpha_{hv} = 0. \end{aligned} \tag{2.22}$$

Assuming $k_z z << 1$, the ensemble average intensity can be approximated as

$$\begin{aligned} \left\langle E_{qp}^s E_{qp}^{s*} \right\rangle \cong \frac{1}{(2\pi)^4} \int\int\int\int_{-\infty}^{\infty} (2k\cos\theta)^2 \left|\alpha_{qp}\right|^2 \left\langle ZZ^* \right\rangle \\ e^{-i(k_x - k_x')x - i(k_y - k_y')y} dk_x dk_y dk_x' dk_y'. \end{aligned} \tag{2.23}$$

Since $Z(k_x, k_y)$ is the Fourier transform of the random function $z(x, y)$ representing the surface height distribution,

$$Z(k_x, k_y) = \int\int_{-\infty}^{\infty} z(x, y) e^{ik_x x - ik_y y} dx dy, \tag{2.24}$$

the ensemble average of ZZ^* can be computed as

$$\begin{aligned}\left\langle Z(k_x,k_y)Z^*(k_x',k_y')\right\rangle &= \int\int_{-\infty}^{\infty}\langle z(x,y)z(x',y')\rangle\, e^{i(k_x-k_x')x'+i(k_y-k_y')y'} \\ &\quad \cdot e^{ik_x(x-x')+ik_y(y-y')}dxdydx'dy' \\ &= W(k_x,k_y)\delta(k_x-k_x')\delta(k_y-k_y'), \end{aligned} \tag{2.25}$$

with

$$W(k_x,k_y) = \int\int_{-\infty}^{\infty} C(u,v)e^{ik_xu+ik_yv}dudv, \tag{2.26}$$

where $u = x-x'$, $v = y-y'$, and $C(u,v) = \langle z(x,y)z(x',y')\rangle$. $W(k_x,k_y)$ is the Fourier transform of the correlation function and hence is the surface roughness spectrum. Substituting (2.25) into (2.23) and integrating with respect to k_x' and k_y', we get

$$\begin{aligned}\left\langle \left|E_{qp}^s\right|^2\right\rangle &= \frac{1}{(2\pi)^2}(2k\cos\theta)^2\left|\alpha_{qp}\right|^2\int\int_{-\infty}^{\infty} W(k_x+k\sin\theta,k_y)dk_xdk_y \\ &\triangleq \int\int_{-\infty}^{\infty} f_{qp}(k_x,k_y)dk_xdk_y \end{aligned} \tag{2.27}$$

Denoting $\Delta\left\langle E_{qp}E_{qp}^*\right\rangle$ as the intensity within the narrow spectral bands $\Delta k_x\Delta k_y$ centered at k_x and k_y,

$$\Delta\left\langle E_{qp}E_{qp}^*\right\rangle \approx f_{qp}(k_x,k_y)\Delta k_x\Delta k_y = f_{qp}(k_x,k_y)k^2\cos\theta_s\Delta\Omega_s. \tag{2.28}$$

The averaged intensity P received at a distance r from the illuminated area A is equal to the average power per unit solid angle times the solid angle subtended by the receiver,

$$P_{qp} = \frac{\Delta\left\langle E_{qp}E_{qp}^*\right\rangle}{\Delta\Omega_s}\times\frac{A\cos\theta_s}{r^2} = \frac{Ak^2\cos^2\theta_s}{r^2}f_{qp}(k_x,k_y). \tag{2.29}$$

Since the scattering coefficient is defined in terms of P by the product of the angle and the solid angle subtended by the receiver,

$$\sigma_{qp}^{\circ} = \lim_{r\to\infty} 4\pi r^2\frac{P}{A}\frac{Re\{1/\eta_s^*\}}{Re\{1/\eta^*\}}, \tag{2.30}$$

σ°_{qp} for backscattering direction is computed as

$$\sigma^{\circ}_{qp} = \frac{4}{\pi} k_0^4 \cos^4\theta \, |\alpha_{qp}|^2 \, W(2k\sin\theta, 0), \tag{2.31}$$

where α_{qp} is given in (2.22).

Two typical normalized correlation functions are the Gaussian and exponential functions given as, respectively,

$$C_G(\xi) = \sigma^2 \exp\left[-\frac{\xi^2}{l^2}\right] = \sigma^2 \rho_G(\xi), \tag{2.32}$$

$$C_e(\xi) = \sigma^2 \exp\left[-\frac{\xi}{l/\sqrt{2}}\right] = \sigma^2 \rho_e(\xi), \tag{2.33}$$

in which

$$\pi l^2 = \int_{-\infty}^{\infty} \rho(u, v) du dv,$$

where l is the correlation length, πl^2 is the correlation area [Eftimu and Pan, 1990], and ξ is $\sqrt{u^2 + v^2}$ for a two-dimensional rough surface. For a Gaussian correlation function of (2.32), the surface roughness spectrum is

$$W_G(2k\sin\theta, 0) = \pi s^2 l^2 e^{-(kl\sin\theta)^2}, \tag{2.34}$$

while the surface roughness spectrum for an exponential correlation function of (2.33) is

$$W_e(2k\sin\theta, 0) = \pi s^2 l^2 \left[1 + 2(kl\sin\theta)^2\right]^{-\frac{3}{2}}. \tag{2.35}$$

When we have a numerical form of correlation instead of a functional form, *e.g.*, a correlation measured directly from a random surface, the roughness spectrum can be computed numerically in the following form;

$$\begin{aligned} W_e(2k\sin\theta, 0) &= s^2 \int\int_{-\infty}^{\infty} \rho(\xi) e^{i2k\sin\theta u} du dv \\ &= 2\pi s^2 \int_0^{\infty} \rho(\xi) \xi J_0(2k\sin\theta\xi) d\xi, \end{aligned}$$

where $J_0(x)$ is the first kind Bessel function of zeroth order, which can be evaluated approximately using the polynomials given in [Abramowitz and Stegun, Ch.9, 1972].

If above computation was extended to second order, the cross-polarized term would not be zero in the backscattering direction. The second-order backscattering coefficient for the cross-polarization has been shown in [Valenzuela, 1967] as,

$$\sigma^\circ_{vh} = \sigma^\circ_{hv} = \frac{1}{(2\pi)^2}\frac{2}{\pi}k^4\cos^2\theta\,|(\epsilon_r - 1)(R_v - R_h)|^2$$
$$\cdot \int\int_{-\infty}^{\infty} \frac{k_x^2 k_y^2}{|k_{1z} + \epsilon_r k_z|^2} W(k_x - k\sin\theta, k_y)W(k_x + k\sin\theta, k_y)dk_x dk_y \qquad (2.36)$$

where $k_z = \sqrt{k_0^2 - k_x^2 - k_y^2}$, $k_{1z} = \sqrt{\epsilon_r k_0^2 - k_x^2 - k_y^2}$, and R_v, R_h are the Fresnel reflection coefficients for vertical and horizontal polarization, respectively. The cross-polarized backscattering coefficients can be obtained by evaluating a two-fold numerical integration with a known surface roughness spectrum $W(k_x \pm k\sin\theta, k_y)$. $W(k_x \pm k\sin\theta, k_y)$ for Gaussian and exponential correlation functions can be computed, respectively,

$$W_G(k_x \pm k\sin\theta, k_y) = s^2 \int\int_{-\infty}^{\infty} e^{-\frac{u^2+v^2}{l^2}} e^{i(k_x \pm k\sin\theta)u + ik_y v}dudv$$
$$= \pi s^2 l^2 e^{-\frac{(k_x \pm k\sin\theta)^2 l^2}{4}} e^{-\frac{k_y^2 l^2}{4}}, \qquad (2.37)$$

$$W_e(k_x \pm k\sin\theta, k_y) = s^2 \int\int_{-\infty}^{\infty} e^{-\frac{\sqrt{u^2+v^2}}{l/\sqrt{2}}} e^{i(k_x \pm k\sin\theta)u + ik_y v}dudv$$
$$= s^2 \int_0^{\infty}\int_0^{2\pi} e^{-\frac{\xi}{l/\sqrt{2}}} e^{i(k_x \pm k\sin\theta)\xi\sin\psi} e^{ik_y\xi\cos\psi}\xi d\xi d\psi$$
$$= s^2 2\pi \int_0^{\infty} \xi e^{-\frac{\xi}{l/\sqrt{2}}} J_0\left(\xi\sqrt{(k_x \pm k\sin\theta)^2 + k_y^2}\right)d\xi$$
$$= \pi s^2 l^2 \left[1 + \left\{(k_x \pm k\sin\theta)^2 + k_y^2\right\} l^2/2\right]^{-\frac{3}{2}}. \qquad (2.38)$$

The validity conditions associated with the small perturbation method are given by [Ulaby et al., 1986; Chen and Fung, 1988] as

$$ks < 0.3, \quad m < 0.3, \quad \text{and}, \quad kl < 3.0. \qquad (2.39)$$

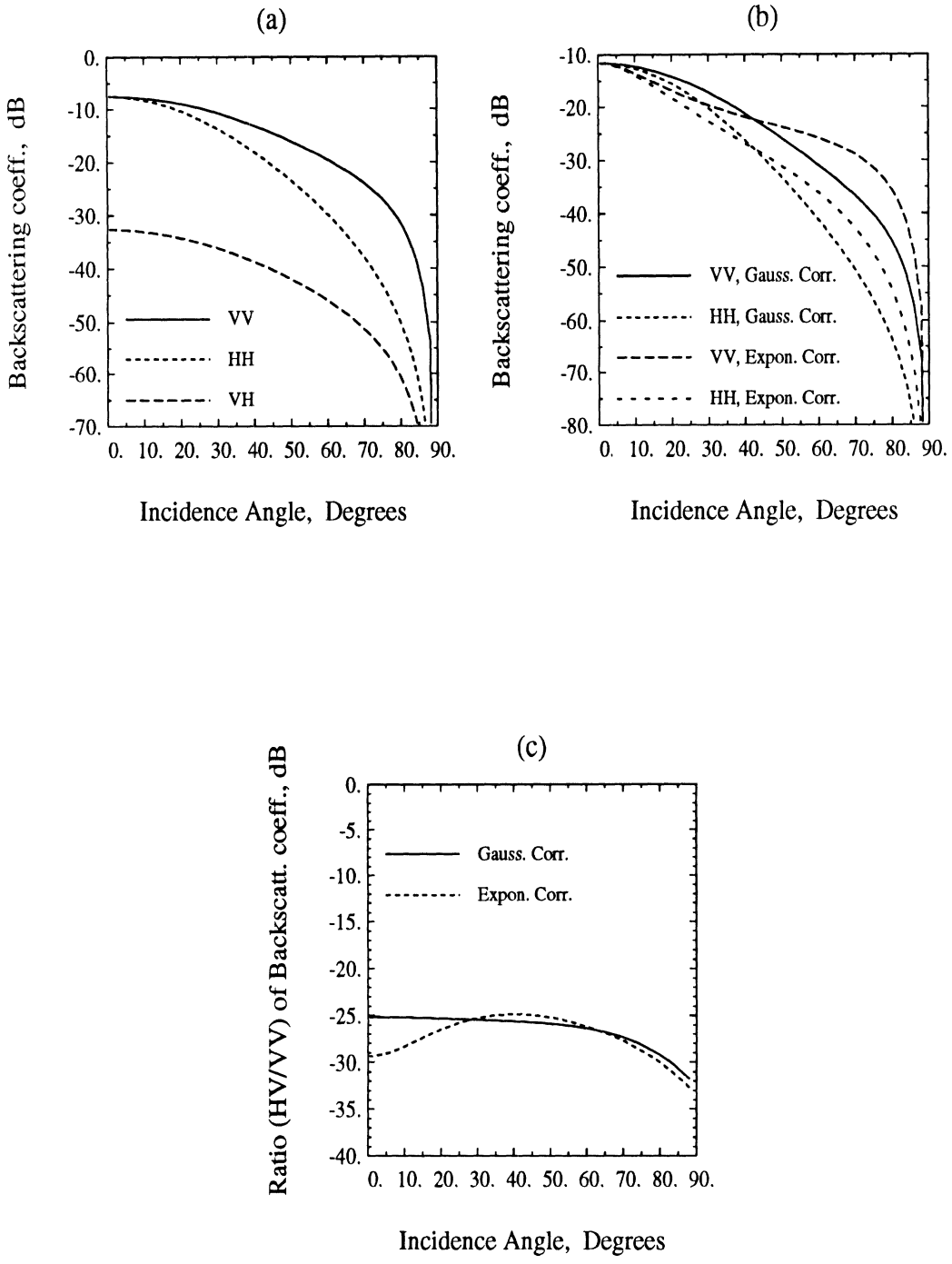

Figure 2.2: Backscattering coefficients of a rough surface with $ks = 0.2, kl = 2.0$, and $\epsilon_r = (10, 1)$ using the SPM; (a) polarization response of the surface of an exponential correlation, (b) σ°_{hh} and σ°_{vv}, and (c) the ratio $\sigma^\circ_{hv}/\sigma^\circ_{vv}$ of the surface with two different correlation functions.

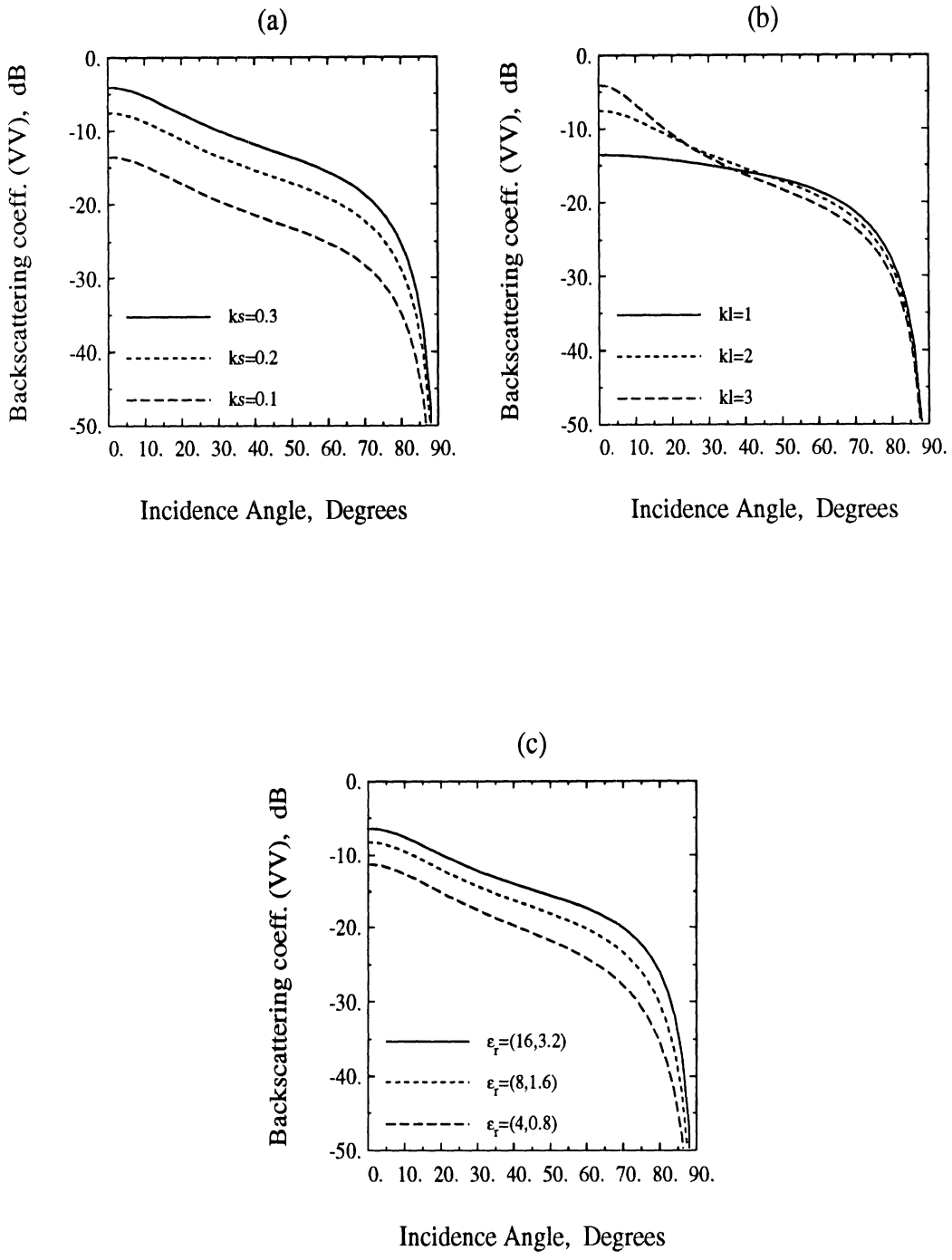

Figure 2.3: Backscattering coefficients at vv-polarization using the SPM for the surface of an exponential correlation, (a) $kl = 2.0$, $\epsilon_r = (10, 2)$, and the various values of ks, (b) $ks = 0.2$, $\epsilon_r = (10, 2)$, and the various values of kl, and (a) $ks = 0.2$, $kl = 2.0$, and the various values of ϵ_r.

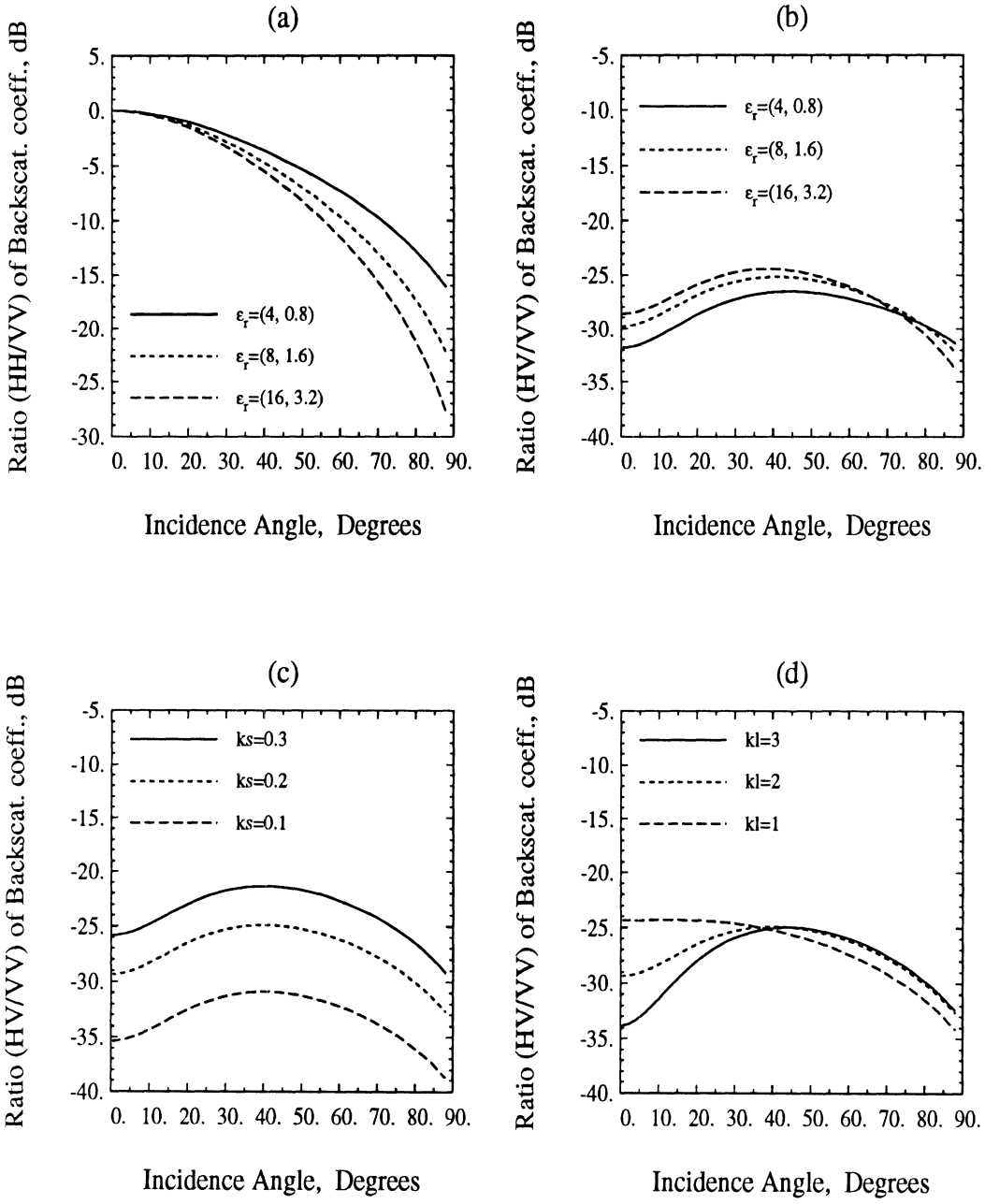

Figure 2.4: The ratios of the backscattering coefficients at vv-polarization using the SPM for the surface of an exponential correlation; (a) $\sigma^\circ_{hh}/\sigma^\circ_{hh}$ and (b) $\sigma^\circ_{hv}/\sigma^\circ_{hh}$ for $ks = 0.2$, $kl = 2.0$, and different ϵ_r, and the ratio $\sigma^\circ_{hv}/\sigma^\circ_{hh}$ for (c) $kl = 2.0$, $\epsilon_r = (10, 2)$, and different ks, and (d) $ks = 0.2$, $\epsilon_r = (10, 2)$, and different kl.

The backscattering coefficients for various rough surfaces computed using the SPM are illustrated in Figs. 2.2-2.4. The polarization responses of a rough surface with $ks = 0.2$, $kl = 2.0$ and $\epsilon_r = (10, 2)$ are plotted as a function of the incidence angle in Figs. 2.2(a)-(c). σ°_{vv} is higher than σ°_{hh} and the ratio $\sigma^\circ_{vv}/\sigma^\circ_{hh}$ increases as θ increases. The cross polarized response σ°_{hv} is much lower than co-polarized response and the ratio of $\sigma^\circ_{hv}/\sigma^\circ_{vv}$ is constant in a wide range of incidence angle as shown in Figs. 2.2(a)-(c). The angular pattern of the backscattering coefficients depends on the type of correlation functions as shown in Fig. 2.2(b).

The sensitivities of σ°_{vv} to surface parameters, ks, kl, and ϵ_r, are illustrated in Figs. 2.3(a), (b), and (c), respectively, for a surface with an exponential correlation function. Figure 2.3(a) shows that σ°_{vv} is very sensitive to ks where $k = 2\pi/\lambda$ and s is the rms height. When kl increases, only the slope of the angular pattern of σ°_{vv} increases especially in the range of small incidence angles, but the level of σ°_{vv} does not change as shown in Fig. 2.3(b). Increasing the dielectric constant ϵ_r also increases σ°_{vv} by a constant value for all incidence angles as shown in Fig. 2.3(c) with less sensitivity compared with the sensitivity to ks. Figures 2.4(a)-(c) show that sensitivities of the ratios, $\sigma^\circ_{hh}/\sigma^\circ_{vv}$ and $\sigma^\circ_{hv}/\sigma^\circ_{vv}$, as functions of surface parameters, ks, kl, and ϵ_r, of a rough surface having an exponential correlation. The ratio $\sigma^\circ_{hh}/\sigma^\circ_{vv}$ is just the ratio of $|\alpha_{hh}|^2/|\alpha_{vv}|^2$ (2.22) which is independent of ks and kl. The ratio $\sigma^\circ_{hh}/\sigma^\circ_{vv}$, however, depends on ϵ_r and θ as shown in Fig. 2.4(a), *i.e.*, $\sigma^\circ_{hh}/\sigma^\circ_{vv}$ decreases as θ increases and the rate of change increases as ϵ_r increases. The ratio $\sigma^\circ_{hv}/\sigma^\circ_{vv}$ is a weak function of ϵ_r and kl but a strong function of ks as shown in Figs. 2.4(b)-(d). $\sigma^\circ_{hv}/\sigma^\circ_{vv}$ decreases by 10 dB as ks decreases from 0.3 to 0.1 for a rough surface with $kl = 2.0$ and $\epsilon_r = (10, 2)$.

2.3 Kirchhoff Approach

The vector formulation of the Kirchhoff method has been often formulated by Stratton-Chu representation [Stratton, 1941]. The scattered field outside or on the surface can be represented by the Hertz vectors which are simple and valid for open and closed surfaces [Senior, 1992].

For a plane wave incident upon a random surface as shown in Fig. 2.1, the orthonormal coordinate systems $(\hat{v}_i, \hat{h}_i, \hat{k}_i)$ and $(\hat{v}_s, \hat{h}_s, \hat{k}_s)$ are given in (2.7)-(2.7). The scattered field $\mathbf{E}^s(\mathbf{r})$ above or on the surface $z(x', y')$ can be written in terms of the Hertz vectors,

$$\mathbf{E}^s(\mathbf{r}) = \nabla \times \nabla \times \Pi_e(\mathbf{r}) + ik_o Z_o \nabla \times \Pi_m(\mathbf{r}) \tag{2.40}$$

The electric and magnetic Hertz vectors, Π_e^s and Π_m^s, are represented using the surface current, $\mathbf{J}_e(\mathbf{r}') = \hat{n}' \times \mathbf{H}(\mathbf{r}')$ and $\mathbf{J}_m(\mathbf{r}') = -\hat{n}' \times \mathbf{E}(\mathbf{r}')$, which are equivalent sources, respectively,

$$\Pi_e^s(\mathbf{r}) = \frac{iZ_o}{k_o} \int\int_s \hat{n}' \times \mathbf{H}(\mathbf{r}') G_o(\mathbf{r}, \mathbf{r}') ds' \tag{2.41}$$

$$\Pi_m^s(\mathbf{r}) = -\frac{iY_o}{k_o} \int\int_s \hat{n}' \times \mathbf{E}(\mathbf{r}') G_o(\mathbf{r}, \mathbf{r}') ds' \tag{2.42}$$

where $G_o(\mathbf{r}, \mathbf{r}')$ is the free-space scalar Green's function given by

$$G_0(\mathbf{r}, \mathbf{r}') = \frac{e^{ik_0|\mathbf{r}-\mathbf{r}'|}}{4\pi|\mathbf{r}-\mathbf{r}'|} \tag{2.43}$$

assuming the time dependence of e^{-iwt}. In the far field ($r > 2D^2/\lambda_0$), the vector operator $\nabla\times$ and the Green's function can be approximated as follows;

$$\begin{aligned} &\nabla \times (\cdots) \approx ik_0 \hat{k}_s \times (\cdots) \\ &G_0(\mathbf{r}, \mathbf{r}') \approx \tfrac{\exp[ik_0 r]}{4\pi r} \exp[-ik_0 \hat{k}_s \cdot \mathbf{r}']. \end{aligned} \tag{2.44}$$

Substituting (2.44) into (2.41) and (2.42), the scattered fields in (2.40) can be obtained in terms of the surface fields,

$$\mathbf{E}^s(\mathbf{r}) = \frac{ik_0}{4\pi r} e^{ik_0 r} \hat{k}_s \times \int\int_S \left[(\hat{n}' \times \mathbf{E}(\mathbf{r}')) - Z_0 \hat{k}_s \times (\hat{n}' \times \mathbf{H}(\mathbf{r}')) \right] e^{-ik_0 \hat{k}_s \cdot \mathbf{r}'} \, ds', \quad (2.45)$$

which is the same form as what has been derived from the Stratton-Chu representation through quite complicated computation [Ulaby et al., 1982].

In order to find the tangential surface fields $\hat{n}' \times \mathbf{E}(\mathbf{r}')$ and $\hat{n}' \times \mathbf{H}(\mathbf{r}')$, we assume the surface fields at any point of the surface can be represented by the fields on the tangent plane at that point (tangent plane approximation). Let the incident field be

$$\mathbf{E}^i = \hat{a} e^{ik_0 \hat{k}_i \cdot \mathbf{r}}, \quad (2.46)$$

where $\hat{a}$ is a unit polarization vector. We can define a local coordinate system $(\hat{t}, \hat{d}, \hat{k}_i)$ for the locally flat tangent plane such that

$$\hat{t} = \frac{\hat{k}_i \times \hat{n}_l}{\left| \hat{k}_i \times \hat{n}_l \right|}, \quad \hat{d} = \hat{k}_i \times \hat{t}, \quad \hat{k}_i = \hat{t} \times \hat{d}, \quad (2.47)$$

where $\hat{n}_l$ is a unit normal vector of the tangent plane, which is given by

$$\hat{n}_l = \frac{-Z_x \hat{x} - Z_y \hat{y} + \hat{z}}{\sqrt{Z_x^2 + Z_y^2 + 1}}, \quad (2.48)$$

and Z_x and Z_y are the local slopes in the x and y directions, respectively,

$$Z_x(x', y') = \frac{\partial z(x', y')}{\partial x'}, \quad \text{and} \quad Z_y(x', y') = \frac{\partial z(x', y')}{\partial y'}. \quad (2.49)$$

The electric and magnetic incident fields can be decomposed into the locally perpendicular and parallel polarizations using the local coordinate system,

$$\begin{aligned} \mathbf{E}^i &= \left[(\hat{a} \cdot \hat{t}) \hat{t} + (\hat{a} \cdot \hat{d}) \hat{d} \right] e^{ik_0 \hat{k}_i \cdot \mathbf{r}'} \quad \text{and} \\ \mathbf{H}^i &= \tfrac{1}{Z_0} \hat{k}_i \times \left[(\hat{a} \cdot \hat{t}) \hat{t} + (\hat{a} \cdot \hat{d}) \hat{d} \right] e^{ik_0 \hat{k}_i \cdot \mathbf{r}'}, \end{aligned} \quad (2.50)$$

respectively. Then, the electric and magnetic local reflected fields are, respectively,

$$\begin{aligned} \mathbf{E}^r &= \left[R_{lh}(\hat{a}\cdot\hat{t})\hat{t} + R_{lv}(\hat{a}\cdot\hat{d})\hat{d}\right] e^{ik_0\hat{k}_i\cdot\mathbf{r}'} \quad \text{and} \\ \mathbf{H}^r &= \tfrac{1}{Z_0}\hat{k}_i \times \left[R_{lh}(\hat{a}\cdot\hat{t})\hat{t} + R_{lv}(\hat{a}\cdot\hat{d})\hat{d}\right] e^{ik_0\hat{k}_i\cdot\mathbf{r}'}, \end{aligned} \tag{2.51}$$

where R_{lh} and R_{lv} are the horizontal and vertical Fresnel reflection coefficients for the local angle θ_{li}, respectively.

Using the boundary conditions of

$$\begin{aligned} \mathbf{E}(\mathbf{r}') &= \mathbf{E}^i(\mathbf{r}') + \mathbf{E}^r(\mathbf{r}') \quad \text{and} \\ \mathbf{H}(\mathbf{r}') &= \mathbf{H}^i(\mathbf{r}') + \mathbf{H}^r(\mathbf{r}') \quad \text{(on the surface)}, \end{aligned} \tag{2.52}$$

we can obtain the following relations,

$$\begin{aligned} \hat{n}_l \times \mathbf{E}(\mathbf{r}') &= \left[(1+R_{lh})(\hat{a}\cdot\hat{t})(\hat{n}_l\times\hat{t}) - (1-R_{lv})(\hat{a}\cdot\hat{d})(\hat{n}_l\cdot\hat{k}_i)\hat{t}\right] e^{ik_0\hat{k}_i\cdot\mathbf{r}'} \quad \text{and} \\ \hat{n}_l \times \mathbf{H}(\mathbf{r}') &= \tfrac{1}{Z_0}\left[(-1+R_{lh})(\hat{a}\cdot\hat{t})(\hat{n}_l\cdot\hat{k}_i)\hat{t} - (1+R_{lv})(\hat{a}\cdot\hat{d})(\hat{n}_l\times\hat{t})\right] e^{ik_0\hat{k}_i\cdot\mathbf{r}'}. \end{aligned} \tag{2.53}$$

Then, the $\hat{b}$-polarized scattered field from a locally flat plane for the $\hat{a}$-polarized incident field can be computed by substituting (2.53) into (2.45),

$$E^s_{ba} = \hat{b}\cdot\mathbf{E}^s_a(\mathbf{r}) = D_0 \int\int_S f_{ba} e^{ik_0\hat{k}_d\cdot\mathbf{r}'}\, dxdy \tag{2.54}$$

with

$$\begin{aligned} D_0 &= \tfrac{ik_0}{4\pi r}e^{ik_0 r} \\ \hat{k}_d &= \hat{k}_i - \hat{k}_s \\ f_{ba} &= \hat{b}\cdot\left\{\hat{k}_s\times[\hat{n}_l\times\mathbf{E}_a(\mathbf{r}')] + Z_0\,[\hat{n}_l\times\mathbf{H}_a(\mathbf{r}')]\right\}\sqrt{Z_x^2+Z_y^2+1}, \end{aligned} \tag{2.55}$$

where the subscripts a and b can be v and h which indicate the vertical and horizontal polarization, respectively.

For the backscattering direction, the scattering amplitudes f_{ba} are obtained after algebraic computation using the coordinate system given in (2.10), (2.11), (2.47), and

(2.48),

$$f_{hh} = \frac{2(\cos\theta + \sin\theta Z_x)[R_{lh}(Z_x\cos\theta - \sin\theta)^2 - R_{lv}Z_y^2]}{(Z_x\cos\theta - \sin\theta)^2 + Z_y^2} \tag{2.56}$$

$$f_{vv} = \frac{2(\cos\theta + \sin\theta Z_x)[R_{lv}(Z_x\cos\theta - \sin\theta)^2 - R_{lh}Z_y^2]}{(Z_x\cos\theta - \sin\theta)^2 + Z_y^2} \tag{2.57}$$

$$f_{vh} = f_{vh} = \frac{2(\cos\theta + \sin\theta Z_x)(\sin\theta - Z_x\cos\theta)(R_{lv} + R_{lh})Z_y}{(Z_x\cos\theta - \sin\theta)^2 + Z_y^2} \tag{2.58}$$

with

$$R_{lh} = \frac{Z_x\sin\theta + \cos\theta - \sqrt{\epsilon_r(1 + Z_x^2 + Z_y^2) - Z_y^2 - (Z_x\cos\theta - \sin\theta)^2}}{Z_x\sin\theta + \cos\theta + \sqrt{\epsilon_r(1 + Z_x^2 + Z_y^2) - Z_y^2 - (Z_x\cos\theta - \sin\theta)^2}}, \tag{2.59}$$

$$R_{lv} = \frac{\epsilon_r(Z_x\sin\theta + \cos\theta) - \sqrt{\epsilon_r(1 + Z_x^2 + Z_y^2) - Z_y^2 - (Z_x\cos\theta - \sin\theta)^2}}{\epsilon_r(Z_x\sin\theta + \cos\theta) + \sqrt{\epsilon_r(1 + Z_x^2 + Z_y^2) - Z_y^2 - (Z_x\cos\theta - \sin\theta)^2}}, \tag{2.60}$$

where the local Fresnel reflection coefficients are obtained using

$$\cos\theta_{li} = -\hat{n}_l \cdot \hat{k}_i = \frac{Z_x\sin\theta + \cos\theta}{\sqrt{Z_x^2 + Z_y^2 + 1}}.$$

Consequently, the backscattered mean intensity is given as the ensemble average of the product of the backscattered field and its complex conjugate,

$$\langle E_{ba}^s E_{ba}^{s*}\rangle = |D_0|^2 \int\int_{-L}^{L} dx_1 dy_1 \int\int_{-L}^{L} dx_2 dy_2 e^{ik_{dx}(x_1 - x_2)} \cdot \left\langle f_{ba}(Z_{x_1}, Z_{y_1}) f_{ba}^*(Z_{x_2}, Z_{y_2}) e^{ik_{dz}(z_1 - z_2)} \right\rangle, \tag{2.61}$$

where z_d, Z_{x_1}, Z_{x_2}, Z_{y_1}, and Z_{y_2} form a random vector, $|D_0|^2 = k_0^2/(4\pi r)^2$, $z_1 = z(x_1, y_1)$, $z_2 = z(x_2, y_2)$, and $z_d = z_1 - z_2$. Since the integrals of the mean intensity are still very difficult to evaluate analytically, we need additional approximations to get a closed form of the mean intensity.

The validity conditions for this kirchhoff approach are given [Ulaby et al., 1982] as

$$kl > 6 \quad \text{and} \quad R_c > \lambda \quad \left(l^2 > 2.76s\lambda \quad \text{for a Gaussian correlation}\right) \tag{2.62}$$

where R_c is the average radius of curvature given in (2.5).

2.3.1 Physical Optics Model

A commonly used approximation is to expand the integrand in (2.45), $f_{ba}(Z_x, Z_y)$, about zero slopes and keep only the first few terms as follows;

$$f_{ba}(Z_x, Z_y) = f_{ba}(0,0) + Z_x \frac{\partial f_{ba}}{\partial Z_x}\bigg|_{Z_x=Z_y=0} + Z_y \frac{\partial f_{ba}}{\partial Z_y}\bigg|_{Z_x=Z_y=0} + \cdots. \tag{2.63}$$

For surfaces with a small rms slope, the scattering amplitude $f_{ba}(Z_x, Z_y)$ can be approximated by the first term of the series (2.63) [Tsang et al., 1985] where

$$\begin{aligned} f_{hh}(0,0) &= 2\cos\theta R_h \\ f_{vv}(0,0) &= 2\cos\theta R_v \\ f_{vh}(0,0) &= f_{hv}(0,0) = 0 \\ R_h, R_v &= \text{ Fresnel reflection coefficients.} \end{aligned} \tag{2.64}$$

This approximation may be called *zeroth order approximation* because the slope terms of Z_x and Z_y are ignored. With this approximation, the cross-polarized backscattered fields are zero as seen in the above equations. Since $f_{ba}(0,0)f_{ba}^*(0,0)$ is not dependent on the random variables anymore, the ensemble average term is given as

$$\left\langle f_{ba}(Z_{x_1}, Z_{y_1}) f_{ba}^*(Z_{x_2}, Z_{y_2}) e^{ik_{dz}(z_1 - z_2)} \right\rangle = |f_{ba}(0,0)|^2 \left\langle e^{ik_{dz}(z_1 - z_2)} \right\rangle \tag{2.65}$$

When the randomly rough surface is assumed to have a stationary Gaussian height distribution,

$$p_z(z) = \frac{1}{\sqrt{2\pi}s} e^{-\frac{z^2}{2s^2}} \tag{2.66}$$

where s is the standard deviation of the surface height distribution, the characteristic function for a Gaussian random vector [Stark and Woods, 1986] is

$$\Phi_{\bar{\xi}}(\bar{\omega}) \triangleq \left\langle e^{i\bar{\omega}^t \bar{\xi}} \right\rangle = \exp\left[-\frac{1}{2} \sum_{m=1}^{M} \sum_{n=1}^{N} \omega_m \omega_n \left\langle \xi_m \xi_n \right\rangle \right] \tag{2.67}$$

in case of zero mean ($\overline{\mu} = \overline{0}$), where $\overline{\xi}$ is a random vector and $\overline{\omega}$ is a parameter vector. Therefore, the ensemble average in (2.65) can be represented as

$$\left\langle e^{ik_{dz}(z_1 - z_2)} \right\rangle = e^{-(k_{dz})^2 s^2 [1 - \rho(u,v)]} \tag{2.68}$$

where $\rho(u, v)$ is the normalized correlation function given in (2.4). Changing variables in a double integral, $u = x_1 - x_2$, $v = y_1 - y_2$, and using the characteristic function of (2.68), the backscattered mean intensity with zeroth order approximation is obtained in the form of

$$\left\langle |E^s_{aa}|^2 \right\rangle_{0th} = \frac{k_0^2}{(4\pi r)^2} (2\cos\theta)^2 |R_a|^2 \int\int_{-2L}^{2L} du dv (2L - |u|)(2L - |v|) \cdot e^{ik_{dx}u} \, e^{-(k_{dz})^2 s^2 [1 - \rho(u,v)]}. \tag{2.69}$$

Instead of a series expansion of $f_{ba}(Z_x, Z_y)$ about zero slopes, $f_{ba}(Z_x, Z_y)$ can be approximated appropriately for surfaces with small rms slope [Fung et al., 1992]. Assuming small rms slope ($Z_x^2, Z_y^2 \ll 1$), $f_{ba}(Z_x, Z_y)$ can be approximated from (2.56)-(2.60) as follows;

$$\begin{aligned} f_{hh}(Z_x, Z_y) &\approx 2(\cos\theta + Z_x \sin\theta) R_h \\ f_{vv}(Z_x, Z_y) &\approx 2(\cos\theta + Z_x \sin\theta) R_v \\ f_{vh}(Z_x, Z_y) &= f_{hv}(Z_x, Z_y) \approx 0 \end{aligned} \tag{2.70}$$

where R_h and R_v are the Fresnel reflection coefficients. This approximation may be called *first order approximation* since the co-polarized scattering amplitudes include the first order of the slope terms. The cross-polarized backscattering fields are zero with this approximation too.

Substituting (2.70) into (2.54) and integrating by part [Beckmann and Spizzichino, 1963], the backscattered fields can be computed as

$$E^s_{aa} = D_{02} R_a \frac{1}{\cos\theta} \int\int e^{ik_0 \hat{k}_d \cdot \mathbf{r}'} \, dx dy + O(L) \tag{2.71}$$

with

$$O(L) = \left[\frac{-\sin\theta}{2ik_0 \cos\theta} e^{ik_0 \hat{k}_d \cdot \mathbf{r}'} \right]_{-L}^{+L}$$

where the term of $O(L)$ is an edge effect [Beckmann, 1968] which is insignificant for a surface of small rms slope and small incidence angles near normal. Therefore, the backscattered mean intensity is given, ignoring the edge effect term,

$$\left\langle |E_{aa}^s|^2 \right\rangle_{1st} = \frac{k_0^2}{(4\pi r)^2} \left(\frac{2}{\cos\theta} \right)^2 |R_a|^2 \int\int_{-2L}^{2L} du dv (2L - |u|)(2L - |v|) \cdot e^{ik_{dx}u} \, e^{-(k_{dz})^2 s^2 [1-\rho(u,v)]}. \tag{2.72}$$

Comparing (2.72) with (2.69), the backscattered mean intensity with first order approximation is that with zeroth order approximation divided by $\cos^4\theta$, *i.e.*,

$$\left\langle |E_{aa}^s|^2 \right\rangle_{1st} = \frac{1}{\cos^4\theta} \left\langle |E_{aa}^s|^2 \right\rangle_{0th}. \tag{2.73}$$

The first and zeroth order approximated PO solutions are examined in more detail in Section 2.5.

In order to get a closed form of the backscattered intensity, we may set $L \longrightarrow \infty$ assuming the illuminated rough surface contains many correlation lengths $L \gg l$. Using a series expansion for the exponential term,

$$e^{k_{dz}^2 s^2 \rho(u,v)} = \sum_{n=0}^{\infty} \frac{\left(k_{dz}^2 s^2 \rho(u,v)\right)^n}{n!}, \tag{2.74}$$

the backscattered mean intensity can be rearranged as

$$\left\langle |E_{aa}^s|^2 \right\rangle_{0th} = \frac{k_0^2}{(4\pi r)^2} (2\cos\theta)^2 |R_a|^2 (2L)^2 e^{-k_{dz}^2 s^2} \sum_{n=0}^{\infty} \frac{\left(k_{dz}^2 s^2\right)^2}{n!} \cdot \int\int_{-\infty}^{\infty} e^{ik_{dx}u} \, \rho^n(u,v) du dv. \tag{2.75}$$

The $n = 0$ term corresponds to coherent scattering [Ulaby et al., 1982] since

$$|\langle E_{aa}^s \rangle|_{0th}^2 = \frac{k_0^2}{(4\pi r)^2} (2\cos\theta)^2 |R_a|^2 (2L)^2 e^{-k_{dz}^2 s^2} \int\int_{-\infty}^{\infty} e^{ik_{dx}u} \, du dv, \tag{2.76}$$

and the rest of the series in (2.75) represents incoherent scattering.

When we consider a Gaussian correlation function given in (2.32), the integral in (2.75) can be computed [Gradshteyn and Ryzhik, Ch6, 1980] to be

$$\mathbf{I}_G = \int\int_{-\infty}^{\infty} e^{ik_{dx}u} e^{-n\frac{u^2+v^2}{l^2}} dudv = \frac{\pi l^2}{n} e^{-\frac{(kl\sin\theta)^2}{n}}, \tag{2.77}$$

while the integral for an exponential correlation function given in (2.33) is computed to be

$$\mathbf{I}_e = \int\int_{-\infty}^{\infty} e^{ik_{dx}u} e^{-n\frac{\sqrt{u^2+v^2}}{l/\sqrt{2}}} dudv = \frac{\pi n l^2}{[n^2 + 2(kl\sin\theta)^2]^{\frac{3}{2}}}, \tag{2.78}$$

where $k_{dx} = 2k\sin\theta$ and l is the correlation length.

Since the backscattering coefficient corresponding to the backscattered mean intensity can be given as

$$\sigma^{\circ}_{ba} = \lim_{r\to\infty} \frac{4\pi r^2}{A} \frac{Re\left\{\left\langle |E^s_{ba}|^2 \right\rangle / \eta^*_s\right\}}{Re\left\{|E_0|^2/\eta^*\right\}}, \tag{2.79}$$

where the intrinsic impedance $\eta^*_s = \eta^* = \eta_0$ and $|E_0| = 1.0$ in this problem, the incoherent backscattering coefficients for PO model are given by

$$\sigma^{\circ}_{aa,in_{0th}} = \frac{k_0^2}{\pi} \cos^2\theta\, |R_a|^2\, e^{-(2ks\cos\theta)^2} \sum_{n=1}^{\infty} \frac{(2ks\cos\theta)^{2n}}{n!} \cdot \mathbf{I} \tag{2.80}$$

where R_a is the Fresnel reflection coefficient for a-polarization and $\mathbf{I}$ is $\mathbf{I}_G$ in (2.77) or $\mathbf{I}_e$ in (2.78) for a Gaussian or an exponential correlation function, respectively.

The additional approximation of the PO model (zeroth or first order approximation) limits the validity conditions to the small slope of the rough surface. Therefore, in addition to the validity conditions in (2.62), another condition that limits the rms slope is usually given [Ulaby et al., 1982] as

$$m < 0.25. \tag{2.81}$$

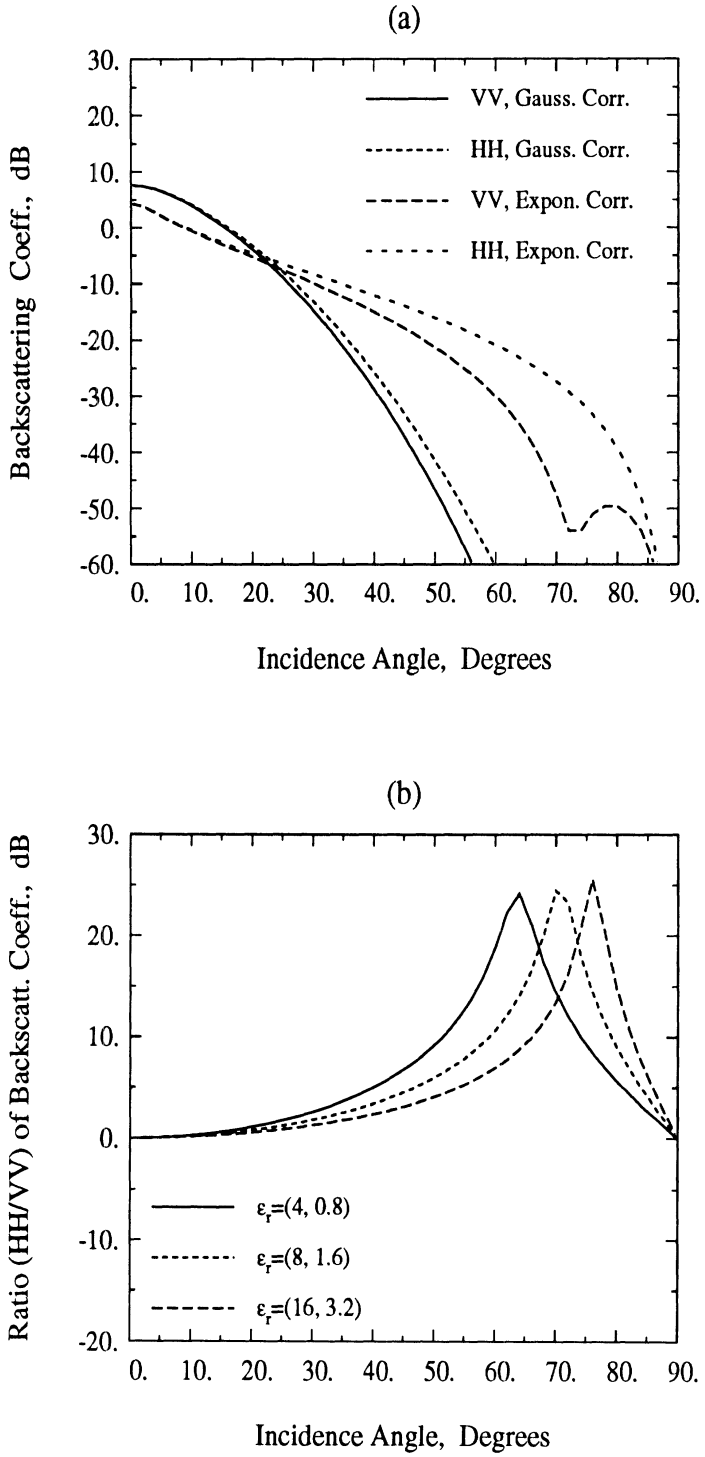

Figure 2.5: Backscattering coefficients of a rough surface with $ks = 1$ and $kl = 8$ using the PO model; (a) σ°_{hh} and σ°_{vv} for two different correlation functions and $\epsilon_r = (10, 2)$ and (b) the ratio $\sigma^{\circ}_{hh}/\sigma^{\circ}_{vv}$ for the various values of ϵ_r with an exponential correlation function.

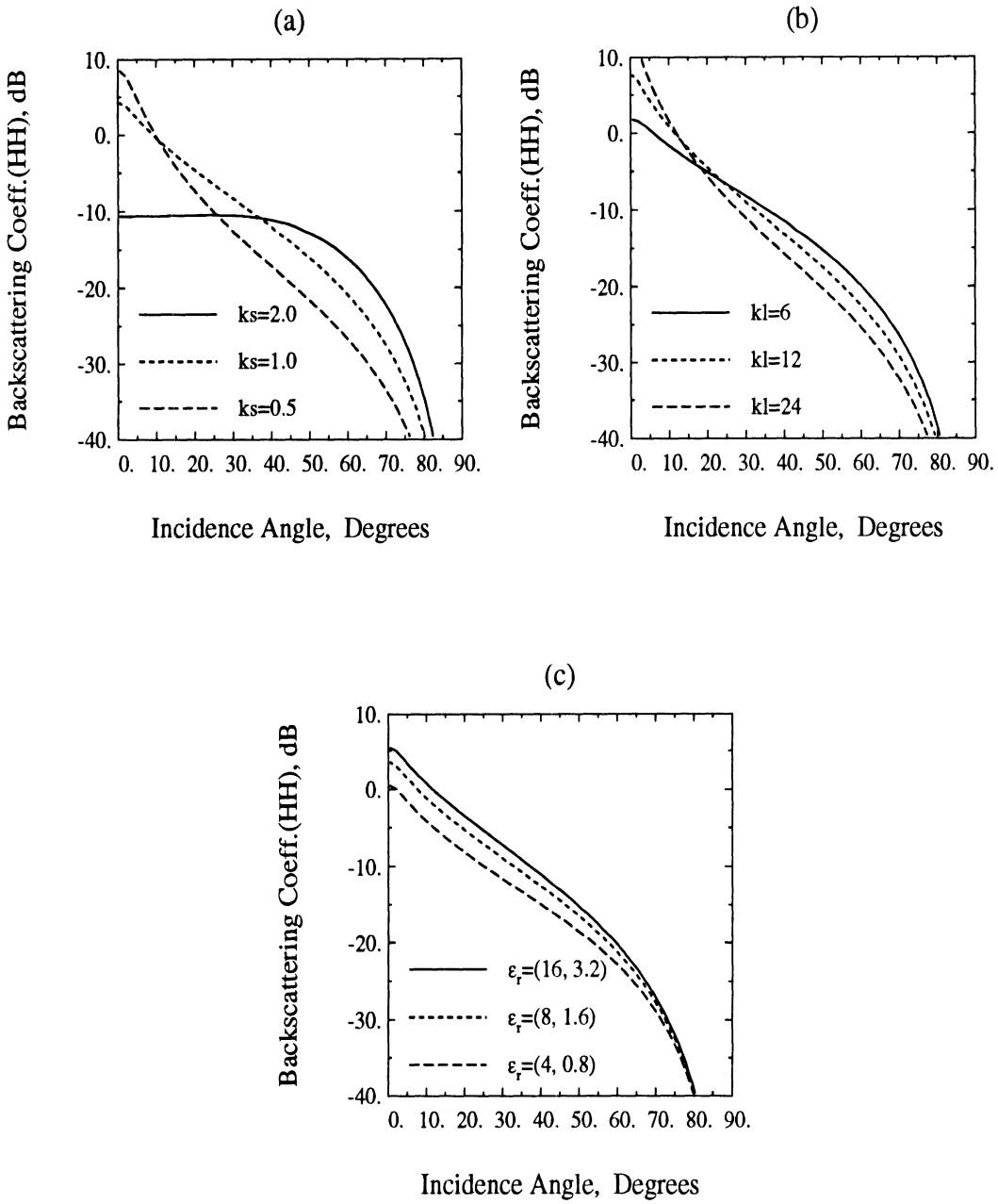

Figure 2.6: Backscattering coefficients at hh-polarization using the PO model for a surface of an exponential correlation, (a) $kl = 8$, $\epsilon_r = (10, 2)$, and the various values of ks, (b) $ks = 1$, $\epsilon_r = (10, 2)$, and the various values of kl, and (a) $ks = 1$, $kl = 8$, and the various values of ϵ_r.

The backscattering coefficients for various rough surfaces computed using the zeroth-order PO model are illustrated in Figs. 2.5 and 2.6. Since the polarization response depends only on the Fresnel reflection coefficients, σ°_{hh} is higher than σ°_{vv} as shown in Figs. 2.5(a) and (b) in contrary to the polarization response in the SPM. The ration $\sigma^\circ_{hh}/\sigma^\circ_{vv}$ has a peak at the corresponding brewster angle as shown in Figs. 2.5(a) and (b). Figures 2.6 show that the backscattering coefficients using PO model are very sensitive to the variation of ks and less sensitive to the variations of kl and ϵ_r. When ks increases (and/or kl decreases) σ°_{hh} decreases at lower incidence angles and σ°_{hh} increases at higher incidence angles as shown in Figs. 2.6(a) and (b). The dependence of σ° versus θ on ks using PO model is quite different with that using the SPM which shows a constant increase in σ° versus θ for increasing ks as shown in Fig. 2.3(a). The dependence of σ° on ϵ_r using PO model is similar to that obtained using the SPM, *i.e.*, increasing ϵ_r produces an approximately constant increase in σ°.

2.3.2 Geometrical Optics Model

The asymptotic solution to the Kirchhoff-diffraction integral (2.54) can be derived using the stationary-phase approximation in the geometric limit as $k \longrightarrow \infty$. Under this approximation, the scattering coefficient will be proportional to the probability of the occurrence of the slopes which will specularly reflect the incident wave to the observation direction. Hence, local diffraction effects are excluded in this approximation.

The phase ψ is said to be stationary at a point if its rate of change is zero at the point where

$$\psi = k_0 \hat{k}_d \cdot \mathbf{r}' = k_{dx} x' + k_{dy} y' + k_{dz} z(x', y'), \tag{2.82}$$

with $k_{dx} = 2k_0 \sin\theta$, $k_{dy} = 0$, and $k_{dz} = -2k_0 \cos\theta$ for the backscattering direction.

The slopes Z_x and Z_y can be found for the backscattering direction as

$$\frac{\partial\psi}{\partial x'} = 0 = k_{dx} + k_{dz}Z_{x0} \Longrightarrow Z_{x0} = \frac{-k_{dx}}{k_{dz}} = \tan\theta,$$
$$\frac{\partial\psi}{\partial y'} = 0 = k_{dy} + k_{dz}Z_{y0} \Longrightarrow Z_{y0} = 0.$$

Using these slopes which are not functions of the random position vectors any more, the mean intensity of (2.61) can be reduced in the form of

$$\langle E^s_{ba} E^{s*}_{ba} \rangle = |D_0|^2 \, |f_{ba}(Z_{x0}, 0)|^2 \cdot \langle II^* \rangle \tag{2.83}$$

where

$$\langle II^* \rangle = \int\int_{-2L}^{2L} (2L - |u|)(2L - |v|) e^{ik_{dx}u} \, e^{-(k_{dz})^2 s^2 [1-\rho(u,v)]} du dv. \tag{2.84}$$

From (2.56)-(2.58) we can find the scattering amplitudes for the backscattering direction as follows;

$$\begin{aligned} f_{hh}(Z_{x0}, 0) &= \tfrac{2}{\cos\theta} R_h(0) \\ f_{vv}(Z_{x0}, 0) &= \tfrac{2}{\cos\theta} R_v(0) \\ f_{vh}(Z_{x0}, 0) &= f_{hv}(Z_{x0}, 0) = 0, \end{aligned} \tag{2.85}$$

where $R_a(0)$ is the Fresnel reflection coefficient evaluated at normal incidence for a-polarization. When we assume $k_{dz}^2 s^2$ is large ($\gg 1$) so that the contribution to the integral in (2.84) is significant only for small values of u and v, the normalized correlation function $\rho(\xi)$ can be approximated by the first two terms of its Taylor series expansion about the origin,

$$\rho(\xi) \approx 1 + \frac{\rho''(0)}{2}.$$

Changing the variables as $\xi = \sqrt{u^2 + v^2}$ and integration limit as $2L \to \infty$, $\langle II^* \rangle$ reduces to

$$\begin{aligned} \langle II^* \rangle &= A \int_0^\infty \int_0^{2\pi} e^{ik_{dx}\xi \sin\psi} \, e^{-(k_{dz})^2 s^2 \frac{|\rho''(0)|}{2} \xi^2} \xi \, d\xi \, d\psi \\ &= \frac{2\pi A}{(2k\cos\theta)^2 s^2 \, |\rho''(0)|} e^{-\frac{\tan^2\theta}{2s^2|\rho''(0)|}} \end{aligned} \tag{2.86}$$

where $A = (2L)^2$. Substituting (2.85) and (2.86) into (2.83), the backscattered mean intensity is computed as

$$\left\langle |E^s_{aa}|^2 \right\rangle = \frac{k_0^2}{(4\pi r)^2} \left(\frac{2}{\cos\theta}\right)^2 |R_a(0)|^2 \frac{2\pi A}{(2k\cos\theta)^2 s^2 |\rho''(0)|} e^{-\frac{\tan^2\theta}{2s^2|\rho''(0)|}}. \tag{2.87}$$

From (2.79) the backscattering coefficients for the geometrical optics (GO) model is

$$\sigma^\circ_{aa}(\theta) = \frac{|R_a(0)|^2}{2m^2\cos^4\theta} \exp\left[-\frac{\tan^2\theta}{2m^2}\right], \tag{2.88}$$

where the rms slope m is $s\sqrt{|\rho''(0)|}$, aa is vv or hh, and $\sigma^\circ_{vh} = \sigma^\circ_{hv} = 0$.

In addition to the validity conditions of (2.62) for the tangent plane approximation, an additional condition is required for the GO model [Ulaby et al., 1982] as

$$k_{dz}^2 s^2 > 10 \quad \text{or} \quad ks > \frac{\sqrt{2.5}}{\cos\theta}. \tag{2.89}$$

When the angle of incidence is large, some points on the rough surface may not be illuminated directly and shadowed by other parts of the surface interrupting the incident wave. Since the PO and the GO models do not include the effect of shadowing, the scattering coefficients for these models should be modified for the shadowing effect. The shadowing function which is the probability that a point on a rough surface will not be illuminated by an incident wave, is given by [Smith, 1967 and Sancer, 1969],

$$R(\theta) = \frac{1}{1 + f(\theta, m)} \tag{2.90}$$

with

$$2f(\theta, m) = \sqrt{\frac{2}{\pi}} \frac{m}{\cot\theta} e^{-\frac{\cot^2\theta}{2m^2}} - erfc\left(\frac{\cot\theta}{\sqrt{2}m}\right)$$

where $erfc$ is the complementary error function, m is the rms slope, and the corrected backscattering coefficients $\sigma^{\circ\prime} = \sigma^\circ \cdot R(\theta)$.

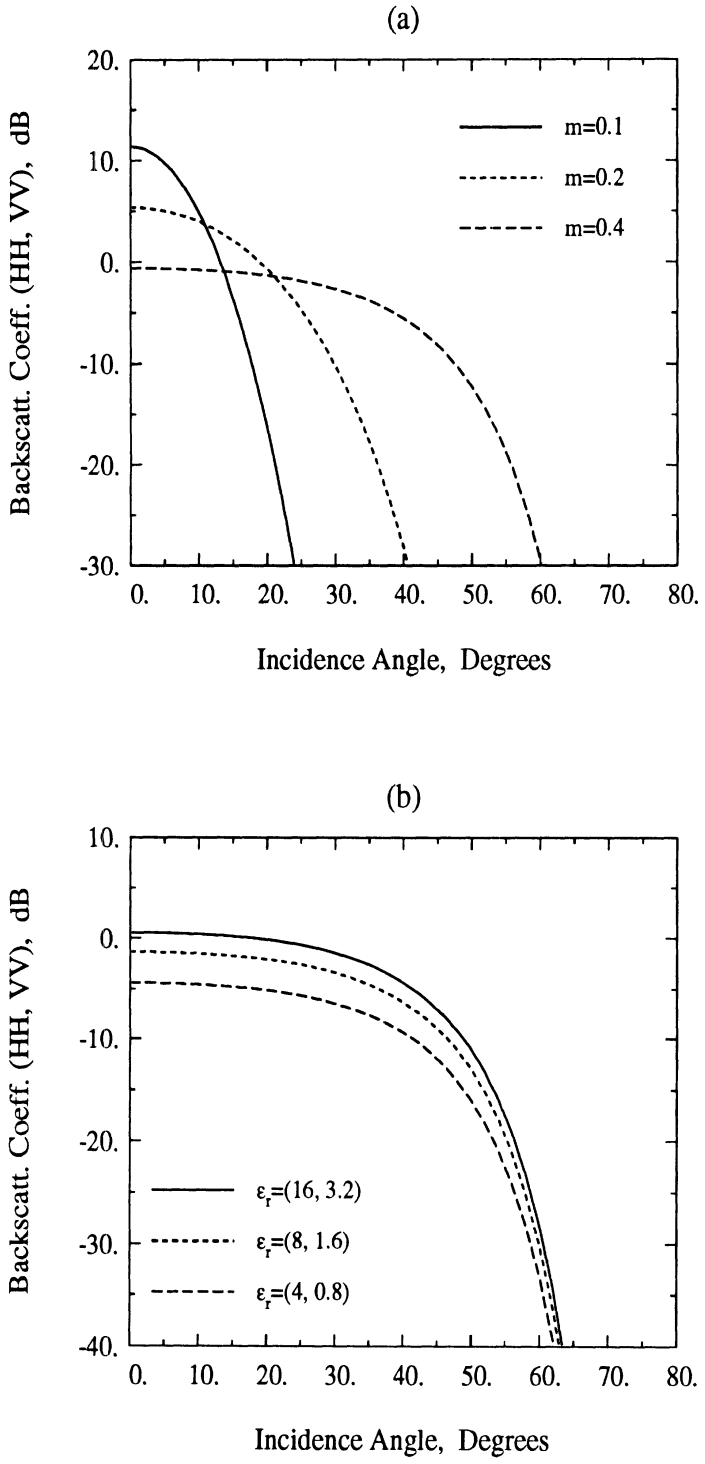

Figure 2.7: Backscattering coefficients of a rough surface at $vv(= hh)$-polarization using the GO model; (a) for $\epsilon_r = (10, 2)$ and the various values of m and (b) for $m = 0.4$ and the various values of ϵ_r.

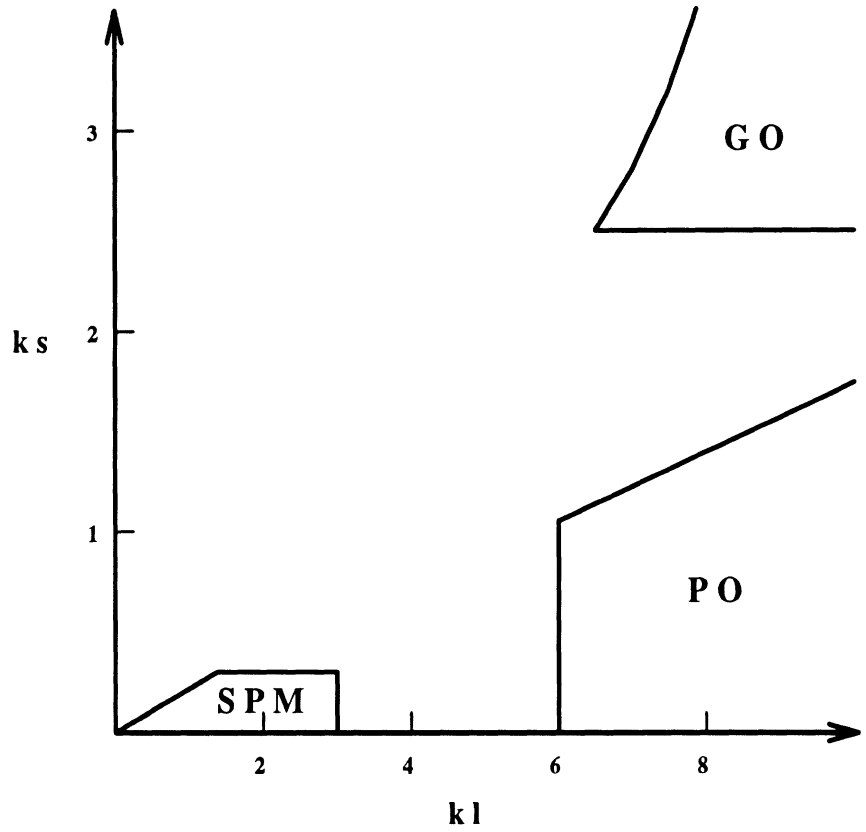

Figure 2.8: The validity regions of the classical models which are the SPM, the PO model and GO model.

Figure 2.7(a) shows the backscattering coefficient using GO model as a function of θ for the various values of the rms slope m. The curve of σ° versus θ drops more slowly as the surface slope m increases, where the backscattering coefficient σ° does not depend on polarization, *i.e.*, $\sigma^\circ_{hh}=\sigma^\circ_{vv}$. Similar to the SPM and PO model, the GO model predicts a constant increase of σ° versus θ for increasing ϵ_r as shown in Fig. 2.7(b).

The validity conditions of the SPM, PO, and GO models for backscatter given in (2.39), (2.62), (2.81), and (2.89) are illustrated in Fig. 2.8 where (2.89) is applied for the case of $\theta < 50°$.

CHAPTER III

NUMERICAL SOLUTION FOR SCATTERING FROM ONE-DIMENSIONAL CONDUCTING RANDOM SURFACES

3.1 Introduction

Since the method of moments [Harrington, 1968] was applied to the estimation of the scattering coefficient of conducting random surfaces [Lentz, 1974], many other numerical methods with some modifications have been introduced to solve the scattering problem of random surfaces [Axline and Fung, 1978; Fung and Chen, 1985; Nieto-vesperinas and Soto-crespo, 1987; Durden and Vesecky, 1990; and Rodriguez et al., 1992]. The incident field in all of these methods was a tapered wave to eliminate the edge-effect contribution due to the finite length of the sample surface. However, at large incidence angles ($\theta > 60°$), the width of the sample surface must be very large to eliminate the edge-effect, which results in excessive computation time. Otherwise, the window should be very narrow to eliminate the edge contribution at a large incidence angle, which results in an incorrect output by excessive smoothing.

In this chapter, a new technique, adding a resistive card at each end of an illuminated surface, is introduced to eliminate the edge contribution even at large incidence angles. To illustrate this technique, one-dimensional random surfaces are generated

in Section 3.2. Integral equations are formulated for one-dimensional conducting random surfaces and solved by the method of moments for vv- and hh-polarizations in Section 3.3, and numerical results are analyzed in Section 3.4. Using this numerical technique, the existing models are evaluated for scattering from one-dimensional conducting random surfaces in Section 3.5.

3.2 Random Surface Generation

A sequence of independent Gaussian deviates with zero mean and unit variance (N[0,1]) can be obtained from a standard routine [Press et al., 1986]. Then these independent Gaussian deviates can be correlated to a specific correlation function using the concept of digital filtering [Fung and Chen, 1985]. At first, the desired surface height profile $\{Z(k)\}$ can be written as the summation of the product of the independent Gaussian deviates $\{X(j+k)\}$ and a discrete weighting factor $\{W(j)\}$ which is to be determined,

$$Z(k) = \sum_{j=-M}^{M} W(j)Z(j+k), \tag{3.1}$$

where Z(k) is the kth point of a discrete height profile and M is the total number of sample points of the weighting factor $W(j)$.

The correlation coefficient function $C(i)$ of the desired surface profile is given by the definition as follows;

$$C(i) = E[Z(k)\ Z(k+i)] = \sum_{j}\sum_{m} W(j)W(m)E[X(j+k)\ X(m+k+i)]. \tag{3.2}$$

Since the Gaussian deviates are mutually independent, *i.e.*,

$$E[X(j+k)\ X(m+k+i)] = \begin{cases} 0, & j \neq m+i \\ 1, & j = m+i, \end{cases} \tag{3.3}$$

the correlation function can be simplified as the self convolution of the weighting factor,

$$C(i) = \sum_j W(j)W(j-i) = W * W. \tag{3.4}$$

Using the Fourier transform theorem, the unknown weighting factors can be found analytically,

$$W(j) = \mathcal{F}^{-1}\left\{\sqrt{\mathcal{F}[\rho(i)]}\right\}. \tag{3.5}$$

When we choose the Gaussian correlation function of the form

$$C(i) = s^2 \exp\left[-\left(\frac{i}{L}\right)^2\right], \tag{3.6}$$

its spectrum is given by

$$\mathcal{F}[\rho(i)] = s^2\sqrt{\pi}L \exp\left[-\frac{L^2 f^2}{4}\right]. \tag{3.7}$$

The corresponding weight factor can be obtained as

$$W(j) = s\frac{2}{\sqrt{\pi L}} \exp\left[-2\left(\frac{j}{L}\right)^2\right], \tag{3.8}$$

where s is the standard deviation of the height distribution (rms height), L is the discrete number given as $l/\Delta x$, l is the correlation length of a random surface, and Δx is the sampling interval. Then, the surface height profile can be computed by (3.1) and (3.8) for given surface statistics such as the rms height, the correlation function. The proper value for the width of an independent surface D and the sampling interval Δx is a function of the surface correlation length and frequency of the incident wave.

In order to get meaningful statistics of the backscattering coefficient, the number of sample surface, N, should be large enough. For example, $N \geq 60$ to suppress the speckle noise in the estimated backscattering coefficient to within ± 1 dB from the

mean value for the 5% and 95% cumulative distribution levels [Ulaby and Dobson, 1989].

Considering finite computer storage and practical restrictions on computer execution time, each surface must have finite length, D. While the upper limit of the surface width is decided by the size of computer storage, the lower limit may be considered as $D \geq 10\lambda$ and $D \geq 10l$ where λ is the wavelength and l is the correlation length.

The sample interval, Δx, is chosen as $\Delta x \leq \lambda/12$, which is comparable with others [Fung and Chen, 1985; Rodriquez et al., 1992]. The backscattering coefficient is approximately proportional to the surface roughness spectrum, $W(2k\sin\theta)$, where the roughness spectrum for a Gaussian correlation function is given as:

$$W(2k\sin\theta) = \sqrt{\pi}s^2 l e^{-(kl\sin\theta)^2}. \tag{3.9}$$

If we choose the width of the spectrum as twice of the frequency where $W(2k\sin\theta)$ has dropped to $e^{-1}\ W(0)$, the spatial frequency $k_x = 2 \cdot 2k\sin\theta = 4/l$. Applying the sampling theorem, $\Delta x \leq \frac{1}{2K_x} = l/8$. Therefore, the sampling interval Δx is chosen to satisfy both conditions of $\Delta x \leq \lambda/12$ and $\Delta x \leq l/8$.

Three different surfaces with given roughness parameters (Table 3.1) are generated according to above criteria with $M = 45000$ and the total length of $N \times D$. Figures 3.1 (a)-(c) show typical sections of the surface height profiles of S-1, S-2, and S-3, respectively. The height distribution of the generated surfaces are compared with

Gaussian probability density functions

$$f_X(x) = \frac{1}{\sqrt{2\pi}s} \exp\left[-\frac{x^2}{2s^2}\right] \tag{3.10}$$

as shown in Fig. 3.2. The autocorrelation functions of the computer generated

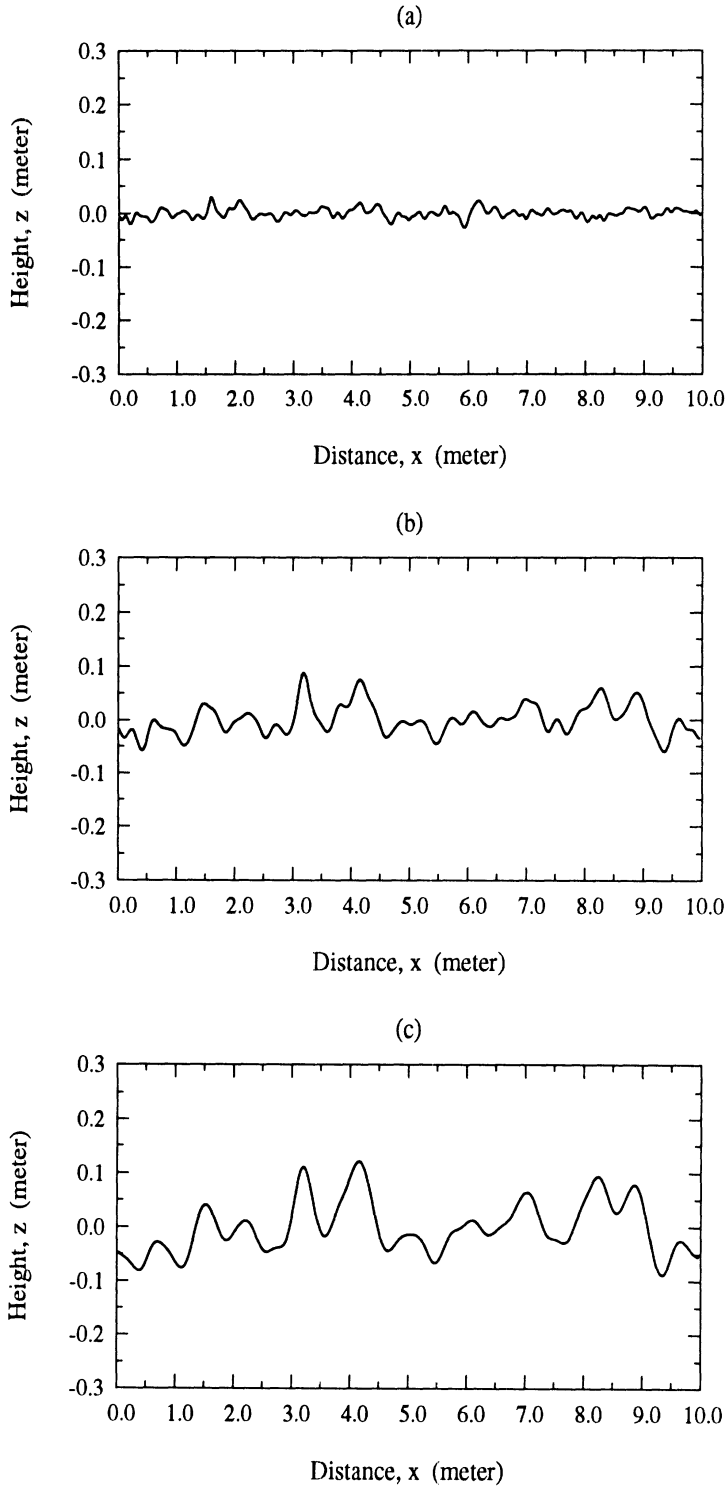

Figure 3.1: Typical sections of height profiles for (a) S-1, (b) S-2, and (c) S-3 surfaces.

Table 3.1: Roughness parameters used for the random surface generation

Surf. Name	ks	kl	λ	s	l	Δx	D	N	Appl. Model
				meters					
S-1	0.21	2.2	0.24	0.0079	0.082	0.01	2.4	60	SPM
S-2	0.62	4.6	0.24	0.0237	0.175	0.02	4.8	60	
S-3	1.04	7.4	0.24	0.0396	0.281	0.02	4.8	60	PO

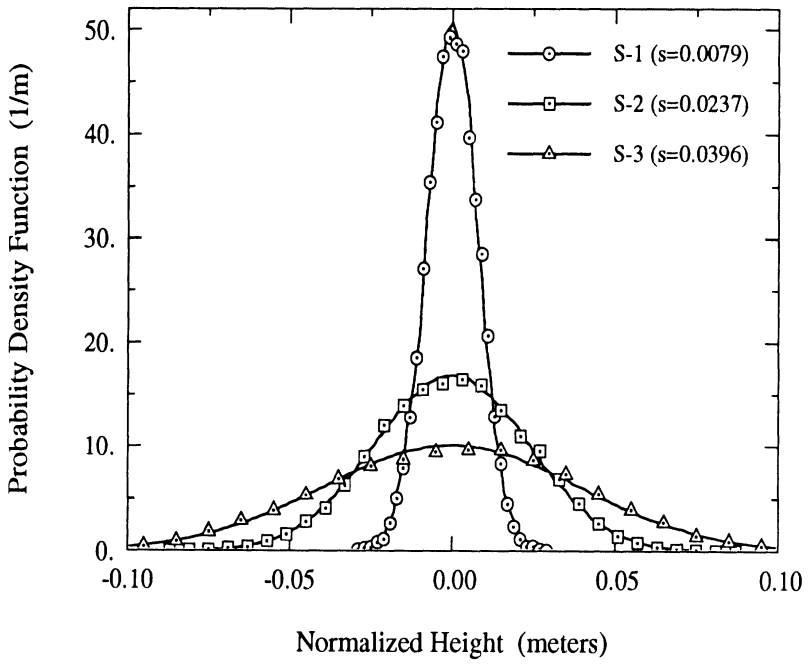

Figure 3.2: The height distribution of the generated surfaces (dots) as compared with Gaussian probability density functions (solid lines).

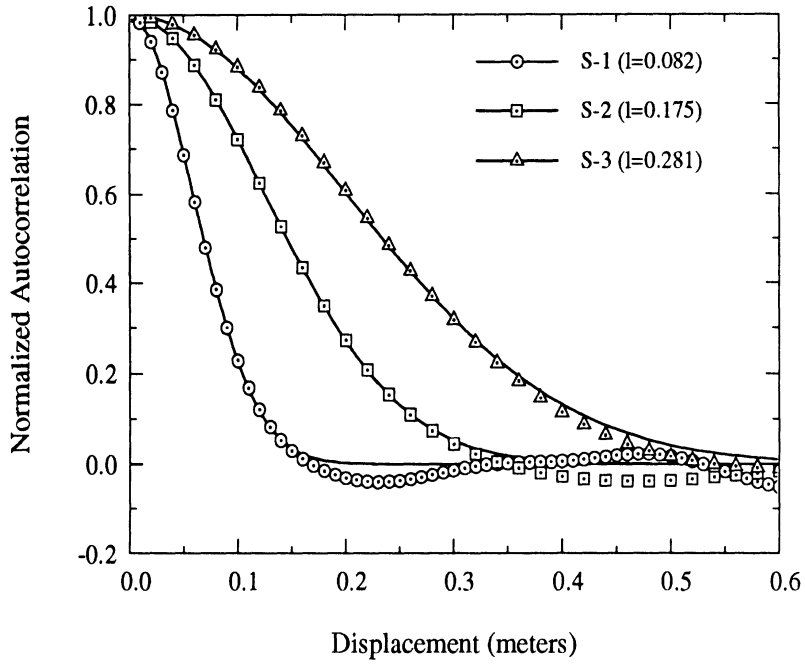

Figure 3.3: The autocorrelations of the generated surfaces (dots) as compared with Gaussian functions (solid lines).

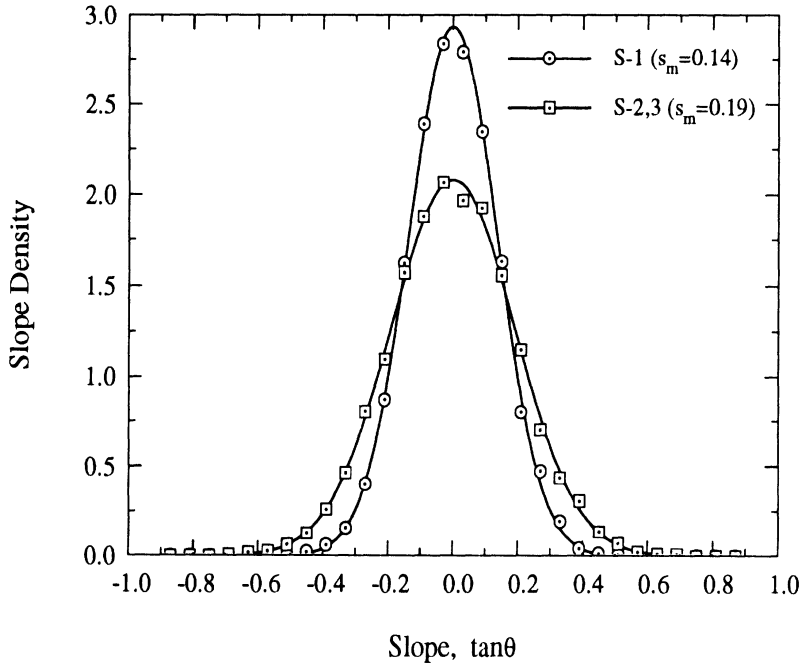

Figure 3.4: The slope distribution of the generated surfaces (dots) as compared with Gaussian probability density functions (solid lines).

surfaces agree well with Gaussian functions of (3.6) as shown in Fig. 3.3. Figure 3.4 shows the slope distributions of the generated surfaces compared with a Gaussian density function given as

$$f_M(m) = \frac{1}{\sqrt{2\pi}s_m} \exp\left[-\frac{m^2}{2s_m^2}\right] \tag{3.11}$$

where m is the slope ($\tan\theta$) and s_m is the standard deviation of slope distribution (rms slope) which can be obtained as $s_m = s^2\rho''(0)$ ($=\sqrt{2}s/l$ for Gaussian correlation).

3.3 Solution by the Method of Moments

The backscattering coefficient of a computer-generated one-dimensional conducting surface can be obtained by N repeated computation of the electric field scattered from each independent segment of a random surface as:

$$\sigma^\circ(\theta)_{pp} = \lim_{\rho\to\infty} \frac{2\pi\rho}{D} \left\{ \frac{1}{N}\sum_{n=1}^{N} \left|E^s_{n,pp}\right|^2 - \frac{1}{N^2}\left|\sum_{n=1}^{N} E^s_{n,pp}\right|^2 \right\}, \quad pp = vv \text{ or } hh, \tag{3.12}$$

where D is the width of each segment of the random surface, vv and hh denote that both the incident and scattered waves are V- and H-polarized, respectively. The scattered field can be represented by the convolution of the surface current density $\mathbf{J}_e$ and the Green's function as follows:

$$\mathbf{E}^s(\overline{\rho}) = -\frac{k_0 Z_0}{4} \int_l \mathbf{J}_e(\overline{\rho}')\, H_0^{(1)}(k_0|\overline{\rho} - \overline{\rho}'|)dl', \tag{3.13}$$

where k_0 and Z_0 are the wave number and the intrinsic impedance of free space, respectively. $H_0^{(1)}$ is the zeroth order Hankel function of the first kind, and $\overline{\rho}$ and $\overline{\rho}'$ are the position vectors of observation and source points, respectively. The surface current density $\mathbf{J}_e(\overline{\rho}')$ due to the incident plane wave in (3.13) is to be determined numerically by the method of moment (MoM) [Harrington, 1968].

hh-Polarization

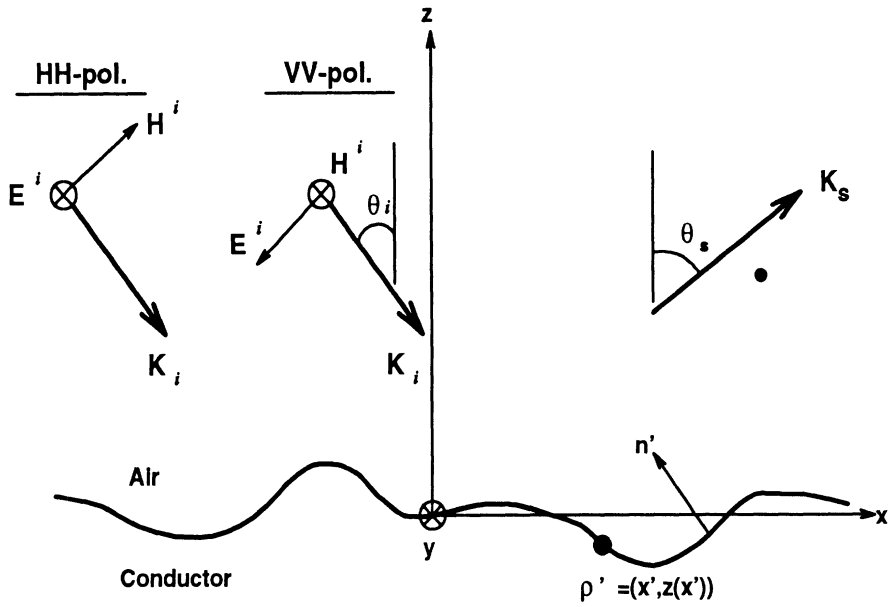

Figure 3.5: Geometry of the scatter problem.

The electric field integral equation (EFIE) for one-dimensional conducting surface can be written as

$$\mathbf{E}^i(\overline{\rho}) = \frac{k_0 Z_0}{4} \int_l \mathbf{J}_e(\overline{\rho}')\, H_0^{(1)}(k_0|\overline{\rho} - \overline{\rho}'|)dl', \qquad \overline{\rho}' \text{ on interface} \tag{3.14}$$

where the incident wave $\mathbf{E}^i(\overline{\rho})$ is given by

$$\mathbf{E}^i(\overline{\rho}) = \hat{y} \exp[ik_0 \hat{k}_i \cdot \overline{\rho}] \;=\; \hat{y} E_y^i(\overline{\rho}), \tag{3.15}$$

and an orthonormal coordinate system of $(\hat{h}_i,\ \hat{v}_i,\ \hat{k}_i)$ is defined by $\hat{k}_i = \sin\theta_i \hat{x} - \cos\theta_i \hat{z}$, $\hat{h}_i = \hat{y}$, and $\hat{v}_i = \cos\theta_i \hat{x} + \sin\theta_i \hat{z}$ as shown in Fig. 3.5.

The simplest MoM solution of (3.14) consists of using the pulse basis and point matching. After discretizing a sample surface into M $(= D/\Delta x)$ cells, the pulse basis function can be applied as:

$$\mathbf{J}_e(\overline{\rho}') = \sum_{n=1}^{M} I_n f_n(\overline{\rho}')\hat{y} \tag{3.16}$$

where

$$f_n(\vec{\rho}') = \begin{cases} 1, & \text{on } \Delta x_n \\ 0, & \text{on all other } \Delta x_m. \end{cases} \tag{3.17}$$

Then, (3.14) can be rearranged using $dl' = \sqrt{1 + (dz(x')/dx')^2}dx'$,

$$\sum_{n=1}^{M} I_n \left\{ \frac{k_0 Z_0}{4} \int_{\Delta x_n} H_0^{(1)}(k_0\sqrt{(x-x_n)^2 + (z-z_n)^2}) \sqrt{1 + \left(\frac{dz_n}{dx_n}\right)^2} dx_n \right\} = \exp[ik_0(\sin\theta_i x - \cos\theta_i z)] \tag{3.18}$$

Since (3.18) can be matched every point on the surface $(x, z) = (x_1, z_1), \cdots, (x_m, z_m), \cdots, (x_M, z_M)$, (3.18) can be casted into a matrix equation,

$$[\mathcal{Z}_{mn}]\,[\mathcal{I}_n] = [\mathcal{V}_m], \tag{3.19}$$

where each element of the impedance matrix $[\mathcal{Z}_{mn}]$ is given by

$$z_{mn} = \frac{k_0 Z_0}{4} \int_{\Delta x_n} H_0^{(1)}(k_0\sqrt{(x_m - x_n)^2 + (z_m - z_n)^2}) \sqrt{1 + \left(\frac{dz_n}{dx_n}\right)^2} dx_n, \tag{3.20}$$

the elements of the excitation vector $[\mathcal{V}_m]$ are given by

$$v_m = \exp[ik_0(\sin\theta_i x_m - \cos\theta_i z_m)], \tag{3.21}$$

and $[\mathcal{I}_n]$ is the surface current vector which is to be determined.

Since $H_0^{(1)}(k_0\rho)$ has an integrable singularity for diagonal elements ($m = n$) of the $\mathcal{Z}$-matrix, small argument expansion of the Hankel function [Harrington, 1961] is used to obtain z_{nn},

$$H_0^{(1)}(x) \approx (1 - \frac{x^2}{4}) + \frac{i2}{\pi}\left[\ln\frac{\gamma x}{2}\left(1 - \frac{x^2}{4}\right) + \frac{x^2}{4}\right], \qquad \gamma = 1.781\cdots. \tag{3.22}$$

Equation (3.20) can be evaluated analytically using (3.22) for the diagonal element as,

$$z_{nn} \approx \frac{k_0 Z_0\, \Delta d}{4} \left[1 + \frac{i2}{\pi}\ln\left(\frac{k_0\gamma\, \Delta d}{4e}\right) - \frac{k_0^2(\Delta d)^2}{24}\left\{\frac{1 - \frac{i2}{\pi}}{2} - \frac{i}{\pi}\ln\left(\frac{k_0\gamma\, \Delta d}{4e^{1/3}}\right)\right\}\right] \tag{3.23}$$

where $\Delta d = \Delta x_n \sqrt{1 + (dz_n/dx_n)^2}$ and $e = 2.718\cdots$. The non-diagonal elements, z_{mn}, can be obtained by evaluating the integral numerically, *e.g.,* using the four-points Gaussian-Quadrature integration technique.

Once the surface current vector $[\mathcal{I}_n]$ is found, the hh-polarized scattered field, E^s_{hh}, in the far-field can be computed using the far-field approximation of $H_0^{(1)}(k_0\rho)$,

$$H_0^{(1)}(k_0|\overline{\rho} - \overline{\rho}'|) \quad \text{for large argument} \longrightarrow \sqrt{\frac{2}{\pi k_0 \rho}} e^{i(k_0\rho - \pi/4)}\, e^{-ik_0 \hat{k}_s \cdot \overline{\rho}'} \tag{3.24}$$

into (3.13), which results in

$$E^s_{hh}(\theta_s) = -\frac{k_0 Z_0}{\sqrt{8\pi k_0 \rho}} e^{i(k_0\rho - \pi/4)} \sum_{n=1}^{M} I_y(x_n, z_n) e^{-ik_0 \hat{k}_s \cdot \overline{\rho}_n} \Delta x_n \sqrt{1 + \left(\frac{dz_n}{dx_n}\right)^2} \tag{3.25}$$

where $\hat{k}_s = \sin\theta_s \hat{x} + \cos\theta_s \hat{z}$, $\hat{h}_s = \hat{y}$, and $\hat{v}_s = -\cos\theta_s \hat{x} + \sin\theta_s \hat{z}$.

vv-Polarization

For the solution of VV-polarization case, the magnetic field integral equation (HFIE) can be used to compute the surface current as follows:

$$-\hat{n} \times \mathbf{H}^i(\overline{\rho}) = -\frac{1}{2}\mathbf{J}_e(\overline{\rho}) + \frac{i}{4}\int_l \hat{n} \times \left\{\mathbf{J}_e(\overline{\rho}') \times \nabla' H_0^{(1)}(k_0|\overline{\rho} - \overline{\rho}'|)\right\} dl', \tag{3.26}$$

where $\overline{\rho}'$ is on interface, and the incident magnetic field is given as

$$\mathbf{H}^i(\overline{\rho}) = \hat{y} e^{ik_0 \hat{k}_i \cdot \overline{\rho}} = \hat{y} H_y.$$

Since

$$\nabla' H_0^{(1)}(k_0|\overline{\rho} - \overline{\rho}'|) = k_0 H_1^{(1)}(k_0|\overline{\rho} - \overline{\rho}'|)\, \hat{R},$$

$$\hat{n} \times \mathbf{J}_e(\overline{\rho}') \times \hat{R} = \mathbf{J}_e(\overline{\rho}') \left(\hat{n} \cdot \hat{R}\right),$$

$$\hat{R} = \frac{\overline{\rho} - \overline{\rho}'}{|\overline{\rho} - \overline{\rho}'|}, \qquad \hat{n} = \frac{-\frac{dz}{dx'}\hat{x} + \hat{z}}{\sqrt{1 + \left(\frac{dz}{dx'}\right)^2}},$$

$$-\hat{n} \times \mathbf{H}^i(\overline{\rho}) = \frac{\hat{x} + \frac{dz}{dx}\hat{z}}{\sqrt{1 + \left(\frac{dz}{dx}\right)^2}}\, e^{ik_0(\sin\theta_i x - \cos\theta_i z)},$$

(3.26) can be rearranged as,

$$\left(-\hat{n}\times\mathbf{H}^{i}(\overline{\rho})\right)_{p}=-\frac{1}{2}J_{e,p}(\overline{\rho})+\frac{ik_0}{4}\int_{l}J_{e,p}(\overline{\rho}')\left(\hat{n}\cdot\hat{R}\right)H_1^{(1)}(k_0|\overline{\rho}-\overline{\rho}'|)\cdot\sqrt{1+\left(\frac{dz'}{dx'}\right)^2}dx',\qquad p=x,y. \tag{3.27}$$

When the pulse basis and point matching technique is used, (3.27) can be casted into matrix equations as,

$$[\mathcal{Z}_{mn}]\,[\mathcal{I}_n^p]=[\mathcal{V}_m^p],\quad p=x,\ z. \tag{3.28}$$

The element of the impedance matrix $[\mathcal{Z}_{mn}]$ is computed by

$$z_{mn}=-\frac{\delta_{mn}}{2}+\frac{ik_0}{4}\int_{\Delta x_n}\left(\hat{n}\cdot\hat{R}\right)H_1^{(1)}(k_0\sqrt{(x_m-x_n)^2+(z_m-z_n)^2})\cdot\sqrt{1+\left(\frac{dz_n}{dx_n}\right)^2}dx_n \tag{3.29}$$

where δ_{mn} is the Kronecker delta function. The excitation vector elements are given as

$$v_m^x=\frac{1}{\sqrt{1+\left(\frac{dz_m}{dx_m}\right)^2}}e^{ik_0(\sin\theta_i x_m-\cos\theta_i z_m)},\qquad v_m^z=\frac{dz_m}{dx_m}v_m^x\quad\circ$$

and $[\mathcal{I}_n^x]$ and $[\mathcal{I}_n^z]$ are the current vectors to be determined where $i_n^z=(dz_m/dx_m)i_m^x$.

Once the surface currents are found similarly as described in the HH-polarization case, the scattered field can be computed as

$$E_{vv}^{s}(\theta_s)=-\frac{k_0Z_0}{\sqrt{8\pi k_0\rho}}e^{i(k_0\rho-\pi/4)}\sum_{n=1}^{M}\left[-\cos\theta_s+\sin\theta_s\frac{dz_n}{dx_n}\right]I_x(x_n,z_n)\cdot e^{-ik_0\hat{k}_s\cdot\overline{\rho}_n}\Delta x_n\sqrt{1+\left(\frac{dz_n}{dx_n}\right)^2}, \tag{3.30}$$

Suppression of Edge Contribution

In order to demonstrate the edge effect, the surface current $\mathbf{J}_e(\overline{\rho})$ is computed for a flat conducting surface of the width of 12 λ at 0° incidence. While the surface

current induced by v-polarized incidence wave does not show any edge effect and agrees with the PO (physical optics) current $\mathbf{J}_{eq} = 2\hat{n} \times \mathbf{H}^i$, the surface current induced by h-polarized incidence wave shows the peak currents at the edges of the surface as shown in Fig. 3.6 (a). Corresponding backscattered radar cross section (RCS) of the conducting strip is computed for both hh- and vv-polarizations as shown in Fig. 3.6 (b). For the simulation of the random surface scattering, the surface is assumed to have infinite width and to give no backscatter at 90° incidence.

To suppress the edge contribution to the backscatter of the finite conducting surface, each end of the surface is extended with a resistive sheet in the hh-polarization case. Using the transition conditions on the resistive sheet given by [Senior et al., 1987]

$$[\hat{n} \times \mathbf{E}]_-^+ = 0, \qquad \hat{n} \times (\hat{n} \times \mathbf{E}) = -R\mathbf{J}, \tag{3.31}$$

where R is the resistivity of the resistive sheet, eq. (3.14) can be revised for a resistive sheet as

$$\mathbf{E}^i(\overline{\rho}) = R(\overline{\rho})\mathbf{J}_e(\overline{\rho}) + \frac{k_0 Z_0}{4} \int_l \mathbf{J}_e(\overline{\rho}')\, H_0^{(1)}(k_0|\overline{\rho} - \overline{\rho}'|)dl', \qquad \overline{\rho}' \text{ on interface.} \tag{3.32}$$

Consequently, the element of impedance matrix in (3.20) is revised as

$$z_{mn} = R(x_n, z_n)\delta_{mn} + \frac{k_0 Z_0}{4} \int_{\Delta x_n} H_0^{(1)}(k_0\sqrt{(x - x_n)^2 + (z - z_n)^2}) \sqrt{1 + \left(\frac{dz_n}{dx_n}\right)^2} dx_n. \tag{3.33}$$

The resistivity profile, $R(x)$, is chosen similarly as the profile used in [Leo et al., 1993] as

$$R(x) = \begin{cases} 0, & |x| \le D/2 + d \\ 0.005 Z_0 \left(\frac{D/2 - |x|}{d}\right)^4, & D/2 - d \ge |x| \le D/2 \end{cases} \tag{3.34}$$

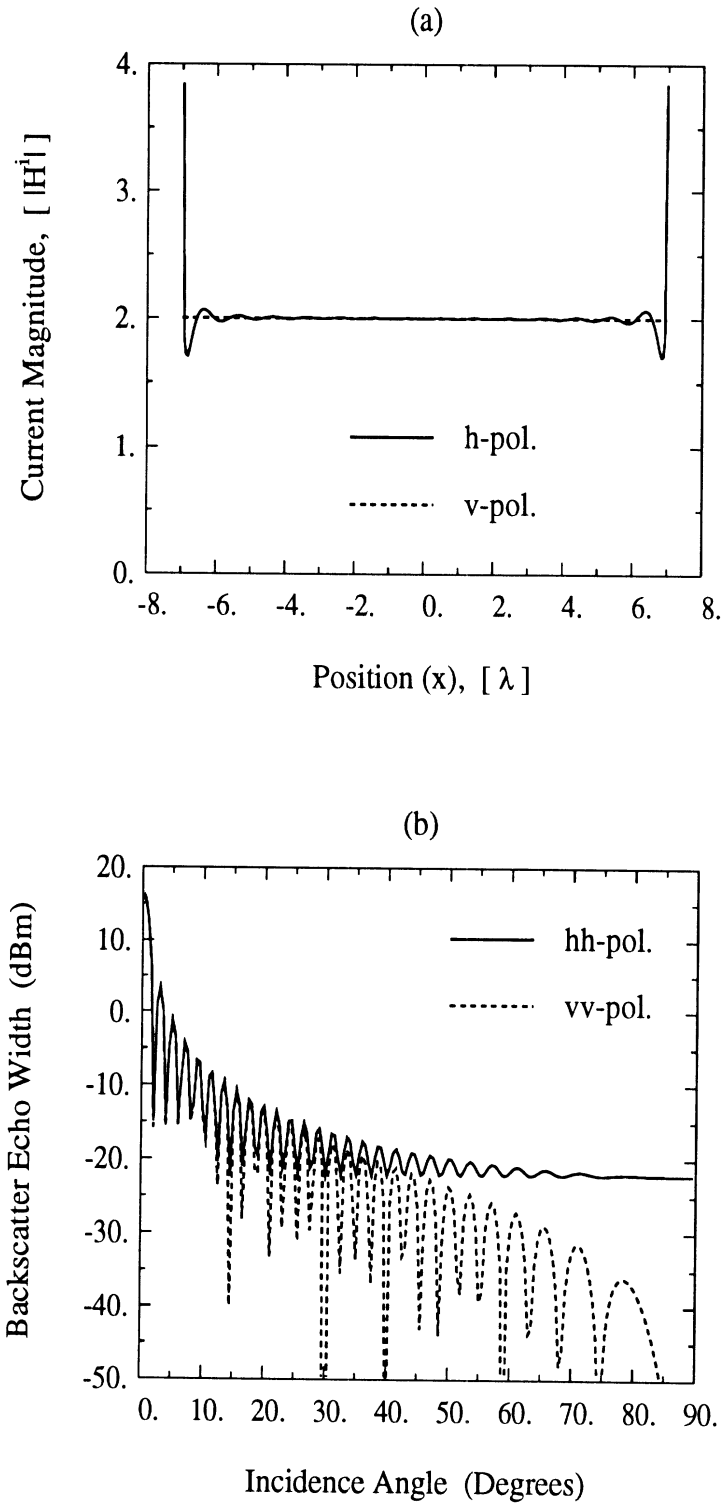

Figure 3.6: Backscattering from a flat conducting strip of the width of 14λ, (a) the current distribution at 0° incidence, and (b) the backscatter echo width.

where D is the total width of the surface and d is the width of the resistive card. The resistivity and the surface currents induced by h- and v-polarized incidence waves are shown in Fig. 3.7 (a) in case of $D = 12\lambda$ and $d = 1\lambda$. Since the current distribution near resistive cards shows ripples, the backscatter RCS is computed ignoring the surface current at each end (1λ) of the surface. In this case, the hh-polarized backscatter RCS also decreases as the incidence angle increases, following the vv-polarized backscatter RCS as shown in Fig. 3.7 (b).

3.4 Numerical Results

The backscattering coefficient of a random surface with given roughness parameters can be computed by a Monte Carlo method as described above, *i.e.*, the scattered fields from N randomly generated segments of the surface are computed numerically, and the backscattering coefficient of the random surface is obtained from the statistics of the scattered fields. Each segment of the surface has the width of D with an extended region of D_E and a resistive sheet of the length D_R at each end as shown in Fig. 3.8. Both D_E and D_R are chosen to be 1λ considering the trade-off between computation time and edge effect reduction. The resistivity of the resistive cards is given in (3.34) and shown in Fig. 3.8. Even though currents on the whole regions are computed by the method of moments, the currents only on the region of consideration are used to compute the scattered field, ignoring those on the extended regions and the resistive regions.

In order to test the numerical technique described above, the backscattering coefficients of the surface S-1 and S-3 in Table 3.1 were computed and compared with the small perturbation method (SPM) solution and the physical optics (PO) solution, respectively. The roughness parameters of the surface S-1 given in Table 3.1 satisfy

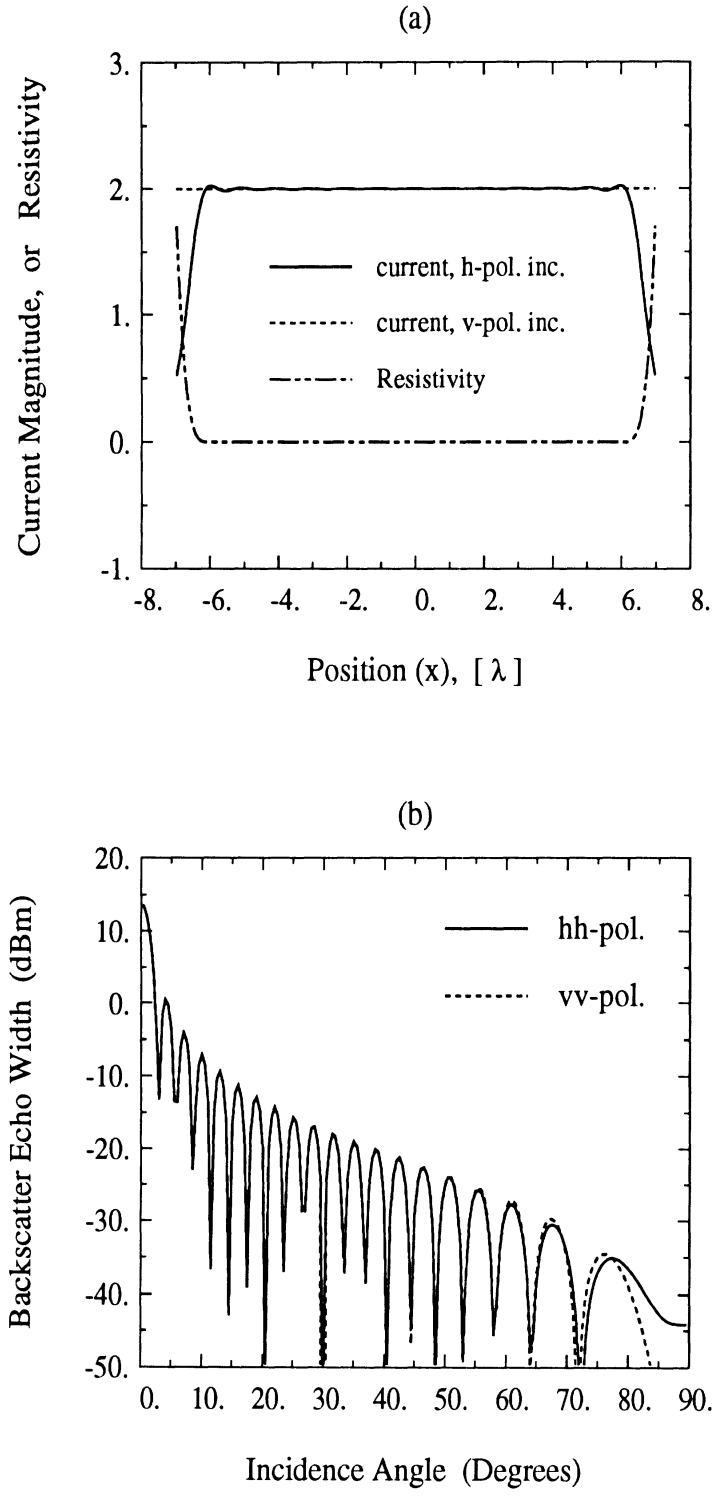

Figure 3.7: Backscattering from a flat conducting strip with resistive cards, (a) the current distribution at 0° incidence and resistivity distribution, and (b) the backscatter echo width.

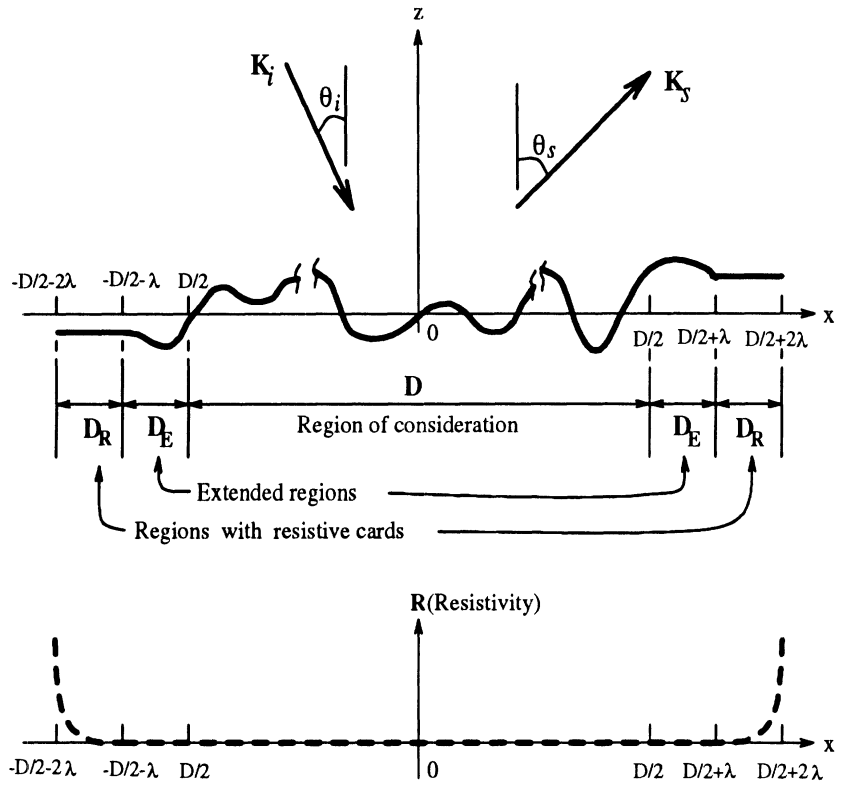

Figure 3.8: The extension of the random surface with resistive cards.

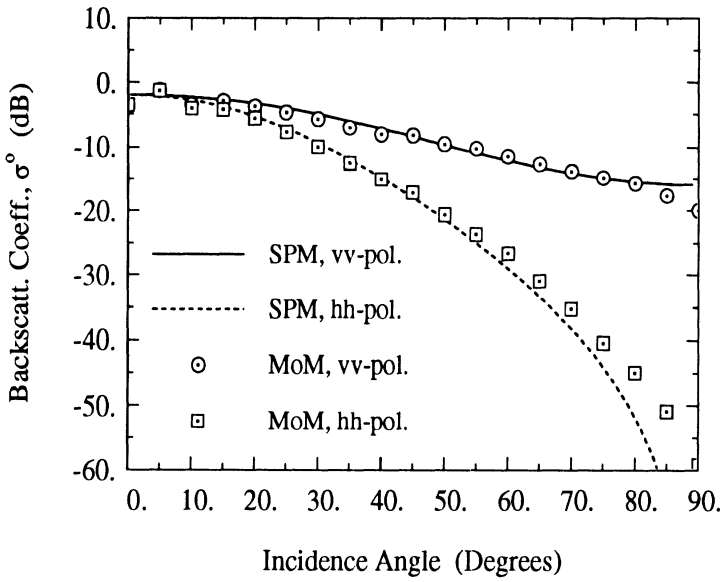

Figure 3.9: The solution by the method of moments compared with the small perturbation method for the random surface, S-1, of ks=0.21 and kl=2.2.

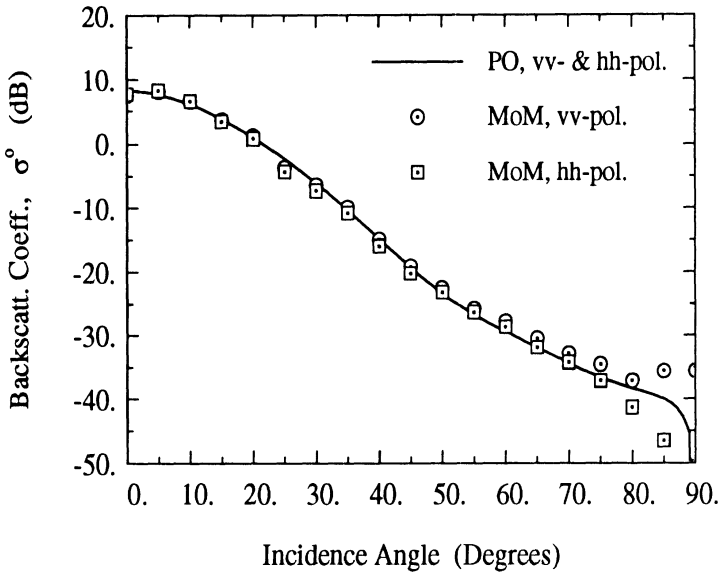

Figure 3.10: The solution by the method of moments compared with the physical optics solution for the random surface, S-3, of ks=1.04 and kl=7.4.

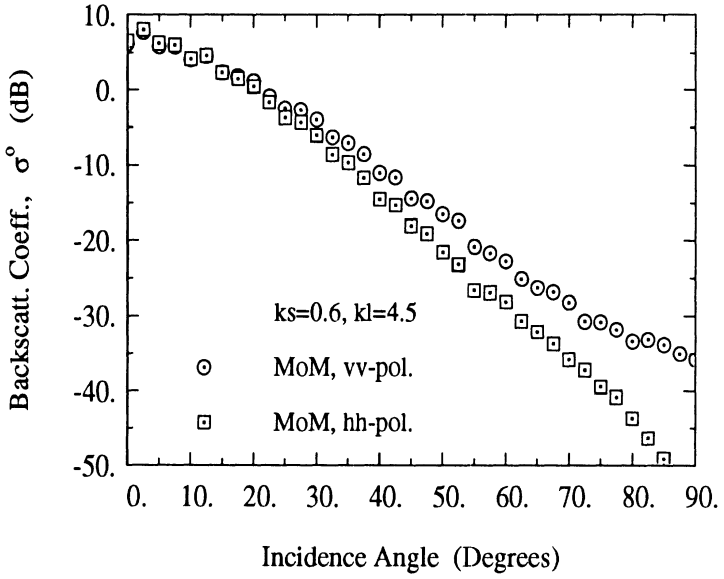

Figure 3.11: The solution by the method of moments for the random surface, S-2, of ks=0.62 and kl=4.6.

the validity condition of the SPM which is $ks < 0.3$, $kl < 3.0$, and $\sqrt{2}s/l < 0.3$ for a Gaussian correlation. The backscattering coefficients by the numerical simulation for vv- and hh-polarizations show an excellent agreement with the solution of the SPM as shown in Fig. 3.9, where the SPM model for a one-dimensional conducting random surface is given in Appendix A. The roughness of the surface S-3 in Table 3.1 is valid for the PO model ($ks < 6$, $\sqrt{2}s/l < 0.25$ [Ulaby et al., 1986]). The numerical solution for S-3 shows an excellent agreement with the PO solution at $\theta < 85°$ as shown in Fig. 3.10, where the PO model is formulated and evaluated exactly for a one-dimensional conducting surface as given in Chapter 2. Since the numerical solutions agree very well with the theoretical models at two extreme roughness conditions, we can apply this numerical technique with confidence to the intermediate roughness conditions which cannot be solved by existing classical theoretical models. The backscattering coefficient for one of such surfaces, S-2 in Table 3.1, is computed and shown in Fig. 3.11.

It is well known that the phase-difference statistics has valuable information in addition to the magnitude as shown in Chapter 5. This numerical technique is used to compute the co-polarized phase-difference statistics of a random surface S-2 ($ks = 0.6$, $kl = 4.5$). The co-polarized phase-difference angle $\phi_c = \phi_{hh} - \phi_{vv}$ for a smaller incidence angle (20°) shows narrower and higher shape of distribution curve than that for a larger incidence angle (50°) as shown in Figs. 3.12 (a) and (b). The standard deviation of the ϕ_c distribution increases as the incidence angle increases while the mean of the distribution stays at zero as shown in Figs. 3.13 (a) and (b). The degree of correlation α and the coherent phase-difference ζ are parameters of the phase-difference statistics defined in [Sarabandi, 1993]. As described in Chapter 5, the degree of correlation α and the coherent phase-difference ζ are the measures of

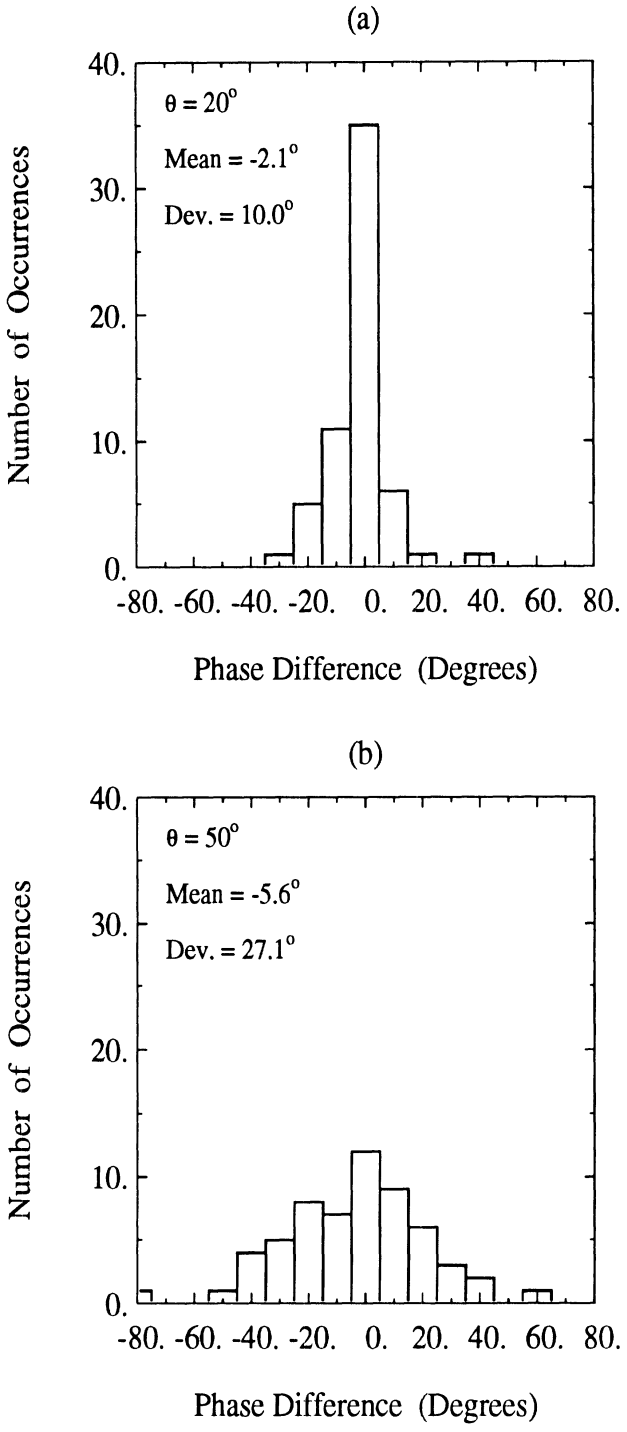

Figure 3.12: The distribution of the phase difference between σ°_{hh} and σ°_{vv} of the surface, S-2, (ks=0.62, kl=4.6), (a) at 20° and (b) at 50° incidences.

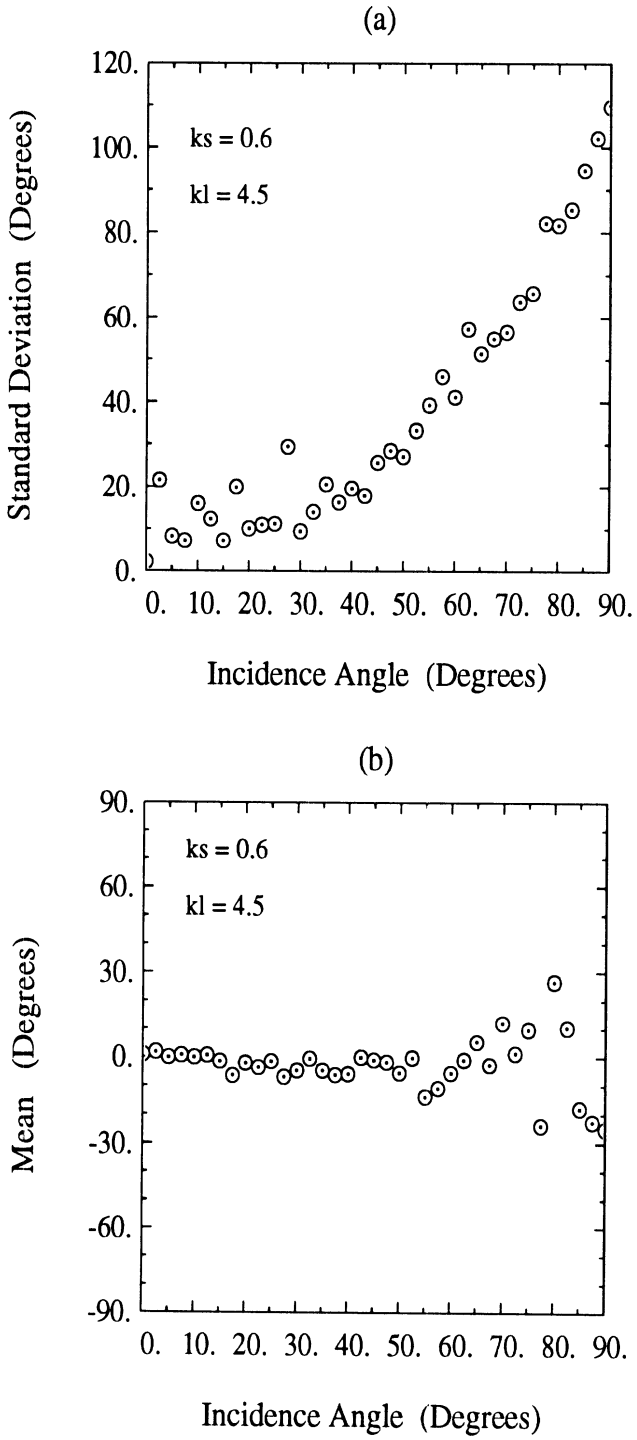

Figure 3.13: The distribution of the phase difference between σ°_{hh} and σ°_{vv} of the surface, S-2, (ks=0.62, kl=4.6), (a) standard deviation and (b) mean values.

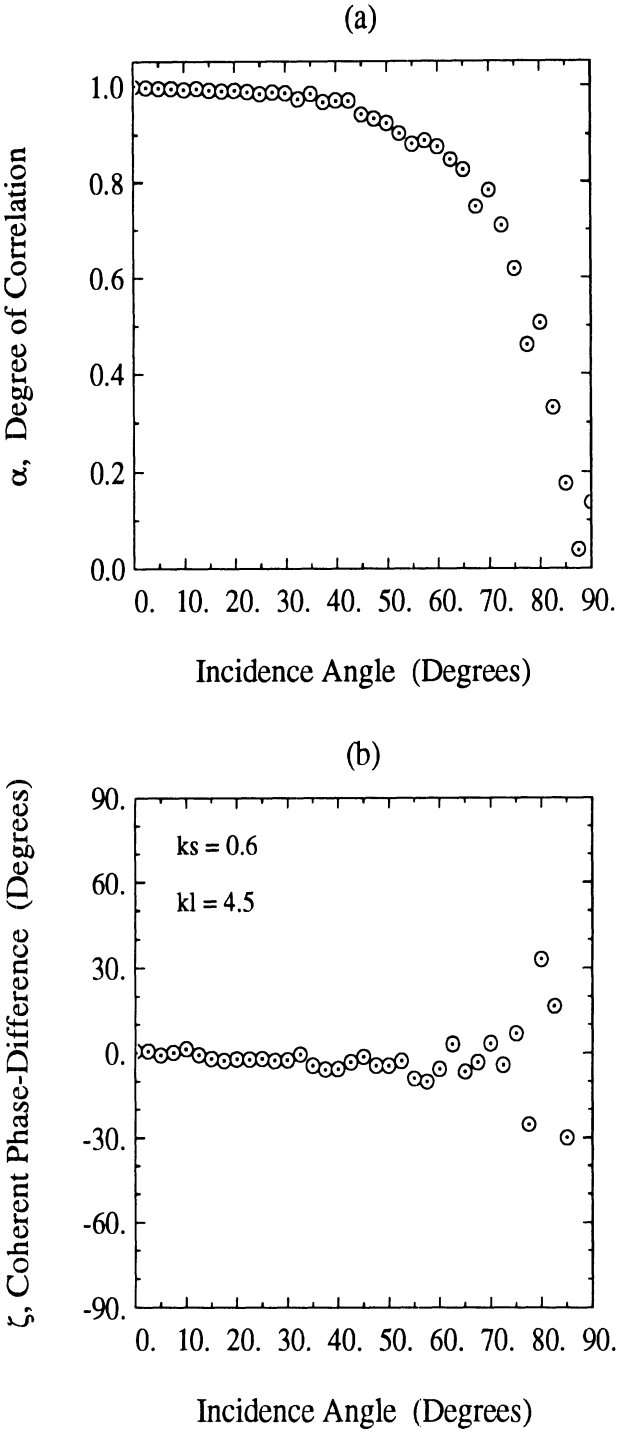

Figure 3.14: The statistics of the phase difference between σ°_{hh} and σ°_{vv} of the surface, S-2, (ks=0.62, kl=4.6), (a) the degree of correlation, α and (b) the coherent phase-difference, ζ.

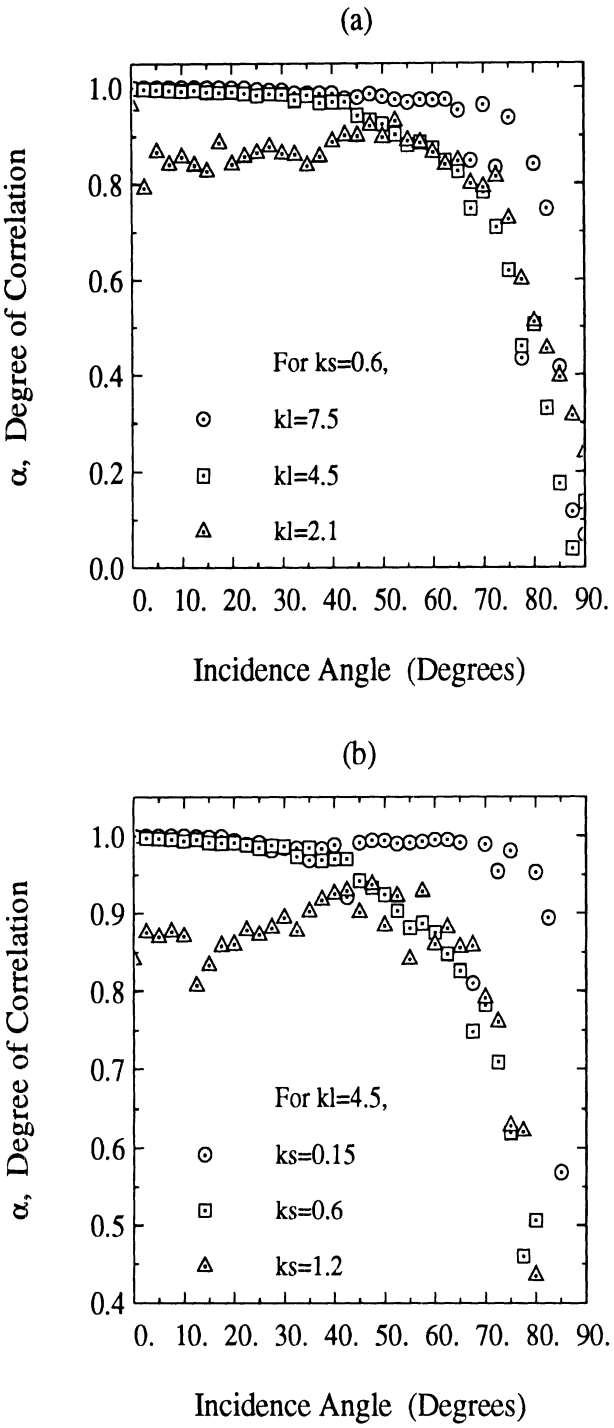

Figure 3.15: The degree of correlation, α, (a) for three different kl values at a fixed value of $ks = 0.6$, and (b) for three different ks values at a fixed value of $kl = 4.5$.

the width (standard deviation) and the mean of ϕ_c distribution, respectively. The degree of correlation α and the coherent phase-difference ζ computed by the numerical simulation for the surface S-2 are shown in Figs. 3.14 (a) and (b), respectively. The degree of correlation α depends on the roughness of random surfaces as shown in Figs. 3.15 (a) and (b). Figures 3.15 (a) and (b) show the kl and ks dependencies of the degree of correlation for fixed ks and kl, respectively. Based on the numerical results, the degree of correlation α seems to be a strong function of the rms slope for one-dimensional conducting random surfaces.

3.5 Evaluation of Theoretical Scattering Models

At first, the formulations of the theoretical models are summarized for scattering from a one-dimensional conducting random surface having a Gaussian correlation. The small perturbation method (SPM), the physical optics (PO) model, and the geometrical optics (GO) model have been presented in the previous chapter for two-dimensional dielectric surfaces, and those will be modified for one-dimensional conducting surfaces in this chapter. Many other scattering models have been presented recently, including phase perturbation method (PPM) [Winebernner and Ishimaru, 1985a], full-wave method (FWM) [Bahar, 1981], and integral equation method (IEM) [Fung and Pan, 1987]. Those models are also evaluated in this section. Since a one-dimensional random surface does not produce depolarization, the cross-polarized backscattering coefficients are zero, $\sigma^\circ_{hv} = \sigma^\circ_{vh} = 0$.

3.5.1 Small Perturbation Method

The like-polarization backscattering coefficients by the first-order small perturbation model (SPM) have the form given in (2.31) for two-dimensional surfaces.

The backscattering coefficients σ°_{pp} for the SPM are proportional to the roughness spectrum which is the Fourier transform of the surface correlation function and also proportional to the magnitude square of the far-field Green's function given in (3.24) and (2.44) for one- and two-dimensional surfaces, respectively. Since the one- and two-dimensional surfaces correspond to the two- and three-dimensional scattering problems, respectively;

$$\sigma^{\circ}_{1d} \propto 2\pi\rho \cdot \frac{1}{8\pi k\rho} \cdot W_{1d}(2k\sin\theta) \tag{3.35}$$

$$\sigma^{\circ}_{2d} \propto 4\pi r^2 \cdot \frac{1}{(4\pi r)^2} \cdot W_{2d}(2k\sin\theta, 0).$$

Comparing $W_{1d}(2k\sin\theta)$ given in (3.9) and $W_{2d}(2k\sin\theta, 0)$ given in (2.34) for a Gaussian correlation function,

$$\frac{\sigma^{\circ}_{1d}}{\sigma^{\circ}_{2d}} = \frac{\pi}{k} \cdot \frac{W_{1d}(2k\sin\theta)}{W_{2d}(2k\sin\theta, 0)} = \frac{\sqrt{\pi}}{kl}. \tag{3.36}$$

Therefore, the backscattering coefficient for the one-dimensional conducting surface can be given from (3.36) and (2.31) for a Gaussian correlation;

$$\sigma^{\circ}_{pp} = 4\sqrt{\pi}\,(ks)^2\,kl\,\cos^4\theta\,\left|\alpha^{c}_{pp}\right|^2\,e^{-(kl\sin\theta)^2} \tag{3.37}$$

where α^{c}_{pp} is modified for a conducting surface as,

$$\alpha^{c}_{hh}(\theta) = -1$$

$$\alpha^{c}_{vv}(\theta) = -\frac{1+\sin^2\theta}{\cos^2\theta}. \tag{3.38}$$

3.5.2 Physical Optics Model

The incoherent like-polarized backscattering coefficient of the physical optics (PO) model for a one-dimensional random surface can be obtained by modifying the model

for a two-dimensional surface given in (2.80). Similarly to (3.36), the ratio between σ°_{1d} and σ°_{2d} for the PO model is

$$\frac{\sigma^{\circ}_{1d}}{\sigma^{\circ}_{2d}} = \frac{\pi}{k} \cdot \frac{\sum_n W^{(n)}_{1d}(2k\sin\theta)}{\sum_n W^{(n)}_{2d}(2k\sin\theta, 0)}, \tag{3.39}$$

where $W^{(n)}_{2d}(2k\sin\theta, 0)$ is the Fourier transform of the nth powered normalized correlation function for a two-dimensional surface and given as $\mathbf{I}_G$ in (2.77). $W^{(n)}_{1d}(2k\sin\theta)$ is the Fourier transform of $\rho^n(\xi)$ for a one-dimensional surface,

$$W^{(n)}_{1d}(2k\sin\theta) = \sqrt{\frac{\pi}{n}} l \, e^{-\frac{(kl\sin\theta)^2}{n}}. \tag{3.40}$$

Therefore, the backscattering coefficients for a one-dimensional conducting surface with the $0th$-order approximation can be obtained as

$$\sigma^{\circ}_{vv_{0th}}(\theta) = \sigma^{\circ}_{hh_{0th}}(\theta) = \sqrt{\pi} kl \, \cos^2\theta \, e^{-(2ks\cos\theta)^2} \sum_{n=1}^{\infty} \frac{(2ks\cos\theta)^{2n}}{n!\sqrt{n}} e^{-\frac{(kl\sin\theta)^2}{n}}, \tag{3.41}$$

when a Gaussian correlation function is assumed. The first-order approximated backscattering coefficient for the PO model is given by (2.73)

$$\sigma^{\circ}_{pp_{0th}}(\theta) = \frac{\sigma^{\circ}_{pp_{1st}}(\theta)}{\cos^4\theta}. \tag{3.42}$$

3.5.3 Phase Perturbation Method

Using a perturbation expansion of the surface field phase from rough surfaces, the phase perturbation method (PPM) was developed in the case of scalar wave scattering from surfaces for which Dirichlet boundary conditions hold [Winebernner and Ishimaru, 1985a and 1985b]. The backscattering coefficient for a one-dimensional surface is expressed as [Broschat et al, 1987],

$$\sigma^{\circ} = k\cos^2\theta \, \exp[-2\mathrm{Re}[N_2]] \int_{-\infty}^{\infty} \exp[i2k\, x\, \sin\theta](\exp[N_{11}(x)] - 1)\, dx \tag{3.43}$$

with

$$N_2 = 2k^2 \cos\theta \int_{-\infty}^{\infty} W(U)\beta\left(\frac{U + k\sin\theta}{k}\right) dU,$$

$$N_{11}(x) = k^2 \int_{-\infty}^{\infty} W(U)\exp[iUx]\left|\cos\theta + \beta\left(\frac{U + k\ \sin\theta}{k}\right)\right|^2 dU,$$

$$\beta\left(\frac{U}{k}\right) = \sqrt{1 - \left(\frac{U}{k}\right)^2},$$

where $W(U)$ is a roughness spectrum for one-dimensional random surfaces given in [Broschat et al, 1987] as

$$W(U) = \frac{s^2 l}{2\sqrt{\pi}} \exp\left[-\frac{U^2 l^2}{4}\right].$$

The PPM does not include polarization dependence, and above formulation is equivalent to electromagnetic wave scattering from perfect conducting rough surfaces for hh-polarization. Calculations of the backscattering coefficient using (3.43) involve a double integral having infinite limits of integration, where the integrand fluctuates by being non-oscillatory and highly oscillatory [Broschat et al, 1987].

It has been claimed that the PPM reduces to the two classical models, namely the SPM and the PO in the appropriate limits and smoothly interpolates between the SPM and the PO [Ivanova et al, 1990; Broschat, 1987].

3.5.4 Full Wave Method

The "full-wave" method (FWM) was developed for random surface scattering by Bahar [Bahar, 1981; Bahar, 1991a; and Bahar,1991b]. Even though the FWM is formally exact, approximations are necessary to obtain results for rough surface scattering since the general form includes ten-fold numerical integrals for two dimensional

surfaces. The scattering coefficient for a one-dimensional perfect conducting Gaussian surface is given as [Bahar, 1991b],

$$\sigma_{pp}^{\circ} = 2kG_0^{P^2}\int_0^{2L}\left[1-\frac{x}{2L}\right]\left\{\chi_2(\nu_y,-\nu_y)\left[1+G_1^{P^2}(m^2A-\nu_y^2B^2)\right]\right.$$
$$\left.-2\chi(\nu_y)\left[1+G_1^{P^2}m^2A\right]+1+G_1^{P^2}m^2A\right\}\cos(\nu_x x)dx$$
$$-2kG_0^{P^2}G_1^P\int_0^{2L}\left[1-\frac{x}{2L}\right]\left[\chi_2(\nu_y,-\nu_y)-\chi(\nu_y)\right]2\nu_y B\sin(\nu_x x)dx \qquad (3.44)$$

with

$$\chi_2(\nu_y,-\nu_y)=\exp\left[-\nu_y^2s^2(1-\rho)\right] \qquad (3.45)$$

$$\chi(\nu_y)=\exp\left[\frac{-\nu_y^2s^2}{2}\right] \qquad (3.46)$$

$$A(x)=-\frac{d^2\rho}{dx^2}\frac{s^2}{m^2}$$

$$B(x)=-\frac{d\rho}{dx}s^2$$

$$G^P(\hat{n})\triangleq\frac{(-\hat{n}^i\cdot\hat{n})F^P(\hat{n})}{(-\hat{n}\cdot\hat{y})}\cong G_0^P\left[1+h_xG_1^P\right],$$

where s is the rms height, m is the rms slope, $\nu_x=-2k\sin\theta$, $\nu_y=2k\cos\theta$, and $G_0^H=\cos\theta$, $G_1^H=\tan\theta$ for the horizontally polarized backscatter.

Bahar has shown analytically that the FWM can reduce to both of the SPM and the PO when appropriate conditions are imposed [Bahar, 1991a; Bahar,1991b]. Thoros and Winebernner, however, claimed that the FWM does not reduce to the SPM in their examinations [Thoros and Winebernner, 1991].

3.5.5 Integral Equation Method

The integral equation method (IEM) was developed based on an approximate solution of a pair of integral equations for the tangential surface fields [Fung et al., 1992].

Backscattering coefficients for a rough dielectric surface are given in a quite lengthy form for each case of $ks < 3$ and $ks > 3$ in [Fung et al., 1992]. The backscattering coefficients for a perfectly conducting rough surface are given in [Fung and Pan, 1987] for a two-dimensional random surface. For a one-dimensional surface, σ°_{vv} and σ°_{hh} can be modified as

$$\sigma^{\circ}_{\substack{vv \\ hh}} = \frac{4k}{\cos^2\theta}\, e^{-2k^2s^2\cos^2\theta} \sum_{n=1}^{\infty} \frac{W_{1d}^{(n)}(2k\sin\theta)}{n!\sqrt{n}} (ks\cos\theta)^{2n} \cdot \left\{ 2^{2n-2}\exp(-2k^2s^2\cos^2\theta) \pm 2^n \sin^2\theta \exp(-k^2s^2\cos^2\theta) + \sin^4\theta \right\}. \tag{3.47}$$

If a Gaussian correlation function is assumed, $W_{1d}^{(n)}(2k\sin\theta)$ can be replaced by (3.40) as

$$\sigma^{\circ}_{\substack{vv \\ hh}} = \frac{\sqrt{\pi}kl}{\cos^2\theta}\, e^{-2k^2s^2\cos^2\theta} \sum_{n=1}^{\infty} \frac{(ks\cos\theta)^{2n}}{n!\sqrt{n}} e^{-\frac{(kl\sin\theta)^2}{n}} \cdot \left[2^n \exp(-k^2s^2\cos^2\theta) \pm 2\sin^4\theta \right]^2. \tag{3.48}$$

It was claimed that the IEM reduces to the SPM and the PO for the low-frequency limit and the high-frequency limit, respectively [Fung and Pan, 1987 and Fung et al., 1992].

3.5.6 Numerical Results

The validity regions of the scattering models and three roughness conditions given in Table 3.1 are illustrated in Fig. 3.16. The validity regions of the phase perturbation method (PPM), the full-wave method (FWM), and the integral equation method (IEM) need to be examined in detail; however, each of these models is assumed to meet the validity conditions of the small perturbation method (SPM) and the physical optics approximation (PO), as well as the intermediate roughnesses between the validity regions of the SPM and the PO model [Bahar, 1991; Broschat et al., 1987; and Fung and Pan, 1987].

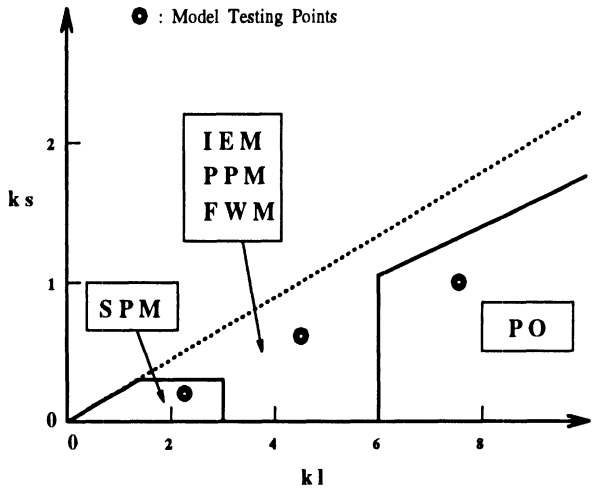

Figure 3.16: The validity regions of the scattering models.

The backscattering coefficients of *vv*- and *hh*-polarizations for a perfectly conducting rough surface are computed by the SPM, the PO, and the IEM at three roughness conditions as indicated (o) in Figure 3.16 and those values are compared with the solution from the method of moments as shown in Figs. 3.17(a)-(c). Since the PPM provides only the *hh*-polarized solution [Winebernner and Ishimaru, 1985] and the only *hh*-polarized scattering amplitude of the FWM is given explicitly in Bahar [1991], the *hh*-polarized backscattering coefficient for a perfectly conducting rough surface is computed by the PPM and the FWM and compared with those of the SPM, the PO, and the IEM as in Figs. 3.18(a)-(c).

3.6 Conclusions

A Monte Carlo method in conjunction with the method of moments (MoM) is applied to obtain an exact solution of scattering from a one-dimensional conducting

random surface. A new approach is introduced in this method to eliminate the edge effect which results from the numerical simulation of scattering from a random surface of finite width. By adding a resistive sheet at each end of an illuminated random surface, the edge effect can be eliminated even at large incidence angles less than 85°. The numerical solution with this technique agrees very well with existing theoretical models, SPM and PO, at their validity regions. In addition to the magnitude, the phase-difference statistics was computed by this technique, and it is shown that the degree of correlation α shows strong dependency not only on the incidence angle but also on the roughness of the surface. This numerical technique has been used to evaluate existing models of SPM, PO, PPM, FWM, and IEM for scattering from one-dimensional conducting random surfaces.

(a)

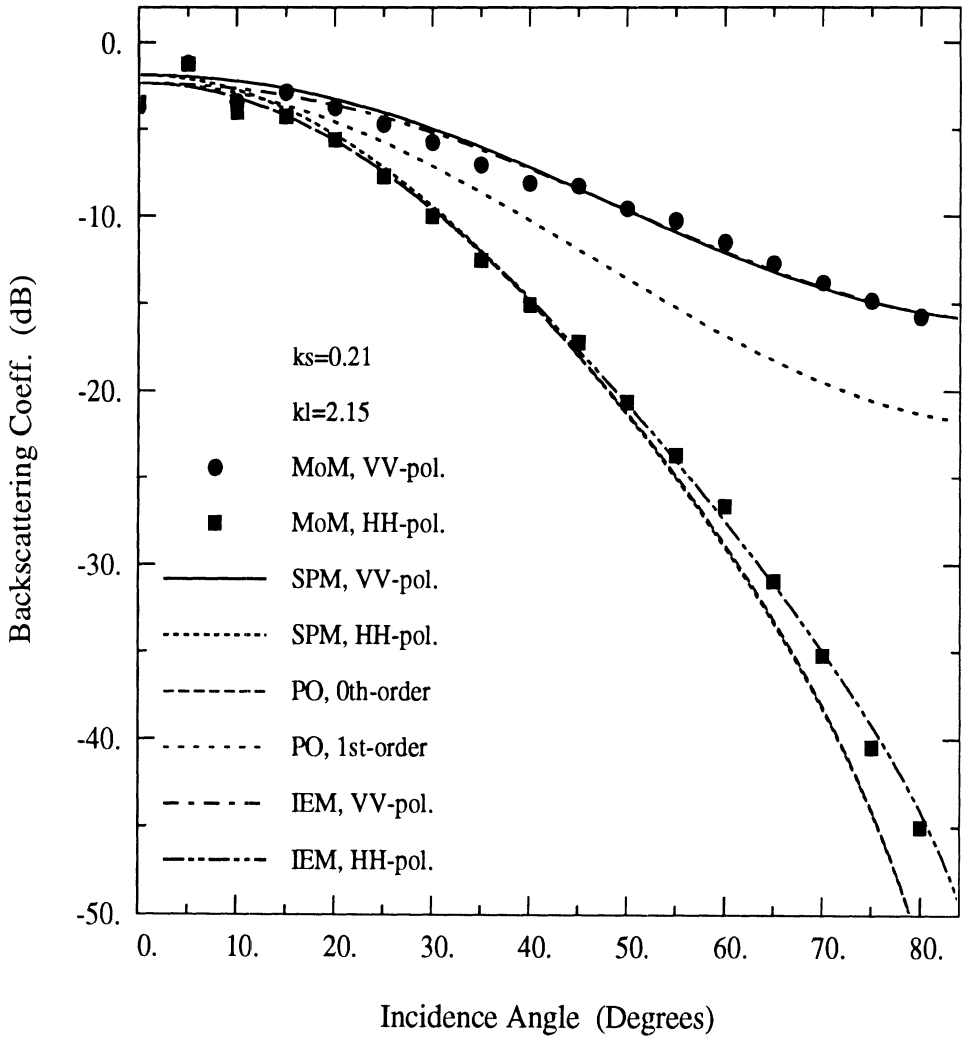
0.
-10.
-20.
-30.
-40.
-50.
0.
10.
20.
30.
40.
50.
60.
70.
80.
Backscattering Coeff. (dB)
Incidence Angle (Degrees)
ks=0.21
kl=2.15
MoM, VV-pol.
MoM, HH-pol.
SPM, VV-pol.
SPM, HH-pol.
PO, 0th-order
PO, 1st-order
IEM, VV-pol.
IEM, HH-pol.

(b)

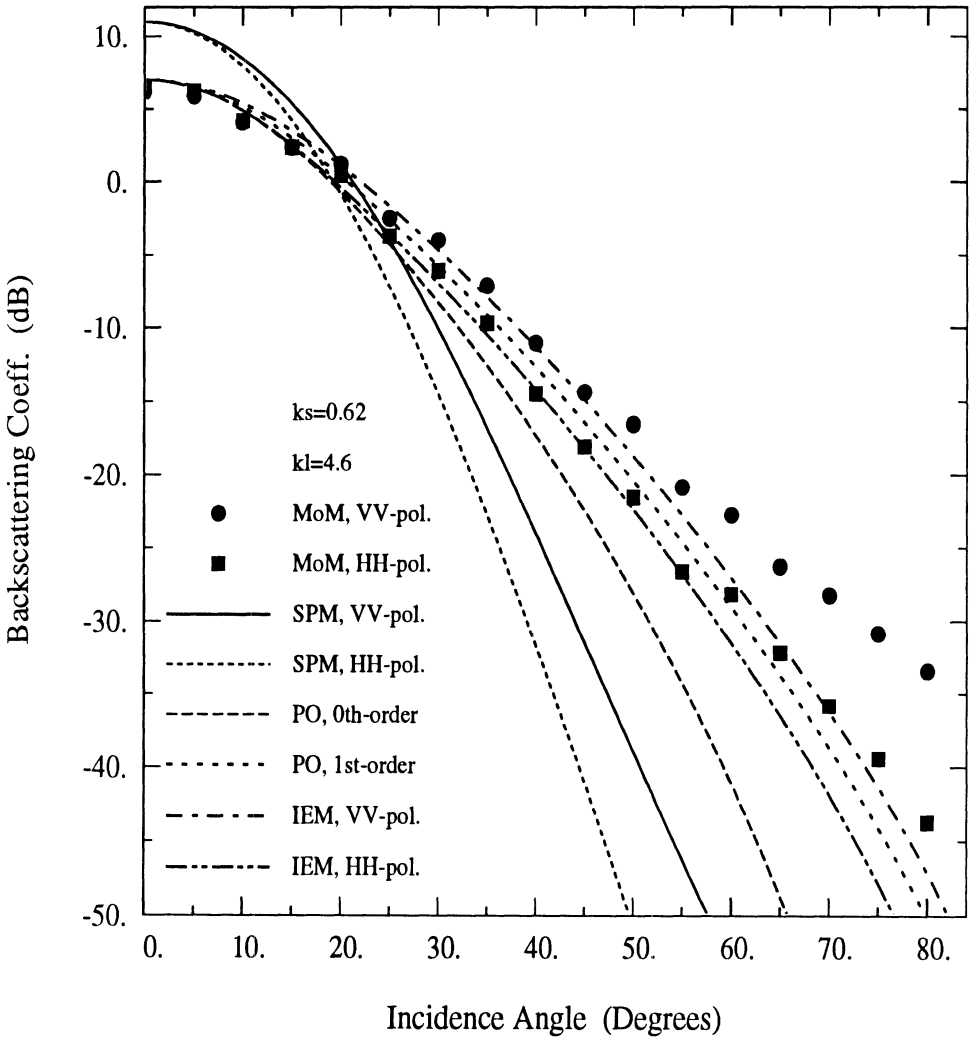
10.
0.
-10.
-20.
-30.
-40.
-50.
0.
10.
20.
30.
40.
50.
60.
70.
80.
Backscattering Coeff. (dB)
Incidence Angle (Degrees)
ks=0.62
kl=4.6
MoM, VV-pol.
MoM, HH-pol.
SPM, VV-pol.
SPM, HH-pol.
PO, 0th-order
PO, 1st-order
IEM, VV-pol.
IEM, HH-pol.

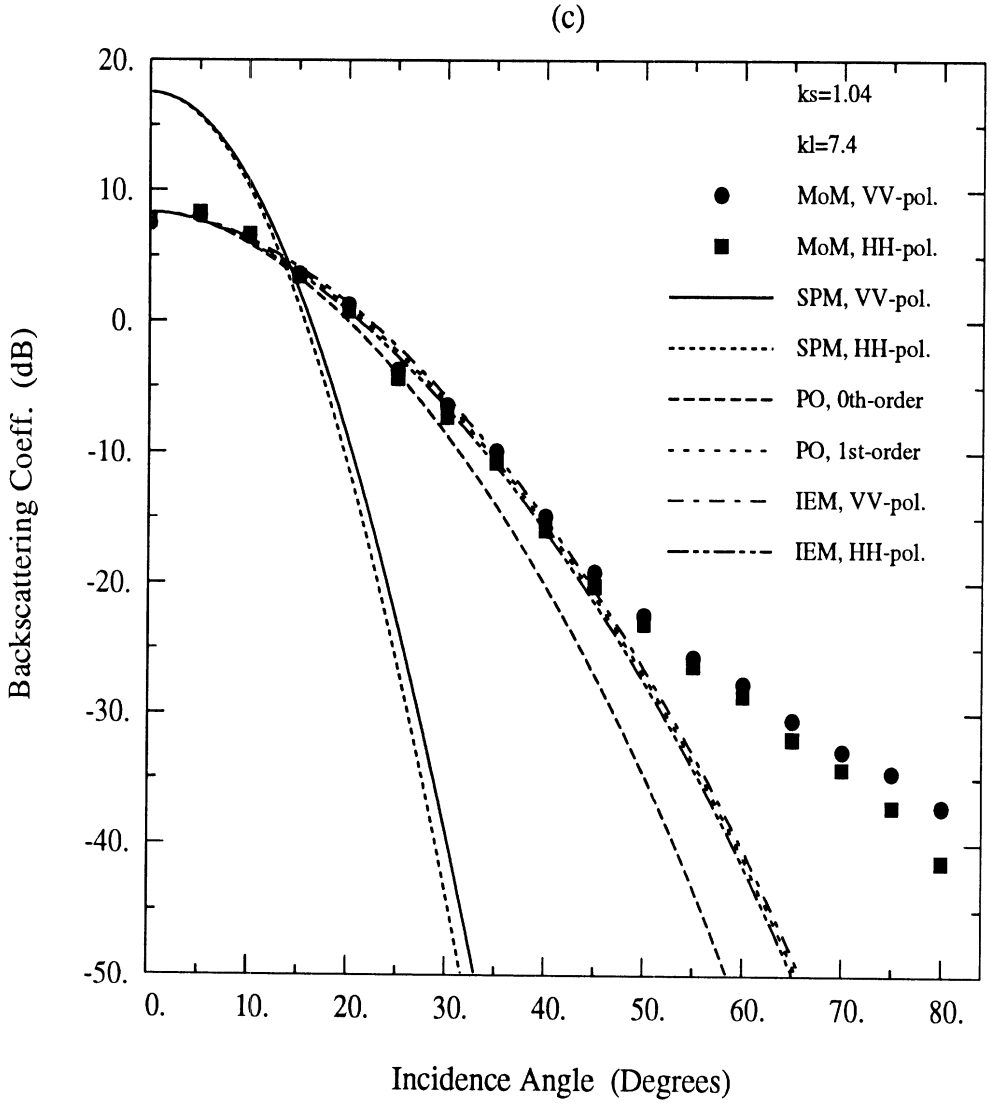

Figure 3.17: Comparison of models with an exact numerical solution for (a) $ks = 0.21$ and $kl = 2.2$, (b) $ks = 0.62$ and $kl = 4.6$, and (c) $ks = 1.04$ and $kl = 7.4$ for both of vv- and hh-polarizations.

(a)

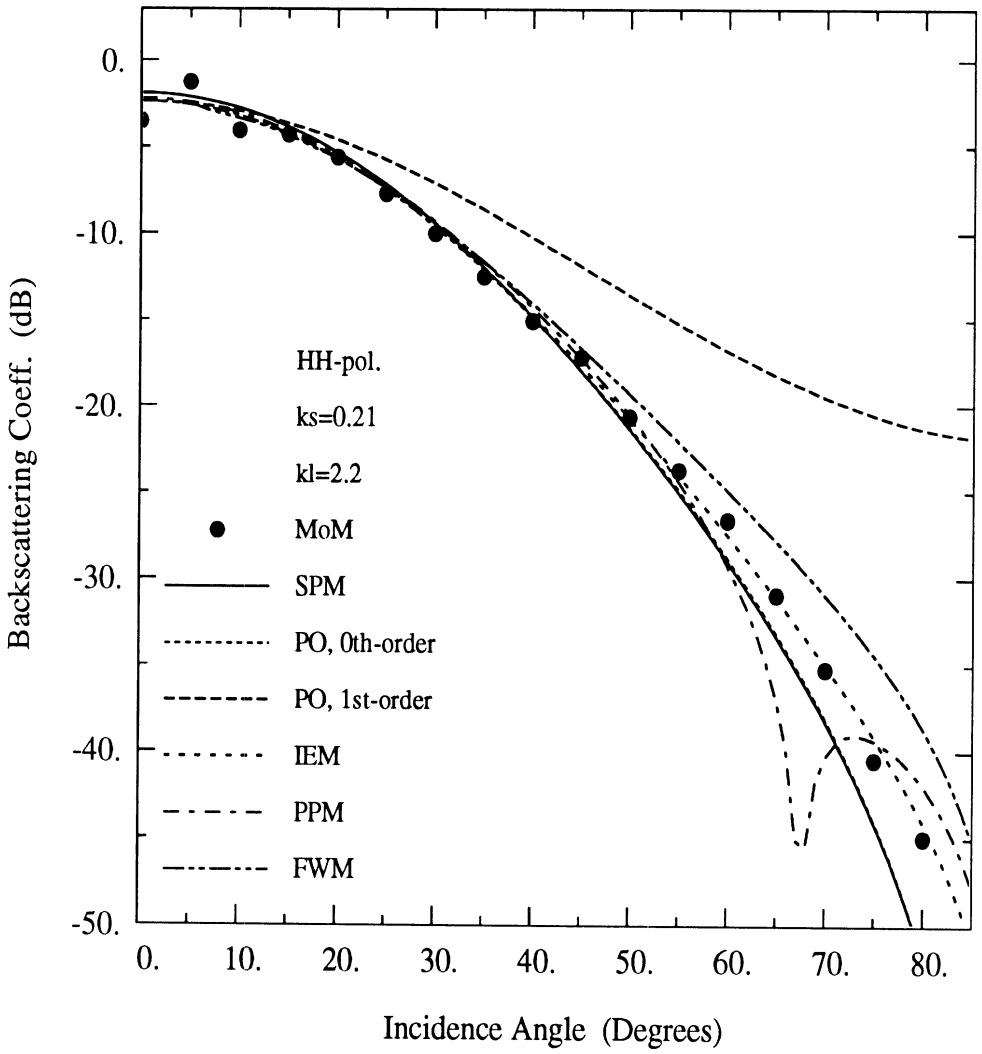
0.
-10.
-20.
-30.
-40.
-50.
0.
10.
20.
30.
40.
50.
60.
70.
80.
Backscattering Coeff. (dB)
Incidence Angle (Degrees)
HH-pol.
ks=0.21
kl=2.2
MoM
SPM
PO, 0th-order
PO, 1st-order
IEM
PPM
FWM

(b)

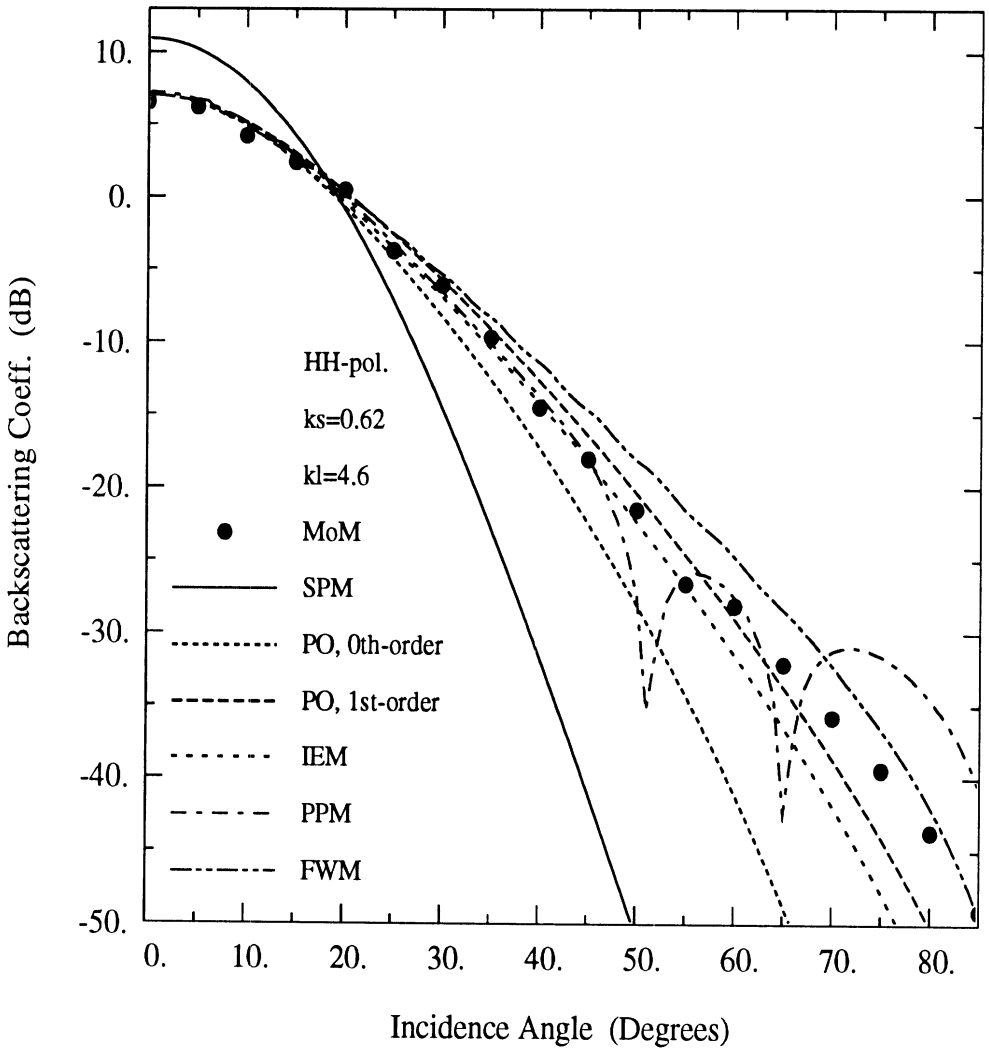
10.
0.
-10.
-20.
-30.
-40.
-50.
0.
10.
20.
30.
40.
50.
60.
70.
80.
Backscattering Coeff. (dB)
Incidence Angle (Degrees)
HH-pol.
ks=0.62
kl=4.6
MoM
SPM
PO, 0th-order
PO, 1st-order
IEM
PPM
FWM

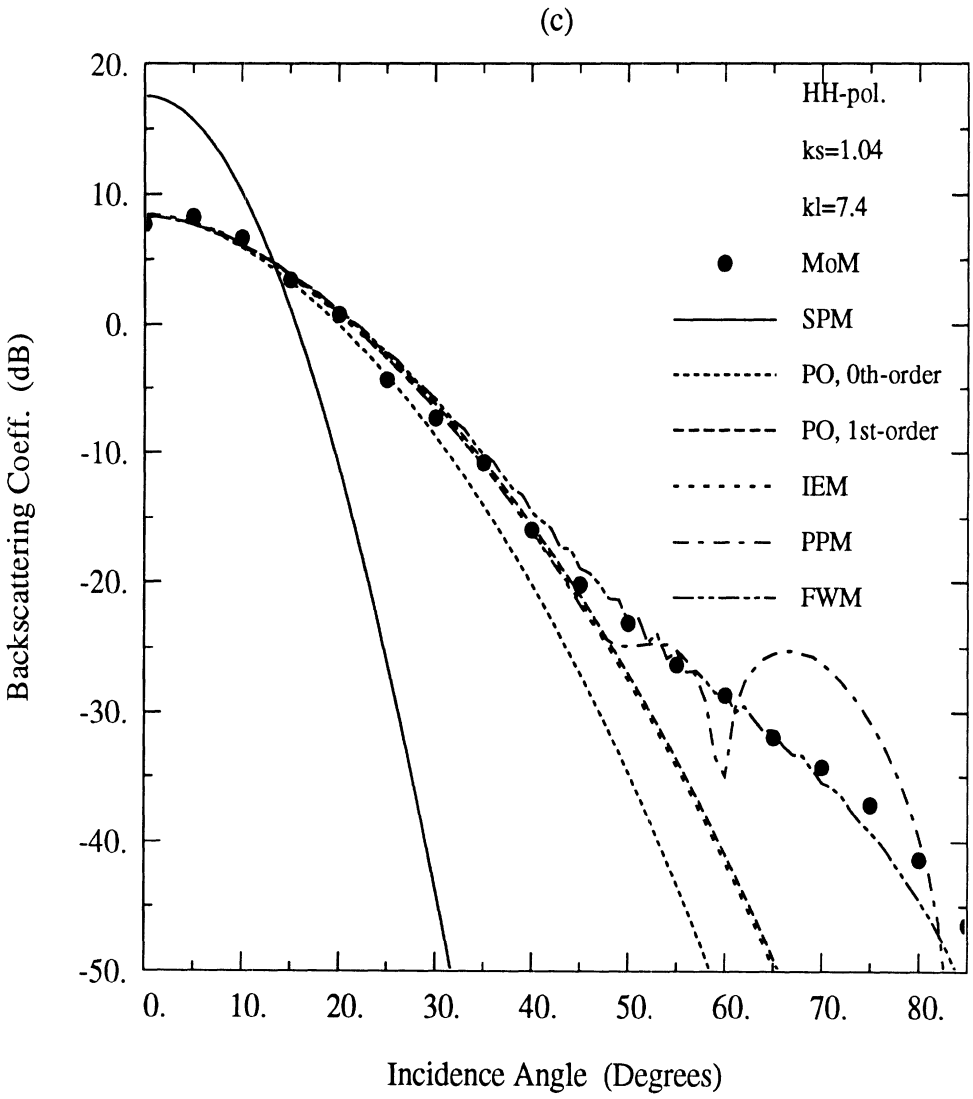

Figure 3.18: Comparison of models with an exact numerical solution for (a) $ks = 0.21$ and $kl = 2.2$, (b) $ks = 0.62$ and $kl = 4.6$, and (c) $ks = 1.04$ and $kl = 7.4$ for hh-polarization.

CHAPTER IV

AN IMPROVEMENT OF PHYSICAL OPTICS MODEL

4.1 Introduction

In Chapter 2 the Kirchhoff approximation in the computation of the radar backscattering coefficient was introduced briefly. The scattered fields from a randomly rough surface can be formulated exactly in terms of surface currents (or equivalent tangential surface fields). Since it is very difficult if not impossible to compute the exact form of tangential fields on the random surface, we have used the tangent plane approximation (or the Kirchhoff approximation) *i.e.*, the surface fields at any point of the surface are represented by the fields computed by approximating the boundary interface as a tangent plane at that point. Then, the backscattered mean intensity, from which the backscattering coefficients can be computed, can be formulated in terms of the ensemble average of the conjugate-multiplied scattering amplitudes. The scattering amplitude is a function of the local surface slopes and the local reflection coefficients where the local reflection coefficients are also the function of the local surface slopes. In order to avoid the complexity of the analytical computation of the ensemble average term, the scattering amplitude has been expanded in a series as a function of surface slope, and only the first few terms have been kept to produce the physical optics (PO)

model. When only the first term is kept and all other slope terms are ignored, the zeroth-order approximated PO model is obtained as shown in the last chapter. On the other hand, when one more additional term (first-order slope term) is kept, and the edge effect term [Beckmann and Spizzichino, 1963; Beckmann, 1968] produced by the integration by parts is ignored, the first-order approximated PO model is obtained. For both of these PO models, the integration limits for the tangent plane have been approximated by infinity to obtained closed form of the models. Instead of using the series expansion of the scattering amplitudes, the stationary-phase approximation can be used in the geometric limit, ignoring the local diffraction effect. This approximation with an assumption of large value of $ks\cos\theta$ (where $k = 2\pi/\lambda$, s is rms height) leads to the geometrical optics (GO) model. The mean intensity has been formulated exactly, without any further approximation, using a spectral representation of the delta function and assuming a Gaussian height distribution, and evaluated approximately in case of a very rough surface [Stogryn, 1967; Holzer and Sung, 1978].

The goal of this chapter is to evaluate exactly the backscattered mean intensity without using any further approximation except the tangent plane approximation so that the exact Kirchhoff solution can be used to examine the zeroth- and first-order approximated PO models. In other words, the slope term effect and the edge term effect (Ch. 2) can be examined using the exact Kirchhoff solution. The exact Kirchhoff solution may also be used to examine other theoretical models and numerical solutions. In this chapter, the backscattered mean intensity is formulated exactly for a two-dimensional dielectric random surface and evaluated exactly for one-dimensional dielectric and conducting surfaces. The exact Kirchhoff solution is compared with a method of moments solution for scattering from a one-dimensional conducting surface,

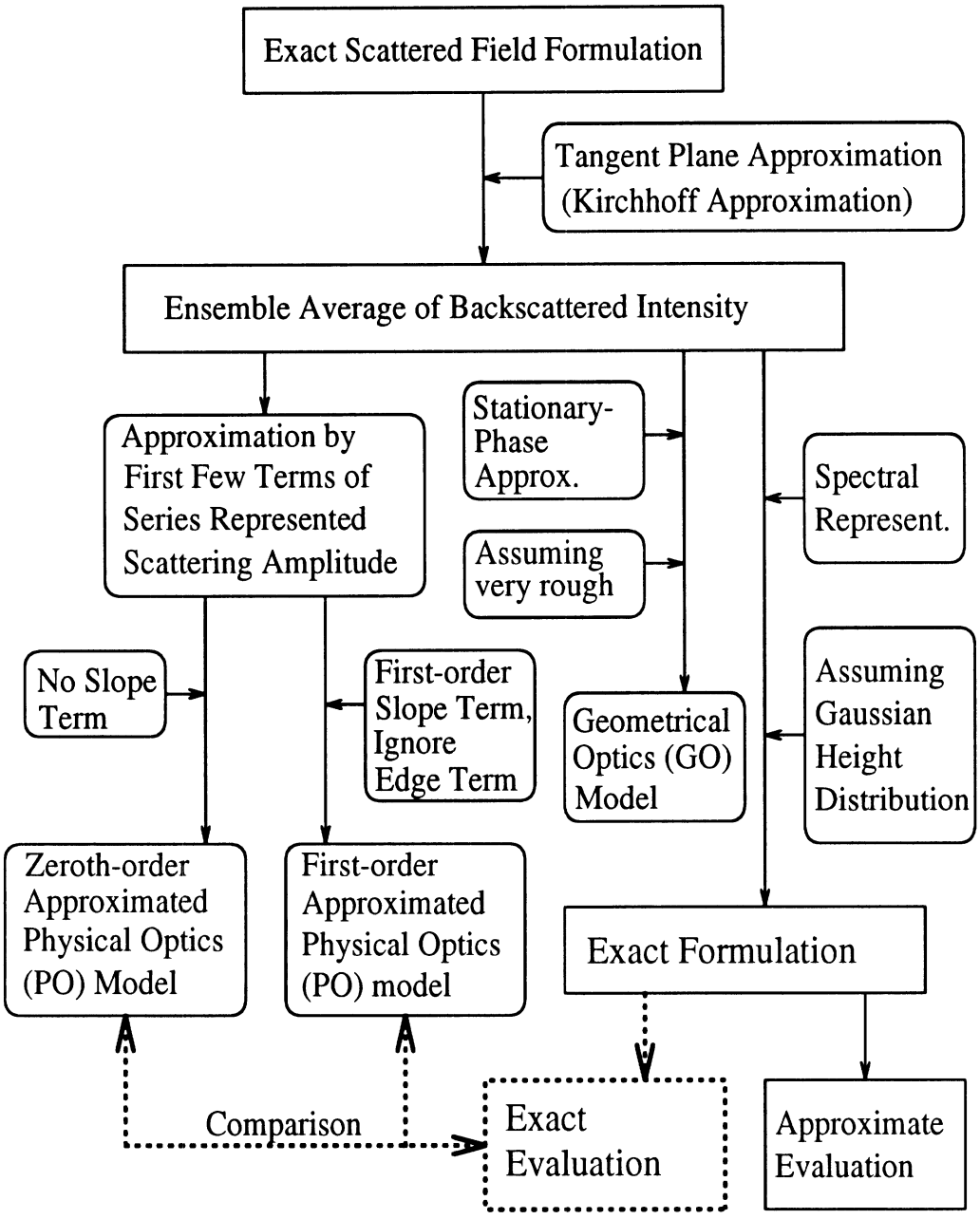

Figure 4.1: Illustration of the development of an exact Kirchhoff solution.

as well as with the zeroth- and first-order approximated PO models. The Kirchhoff approach previously studied is illustrated by solid boxes and lines, and the work to be studied in this chapter is indicated in dotted box and lines in Fig. 4.1.

4.2 Formulation for a Two-dimensional Dielectric Surface

The backscattered mean intensity for the Kirchhoff approximation has been given in (2.61) and will be presented here again for convenience;

$$\langle E^s_{ba} E^{s*}_{ba} \rangle = |D_0|^2 \int\int_{-L}^{L} dx_1 dy_1 \int\int_{-L}^{L} dx_2 dy_2 \; e^{ik_{dx}(x_1 - x_2)} \cdot \left\langle f_{ba}(Z_{x_1}, Z_{y_1}) \, f^*_{ba}(Z_{x_2}, Z_{y_2}) \, e^{ik_{dz} z_d} \right\rangle, \tag{4.1}$$

with $f_{ba}(Z_x, Z_y)$ given in (2.56-2.58) where

$$Z_{x_1} = \frac{\partial z(x_1, y_1)}{\partial x}, \quad Z_{x_2} = \frac{\partial z(x_2, y_2)}{\partial x}, \quad Z_{y_1} = \frac{\partial z(x_1, y_1)}{\partial y}, \quad Z_{y_2} = \frac{\partial z(x_2, y_2)}{\partial y},$$

$z_d = z_1 - z_2$, $z_1 = z(x_1, y_1)$, $z_2 = z(x_2, y_2)$, $k_{dx} = 2k_0 \sin\theta$, $k_{dz} = -2k_0 \cos\theta$, and $|D_0|^2 = k_0^2/(4\pi r)^2$. Since the integral of the ensemble average term in (4.1) is very difficult to evaluate, additional approximations were used to get the PO and GO models as summarized in Ch. 2. The ensemble average term of the integrand in (4.1), however, can be evaluated exactly by using the spectral representation of the delta function and the sifting property of the delta function integration. Since the delta function can be represented by

$$\delta(x, y) = \frac{1}{(2\pi)^2} \int\int_{-\infty}^{\infty} e^{i\alpha x} \, e^{i\beta y} \, d\alpha d\beta, \tag{4.2}$$

the scattering amplitude can be written in terms of the dummy variables α and β as

$$\begin{aligned} f_{ba}(Z_x, Z_y) &= \int\int_{-\infty}^{\infty} f_{ba}(\beta_x, \beta_y) \delta\left(\beta_x - Z_x, \beta_y - Z_y\right) d\beta_x d\beta_y \\ &= \frac{1}{(2\pi)^2} \int\int_{-\infty}^{\infty} f_{ba}(\beta_x, \beta_y) \left\{ \int\int_{-\infty}^{\infty} e^{i\alpha_x(\beta_x - Z_x) + i\alpha_y(\beta_y - Z_y)} d\alpha_x d\alpha_y \right\} d\beta_x d\beta_y. \end{aligned} \tag{4.3}$$

In the above equation, $f_{ba}(Z_x, Z_y)$ is replaced by $f_{ba}(\beta_x, \beta_y)$ which is not a function of random variables anymore. Applying above relations to (4.1), the ensemble average term can be represented by

$$\begin{aligned}\left\langle f_{ba}(Z_{x_1}, Z_{y_1}) f^*_{ba}(Z_{x_2}, Z_{y_2}) e^{i2k_{iz}z_d} \right\rangle \\ = \frac{1}{(2\pi)^4} \int\int_{-\infty}^{\infty} d\beta_{x_1} d\beta_{x_2} \int\int_{-\infty}^{\infty} d\beta_{y_1} d\beta_{y_2} f_{ba}(\beta_{x_1}, \beta_{y_1}) f^*_{ba}(\beta_{x_2}, \beta_{y_2}) \\ \cdot \int\int_{-\infty}^{\infty} d\alpha_{x_1} d\alpha_{x_2} \int\int_{-\infty}^{\infty} d\alpha_{y_1} d\alpha_{y_2} e^{i\alpha_{x_1}\beta_{x_1} + i\alpha_{y_1}\beta_{y_1}} \cdot e^{-i\alpha_{x_2}\beta_{x_2} - i\alpha_{y_2}\beta_{y_2}} \\ \cdot \left\langle e^{-i\alpha_{x_1} Z_{x_1} - i\alpha_{y_1} Z_{y_1}} \cdot e^{i\alpha_{x_2} Z_{x_2} + i\alpha_{y_2} Z_{y_2}} \cdot e^{ik_{dz} z_d} \right\rangle . \end{aligned} \tag{4.4}$$

When we assume the random surface of this problem has a Gaussian height distribution, the ensemble average term, $\langle \cdots \rangle$, is a characteristic function for a random vector, $\overline{x} = [Z_{x_1}, Z_{x_2}, Z_{y_1}, Z_{y_2}, z_d]^T$, and a parameter vector, $\overline{\omega} = [-\alpha_{x_1}, \alpha_{x_2}, -\alpha_{y_1}, \alpha_{y_2}, k_{dz}]^T$. In fact, the most natural rough surfaces have Gaussian height distribution. A typical example of surface height distributions which were measured from bare soil surfaces is shown in Fig. 4.2. Figure 4.2 includes a large number of points (> 8000) measured by a laser profile meter and shows an excellent agreement between the measured height distribution and the Gaussian probability function for the same standard deviation of $1.12cm$.

The characteristic function of the ensemble average form, $\langle \cdots \rangle$, for the Gaussian random vector can be computed using the parameter vector and the correlation matrix, where the correlation matrix components are functions of a correlation coefficient and its derivatives as shown in Appendix A. By changing integral variables from dx_1 dy_1 to du dv (where $u = x_1 - x_2$, $v = y_1 - y_2$) and integrating over dx_2 dy_2, the following integral identity can be obtained;

$$\int\int_{-L}^{L} dx_1 dx_2 \int\int_{-L}^{L} dy_1 dy_2 \Longrightarrow \int\int_{-2L}^{2L} (2L - |u|)\ (2L - |v|)\, du dv, \tag{4.5}$$

Using the characteristic function and the integral identity, the backscattered mean

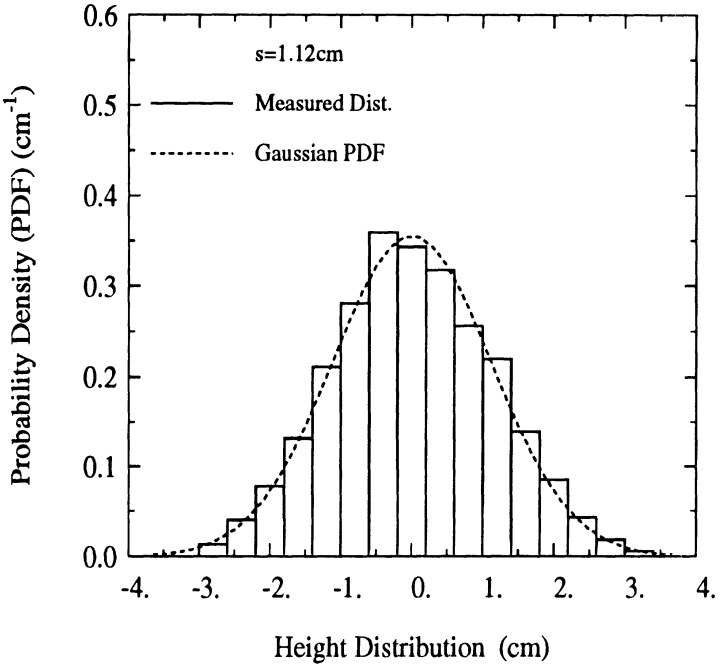

Figure 4.2: A typical example of surface height distributions measured from natural rough surfaces.

intensity, $\langle |E^s_{ba}|^2 \rangle$, in (4.1) can be written in a ten-fold integral equation of which the integrand is an algebraic equation without ensemble averaging terms given as

$$< |E^s_{ba}|^2 >= \frac{|D_o|^2}{(2\pi)^4} \int\int_{-2L}^{2L} dudv(2L-|u|)(2L-|v|)e^{ik_{dx}u} \cdot \int\int_{-\infty}^{\infty} d\beta_{x_1} d\beta_{x_2} \int\int_{-\infty}^{\infty} d\beta_{y_1} d\beta_{y_2} f_{ba}(\beta_{x_1},\beta_{y_1}) f^*_{ba}(\beta_{x_2},\beta_{y_2}) \cdot \mathbf{S} \tag{4.6}$$

with

$$\mathbf{S} = \int\int_{-\infty}^{\infty} d\alpha_{x_1} d\alpha_{x_2} \int\int_{-\infty}^{\infty} d\alpha_{y_1} d\alpha_{y_2} e^{i\alpha_{x_1}\beta_{x_1}+i\alpha_{y_1}\beta_{y_1}} \cdot e^{i\alpha_{x_1}\beta_{x_1}+i\alpha_{y_1}\beta_{y_1}} \cdot \exp\left[\frac{\sigma^2}{2}\rho_{uu}(0,0)\left\{\alpha^2_{x_1}+\alpha^2_{x_2}+\alpha^2_{y_1}+\alpha^2_{y_2}\right\} - \sigma^2 k^2_{dz}\left\{1-\rho(u,v)\right\}\right] \cdot \exp\left[-\sigma^2\left\{\alpha_{x_1}\alpha_{x_2}\rho_{uu}(u,v)+\alpha_{y_1}\alpha_{y_2}\rho_{uv}(u,v)+(\alpha_{x_1}\alpha_{y_2}+\alpha_{x_2}\alpha_{y_1})\rho_{vv}(u,v)\right\}\right] \cdot \exp\left[-\sigma^2 k_{dz}\left\{(\alpha_{x_1}-\alpha_{x_2})\rho_u(u,v)+(\alpha_{y_1}-\alpha_{y_2})\rho_v(u,v)\right\}\right]. \tag{4.7}$$

The terms involving the cross correlation function $\rho_{uv}(u,v)$ have been ignored in [Holzer and Sung, 1978]; however, $\rho_{uv}(u,v)$ is not small enough to be ignored as

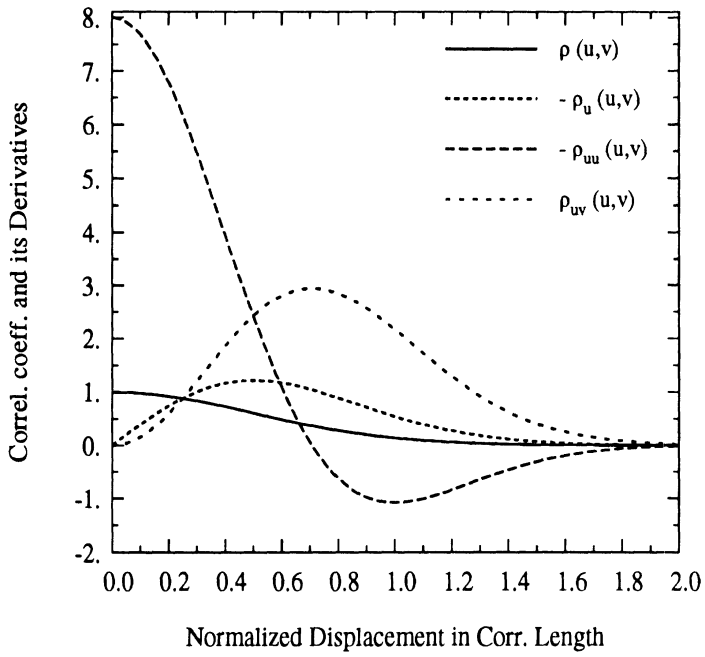

Figure 4.3: Comparison between a Gaussian correlation coefficient and its derivatives in case of $l = 0.5m$.

illustrated in Fig. 4.3. In Fig. 4.3, a Gaussian correlation coefficient function is considered as an example with the correlation length of $l = 0.5m$ and the magnitudes of $\rho(u,v)$ and its derivatives, $\rho_u(u,v)$, $\rho_{uu}(u,v)$, and $\rho_{uv}(u,v)$, are compared among one another.

In order to integrate the last term **S** analytically, it will be better to rearrange it as follows;

$$\mathbf{S} = \exp\left[-\sigma^2 k_{dz}^2 \{1 - \rho(u,v)\}\right] \cdot \mathbf{I}_{\alpha_{x_1}}, \tag{4.8}$$

with

$$\mathbf{I}_{\alpha_{x_1}} = \int_{-\infty}^{\infty} d\alpha_{x_1} e^{i\beta_{x_1}\alpha_{x_1}} \cdot e^{\frac{\sigma^2}{2}\rho_{uu}(0,0)\alpha_{x_1}^2} \cdot e^{-\sigma^2 k_{dz}\rho_u(u,v)\alpha_{x_1}} \cdot \mathbf{I}_{\alpha_{x_2}}, \tag{4.9}$$

where

$$\mathbf{I}_{\alpha_{x_2}} = \int_{-\infty}^{\infty} d\alpha_{x_2} e^{-i\beta_{x_2}\alpha_{x_2}} \cdot e^{\frac{\sigma^2}{2}\rho_{uu}(0,0)\alpha_{x_2}^2} \cdot e^{-\sigma^2\rho_{uu}(u,v)\alpha_{x_1}\alpha_{x_2}} \cdot e^{\sigma^2 k_{dz}\rho_u(u,v)\alpha_{x_2}} \cdot \mathbf{I}_{\alpha_{y_1}}, \tag{4.10}$$

where

$$\mathbf{I}_{\alpha_{y_1}} = \int_{-\infty}^{\infty} d\alpha_{y_1} e^{i\beta_{y_1}\alpha_{y_1}} \cdot e^{\frac{\sigma^2}{2}\rho_{uu}(0,0)\alpha_{y_1}^2} \cdot e^{-\sigma^2\rho_{uv}(u,v)\alpha_{x_2}\alpha_{y_1}} \cdot e^{-\sigma^2 k_{dz}\rho_u(u,v)\alpha_{y_1}} \cdot \mathbf{I}_{\alpha_{y_2}}, \tag{4.11}$$

and where

$$\mathbf{I}_{\alpha_{y_2}} = \int_{-\infty}^{\infty} d\alpha_{y_2} e^{-i\beta_{y_2}\alpha_{y_2}} \cdot e^{\frac{\sigma^2}{2}\rho_{uu}(0,0)\alpha_{y_2}^2} \cdot e^{-\sigma^2\left[\rho_{uu}(u,v)\alpha_{y_1}+\rho_{uv}(u,v)\alpha_{x_1}\right]\alpha_{y_2}} \cdot e^{\sigma^2 k_{dz}\rho_u(u,v)\alpha_{y_2}}. \tag{4.12}$$

Since all of the above integrals in (4.9)-(4.12) have the same form of

$$A\int_{-\infty}^{\infty} e^{iBx}e^{-Cx^2-Dx}dx = A\sqrt{\frac{\pi}{C}}e^{\frac{D^2-B^2}{4C}} \cdot e^{-i\frac{BD}{2C}},$$

the integrals $\mathbf{I}_{\alpha_{x_1}}$, $\mathbf{I}_{\alpha_{x_2}}$, $\mathbf{I}_{\alpha_{y_1}}$, and $\mathbf{I}_{\alpha_{y_2}}$ can be computed consequently by backward substitutions. After a quite complicated algebraic computation, the final form of $\mathbf{S}$ in (4.8) can be obtained as

$$\begin{aligned}\mathbf{S} = {} & \frac{(2\pi)^2}{s^4\rho_0^2\sqrt{1-\rho_B^2}\sqrt{1-\rho_E^2}} e^{-s^2(k_{dz})^2(1-\rho)} \cdot e^{[s^2(2k_{iz})^2\rho_v^2]/[\rho_0(1+\rho_B)]} \\ & \cdot e^{[s^2(k_{dz})^2(\rho_u^2-\frac{\rho_D\rho_v}{1+\rho_B})^2]/[\rho_0(1+\rho_B)]} \cdot e^{-[\beta_{y_1}^2+\beta_{y_2}^2-2\rho_B\beta_{y_1}\beta_{y_2}]/[2\rho_0 s^2(1-\rho_B^2)]} \\ & \cdot e^{-\left[\beta_{x_2}-\frac{\rho_D}{1-\rho_B^2}(\beta_{y_1}-\rho_B\beta_{y_2})\right]^2/[2\rho_0 s^2]} \cdot e^{-i[2k_{iz}\rho_v(\beta_{y_1}+\beta_{y_2})]/[\rho_0(1+\rho_B)]} \\ & \cdot e^{-\left[\beta_{x_1}-\rho_E\beta_{x_2}\rho_D\beta_{y_2}+\frac{\rho_D}{1-\rho_B^2}(\beta_{y_1}-\rho_B\beta_{y_2})(\rho_B+\rho_E)\right]^2/[2\rho_0 s^2(1-\rho_E^2)]} \\ & \cdot e^{-i2k_{iz}(\rho_u-\frac{\rho_D\rho_v}{1+\rho_B})\left[\beta_{x_1}+\beta_{x_2}-\rho_D\beta_{y_2}+\frac{\rho_D}{1-\rho_B^2}(\beta_{y_1}-\rho_B\beta_{y_2})(1-\rho_B)\right]/[\rho_0(1+\rho_E)]},\end{aligned} \tag{4.13}$$

where more simplified notations have been defined as $\rho_u \triangleq \partial\rho(u,v)/\partial u$, $\rho_{uu} \triangleq \frac{\partial^2\rho(u,v)}{\partial u^2}$, $\rho_0 \triangleq -\rho_{uu}(0,0)$ $\rho_B \triangleq \rho_{uu}(u,v)/\rho_{uu}(0,0)$, $\rho_D \triangleq \rho_{uv}(u,v)/\rho_{uu}(0,0)$, $\rho_E \triangleq \rho_{vv}(u,v)/\rho_{uu}(0,0)$, and $s \triangleq \sigma$. Above formulation is good for any type of correlation function which has derivatives throughout the coordinate system.

Once we found the mean intensity $< |E_{ba}^s|^2 >$ in (4.6) with $\mathbf{S}$ given in (4.13), the backscattering coefficient σ_{ba}° can be computed using (2.79) for a two-dimensional

dielectric random surface. The exact formulation of the Kirchhoff approximated mean intensity in (4.6), however, is in the form of six-fold integrals and should be solved numerically. Since the six-fold numerical integration is a challenging problem with the present computer powers, we can reduce the computation either by approximating the integrand in (4.6) and (4.13) or by simplifying the problem itself. Since the goal of this chapter is to get an exact solution of the backscattering coefficient for examination of the zeroth- and first-order PO models (or the effects of the slope term and the edge term), a simple problem of a one-dimensional random surface will be considered in the next section.

4.3 Evaluation for a One-dimensional Dielectric Surface

An exact formulation for the Kirchhoff approximated backscattering coefficient for a one-dimensional dielectric random surface will be derived and also solved numerically in this section. For a one-dimensional random surface (no surface height variation in y direction, *i.e.* $Z_y = 0$), the scattered field can be obtained similarly as the problem of a two-dimensional surface given in (2.40) except that the Green's function for a two-dimension scattering problem (corresponding to a one-dimensional random surface) is given by

$$G_0(\overline{r}, \overline{r}') = \frac{i}{4} H_0^{(1)}(kr), \tag{4.14}$$

where the position vector $\overline{r}$ is employed instead of $\overline{\rho}$ for a one-dimensional surface (two-dimensional scattering problem) in order to avoid confusion between the position vector and the correlation coefficient function $\rho(u)$. The first-kind Hankel function of order zero, $H_0^{(1)}$, can be approximated in the far field ($r > 2D^2/\lambda_0$) as

$$H_0^{(1)}(kr) \approx \sqrt{\frac{2}{\pi k r_0}} e^{i(kr_0 - \pi/4)} \, e^{-ik_0 \hat{k}_s \cdot \overline{r}'}. \tag{4.15}$$

Therefore, the corresponding backscattered mean intensity can be computed as

$$\left\langle |E_{ba}^{s}|^2 \right\rangle = |D_0|^2 \int_{-2L}^{2L} (2L - |u|)\, e^{ik_{dx}u} \left\langle f_{ba}(Z_{x_1})\, f_{ba}^{*}(Z_{x_2})\, e^{ik_{dz}z_d} \right\rangle du, \tag{4.16}$$

where $|D_0|^2 = k_0/(8\pi r_0)$. The scattering amplitude $f_{ba}(Z_x)$ can be obtained by substituting $Z_y = 0$ into (2.56)-(2.58) as

$$\begin{aligned} f_{hh} &= 2R_{lh}\,(Z_x, \theta)(\cos\theta + \sin\theta Z_x) \\ f_{vv} &= 2R_{lv}\,(Z_x, \theta)(\cos\theta + \sin\theta Z_x) \\ f_{vh} &= f_{hv} = 0 \end{aligned} \tag{4.17}$$

with

$$\begin{aligned} R_{lh} &= \frac{Z_x \sin\theta + \cos\theta - \sqrt{\epsilon_r(1 + Z_x^2) - (Z_x\cos\theta - \sin\theta)^2}}{Z_x \sin\theta + \cos\theta + \sqrt{\epsilon_r(1 + Z_x^2) - (Z_x\cos\theta - \sin\theta)^2}} \\ R_{lv} &= \frac{\epsilon_r(Z_x \sin\theta + \cos\theta) - \sqrt{\epsilon_r(1 + Z_x^2) - (Z_x\cos\theta - \sin\theta)^2}}{\epsilon_r(Z_x \sin\theta + \cos\theta) + \sqrt{\epsilon_r(1 + Z_x^2) - (Z_x\cos\theta - \sin\theta)^2}}. \end{aligned} \tag{4.18}$$

No cross-polarized backscattering coefficient can be obtained for a one-dimensional surface as indicated in (4.17). When the spectral representation of the delta function is used, the scattering amplitude and its conjugate can be pulled out of the ensemble average term as

$$\begin{aligned} \left\langle f_{aa}(Z_{x_1}) f_{aa}^{*}(Z_{x_2}) e^{i2k_{iz}z_d} \right\rangle &= \frac{1}{(2\pi)^2} \int\int_{-\infty}^{\infty} d\beta_1 d\beta_2\; f_{aa}(\beta_1) f_{aa}^{*}(\beta_2) \\ &\cdot \int\int_{-\infty}^{\infty} d\alpha_1 d\alpha_2\; e^{i\alpha_1\beta_1 - i\alpha_2\beta_2} \left\langle e^{-i\alpha_1 Z_{x_1}} \cdot e^{i\alpha_2 Z_{x_2}} \cdot e^{ik_{dz}z_d} \right\rangle. \end{aligned} \tag{4.19}$$

The term $\langle \cdots \rangle$ at the right hand side of (4.19) is the characteristic function of the Gaussian random vector $\overline{x} = [Z_{x_1}, Z_{x_2}, z_d]^T$ and the parameter vector $\overline{\omega} = [-\alpha_1, \alpha_2, k_{dz}]^T$. The characteristic function for a one-dimensional surface is a quite simple form compared with that for a two-dimensional surface and is represented as a function of the parameter vector components, the correlation coefficient and its derivatives

as shown in Appendix A. The backscattering mean intensity for a one-dimensional dielectric random surface is

$$< |E^s_{aa}|^2 >= \frac{|D_o|^2}{(2\pi)^2} \int_{-2L}^{2L} du(2L - |u|) e^{ik_{dx}u} \cdot \int\int_{-\infty}^{\infty} d\beta_1 d\beta_2 \; f_{aa}(\beta_1) f^*_{aa}(\beta_2) \cdot \mathbf{S} \quad (4.20)$$

with

$$\mathbf{S} = \exp\left[-\sigma^2 k_{dz}^2 \{1 - \rho(u)\}\right] \cdot \mathbf{I}_{\alpha_1}, \quad (4.21)$$

where

$$\mathbf{I}_{\alpha_1} = \int_{-\infty}^{\infty} d\alpha_1 \; \exp[i\beta_1\alpha_1] \cdot \exp\left[-\frac{\sigma^2}{2}\rho_{uu}(0)\alpha_1^2\right] \cdot \exp\left[-\sigma^2 k_{dz}\rho_u(u)\alpha_1\right] \cdot \mathbf{I}_{\alpha_2}, \quad (4.22)$$

and

$$\mathbf{I}_{\alpha_2} = \int_{-\infty}^{\infty} d\alpha_2 \; \exp[-i\beta_2\alpha_2] \cdot \exp\left[-\frac{\sigma^2}{2}\rho_{uu}(0)\alpha_2^2\right] \cdot \exp\left[-\sigma^2\rho_{uu}(u)\alpha_1\alpha_2\right] \cdot \exp\left[\sigma^2 k_{dz}\rho_u(u)\alpha_1\right]. \quad (4.23)$$

After integrating $\mathbf{I}_{\alpha_1}$ and $\mathbf{I}_{\alpha_2}$ analytically, the backscattered mean intensity is obtained as,

$$\left\langle |E^s_{aa}|^2 \right\rangle = \frac{|D_o|^2}{2\pi s^2 \rho_0} \int_{-2L}^{2L} du \; (2L - |u|) \cdot \exp[ik_{dx}u] \cdot \exp\left[-s^2 k_{dz}^2 \{1 - \rho(u)\}\right] \cdot \exp\left[\frac{\sigma^2 k_{dz}^2 \rho_u^2}{\rho_0(1 + \rho_B)}\right] \cdot \frac{1}{\sqrt{1 - \rho_B^2}} \int_{-\infty}^{\infty} d\beta_1 \; f_{aa}(\beta_1) \int_{-\infty}^{\infty} d\beta_2 \; f^*_{aa}(\beta_2) \cdot \exp\left[-\frac{\beta_1^2 + \beta_2^2 - 2\rho_B\beta_1\beta_2}{2\rho_0 s^2(1 - \rho_B^2)}\right] \cdot \exp\left[-i\frac{k_{dz}\rho_u(\beta_1 + \beta_2)}{\rho_0(1 + \rho_B)}\right] \quad (4.24)$$

where $\rho_u \triangleq \partial\rho(u)/\partial u$, $\rho_0 \triangleq -\rho_{uu}(0)$, $\rho_B \triangleq \rho_{uu}(u)/\rho_{uu}(0)$, and $s \triangleq \sigma$.

The effect of shadowing can be properly accounted for the mean intensity in (4.24) just by restricting the limits of integration with respect to $d\beta_1$ and $d\beta_2$ corresponding to the surface slopes. In the backscattering case, maximum slope can be infinity $\beta_{max} = \infty$; however, the minimum slope should be restricted by the incidence angle

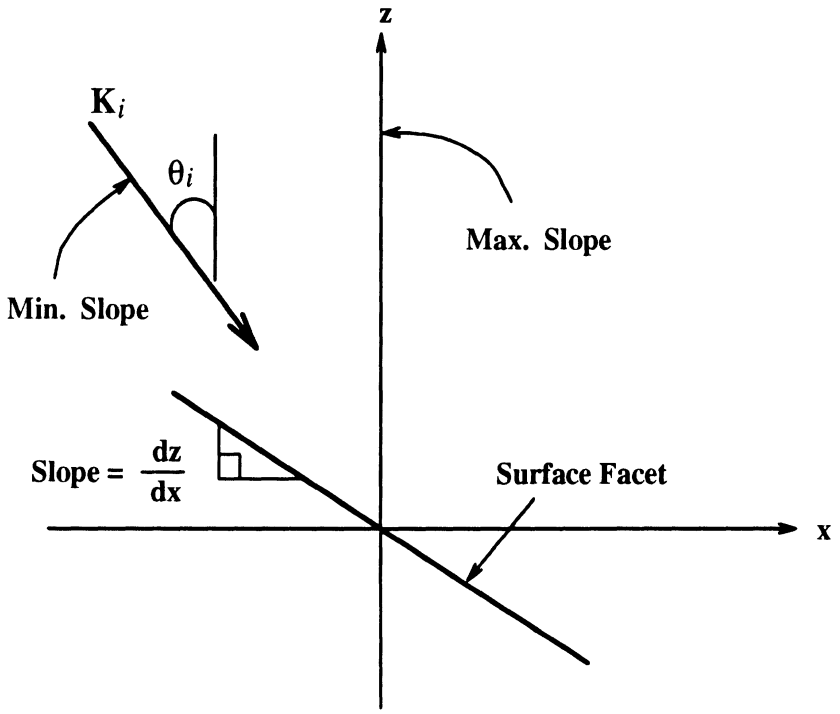

Figure 4.4: Illustration of the shadowing correction in backscattering direction.

θ_i as $\beta_{min} = -\cot\theta_i$ to get proper orientations of surface facets as illustrated in Fig. 4.4. Therefore, the integration in (4.24) with respect to $d\beta_1$ and $d\beta_2$ should be restricted for the shadowing correction as

$$\int_{-\infty}^{\infty}\int_{-\infty}^{\infty} F(\beta_1,\beta_2)d\beta_1 d\beta_1 \implies \int_{-\cot\theta_i}^{\infty}\int_{-\cot\theta_i}^{\infty} F(\beta_1,\beta_2)d\beta_1 d\beta_1 \,.$$

Since the incoherent backscattering coefficient for a one-dimensional random surface is defined by

$$\sigma^{\circ}_{ba} = \lim_{\rho\to\infty}\frac{2\pi\rho}{2L}\cdot\frac{\left\langle|E^s_{ba}|^2\right\rangle - |\langle E^s_{ba}\rangle|^2}{|E^i_a|^2}\,, \tag{4.25}$$

where $|\langle E^s_{ba}\rangle|^2$ is the coherent intensity and $|E^i_a|^2$ is the incident intensity given as 1. The coherent scattered field $\langle E^s_{ba}\rangle$ can be obtained from (2.54) as

$$\langle E^s_{aa}\rangle = D_o\int_{-L}^{L} dx\ \exp[ik_{dx}x]\cdot\langle f_{aa}(Z_x)\ \exp[ik_{dz}z]\rangle\,. \tag{4.26}$$

Using the spectral representation of the delta function, the ensemble average term at the right-hand side of (4.25) becomes

$$\langle f_{aa}(Z_x)\ \exp[ik_{dz}z]\rangle = \frac{1}{2\pi}\int_{-\infty}^{\infty} d\beta \int_{-\infty}^{\infty} d\alpha\ \exp[i\alpha\beta] \cdot \langle \exp[-i\alpha Z_x]\ \exp[ik_{dz}z]\rangle . \tag{4.27}$$

For a Gaussian height distribution, the term $\langle \exp[-i\alpha Z_x]\ \exp[ik_{dz}z]\rangle$ is the characteristic function for the random vector $\overline{x} = [Z_x, z]^T$ and the parameter vector $\overline{\omega} = [-\alpha, k_{dz}]^T$. Since the components of the correlation matrix are computed as

$$\left\langle Z_x^2 \right\rangle = -\sigma^2\rho_{uu}(0), \quad \langle Z_x\ z\rangle = 0, \quad \text{and} \quad \left\langle z^2 \right\rangle = \sigma^2), \tag{4.28}$$

the characteristic function can be computed as follow;

$$\begin{aligned}\langle \exp[-i\alpha Z_x] \exp[ik_{dz}z]\rangle &= \exp\left[-\frac{\sigma^2}{2}(-\alpha, k_{dz}) \begin{pmatrix} -\rho_{uu}(0) & 0 \\ 0 & 1 \end{pmatrix} \begin{pmatrix} -\alpha \\ k_{dz} \end{pmatrix}\right] \\ &= \exp\left[-\frac{\sigma^2}{2}\left(-\alpha^2\rho_{uu}(0) + k_{dz}^2\right)\right]. \end{aligned} \tag{4.29}$$

Integrating with respect to $d\alpha$, the coherent intensity can be rearranged as

$$\begin{aligned}\langle E_{aa}^s\rangle = \frac{D_o}{\sqrt{2\pi\rho_0 s}} \exp\left[-\frac{s^2}{2}k_{dz}^2\right] \int_{-L}^{L} dx\ \exp[ik_{dx}x] \\ \cdot \int_{-\cot\theta}^{\infty} d\beta\ f_{aa}(\beta) \exp\left[\frac{-\beta^2}{2s^2\rho_{uu}(0)}\right]. \end{aligned} \tag{4.30}$$

The backscattering coefficient of the Kirchhoff method has been evaluated exactly for the one-dimensional dielectric random surface having a Gaussian height distribution and an arbitrary correlation coefficient function. The backscattering coefficient can be evaluated by integrating three-fold integral given in (4.24), and the numerical results will be given in Sec. (3.5).

4.4 Evaluation for a One-dimensional Conducting Surface

In the last chapter a numerical solution for scattering from a one-dimensional conducting random surface has been developed. In order to compare the exact PO solution described in this chapter with the numerical solution, we would need the evaluation of the exact PO solution for a one-dimensional conducting surface. For a conducting surface, the mean intensity can be further simplified from (4.24) since the local reflection coefficients are constant ($R_h = -1$, $R_v = 1$). The scattering amplitudes can be simplified from (4.17) for a one-dimensional conducting surface, and the backscattered mean intensity can be rewritten as

$$\left\langle |E^s_{aa}|^2 \right\rangle = \frac{|D_o|^2}{2\pi s^2 \rho_0} \int_{-2L}^{2L} du\ (2L - |u|) \cdot \exp\left[ik_{dx}u\right] \cdot \exp\left[-s^2 k_{dz}^2 \left\{1 - \rho(u)\right\}\right] \cdot \exp\left[\frac{\sigma^2 k_{dz}^2 \rho_u^2}{\rho_0(1+\rho_B)}\right] \cdot \mathbf{I}_{\beta_1} \tag{4.31}$$

with

$$\mathbf{I}_{\beta_1} = \frac{1}{\sqrt{1-\rho_B^2}} \int_{-\infty}^{\infty} d\beta_1\ f_{aa}(\beta_1) \cdot \mathbf{I}_{\beta_2} \quad \text{and} \tag{4.32}$$

$$\mathbf{I}_{\beta_2} = \int_{-\infty}^{\infty} d\beta_2\ f^*_{aa}(\beta_2)\ \cdot \exp\left[-\frac{\beta_1^2 + \beta_2^2 - 2\rho_B\beta_1\beta_2}{2\rho_0 s^2(1-\rho_B^2)}\right] \cdot \exp\left[-i\frac{k_{dz}\rho_u(\beta_1+\beta_2)}{\rho_0(1+\rho_B)}\right], \tag{4.33}$$

where

$$\begin{aligned} f_{hh}(\beta_i) &= -2(\cos\theta + \sin\theta\beta_i) \\ f_{vv}(\beta_i) &= 2(\cos\theta + \sin\theta\beta_i) \\ f_{vh}(\beta_i) &= f_{hv}(\beta_i) = 0. \end{aligned} \tag{4.34}$$

The integrals, $\mathbf{I}_{\beta_2}$ and $\mathbf{I}_{\beta_1}$, can be integrated analytically, and the results are, respectively,

$$\mathbf{I}_{\beta_2}{}^{vv}_{hh} = \pm 2\sqrt{2\pi\rho_0}\sqrt{1-\rho_B^2}\, s \exp\left[-\frac{\rho_B^2\beta_1^2}{2\rho_0 s^2(1-\rho_B^2)}\right] \cdot \exp\left[-\frac{s^2(1-\rho_B)(k_{dz}\rho_u)^2}{2\rho_0(1+\rho_B)}\right] \cdot \exp\left[-i\frac{k_{dz}\rho_u\rho_B\beta_1}{\rho_0(1+\rho_B)}\right] \cdot \left[\sin\theta\left\{\rho_B\beta_1 - is^2(1-\rho_B)k_{dz}\rho_u\right\} + \cos\theta\right], \tag{4.35}$$

and

$$\mathbf{I}_{\beta_1}{}_{hh}^{vv} = (\pm 2)^2 2\pi\rho_0 s^2 \exp\left[-\frac{s^2(1-\rho_B)(k_{dz}\rho_u)^2}{2\rho_0(1+\rho_B)}\right] \cdot \exp\left[-\frac{s^2(k_{dz}\rho_u)^2}{2\rho_0}\right]$$
$$\cdot \left[s^2\rho_0 \sin^2\theta\rho_B \left\{1 - \frac{(\rho_u k_{dz} s)^2}{\rho_0}\right\} + \cos^2\theta - i\sin\theta\cos\theta s^2(1-\rho_B)k_{dz}\rho_u\right.$$
$$\left. -s^2 k_{dz}\rho_u \left\{i\sin\theta\cos\theta(1+\rho_B) + s^2 k_{dz}\rho_u \sin^2\theta(1-\rho_B)\right\}\right]. \qquad (4.36)$$

Substituting (4.36) into (4.31), the exact evaluation of the Kirchhoff mean intensity for a one-dimensional conducting surface can be obtained as

$$\left\langle |E_{vv}^s|^2 \right\rangle = \left\langle |E_{hh}^s|^2 \right\rangle = 4\frac{|D_o|^2}{2\pi s^2\rho_0} \int_{-2L}^{2L} du\ (2L - |u|) \cdot \exp\left[ik_{dx}u\right]$$
$$\cdot \exp\left[-s^2 k_{dz}^2 \left\{1 - \rho(u)\right\}\right] \cdot \left\{\left(\cos\theta - i\sin\theta s^2 k_{dz}\rho_u\right)^2 + \sin^2\theta s^2\rho_0\rho_B\right\}, \qquad (4.37)$$

where $|D_0|^2 = k_0/(8\pi r_0)$, $\rho_u = \partial\rho(u)/\partial u$, $\rho_0 = -\rho_{uu}(0)$, $\rho_B = \rho_{uu}(u)/\rho_{uu}(0)$, $s = \sigma$, $k_{dx} = 2k_0\sin\theta$, and $k_{dz} = -2k_0\cos\theta$. The coherent intensity for a conducting surface can be computed from (4.30) using the scattering amplitudes given in (4.34) as

$$|\langle E_{vv}^s \rangle|^2 = |\langle E_{hh}^s \rangle|^2 = 4\,|D_o|^2 \exp\left[-s^2 k_{dz}^2\right] \frac{\sin^2(k_{dz}L)}{(k_{dz}/2)^2}. \qquad (4.38)$$

The backscattering coefficient of a one-dimensional conducting surface using the Kirchhoff approximation can be evaluated exactly using (4.25), (4.37), and (4.38). Since the integrals, $\mathbf{I}_{\beta_2}$ and $\mathbf{I}_{\beta_1}$, are integrated over $-\infty$ to ∞, the shadowing effect should be accounted for by the shadowing function given in (2.90).

4.5 Numerical Results

A numerical technique introduced in the previous chapter for scattering from a one-dimensional conducting random surface will be used to examine the exact PO model evaluated in this chapter. Since the generated random surfaces given in the last chapter have a Gaussian correlation function, the same form of correlation function

will be used for numerical examples as

$$\begin{aligned} \rho(u) &= e^{-u^2/l^2}, \\ \rho_u(u) &= -\frac{u}{l} e^{-u^2/l^2}, \\ \rho_{uu}(u) &= \left[-\frac{2}{l^2} + \frac{4u^2}{l^4} \right] e^{-u^2/l^2}, \\ \rho_0 &= -\rho_{uu}(0) = \frac{2}{l^2}. \end{aligned} \tag{4.39}$$

The exact PO solution is tested against the exact numerical solution (Monte Carlo method with the method of moments technique) for conducting random surfaces at five roughness conditions. Figure 4.5(a) illustrates the five roughnesses, $ks_1 = 0.62$, $kl_1 = 4.6$; $ks_2 = 0.6$, $kl_2 = 6$; $ks_3 = 1$, $kl_3 = 6$; $ks_4 = 1$, $kl_4 = 8$; and $ks_5 = 1$, $kl_5 = 10$ where $k = 2\pi/\lambda$, s is the rms height, and l is the correlation length. Figures 4.5(b)-(f) show good agreements between the exact PO model and the method of moments(MoM) solution. There is no distinction between the hh- and vv-polarizations for the exact PO solution for a one-dimensional conducting surface. The vv-polarized backscattering coefficient of the method of moments solution is higher than the hh-polarized one; however, the difference becomes negligible when the roughness condition satisfies the validity region of the PO solution as shown in Figs. 4.5(e) and 4.5(f). The difference between the two polarizations is large for smooth surfaces and the σ° of the exact PO solution has the values between the hh- and vv-polarized σ° of the MoM solution as shown in Fig. 4.5(b).

Since the exact PO solution shows an excellent agreement with the MoM solution, the exact PO solution can be used to examine the zeroth- and first-order approximated PO models (see Ch. 2). In order to examine the zeroth- and first-order approximated PO models using the exact PO solution derived in the previous sections, the approximated models for a one-dimensional dielectric random surface are

(a)

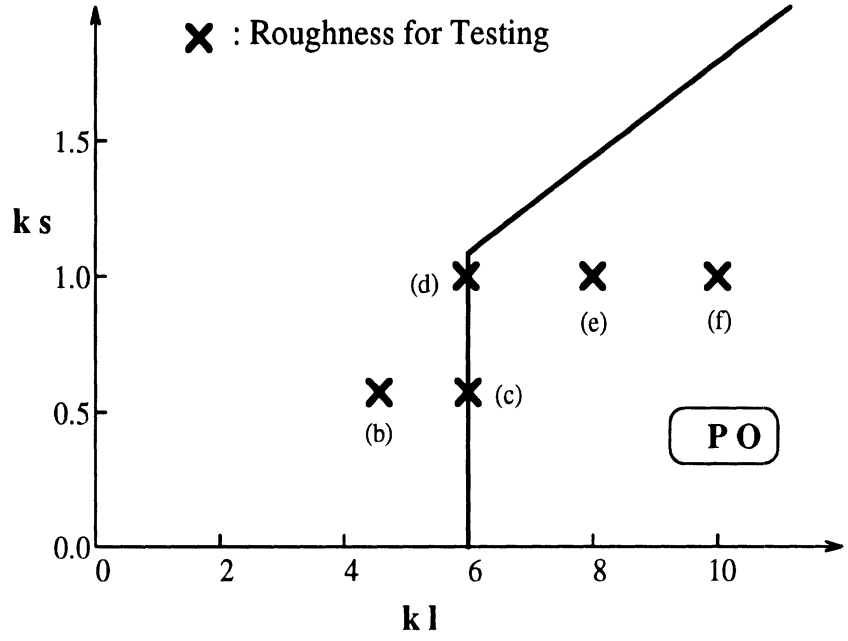
: Roughness for Testing
1.5
k s
1.0
0.5
0.0
0
2
4
6
8
10
k l
(d)
(e)
(f)
(c)
(b)
P O

(b)

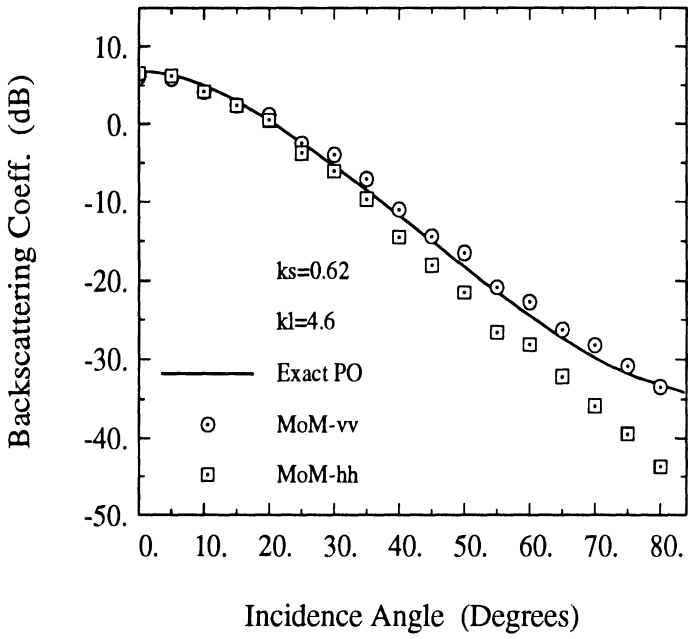
10.
0.
-10.
-20.
-30.
-40.
-50.
Backscattering Coeff. (dB)
ks=0.62
kl=4.6
Exact PO
MoM-vv
MoM-hh
0.
10.
20.
30.
40.
50.
60.
70.
80.
Incidence Angle (Degrees)

(c)

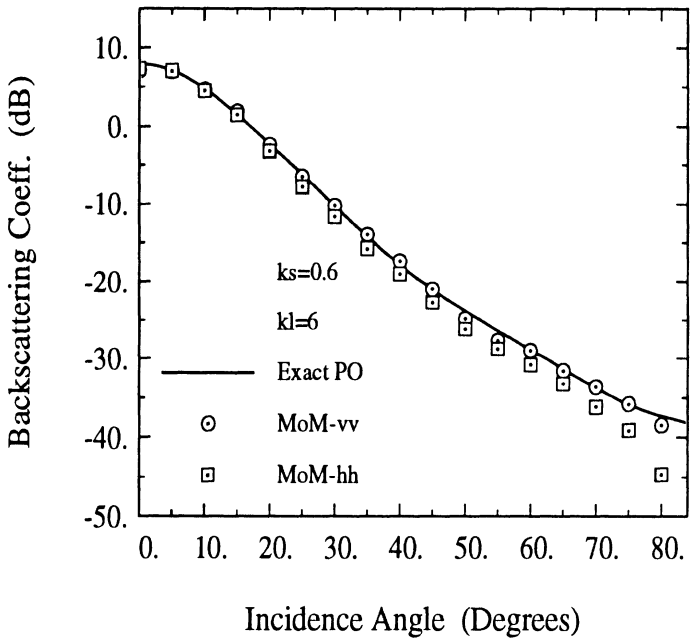
Backscattering Coeff. (dB)
10.
0.
-10.
-20.
-30.
-40.
-50.
ks=0.6
kl=6
Exact PO
MoM-vv
MoM-hh
0. 10. 20. 30. 40. 50. 60. 70. 80.
Incidence Angle (Degrees)

(d)

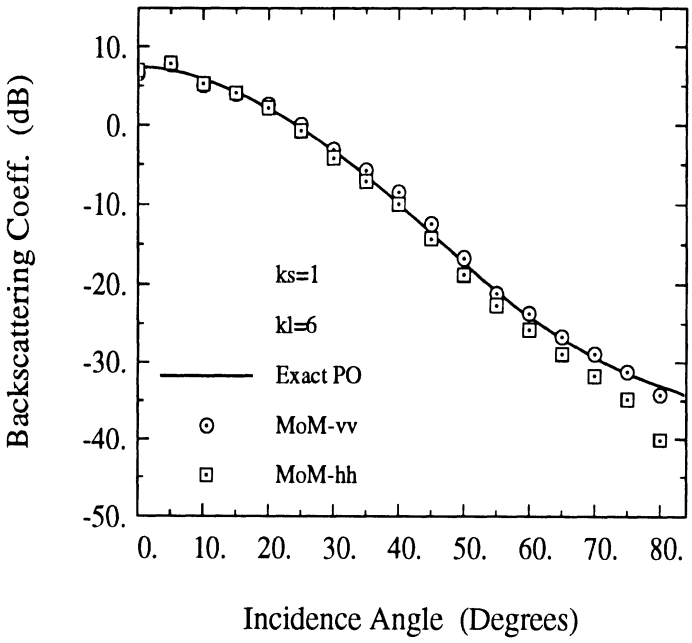
Backscattering Coeff. (dB)
10.
0.
-10.
-20.
-30.
-40.
-50.
ks=1
kl=6
Exact PO
MoM-vv
MoM-hh
0. 10. 20. 30. 40. 50. 60. 70. 80.
Incidence Angle (Degrees)

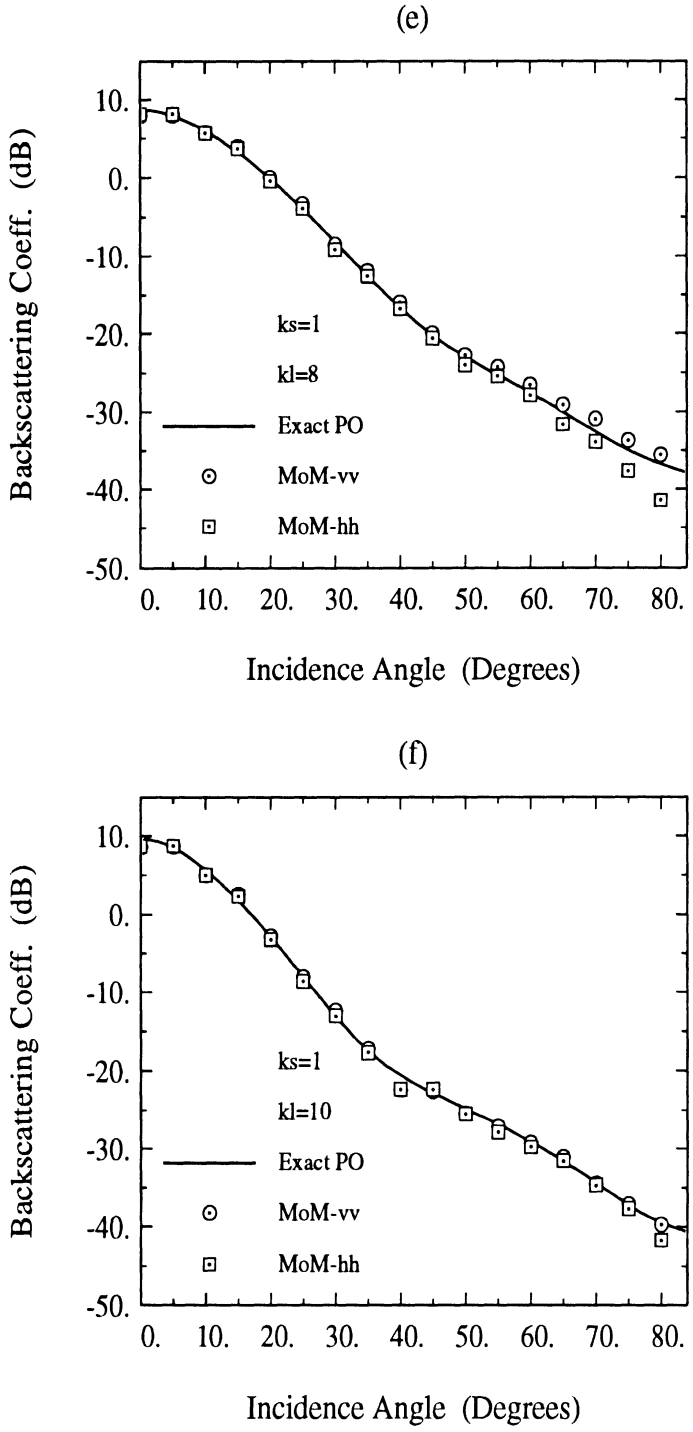

Figure 4.5: Comparison between the exact physical optics model and the method of moments solution; (a) illustration of the roughness conditions and the backscattering coefficients for (b) $ks = 0.62$, $kl = 4.6$, (c) $ks = 0.6$, $kl = 6$, (d) $ks = 1$, $kl = 6$, (e) $ks = 1$, $kl = 8$, and (f) $ks = 1$, $kl = 10$.

summarized as;

$$\left\langle |E^s_{aa}|^2 \right\rangle_{0th} = |D_o|^2 4\cos^2\theta |R_a|^2 \int_{-2L}^{2L} (2L - |u|) e^{ik_{dx}u} \cdot e^{-s^2(k_{dz})^2[1-\rho(u)]} du, \quad (4.40)$$

$$|\langle E^s_{aa} \rangle_{0th}|^2 = |D_o|^2 4\cos^2\theta |R_a|^2 e^{-s^2 k_{dz}^2} \cdot \frac{\sin^2(k_{dx}L)}{(k_{dx}/2)^2}, \quad (4.41)$$

$$\frac{\langle |E^s_{aa}|^2 \rangle_{1st}}{\langle |E^s_{aa}|^2 \rangle_{0th}} = \frac{|\langle E^s_{aa} \rangle_{1st}|^2}{|\langle E^s_{aa} \rangle_{0th}|^2} = \frac{1}{\cos^4\theta}. \quad (4.42)$$

The backscattering coefficients of the zeroth- and first-order approximated PO models for a one-dimensional conducting random surface can be obtained by substituting $|R_a|^2 = 1$ into (4.40)-(4.42). It should be noted that if the edge term is included in the evaluation of the coherent intensity of the first-order PO model, the coherent intensity $|\langle E^s_{aa} \rangle_{1st}|^2$ becomes $|\langle E^s_{aa} \rangle_{0th}|^2$.

Figures 4.6(a) and (b) show the comparison between the exact PO solution and the zeroth-order approximated PO model (no slope term in the series of scattering amplitude) for a conducting and a dielectric surface, respectively. The zeroth-order approximated PO model underestimates the backscattering coefficients. For example, for a relatively smooth surface ($ks = 1$, $kl = 8$) the slope term effect is about $2 \sim 5$ dB at $20° - 70°$ as shown in Figs. 4.6(a) and (b). Figures 4.7(a) and (b) show the comparison between the exact PO solution and the first-order approximated PO model for a conducting and a dielectric surface, respectively. The first-order approximated PO model was obtained by including the first-order slope term in the series of scattering amplitude, integrating by parts, and discarding the edge term (see Ch. 2). The first-order approximated PO model shows a good agreement with the exact PO model at lower incidence angles ($\theta < 40°$), but, overestimates at large incidence angles ($\theta > 40°$). For example, the edge term effect is about 5 dB at 45° and 15 dB at 70° for a relatively smooth surface ($ks = 1$, $kl = 8$) as shown in Figs.

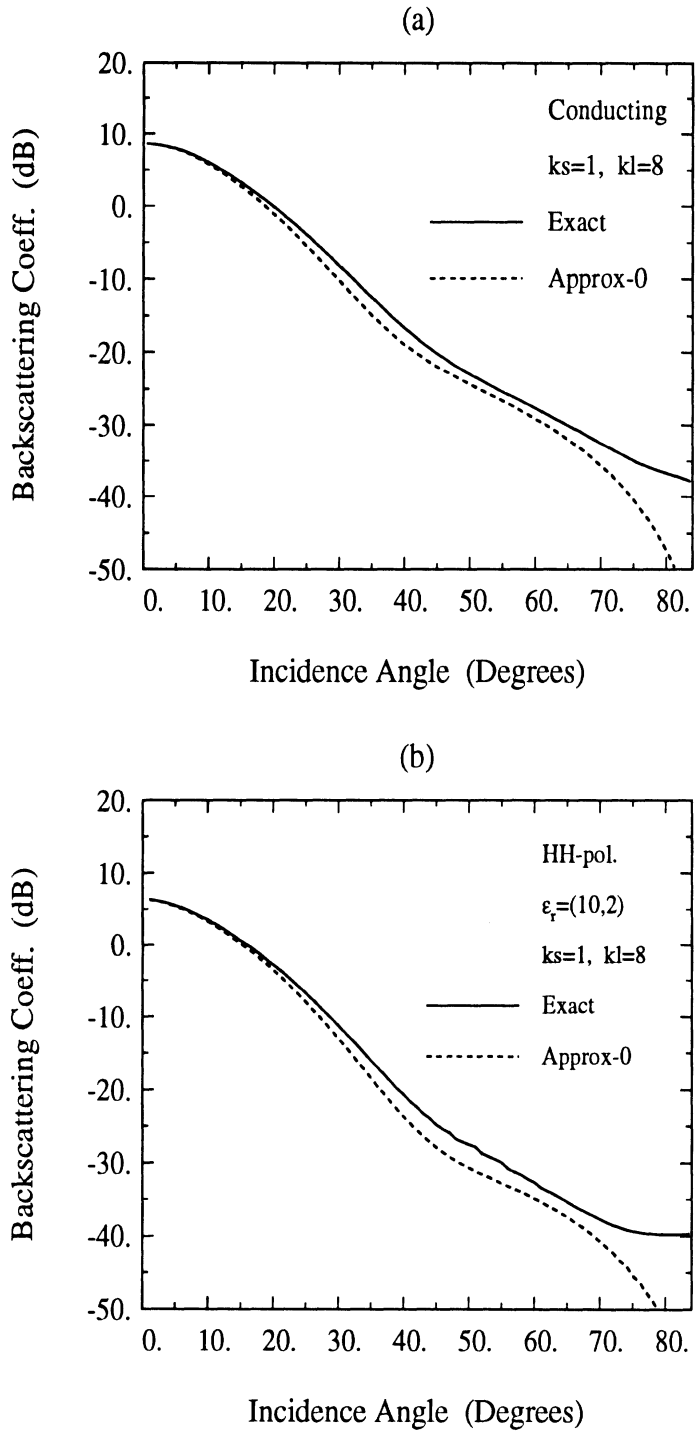

Figure 4.6: Comparison between the exact physical optics model and the method of moments solution for the roughness of $ks = 1$, $kl = 8$ for (a) a conducting surface and (b) for a dielectric surface of $\epsilon = (10, 2)$ for hh-polarization.

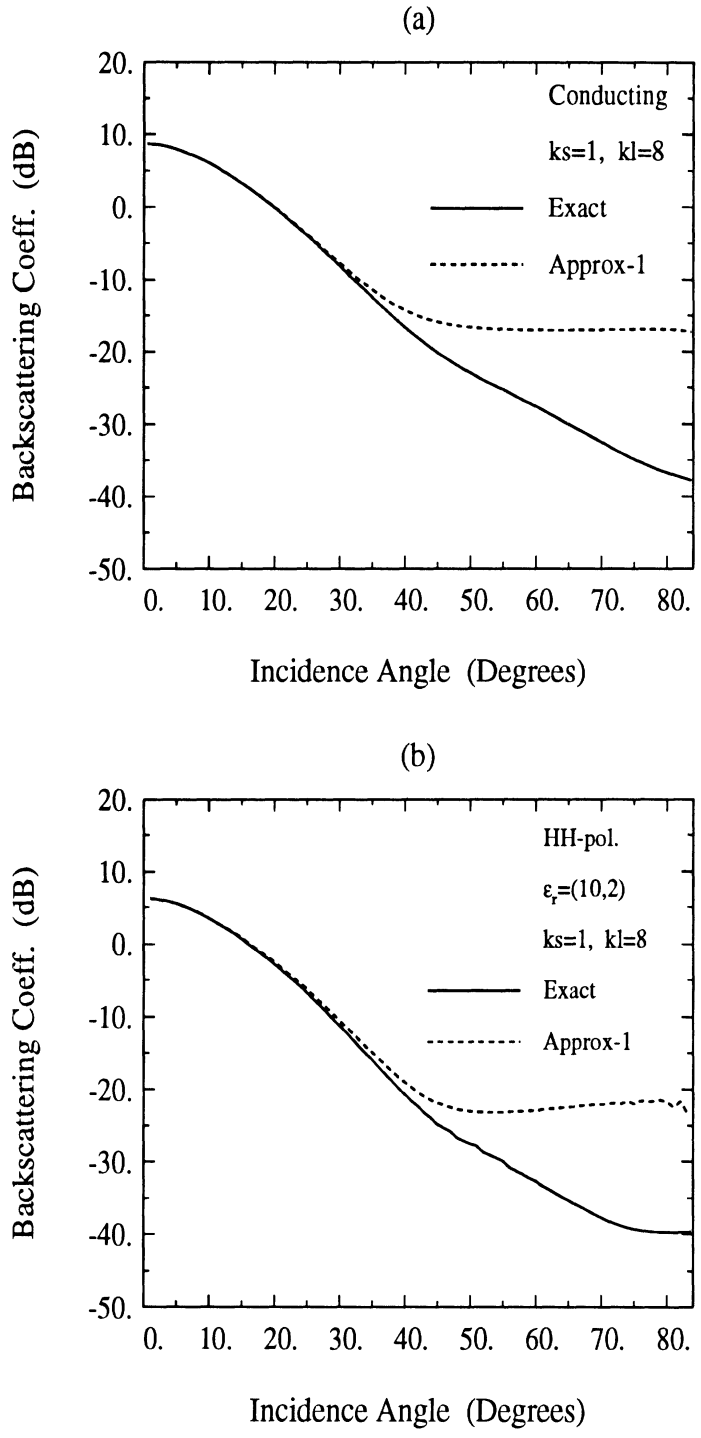

Figure 4.7: Comparison between the exact physical optics model and the method of moments solution for the roughness of $ks = 1$, $kl = 8$ for (a) a conducting surface and (b) for a dielectric surface of $\epsilon = (10, 2)$ for hh-polarization.

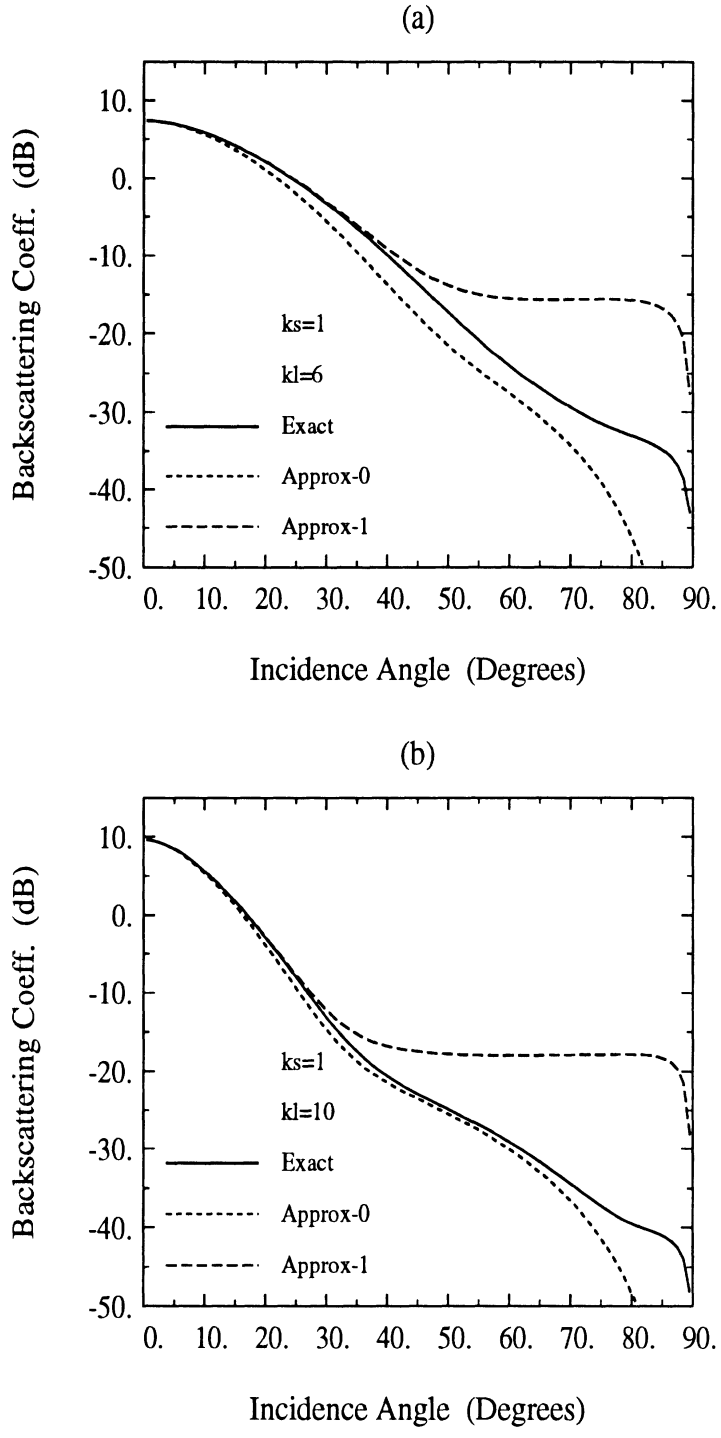

Figure 4.8: Comparison between the exact PO solution and the approximated PO solutions for a one-dimensional conducting surface of (a) $ks = 1$, $kl = 6$ and (b) $ks = 1$, $kl = 10$.

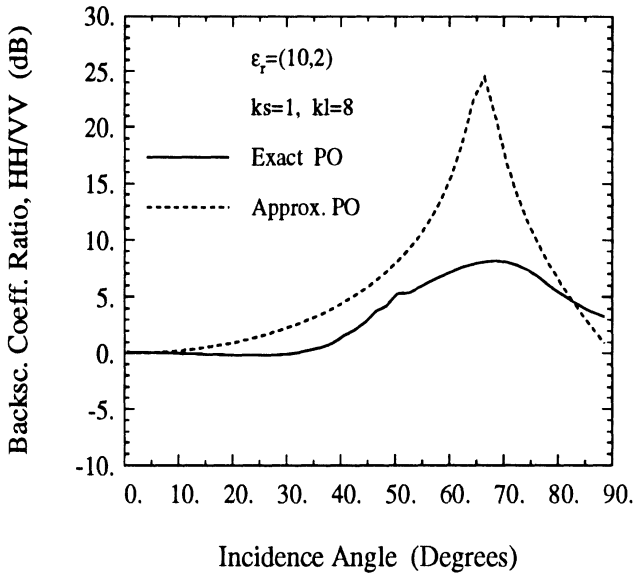

Figure 4.9: The ratio $\sigma^{\circ}_{hh}/\sigma^{\circ}_{vv}$ of the exact PO solution and the approximated PO solutions for a one-dimensional dielectric random surface of $ks = 1$, $kl = 8$, and $\epsilon_r = (10, 2)$.

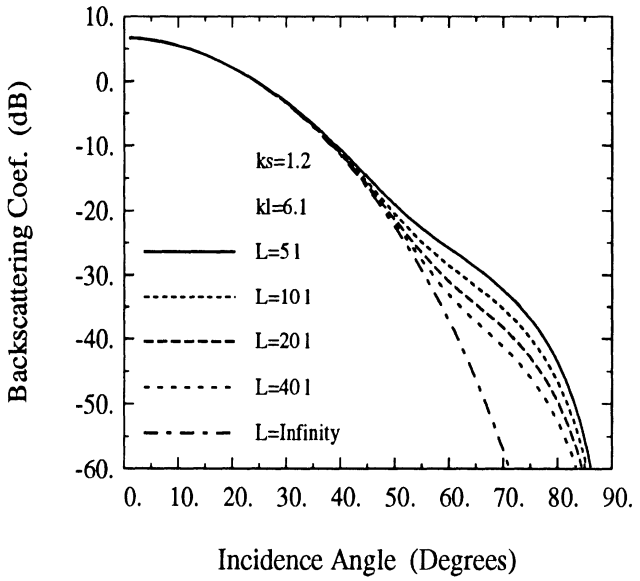

Figure 4.10: The backscattering coefficients of the exact PO solution for a various values of the integration limits for a one-dimensional conducting random surface of $ks = 1.2$, $kl = 6.1$.

4.7(a) and (b). Figures 4.8(a) and (b) show the comparison between the exact PO solution and the approximated PO solutions for a relatively rough surface ($ks = 1$, $kl = 6$) and a relatively smooth surface ($ks = 1$, $kl = 10$), respectively. The slope term effect for a rough surface is larger than for a smooth surface, and the edge term effect for a rough surface is smaller than for a smooth surface as shown in Figs. 4.8(a) and (b). The difference between hh- and vv-polarized backscattering coefficients is the ratio of the Fresnel reflectivity $|R_h|^2$ and $|R_v|^2$. For the exact PO solution, the local reflection coefficient which is a function of the surface local slope affects the polarization differences. Figure 4.9 shows the comparison between the ratio $\sigma^\circ_{hh}/\sigma^\circ_{vv}$ of the approximated PO model and the ratio of the exact PO model for the roughness of $ks = 1$, $kl = 8$ and the dielectric constant of $\epsilon_r = (10, 2)$. The ratio $\sigma^\circ_{hh}/\sigma^\circ_{vv}$ for the approximated PO model has a peak at $\theta \approx 66°$ which is the brewster angle for $\epsilon_r = (10, 2)$, while the ratio for the exact PO solution is < 0 dB at low incidence angles and > 0 dB at large incidence angles as shown in Fig. 4.9. In order to get a closed form of the backscattering coefficient, the integration limit in (4.40) is changed as $L \to \infty$ assuming $L \gg l$ where l is the correlation length. Figure 4.10 shows the backscattering coefficients of the exact PO solution for the one-dimensional conducting random surface of $ks = 1.2$, $kl = 6.1$ for the values of $L_1 = 5l$, $L_2 = 10l$, $L_3 = 20l$, $L_4 = 40l$, and $L_5 = \infty$. At low incidence angle ($\theta < 45°$) the backscattering coefficient is independent of the integration limit L. The backscattering coefficient with $L = 5l$, however, is much higher than σ° with $L = \infty$ as shown in Fig. 4.10. The exact PO solutions presented in Figs. 4.5, 4.6, 4.7, and 4.8 have been computed for the integration limit of $L = 10l$.

4.6 Conclusions

The backscattering coefficient of a two-dimensional dielectric random surface has been formulated exactly without further approximation other than the tangent plane approximation (or Kirchhoff approximation). The exact PO solutions for a one-dimensional random surface have been computed numerically and compared with the exact numerical solution (Monte Carlo method with the method of moments) in the case of conducting surfaces. The exact PO solution was used to examine the zeroth-order and the first-order approximated PO models, which is equivalent to the examination of the effects of the slope term in the series of scattering amplitude and the edge term in the formulation of scattered field, respectively. The zeroth-order approximated PO model (no slope term) underestimates the backscattering coefficient in the range of $2 \sim 5$ dB at $20° - 70°$. The first-order approximated PO model shows an excellent agreement with the exact PO solution at small incidence angles $\theta < 40°$ and overestimates at large incidence angles $\theta > 40°$ in the range of $5 \sim 20$ dB depending on the incidence angle.

CHAPTER V

A NUMERICAL SOLUTION FOR SCATTERING FROM INHOMOGENEOUS DIELECTRIC RANDOM SURFACES

5.1 Introduction

An exact solution for scattering by inhomogeneous, dielectric, random surfaces does not exist at the present time. This chapter presents an efficient numerical technique for computing the scattering by inhomogeneous dielectric rough surfaces. The inhomogeneous dielectric random surface, which is intended to represents a bare soil surface, is considered to be comprised of a large number of randomly positioned dielectric humps of different sizes, shapes, and dielectric constants, lying on an impedance surface. Clods with non-uniform moisture content and rocks are modeled as inhomogeneous dielectric humps and the underlying smooth wet soil surface is modeled as an impedance surface. In this technique an efficient numerical solution for the constituent dielectric humps is obtained using the method of moments in conjunction with a new Green's function representation based on the exact image theory. The scattered field from a sample of the rough surface is obtained by summing the scattered fields from all the individual humps of the surface coherently, ignoring the effects of multiple scattering between the humps. The behavior of the scattering coefficient

σ° and the phase difference statistics are obtained from calculations of the scattered fields for many different surface samples of the same process. Numerical results are presented for several different roughnesses and dielectric constants of the random surface. The numerical technique is verified by comparing the numerical solution with the solution based on the small-perturbation method and the physical-optics model for homogeneous rough surfaces. This technique can be used to study the behavior of the scattering coefficient and phase difference statistics of rough soil surfaces.

Investigation of the radar scattering response of natural surfaces is an important problem in remote sensing because of its potential in retrieving desired physical parameters of the surface, namely its soil moisture content and surface roughness. Soil moisture is a key ingredient of the biochemical cycle and an important variable in hydrology and land processes. Although the problem of electromagnetic wave scattering from random surfaces has been investigated for many years, because of its complexity, theoretical solutions exist only for simple limiting cases. These include the small perturbation method (SPM) [Rice, 1951] and the Kirchhoff approximation (KA) [Beckmann and Spizzichino, 1987], both of which are applicable for homogeneous surfaces over restricted regions of validity. Numerous techniques based on the basic assumptions of the SPM and KA have been developed in the past in an attempt to extend the regions of validity of these models; however, they all have the basic limitations of the original models [Brown, 1978]. Other theoretical models are available also, such as the full wave analysis technique [Bahar, 1981], the phase perturbation technique [Wineberner and Ishimaru, 1985], and the integral equation method [Fung and Pan, 1987], but they are not applicable for inhomogeneous surfaces and their regions of validity have not been fully determined yet. Several numerical solutions of the scattering problem have been proposed to identify the regions of validity and ac-

curacies of these theoretical models. A scattering solution for a perfectly conducting random surface using the method of moments has been suggested by Axline and Fung [1987] who used a tapered incident field as the excitation to eliminate the edge-effect contribution due to the boundaries of the illuminated area. Since then, many other numerical solutions with some modifications have been introduced [Fung and Chen, 1985; Nieto-Vesperinas and Soto-Crespo, 1987; Thorsos, 1988; Durden and Vesecky, 1990; Lou et al., 1991; Rodriguez et al., 1992], all for scattering from perfectly conducting random surfaces. A numerical solution for homogeneous dielectric random surfaces has recently been reported [Sanchez-Gil and Nieto-Vesperinas, 1991] where again a tapered illumination is used to limit the size of the scattering area. The accuracy of the numerical solution with tapered illumination decreases with increasing incidence angle. To our knowledge, a solution for scattering from an inhomogeneous rough surfaces does not yet exist.

Analysis of microwave backscatter observations by Oh et al. [1992] reveals that the existing theoretical models cannot adequately explain the scattering behavior of soil surfaces. The deviation between theoretical predictions and experimental data is attributed to three factors. First, the roughness parameters of some surfaces are often outside the region of validity of the theoretical models. Second, the autocorrelation functions associated with the measured height profiles of natural surfaces are very complicated and are not Gaussian or exponential functions. Finally, the most important reason is that in most cases natural surfaces are not homogeneous dielectric surfaces, *i.e.*, the moisture content is not uniform in depth. The top rough layer, which includes clods and rocks, is usually dry and the underlying soil layer is moist and smooth.

In this chapter we model a soil surface as an inhomogeneous dielectric random

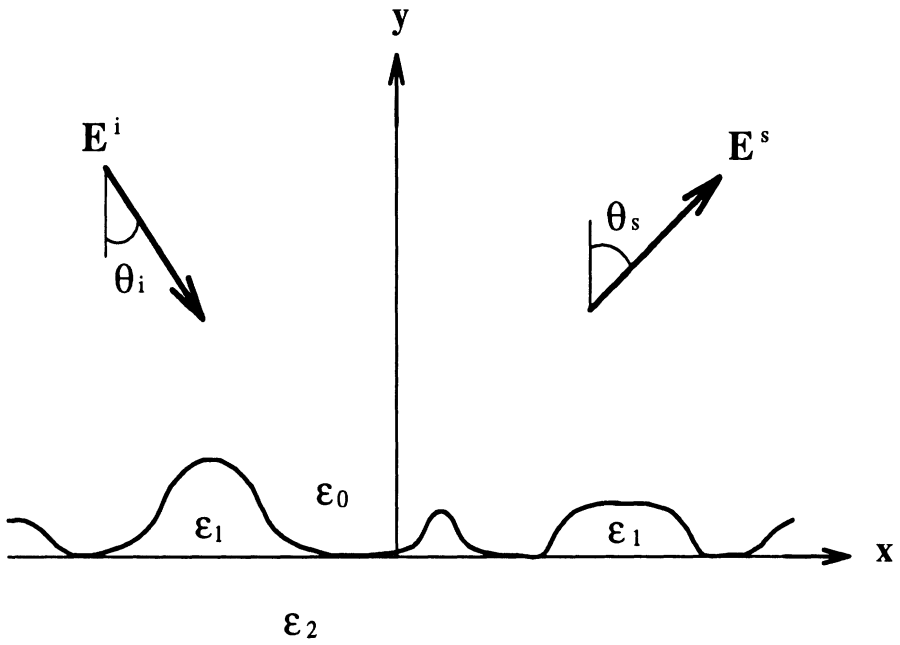

Figure 5.1: Geometry of the scatter problem for a two-dimensional rough surface.

surface comprised of a large number of randomly positioned two-dimensional dielectric humps of different sizes, shapes, and dielectric constants, all lying over an impedance surface as shown in Fig. 5.1. At microwave frequencies, the moist and smooth underlying soil layer can be modeled as an impedance surface, and the irregularities above it can be treated as dielectric humps of different dielectric constants and shapes. For the field scattered by a single dielectric hump over an impedance surface, we have an available efficient numerical solution that uses the exact image theory for the Green's function in conjunction with the method of moments [Sarabandi, 1992]. In the solution of a single hump, it has been shown that the bistatic scattered field is very weak at points in close pproximity to the impedance surface; thus, the effects of multiple scattering between humps can be ignored. In this case the scattered field from a collection of randomly positioned dielectric humps can easily be obtained by

summing the scattered field of all the constituent humps coherently. The scattering coefficients (σ°) and the phase difference statistics are obtained by a Monte Carlo simulation.

In Section 2 we summarize the procedure for the numerical solution of a single hump above an impedance surface. Section 3 outlines the procedures used for generating the random surfaces and for evaluating the statistics of the scattered field. Numerical results and their comparison with theoretical models are presented in Section 4.

5.2 Scattering From Individual Humps

In this section we briefly review the procedure used for the numerical solution of scattering from a two-dimensional dielectric object above a uniform impedance surface [Sarabandi, 1992]. The radiated field for a dipole source above a dissipative half-space medium (Green's function) is usually evaluated using the Sommerfeld integral [Stratton, 1941]. This infinite integral, in general, is highly oscillatory and computationally rather inefficient. Recently, the Green's function of an impedance surface was derived in terms of rapidly converging integrals using appropriate integral transforms similar to those employed by Lindell and Alanen [1984] in their derivation of the exact image theory. The scattering problem was then formulated by integral equations which were solved numerically using the method of moments.

Suppose a dielectric object, possibly inhomogeneous, is located above an impedance surface and is illuminated by a plane wave. The incident field $\mathbf{E}^i$ induces conduction and displacement currents in the dielectric object which together are known as the polarization current $\mathbf{J}_e$. The polarization current can be represented in terms of the total electric field inside the dielectric object, which is comprised of the incident,

reflected, and scattered fields denoted by $\mathbf{E}^i$, $\mathbf{E}^r$, and $\mathbf{E}^s$, respectively. Thus

$$\mathbf{J}_e(\overline{\rho}) = -ik_0 Y_0(\epsilon(\overline{\rho}) - 1)(\mathbf{E}^i(\overline{\rho}) + \mathbf{E}^r(\overline{\rho}) + \mathbf{E}^s(\overline{\rho})), \tag{5.1}$$

where $k_0 = \omega\sqrt{\mu_0\epsilon_0}$, $Y_0 = \sqrt{\epsilon_0/\mu_0}$, and $\epsilon(\overline{\rho})$ is the relative dielectric constant of the object at the point $\overline{\rho}(= x\hat{x} + y\hat{y})$. The fields $\mathbf{E}^i$, $\mathbf{E}^r$, and $\mathbf{E}^s$ are, respectively, given by

$$\mathbf{E}^i(\overline{\rho}) = (E_h^i \hat{h}_i + E_v^i \hat{v}_i)\exp[ik_0 \hat{k}_i \cdot \overline{\rho}], \tag{5.2}$$

$$\mathbf{E}^r(\overline{\rho}) = (R_h E_h^i \hat{h}_r + R_v E_v^i \hat{v}_r)\exp[ik_0 \hat{k}_r \cdot \overline{\rho}], \tag{5.3}$$

$$\mathbf{E}^s(\overline{\rho}) = ik_0 Z_0 \int_S \overline{\overline{\mathbf{G}}}(\overline{\rho}, \overline{\rho}') \cdot \mathbf{J}(\overline{\rho}')d\overline{\rho}', \tag{5.4}$$

where E_h^i and E_v^i are the horizontal (E-polarized) and vertical (H-polarized) components of the incident field, respectively. R_h and R_v are the horizontal and vertical Fresnel reflection coefficients and $\overline{\overline{\mathbf{G}}}(\overline{\rho}, \overline{\rho}')$ is the dyadic Green's function of the problem. The dyadic Green's function can be decomposed into two components: (1) the dyadic Green's function of the free space $\overline{\overline{\mathbf{G}}}_0(\overline{\rho}, \overline{\rho}')$ and (2) the dyadic Green's function due to the presence of the impedance surface $\overline{\overline{\mathbf{G}}}_r(\overline{\rho}, \overline{\rho}')$; that is:

$$\overline{\overline{\mathbf{G}}}(\overline{\rho}, \overline{\rho}') = \overline{\overline{\mathbf{G}}}_0(\overline{\rho}, \overline{\rho}') + \overline{\overline{\mathbf{G}}}_r(\overline{\rho}, \overline{\rho}')\ . \tag{5.5}$$

Since $\frac{\partial}{\partial z} = 0$ in a two-dimensional scattering problem, the dyadic Green's function of free space $\overline{\overline{\mathbf{G}}}_0(\overline{\rho}, \overline{\rho}')$ takes the following form

$$\overline{\overline{\mathbf{G}}}_0(\overline{\rho}, \overline{\rho}') = \begin{bmatrix} \left(1 + \frac{\partial^2}{k_0^2 \partial x'^2}\right) g_0(\overline{\rho}, \overline{\rho}') & \frac{\partial^2}{k_0^2 \partial x' \partial y'} g_0(\overline{\rho}, \overline{\rho}') & 0 \\ \frac{\partial^2}{k_0^2 \partial y' \partial x'} g_0(\overline{\rho}, \overline{\rho}') & \left(1 + \frac{\partial^2}{k_0^2 \partial y'^2}\right) g_0(\overline{\rho}, \overline{\rho}') & 0 \\ 0 & 0 & g_0(\overline{\rho}, \overline{\rho}') \end{bmatrix}, \tag{5.6}$$

where $g_0(\overline{\rho}, \overline{\rho}')$ is the scalar free-space Green's function given by

$$g_0(\overline{\rho}, \overline{\rho}') = \frac{i}{4} H_0^{(1)}(k_0\, \rho_0), \quad \rho_0 = \sqrt{(x - x')^2 + (y - y')^2}\ , \tag{5.7}$$

and $H_0^{(1)}$ is the Hankel function of the first kind and zeroth order. The computationally efficient dyadic Green's function $\overline{\overline{\mathbf{G}}}_r(\overline{\rho},\overline{\rho}')$ is given by [16]:

$$\overline{\overline{\mathbf{G}}}_r(\overline{\rho},\overline{\rho}') = \begin{bmatrix} -\left(1+\frac{\partial^2}{k_0^2\partial x'^2}\right) g_r^V(\overline{\rho},\overline{\rho}') & \frac{\partial^2}{k_0^2\partial x'\partial y'} g_r^V(\overline{\rho},\overline{\rho}') & 0 \\ -\frac{\partial^2}{k_0^2\partial y'\partial x'} g_r^V(\overline{\rho},\overline{\rho}') & \left(1+\frac{\partial^2}{k_0^2\partial y'^2}\right) g_r^V(\overline{\rho},\overline{\rho}') & 0 \\ 0 & 0 & g_r^H(\overline{\rho},\overline{\rho}') \end{bmatrix}, \quad (5.8)$$

where

$$\begin{aligned} g_r^H(\overline{\rho},\overline{\rho}') &= g_1(\rho_1) - 2\alpha \int_0^\infty e^{-\alpha\nu} g_2(\rho_2) d\nu \\ g_r^V(\overline{\rho},\overline{\rho}') &= g_1(\rho_1) - 2\beta \int_0^\infty e^{-\beta\nu} g_2(\rho_2) d\nu \end{aligned} \quad (5.9)$$

with

$$g_i(\rho_i) = \frac{i}{4} H_0^{(1)}(k_0\,\rho_i), \;\; i=1,2, \qquad \rho_1 = \sqrt{(x-x')^2+(y+y')^2}\,, \quad (5.10)$$
$$\rho_2 = \sqrt{(x-x')^2+(y+y'+i\nu)^2}\,,$$

and $\alpha = k_0/\eta$, $\beta = k_0\eta$. Here η is the normalized impedance of the impedance surface defined by $\eta = Z/Z_0$.

There is no known exact solution for the integral equation given by (5.1). Hence, an approximate numerical solution of this equation must be obtained using the method of moments. This is done by dividing the cross section of the dielectric structure into N_c sufficiently small rectangular cells such that the dielectric constant and the polarization current over each cell can be approximated by constant values. Using the point-matching technique, the integral equation can be cast into a matrix equation of the following form:

$$\begin{bmatrix} [\mathcal{Z}_{xx}] & [\mathcal{Z}_{xy}] & 0 \\ [\mathcal{Z}_{yx}] & [\mathcal{Z}_{yy}] & 0 \\ 0 & 0 & [\mathcal{Z}_{zz}] \end{bmatrix} \begin{bmatrix} [\mathcal{I}_x] \\ [\mathcal{I}_y] \\ [\mathcal{I}_z] \end{bmatrix} = \begin{bmatrix} [\mathcal{V}_x] \\ [\mathcal{V}_y] \\ [\mathcal{V}_z] \end{bmatrix} \quad (5.11)$$

where $[\mathcal{Z}_{pq}]$ is the impedance matrix, $[\mathcal{I}_p]$ is the unknown vector whose entries are the values of the polarization current at the center of each cell, and $[\mathcal{V}_p]$ is the excitation vector with $p = x$, y, or z. The entries of $[\mathcal{V}_p]$ are simply given by

$$v_{p,n} = ik_0 Y_0[\epsilon(x_n, y_n) - 1]\left([\mathbf{E}_p^i(x_n, y_n) + \mathbf{E}_p^r(x_n, y_n)]\right) \cdot \hat{p} \ , \tag{5.12}$$

and the entries of $[\mathcal{Z}_{pq}]$ can be evaluated from

$$\begin{aligned} z_{pqmn} = &-\delta_{pq}\delta_{mn} + k_0^2[\epsilon(x_m, y_m) - 1] \\ &\cdot \int_{\Delta S_m} [G_{pq}(x_m, y_m; x_n, y_n) + G_{rpq}(x_m, y_m; x_n, y_n)] ds_m \ , \end{aligned} \tag{5.13}$$

where δ_{pq} and δ_{mn} are the Kronecker delta functions, and $p, q = x, y$, or z.

Explicit expressions for the elements of the impedance matrix are given in [Sarabandi, 1992] where off-diagonal elements are obtained by approximating the Green's function *via* its Taylor series expansion around the midpoint of each cell and then the integration over the cell surface is performed analytically. For diagonal elements the free-space Green's function is approximated by its small argument expansion and then integration is performed analytically.

Once the impedance matrix for a given dielectric hump is calculated and inverted, the scattered far-field can be computed from (5.4) for any desired combinations of incident and scattered directions.

5.3 Monte Carlo Simulation of Rough Surface Scattering

Monte Carlo simulation of scattering by a rough surface comprised of a finite collection of dielectric humps involves the execution of five major steps, as shown in Fig. 5.2. The first step is to choose the type (size, shape, and dielectric constant) and number of constituent humps. The second step deals with generating a surface sample by positioning a large number of humps with a prescribed probability distribution

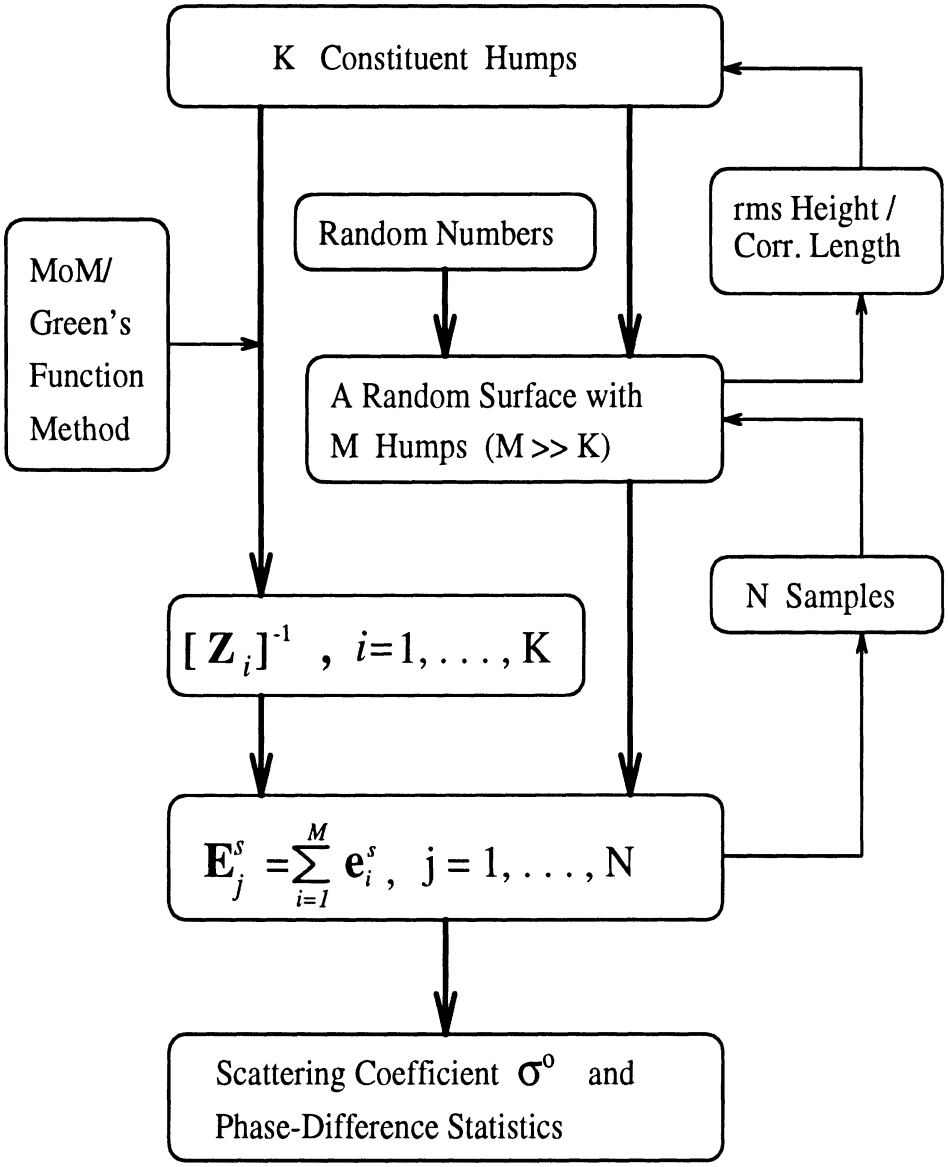

Figure 5.2: Flow chart of the Monte Carlo simulation for the rough surface scattering problem.

function. The number of humps in the surface sample must be chosen large enough so that the surface length is longer than fifty correlation length. The third step in this algorithm is to compute the inverse impedance matrices for all constituent humps using the numerical method explained in the previous section. Next, the scattered field from the surface is computed by coherent summation of the scattered fields from all of the humps in the surface sample. Finally, the scattering coefficient σ° and the phase-difference statistics are obtained by repeating the fourth step for a large number of independently generated surface samples. For example, N is chosen to be around 100 to reduce the standard deviation associated with the estimation of mean backscattered power (σ°). The standard deviation of estimated σ° is inversely proportional to $\sqrt{N}$ [Ulaby and Dobson, 1989].

The types of constituent humps, in addition to their probability of occurrence, fully characterize the statistics of the random surface. Figure 5.3 shows the geometry and dielectric profiles of different types of dielectric humps that can be handled by this algorithm. For example, Figure 5.3(a) shows a typical hump arrangement for a dry clod above a moist and smooth underlying soil layer ($\epsilon_0 < \epsilon_1 < \epsilon_2$), and Figure 5.3(b) shows the same hump when the clod and underlying layer are both moist (a homogeneous surface). The hump itself may be considered to be inhomogeneous as shown in Fig. 5.3(c). Isolated irregularities such as rocks above a flat surface can be represented by the hump example shown in Fig. 5.3(d) where the bump occupies only a part of the total width allocated to an individual hump. When the surface is very rough with a short correlation length, the geometry of the humps are more complicated. Two examples of such humps are shown in Figs. 5.3(e) and (f). The profiles of Figs. 5.3(a)-(e) used in this chapter are given by the following functionals;

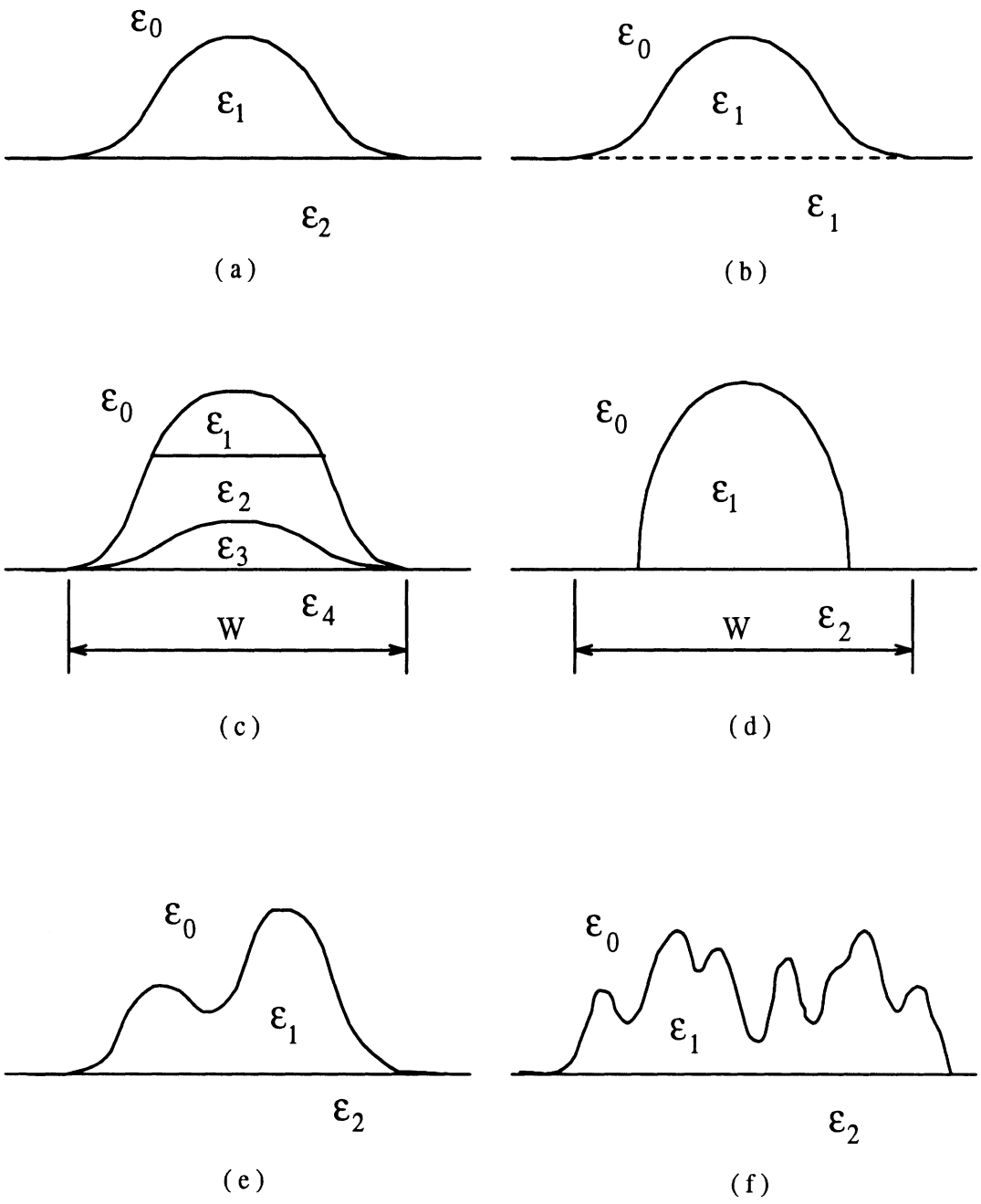

Figure 5.3: Hump types for the rough surface considered in this chapter.

for (a)-(c)

$$y(x) = \frac{W}{A}\cos^2\left(\frac{\pi x}{W}\right) , \quad -\frac{W}{2} \le x \le \frac{W}{2} , \tag{5.14}$$

for (d)

$$y(x) = A\left(1 - \frac{x^2}{B^2}\right) , \quad -B \le x \le B, \ B \le W , \tag{5.15}$$

and for (e)

$$y(x) = A\, F_1(x) \ + \ B\, F_2(x) ,$$

with

$$\left.\begin{aligned} F_1(x) &= \cos^n\left(\tfrac{\pi x}{W} - \tfrac{\pi}{2}\right)\left(\tfrac{x}{W}\right)^m \\ F_2(x) &= \cos^n\left(\tfrac{\pi x}{W} - \tfrac{\pi}{2}\right)\left(1 - \tfrac{x}{W}\right)^m \end{aligned}\right\} , \ 0 \le x \le W , \tag{5.16}$$

where A and B are constants, n and m are integers, and W is the width of a hump. The set of constituent humps for a surface can be constructed by choosing a finite number of parameters and desired dielectric constants in the desired functionals. The profile of Fig. 5.3(f) is very complicated and should be obtained numerically by the procedure outlined in [Fung and Chen, 1985]. In this procedure the hump profile is obtained from a sequence of independent Gaussian deviates with zero mean and unit variance which are correlated by a set of weighting factors derived from the desired correlation function.

Suppose the set of individual humps includes K different humps (including size, shape, and dielectric constant) and the profiles of the humps in the set are represented by $f_i(x)$, $i = 1, \cdots, K$. Then a sequence of random numbers ranging from 1 to K, which is generated by a random number generator with the prescribed probability distribution function, is used to position a large number of humps randomly to construct a surface sample. If the total number of humps (M) in the surface sample

is much larger than the number of constituent humps (K) and the random number generator has a uniform distribution, the probability of occurrence of each hump in the surface will be about M/K. A functional form of the generated surface profile can be represented by

$$y(x) = \sum_{m=1}^{M} f_{i_m}\left(x - \sum_{l=1}^{m-1} W_{i_l}\right) \tag{5.17}$$

where $i_m, i_l \in \{1, \cdots, K\}$ and W_{i_l} represents the width of the hump of the i_lth type. The roughness parameters, rms height s, correlation length l, and rms slope m [Ulaby et al, 1982], can be computed either numerically or analytically from the surface profile given in (5.17). The analytical computation is possible for simple functional forms. The average height of the surface can be computed from

$$\overline{y}(x) = \frac{1}{L}\sum_{i=1}^{K} p_i \int_0^{W_i} f_i(x)dx \ , \tag{5.18}$$

where $L = \sum_{i=1}^{K} p_i W_i$ and p_i is the probability of occurrence of the hump of type i. The rms height s and the rms slope m, respectively, can be evaluated from

$$s = \left\langle (y(x) - \overline{y}(x))^2 \right\rangle^{\frac{1}{2}} = \left[\frac{1}{L}\sum_{i=1}^{K}\int_0^{W_i} (p_i f_i(x) - \overline{y}(x))^2 \, dx\right]^{\frac{1}{2}} , \tag{5.19}$$

and

$$m = \left\langle \left(\frac{d\,y(x)}{dx} - \left\langle \frac{d\,y(x)}{dx} \right\rangle\right)^2 \right\rangle^{\frac{1}{2}} = \left[\frac{1}{L}\sum_{i=1}^{K} p_i \int_0^{W_i} (f_i'(x))^2 \, dx\right]^{\frac{1}{2}} . \tag{5.20}$$

Assuming the surface has a Gaussian correlation function, the correlation length l is related to rms height and rms slope by,

$$l = \sqrt{2}\,\frac{s}{m} \ . \tag{5.21}$$

It is often required to generate a random surface of a specified rms height s and correlation length l. In that case, the required surface can be obtained by an iterative

process where some initial values for the hump parameters are chosen. Then the roughness parameters are calculated and compared with the desired ones. Depending on the difference between the calculated s and l and the desired ones the hump parameters are modified and this process is repeated until the difference becomes smaller than a tolerable error.

Once the set of individual humps for a random surface with given s and l is formed, the impedance matrices, $[\mathcal{Z}_{pq}]_i$, $i = 1, \cdots, K$, can be computed using the method of moments described in the previous section. Since the scattered field of a hump near the impedance surface is very weak [16], the effect of multiple interaction between humps in a surface sample can be ignored. Therefore by inverting and storing the impedance matrices of the constituent humps, the scattered field of any surface sample comprised of M humps ($M \gg K$) can be computed very efficiently for any incidence and observation directions. For a given direction of incidence the polarization currents in the jth hump for the vertical and horizontal polarizations, respectively, are given by

$$\begin{bmatrix} [\mathcal{I}_x] \\ [\mathcal{I}_y] \end{bmatrix}_j = \begin{bmatrix} [\mathcal{Z}_{xx}] & [\mathcal{Z}_{xy}] \\ [\mathcal{Z}_{yx}] & [\mathcal{Z}_{yy}] \end{bmatrix}^{-1}_{i_j} \begin{bmatrix} [\mathcal{V}_x] \\ [\mathcal{V}_y] \end{bmatrix}_j \quad \text{and} \tag{5.22}$$

$$[\mathcal{I}_z]_j = [\mathcal{Z}_{zz}]^{-1}_{i_j} \; [\mathcal{V}_z]_j \,, \tag{5.23}$$

where $j \in \{1, \cdots, M\}$ and $i_j \in \{1, \cdots, K\}$ representing the hump of the ith type. The excitation vector $[\mathcal{V}]_j$ is computed from (5.12) where the position vector $\overline{\rho}$ is specified by the discretization procedure and the profile function (5.17). The electric polarization current induced inside the surface sample can be represented by

$$[\mathcal{J}_p] = \left[[\mathcal{I}_p]_1^T, \cdots, [\mathcal{I}_p]_i^T, \cdots, [\mathcal{I}_p]_M^T \right]^T \,, \quad p = x, y, z \tag{5.24}$$

where $[\mathcal{I}_p]_i$ is the p-polarized current inside the ith hump. The radiated far field can be evaluated from

$$E^s_{pp} = \sqrt{\frac{2}{\pi k_0 \rho}} e^{i(k_0\rho - \pi/4)} S_{pp}\,, \quad pp = hh \text{ or } vv \tag{5.25}$$

where S_{pp} is the far-field amplitude given by

$$S_{hh} = -\frac{k_0 Z_0}{4} \sum_{n=1}^{N_t} J_z(x_n, y_n) \Delta x_n \Delta y_n e^{-ik_0 \sin\theta_s x_n} \left[e^{-ik_0 \cos\theta_s y_n} + R_E(\theta_s) e^{ik_0 \cos\theta_s y_n} \right] \tag{5.26}$$

$$\begin{aligned} S_{vv} = \frac{k_0 Z_0}{4} \sum_{n=1}^{N_t} & \Delta x_n \Delta y_n e^{-ik_0 \sin\theta_s x_n} \\ & \cdot \Big\{ J_x(x_n, y_n) \cos\theta_s \left([e^{-ik_0 \cos\theta_s y_n} - R_H(\theta_s) e^{ik_0 \cos\theta_s y_n} \right) \\ & - J_y(x_n, y_n) \sin\theta_s \left(e^{-ik_0 \cos\theta_s y_n} + R_H(\theta_s) e^{ik_0 \cos\theta_s y_n} \right) \Big\}. \end{aligned} \tag{5.27}$$

Here N_t is the total number of cells in the surface sample.

The statistical behavior of the scattered field is obtained from evaluation of E^s_{pp} for many independent surface samples. For a sufficiently large number of surface samples (N_s), the incoherent scattering coefficient is computed from

$$\sigma^\circ_{pp} = \lim_{\rho\to\infty} \frac{2\pi\rho}{N_s L_{av}} \left[\sum_{j=1}^{N_s} \left| \mathbf{E}^s_{pp,j} \right|^2 - \frac{1}{N_s} \left| \sum_{j=1}^{N_s} \mathbf{E}^s_{pp,j} \right|^2 \right], \qquad pp = hh,\ vv, \tag{5.28}$$

where $L_{av} = \frac{1}{N_s} \sum_{j=1}^{N_s} L_j$, and L_j is the total length of the jth random surface.

In the past, the study of scattering by random surfaces was confined to examination of the incoherent scattering coefficients, σ°_{vv}, σ°_{hh}, and σ°_{hv}. With the introduction of radar polarimetry, it was recently shown that the co-polarized phase angle ϕ_c, defined as the phase difference between the HH- and VV-polarized scattering amplitudes: $\phi_c = \phi_{hh} - \phi_{vv}$, also depends on the roughness and dielectric constant of the surfaces [Sarabandi et a]., 1992; Oh et al., 1993]. In this chapter, the statistics of the phase difference, in addition to the scattering coefficients, are used to study the radar response of rough surfaces. It is shown that the PDF of ϕ_c, $f(\phi_c)$, can be obtained from the Mueller matrix of the distributed target and characterized completely

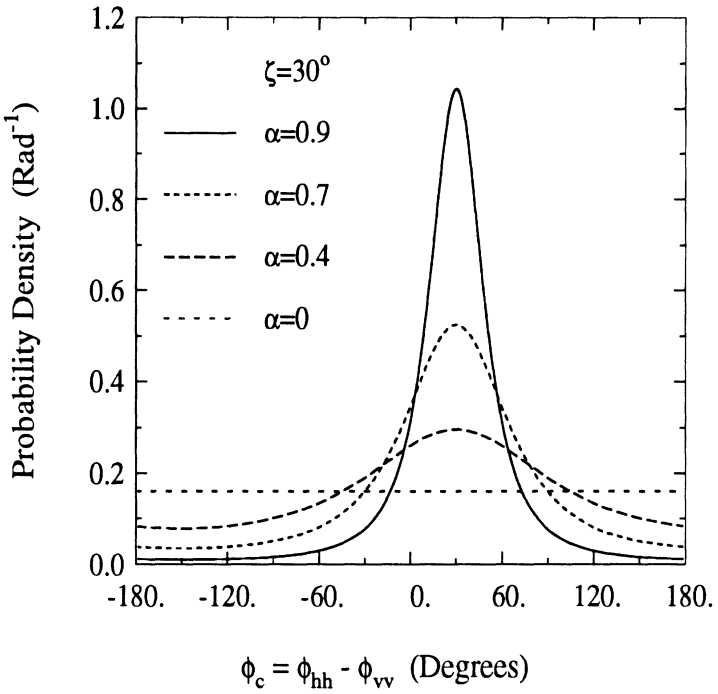

Figure 5.4: Probability density function of the co-polarized phase angle $\phi_c = \phi_{hh} - \phi_{vv}$ for a fixed value of ζ and four different values of α.

by two parameters; the degree of correlation α and the polarized-phase difference ζ [Sarabandi, 1992]. The degree of correlation is a measure of the width of the PDF and the polarized-phase difference is the value of ϕ_c at which the PDF is maximum as shown in Fig. 5.4. The $f(\phi_c)$ is given by

$$f(\phi_c) = \frac{1-\alpha^2}{2\pi[1-\alpha^2\cos^2(\phi_c-\zeta)]}\left\{1+\frac{\alpha\cos(\phi_c-\zeta)}{\sqrt{1-\alpha^2\cos^2(\phi_c-\zeta)}} \times\left[\frac{\pi}{2}+\tan^{-1}\frac{\alpha\cos(\phi_c-\zeta)}{\sqrt{1-\alpha^2\cos^2(\phi_c-\zeta)}}\right]\right\} \tag{5.29}$$

with

$$\alpha = \frac{1}{2}\sqrt{\frac{(M_{33}+M_{44})^2+(M_{34}-M_{43})^2}{M_{11}\,M_{22}}}\,, \tag{5.30}$$

$$\zeta = \tan^{-1}\left[\frac{M_{34}-M_{43}}{M_{33}+M_{44}}\right]\,, \tag{5.31}$$

where M_{ij} are the elements of the ensembled Mueller matrix.

Table 5.1: Roughness parameters corresponding to constants A and B.

Case	A	B	Approx. †		Exact ‡		At 5 GHz		Remarks
			s	l	s	l	ks	kl	
			in cm		in cm				
1	15	0.20	0.115	2.21	0.115	2.03	0.12	2.13	SPM region
2	15	0.36	0.208	3.98	0.207	3.63	0.22	3.80	
3	15	0.70	0.405	7.74	0.405	7.15	0.42	7.49	PO region

† Approximation by equations (32-33) and (21),

‡ Numerical evaluation with 4000 humps,

s : rms surface height,

l : correlation length.

5.4 Numerical Results

To demonstrate the performance of the technique proposed in this chapter, we shall use it to compute the scattering for some sample surfaces and then compare the results with those predicted by the available theoretical scattering models, when conditions apply. First, we consider a surface with homogeneous dielectric humps as shown in Fig. 5.3(a). The functional form of the humps are given by (5.14) where the parameters A and W are varied to generate the set of the constituent humps. Keeping A as a constant controlling the height and varying W, a set of similar humps can be generated. A random number generator with output $i \in \{1, \cdots, K\}$ selects the parameter $W_i = B\lambda i$, where B is a constant controlling the width of the humps and λ is the wavelength. In this example the hump parameters were chosen according to Table 5.1 and the random number generator was given a uniform distribution with $K = 10$. Before presenting the statistical scattering behavior of the surface, it is useful

to demonstrate the validity of the assumption regarding the significance of the effects of multiple scattering among the humps. Figures 5.5 (a) and (b) show the bistatic echo width of a squared-cosine hump with $W = 0.72\lambda$, $H = 0.07\lambda$, $\epsilon_1 = 15 + i3$ above a surface with $\eta = 0.254 - i0.025$ (which corresponds to $\epsilon_2 = 15 + i3$) at 5 GHz when the incidence angle $\theta_i = 0°$ and $\theta_i = 45°$, respectively. It is shown that the bistatic echo widths at the large scatter angles (near the surface) are very weak which implies that the effect of multiple scattering between humps can be ignored. In order to illustrate the effect of multiple scattering, a surface segment comprised of three squared-cosine humps with $\epsilon_1 = 15 + i3$ above an impedance surface with $\eta = 0.254 - i0.025$ was considered (see Fig. 5.6). Dimensions of the three humps are, respectively, given by: $W_1 = 0.8\lambda$, $H_1 = 0.08\lambda$; $W_2 = 1.0\lambda$, $H_2 = 0.1\lambda$; and $W_3 = 0.6\lambda$, $H_3 = 0.06\lambda$. The backscatter echo width of the surface segment was computed twice. In one case the scattered field was computed from the polarization current of isolated humps (ignoring the effect of mutual coupling) and in the other case the polarization current of the three-hump structure was obtained directly from the method of moments solution (including the effect of mutual coupling). Figures 5.6(a) and (b) show that the effect of multiple scattering is negligible for both polarizations. As long as the ratio of rms height to correlation length of the surface (s/l) is small, this approximation provides accurate results. For most natural surfaces $s/l < 0.3$ which satisfies this condition [Oh et al., 1992]. However if the ratio (s/l) is relatively large, the hump type of Fig. 5.3(f) must be used to include the effect of multiple scattering at the expense of computation time.

The rms surface height s and the rms surface slope m for this surface can be

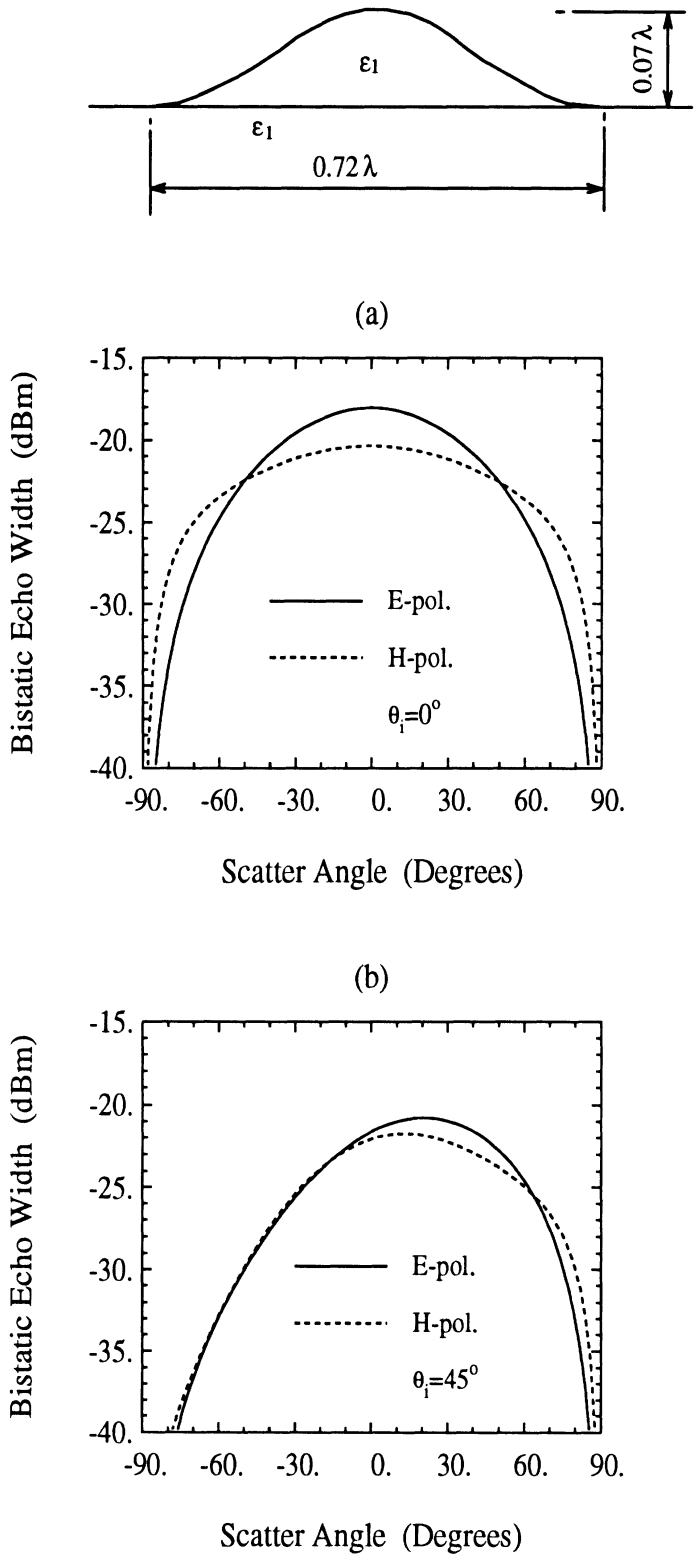

Figure 5.5: Bistatic echo width of a squared-cosine hump of $\epsilon_1 = 15 + i3$, W = 0.72λ, H = 0.07λ over an impedance surface of $\eta = 0.254 - i0.025$ at (a) $\theta_i = 0°$ and (b) $\theta_i = 45°$ at $f = 5$ GHz for E- and H-polarizations.

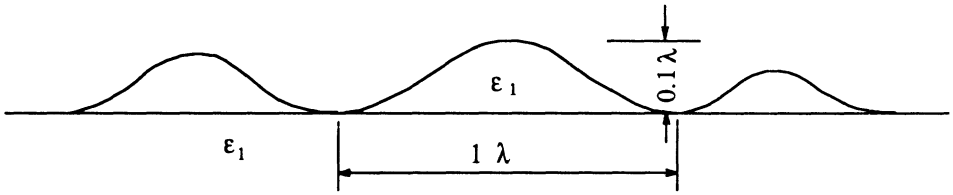

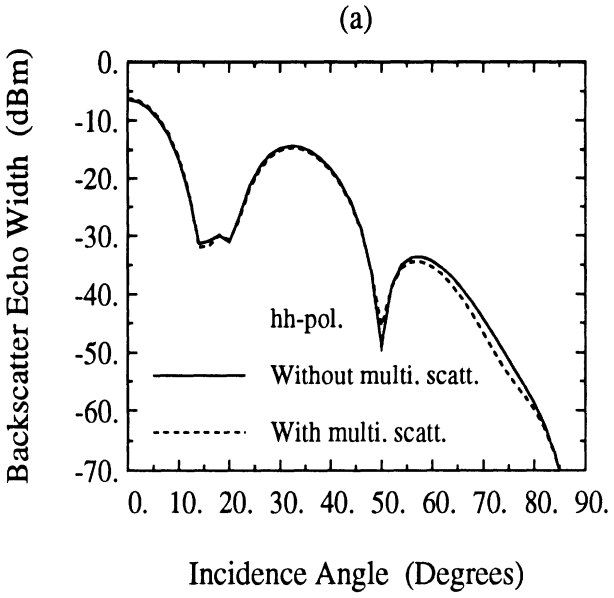

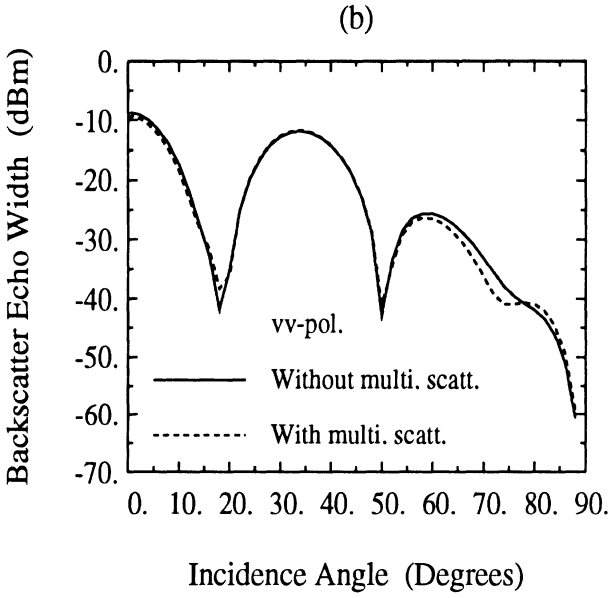

Figure 5.6: Multiple scattering effect on the backscatter echo width of a surface segment consisting of hump-4 , hump-5, and hump-3, corresponding to the roughness of $ks = 0.36$, $kl = 2.2$, with $\epsilon_1 = 15 + i3$ over an impedance surface of $\eta = 0.254 - i0.025$ at (a) hh-polarization and (b) vv-polarization at $f = 5$ GHz .

computed from (5.19) and (5.20) respectively and are given by

$$s = \left[\frac{1}{L_W} \sum_{i=1}^{K} \left(\frac{3}{8} \frac{W_i^3}{A^2} - \frac{W_i^2}{A} \overline{y} + W_i \overline{y}^2 \right) \right]^{\frac{1}{2}} , \tag{5.32}$$

$$m = \frac{\pi}{\sqrt{2}\, A}. \tag{5.33}$$

where

$$\overline{y} = \frac{1}{2\, A\, L_W} \sum_{i=1}^{K} W_i^2 , \quad \text{and} \quad L_W = \sum_{i=1}^{K} W_i ,$$

It should be noted that the rms surface slope m of this surface depends only on the constant A. Therefore for a fixed value of A, both the rms height and the correlation length increase at the same rate with increasing B. Table 5.1 shows several values of roughness parameters, s and l, corresponding to different values of A and B.

A random number generator was used to select and position 4000 squared-cosine humps over the impedance surface ($\eta = 0.254 - i0.025$). Then this surface was divided into 100 segments to obtain 100 independent surface samples each having 40 humps. The length of the surface segment was chosen to be in the range of 44λ to 154λ depending on the correlation length of the surface which corresponds to the size of individual humps. In the method of moments solution of individual humps, the size of a discretized cell was chosen such that $\Delta x = \Delta y = \lambda/15$ (where $\lambda = \lambda_0/\sqrt{\epsilon_{r1}}$). Table 5.2 summarizes the characteristics of the surfaces and their constituent humps used in the examples considered in this study. Figure 5.7(a) shows a surface sample with A=30 and B=0.2 (Case 1 in Tables 5.1 and 5.2). In Fig. 5.7(b) the correlation function of the surface is shown. The correlation function, as computed from the surface samples, is compared with Gaussian and exponential correlation functions with the same correlation length. Within the mainlobe of the correlation function (small displacements), the actual correlation function is very similar to the Gaussian function; however, the tail of the correlation function is very much different from

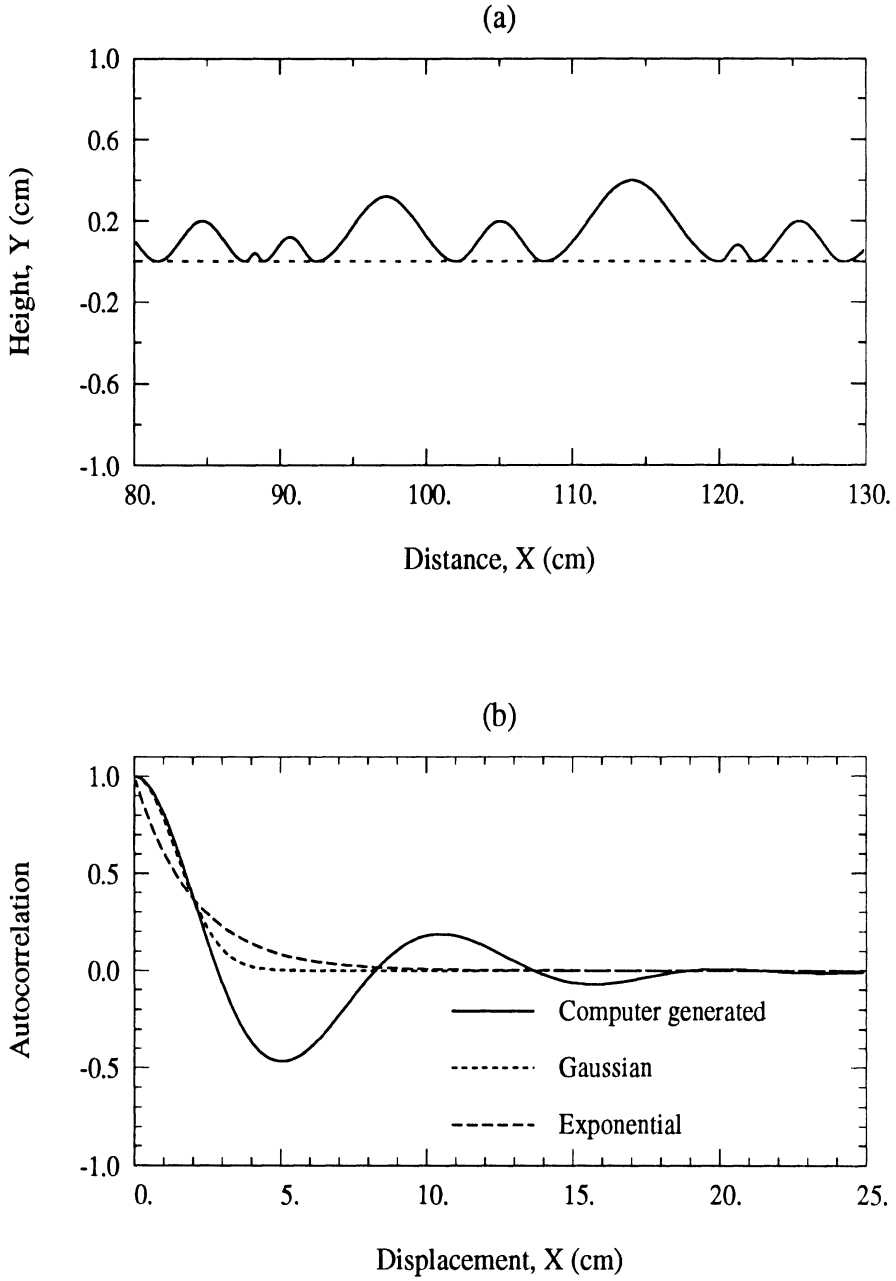

Figure 5.7: A random surface generated using squared-cosine humps, (a) a sample surface profile, (b) the autocorrelation function of the surface as compared with a Gaussian and an exponential function with identical correlation length.

Table 5.2: Constants used in the numerical computations.

Case No.	Individual hump size				No. of humps for each surface segment	Length of surface segment (λ)	No. of segments for a surface
	Width		Height				
	min. (λ)	max. (λ)	min. (λ)	max. (λ)			
1	0.2	2.0	0.0066	0.066	40	44	100
2	0.36	3.6	0.012	0.120	40	79	100
3	0.7	7.0	0.023	0.233	40	154	100

the Gaussian function. The correlation function of this surface is very similar to the correlation functions determined from measured height profiles of natural rough surfaces [Oh et al., 1992].

The backscattering coefficients for the surface at 5 GHz with $ks = 0.12$ and $kl = 2.13$ (Case 1 in Table 5.1) are computed by the Monte Carlo simulation technique for a homogeneous surface with $\epsilon_1 = \epsilon_2 = 15 + i3$ (Fig. 5.3(b)), and compared with the analytical results based on the SPM as shown in Figs. 5.8(a) and (b). For the SPM solution, the scattering coefficient σ° is proportional to the roughness spectrum (Fourier transform of the correlation function). Both the actual and Gaussian correlation functions are used in the calculation of the backscattering coefficients using the SPM. It is shown that the Monte Carlo simulation agrees very well with the SPM prediction when the actual correlation function is used. The discrepancies between the Monte Carlo simulation and the SPM with Gaussian correlation function indicate the importance of the tail section of the correlation function in the estimation of σ^c.

Using the first-order SPM solution [Ulaby et al., 1982; Tsang et al., 1982], it

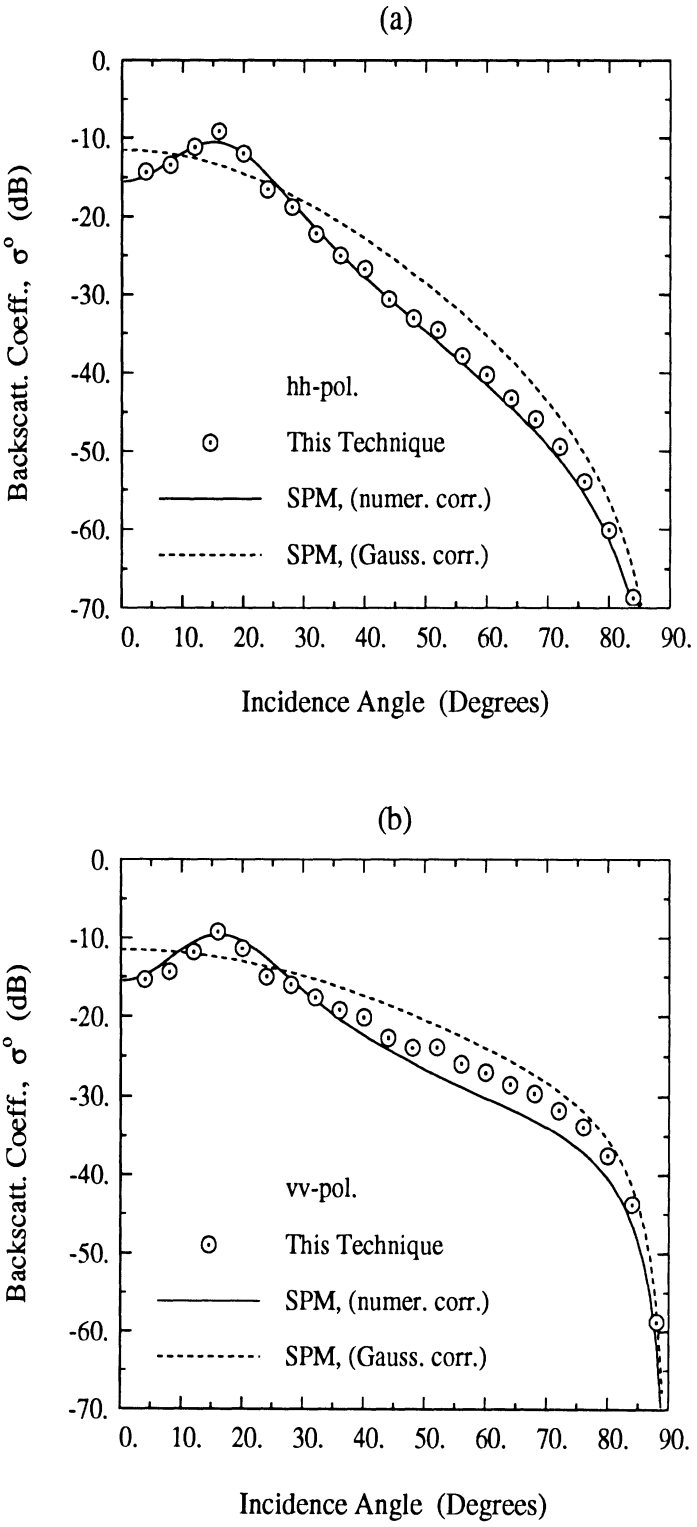

Figure 5.8: Backscattering coefficient σ° of the random surface with $ks = 0.12$, $kl = 2.13$, and $\epsilon_1 = \epsilon_2 = 15 + i3$ as computed by the SPM and the numerical technique; (a) HH-polarization and (b) VV-polarization.

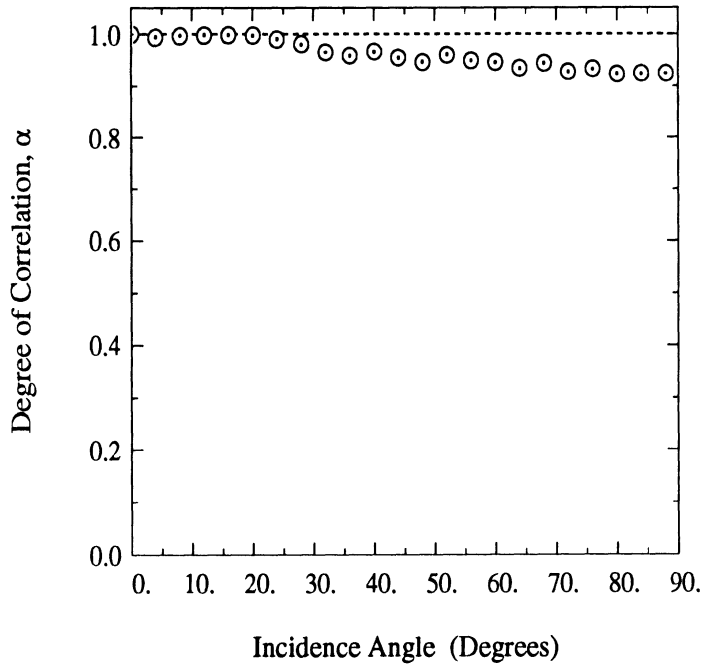

Figure 5.9: Degree of correlation α of the random surface with $ks = 0.12$, $kl = 2.13$, and $\epsilon_1 = \epsilon_2 = 15 + i3$.

can easily been shown that the degree of correlation (α) for the phase difference ($\phi_{vv} - \phi_{hh}$) is equal to unity (α=1). For the surface under consideration (case 1), Fig. 5.9 compares the values of co-polarized α computed using the numerical simulation with those derived from the SPM. The SPM is a first-order solution; hence, it predicts that the degree of correlation α between the HH- and VV- polarized scattering fields is always equal to unity (α=1). A plot of α, computed using the numerical simulation technique, is shown in Fig. 5.9. At small incidence angles ($\theta_i \leq 20°$), the degree of correlation $\alpha \approx 1$, and then it decreases slowly as θ_i increases. It should be noted that the measured angular response of α for smooth bare soil surfaces at L-band frequencies shows a similar trend [Sarabandi et al., 1992; Oh et al., 1993].

The numerical simulation was also performed for a surface at 5 GHz with $ks = 0.42$, $kl = 7.49$ (Case 3 in Table 5.1), and $\epsilon_1 = \epsilon_2 = 15 + i3$. The roughness

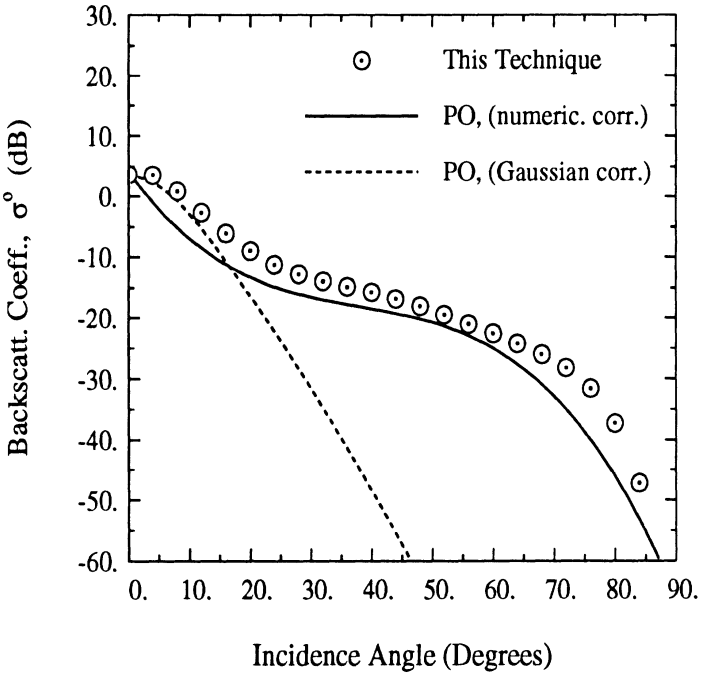

Figure 5.10: Backscattering coefficient σ° of the random surface with $ks = 0.42$, $kl = 7.49$, and $\epsilon_1 = \epsilon_2 = 15 + i3$ as computed by the PO model and the numerical technique for HH-polarization.

parameters of this surface fall within the validity region of the physical optics (PO) model; therefore the numerical solution can be compared with the PO solution. The scattering coefficient σ°_{hh} predicted by the PO model using the actual correlation function agrees very well with the results computed by the numerical technique, as shown in Fig. 5.10. In this figure the PO solution using a Gaussian correlation function with the same correlation length as the actual correlation function is also compared with the numerical simulation. It is shown that the agreement is good only for low incidence angles ($\theta_i \leq 20^\circ$) and the discrepancy between the two solutions becomes very significant for higher incidence angles. In this case, similar to the previous case (SPM), it is shown that the tail of the correlation function plays an important role in determining the angular patterns of the backscattering coefficients.

With the success of the Monte Carlo simulation in predicting the scattering be-

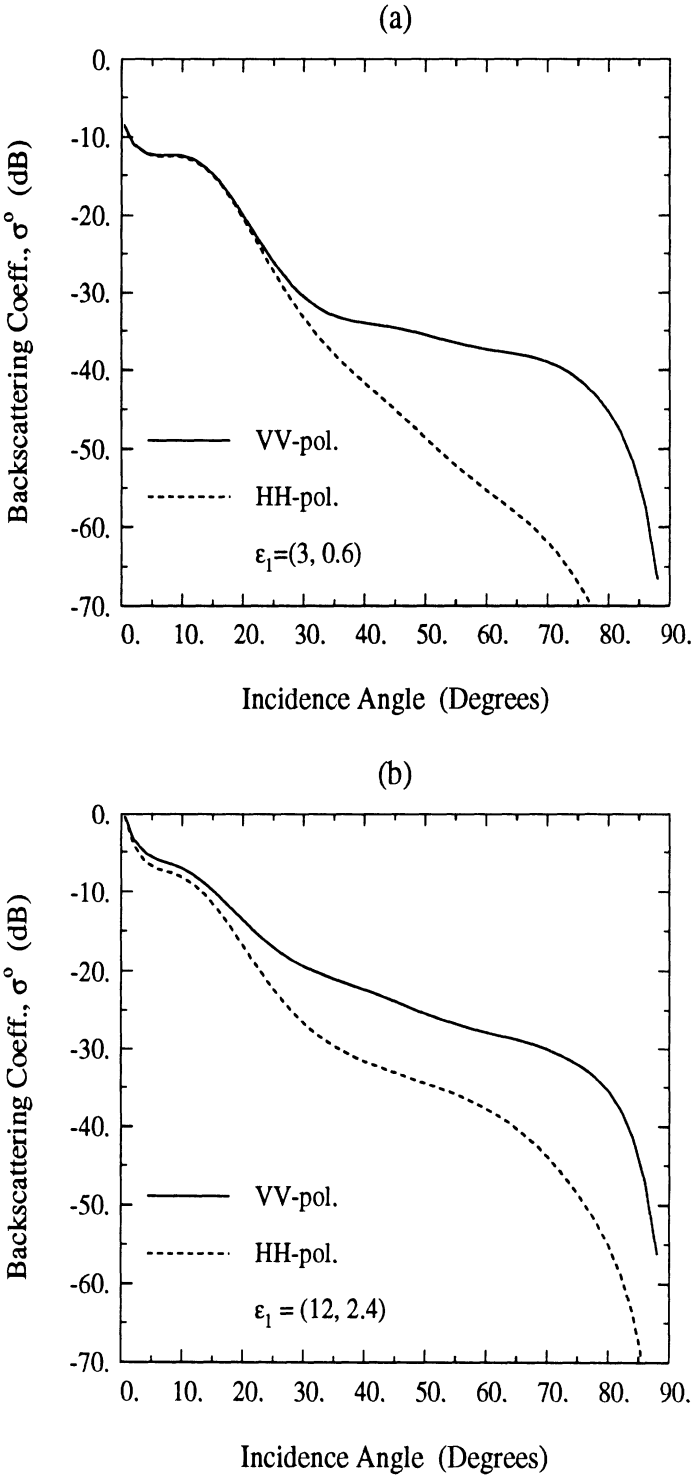

Figure 5.11: Backscattering coefficient σ° of the random surface with $ks = 0.22$, $kl = 3.8$, (a) $\epsilon_1 = 6 + i0.6$ and $\epsilon_2 = 15 + i3$, (b) $\epsilon_1 = 12 + i2.4$ and $\epsilon_2 = 15 + i3$ for VV- and HH-polarizations.

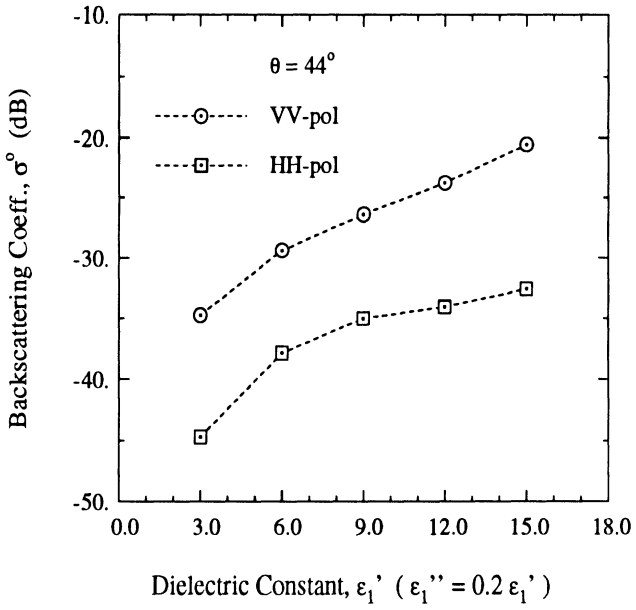

Figure 5.12: The sensitivity of the backscattering coefficient σ° to the dielectric constant, in case of $ks = 0.22$, $kl = 3.8$, and $\epsilon_2 = 15 + i3$ at $\theta = 44^\circ$.

havior of rough surfaces in the small perturbation and physical optics regions, the numerical model can be used to study complex surfaces with intermediate roughness parameters and inhomogeneous dielectric profiles. For example, consider an inhomogeneous surface at 5 GHz with $ks = 0.22$ and $kl = 3.80$ (Case 2 in Table 5.1). Figures 5.11(a) and 10 (b) show the backscattering coefficients of the surface for both polarizations with $\epsilon_2 = 15+i3$ and two values of ϵ_1, namely $\epsilon_1 = 3+i0.6$ and $\epsilon_1 = 12+i2.4$. To demonstrate the sensitivity of radar backscatter to the moisture content of the top layer, the scattered fields for three other surfaces with $\epsilon_1 = 6+i1.2$, $\epsilon_1 = 9+i1.8$, and $\epsilon_1 = 15 + i3$ were also computed. The backscattering coefficients σ° and the degree of correlation α are shown in Figs. 5.12 and 5.13, respectively, as functions of the dielectric constants ϵ_1 at $\theta = 44^\circ$. We note that the scattering coefficients, σ°_{vv} and σ°_{hh}, as well as the ratio of $\sigma^\circ_{vv}/\sigma^\circ_{hh}$, increase as the dielectric constant increases. The degree of correlation α also shows sensitivity to the dielectric constant of the surface;

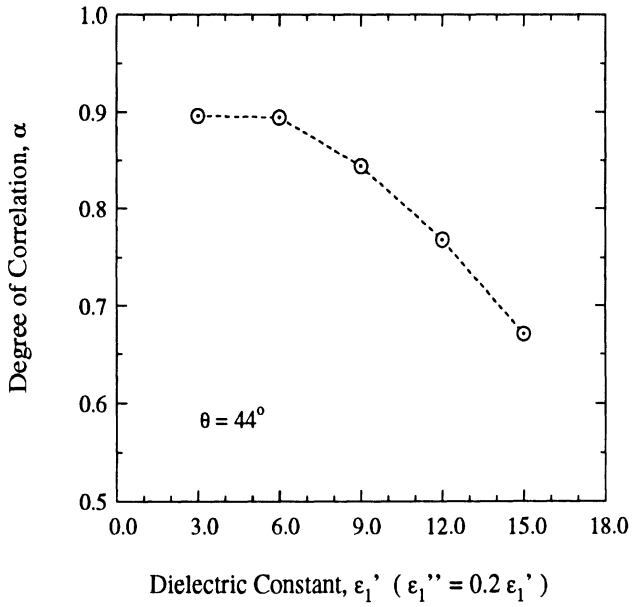

Figure 5.13: The sensitivity of the degree of correlation α to the dielectric constant in case of $ks = 0.22$, $kl = 3.8$, and $\epsilon_2 = 15 + i3$ at $\theta = 44°$.

i.e., α decreases as ϵ_1 increases. All of these trends are in line with experimental observations [Oh et al., 1992; Oh et al., 1993].

5.5 Conclusions

In this chapter an efficient Monte Carlo simulation technique is proposed for computing electromagnetic scattering by inhomogeneous one-dimensional rough surfaces. The surface irregularities are represented by inhomogeneous dielectric humps of different shapes and the underlying layer is represented by an impedance surface. A moment-method procedure, in conjunction with the exact image theory, is used for calculation of the field scattered by the dielectric humps. It was shown that the scattered field near the impedance surface is weak , and hence the effect of multiple scattering between humps can be ignored.

To check the validity of the Monte Carlo simulation, the numerical results were compared with the existing analytical solutions for surfaces at extreme roughness con-

ditions. A smooth surface that satisfies the validity region of the SPM and a surface that satisfies the validity region of the PO model were considered, and in both cases excellent agreement was obtained between the analytical results and those computed using the proposed technique. It was found that away from normal incidence the tail of the correlation function plays an important role in the determination of the backscattering coefficients.

The analysis presented in this chapter is only for one-dimensional surfaces and therefore is incapable of predicting the cross-polarized scattering coefficients. A numerical simulation for a two-dimensional rough surface using a similar method is computationally tractable.

CHAPTER VI

MEASUREMENT PROCEDURE - RADAR CALIBRATION FOR DISTRIBUTED TARGETS

6.1 Introduction

The recent interest in radar polarimetry has led to the development of several calibration techniques to retrieve the Mueller matrix of a distributed target from the multi-polarization backscatter measurements recorded by the radar system. Because a distributed target is regarded as a statistically uniform random medium, the measurements usually are conducted for a large number of independent samples (usually spatially independent locations), from which the appropriate statistics characterizing the elements of the Mueller matrix can be derived. Existing calibration methods rely on two major assumptions. The first is that the illuminated area of the distributed target is regarded as a single equivalent point target located along the antenna's boresight direction, and that the statistics of the scattering from all of the measured equivalent point targets (representing the spatially independent samples observed by the radar) are indeed the same as the actual scattering statistics of the distributed target. The second assumption pertains to the process by which the actual measurements made by the radar for a given illuminated area are transformed into the

scattering matrix of that area. The process involves measuring the radar response of a point calibration target of known scattering matrix, located along the boresight direction of the antenna, and then modifying the measured response by a constant, known as the illumination integral, when observing the distributed target. The illumination integral accounts for only magnitude variations of the illuminating fields. Thus, possible phase variations or antenna cross-talk variations (between orthogonal polarization channels) across the beam are totally ignored, which may compromise the calibration accuracy. To rectify this deficiency of existing calibration techniques, a new technique is proposed with which the radar polarization distortion matrix is characterized completely by measuring the polarimetric response of a sphere over the entire main lobe of the antenna, rather than along only the boresight direction. Additionally, the concept of a "differential Mueller matrix" is introduced, and by defining and using a correlation-calibration matrix derived from the measured radar distortion matrices, the differential Mueller matrix is accurately calibrated. Comparison of data based on the previous and the new techniques shows significant improvement in the measurement accuracy of the co-polarized and cross-polarized phase difference statistics.

The literature contains a variety of different methods for measuring the backscattering cross section of point targets. In all cases, however, the calibration part of the measurement process involves a comparison of the measured radar response due to the unknown target with the measured response due to a calibration target of known radar cross section. Under ideal conditions, both the unknown and calibration targets are placed along the antenna boresight direction, thereby insuring that both targets are subjected to the same illumination by the radar antenna. The situation is markedly different for distributed targets; the unknown distributed target

is illuminated by the full antenna beam, whereas the calibration target – being of necessity a point target – is illuminated by only a narrow segment of the beam centered around the boresight direction. Consequently, both the magnitude and phase variations across the antenna pattern become part of the measurement process.

Accurate calibration of polarimetric radar systems is essential for extracting accurate biophysical information of earth terrain. The concept and formulation of polarimetric calibration were developed by Barnes [Barnes, 1986], who used three in-scene calibration targets. Many other polarimetric calibration techniques were reported, including the generalized calibration technique (GCT) [Whitt et al, 1991], the isolated-antenna calibration technique (IACT) [Sarabandi et al, 1990], and the single-target calibration technique (STCT) [Sarabandi and Ulaby, 1991]. The phase variation across the antenna pattern, however, has been ignored among those calibration techniques while the magnitude variation usually is taken into account through a calculation of the illumination integral [Ulaby et al., 1982; Sarabandi et al., 1991; Tassoudji et al., 1989; and Ulaby and Elachi, 1990]. The role of this phase variation across the beam with regard to polarimetric radar measurements and the means for taking it into account in the measurement process are the subject of this paper.

Terrain Surfaces, including vegetation-covered and snow-covered ground, are treated as random media with statistically uniform properties. In radar measurements, the quantities of interest are the statistical properties of the scattered field per unit area. One such quantity is the scattering coefficient σ°, which is defined in terms of the second moment of the scattered field:

$$\sigma^\circ = \lim_{r\to\infty} \lim_{A\to\infty} \frac{4\pi r^2}{A} \cdot \frac{<|\, E^s \,|^2>}{|\, E^i \,|^2}$$

where E^i and E^s are the incident and scattered fields, A is the illuminated area, and r is the range between the target area and the observation point. The above definition of

σ° is based on the assumption that the target is illuminated by a plane wave. Although in practice such a condition cannot be absolutely satisfied, it can be approximately satisfied under certain circumstances. The correlation length ℓ of a distributed target represents the distance over which two points are likely to be correlated, implying that the currents induced at the two points due to an incident wave will likely be correlated as well. Thus, the correlation length may serve as the effective dimension of individual scatterers comprising the distributed target. The plane-wave approximation may be considered valid so long as the magnitude and phase variations of the incident wave are very small across a distance of several correlation lengths. In most practical situations, this "local" plane-wave approximation is almost always satisfied. When this is not the case, the measured radar response will depend on both the illumination pattern and the statistics of the distributed target [Eom and Boerner, 1991; Fung and Eom, 1983].

An implied assumption in the preceding discussion is that the phase variation across the antenna beam is the same for both the transmit and receive antennas. When making polarimetric measurements with dual-polarized transmit and receive antennas, the phase variation of the transmit and receive patterns may be different, which may lead to errors in the measurement of the scattering matrix of the target, unless the variations are known for all of the polarization combinations used in the measurement process and they are properly accounted for in the calibration process.

In this paper, we introduce a calibration procedure that accounts for magnitude and phase imbalances and antenna cross-talk across the entire main beam of the antenna. By applying this procedure, we can make accurate measurements of the differential Mueller matrix of a distributed target using the local plane-wave approximation. The differential Mueller matrix can then be used to compute the scattering

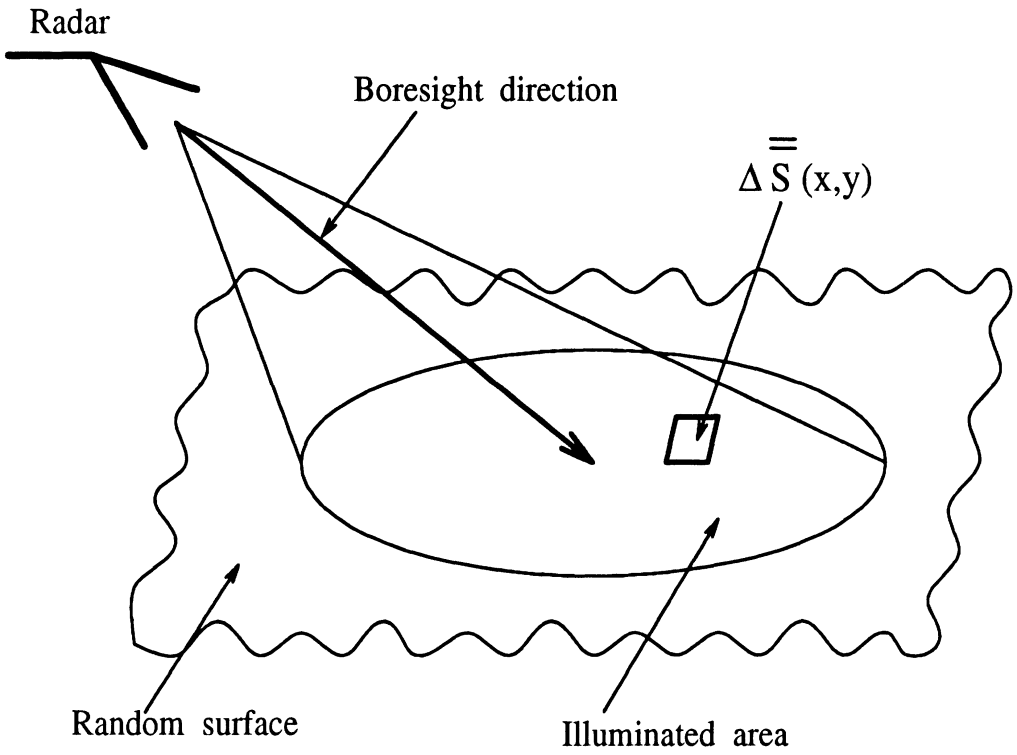

Figure 6.1: Geometry of a radar system illuminating a homogeneous distributed target.

coefficient for any desired combination of receive and transmit antenna polarizations, and by employing a recently developed technique [Sarabandi, 1992], the statistics of the polarization phase differences can also be obtained. By way of illustrating the utility of the proposed measurement technique, we will compare the results of backscatter measurements acquired by a polarimetric scatterometer system for bare soil surfaces using the new technique with those based on calibrating the system with the traditional approach which relies on measuring the response due to a calibration target placed along only the boresight direction of the antenna beam.

6.2 Theory

Consider a planar distributed target illuminated by a polarimetric radar system as shown in Figure 6.1. Suppose the distributed target is statistically homogeneous

and the antenna beam is narrow enough so that the backscattering statistics of the target can be assumed constant over the illuminated area. Let us subdivide the illumination area into a finite number of pixels, each including many scatterers (or many correlation lengths) and denote the scattering matrix of the ijth pixel by $\Delta\overline{\overline{\mathbf{S}}}(x_i, y_j)$. The scattering matrix of each pixel can be considered as a complex random vector. If the radar system and its antenna are ideal, the scattered field associated with the ijth pixel is related to the incident field by

$$\begin{bmatrix} E_v^s \\ E_h^s \end{bmatrix} = K\frac{e^{2ik_0r(x_i,y_j)}}{r(x_i,y_j)^2}\begin{bmatrix} \Delta S_{vv}(x_i,y_j) & \Delta S_{vh}(x_i,y_j) \\ \Delta S_{hv}(x_i,y_j) & \Delta S_{hh}(x_i,y_j) \end{bmatrix}\begin{bmatrix} E_v^i \\ E_h^i \end{bmatrix} \tag{6.1}$$

where E_v and E_h are the components of the electric field along two orthogonal directions in a plane perpendicular to the direction of propagation, and K is a constant. In reality, radar systems are not ideal in the sense that the vertical and horizontal channels of the transmitter and receiver are not identical and the radar antenna introduces some coupling between the vertical and horizontal signals at both transmission and reception. Consequently, the measured scattering matrix $\overline{\overline{\mathbf{U}}}$ is related to the actual scattering matrix of a point target $\overline{\overline{\mathbf{S}}}$ by [Sarabandi and Ulaby, 1990]

$$\overline{\overline{\mathbf{U}}} = \frac{e^{2ik_0r}}{r^2}\overline{\overline{\mathbf{R}}}\,\overline{\overline{\mathbf{S}}}\,\overline{\overline{\mathbf{T}}} \tag{6.2}$$

where $\overline{\overline{\mathbf{R}}}$ and $\overline{\overline{\mathbf{T}}}$ are known as the receive and transmit distortion matrices. For small point targets where the illumination pattern of the incident field can be approximated by a uniform plane wave, measurement of $\overline{\overline{\mathbf{S}}}$ is rather straightforward and in recent years this problem has been investigated thoroughly by many investigators [Barnes, 1986; Whitt et al., 1991; Sarabandi et al., 1990]. The distortion matrices are obtained by measuring one or more targets of known scattering matrices, and then by inverting (6.2) the scattering matrix of the unknown target is obtained. In the case of

distributed targets, however, distributed calibration targets do not exist. Moreover, the distortion matrices and the distance to the scattering points are all functions of position. That is for the ijth pixel the measured differential scattering matrix $\Delta\overline{\overline{\mathbf{U}}}$ can be expressed by

$$\Delta\overline{\overline{\mathbf{U}}} = \frac{e^{2ik_0r(x_i,y_j)}}{r^2(x_i,y_j)}\overline{\overline{\mathbf{R}}}(x_i,y_j)\begin{bmatrix} \Delta S_{vv}(x_i,y_j) & \Delta S_{vh}(x_i,y_j) \\ \Delta S_{hv}(x_i,y_j) & \Delta S_{hh}(x_i,y_j) \end{bmatrix}\overline{\overline{\mathbf{T}}}(x_i,y_j) \tag{6.3}$$

The radar measures the sum of fields backscattered from all pixels within the illuminated area coherently; i.e.,

$$\overline{\overline{\mathbf{U}}} = \sum_i\sum_j \frac{e^{2ik_0r(x_i,y_j)}}{r^2(x_i,y_j)}\overline{\overline{\mathbf{R}}}(x_i,y_j)\ \Delta\overline{\overline{\mathbf{S}}}(x_i,y_j)\ \overline{\overline{\mathbf{T}}}(x_i,y_j) \tag{6.4}$$

Thus, the measured scattering matrix is a linear function of the random scattering matrices of the pixels. For uniform distributed targets, we are interested in deriving information about the statistics of the differential scattering matrix from statistics of the measured scattering matrix $\overline{\overline{\mathbf{U}}}$. One step in relating the desired quantities to the measured ones is to perform a calibration procedure to remove the distortions caused by the radar and the antenna systems. The traditional approach used for calibrating polarimetric measurements of extended-area targets relies on two approximations. First, it is assumed that for each measured sample, the differential scattering matrix of the illuminated area is equal to some equivalent scattering matrix at boresight. Using this approximation it is hoped that the equivalent scattering matrix has the same statistics as the original differential scattering matrix. This approximation is purely heuristic and cannot be justified mathematically. Second, the measured data for each sample is calibrated as if it were a point target and the result is modified by a constant known as the illumination integral to account for the non-uniform illumination [Tassoudji et al, 1989; Ulaby and Elachi, 1990]; thus, the cross-talk

variations away from the antenna's boresight direction over the illuminated area are ignored. The illumination integral accounts for only magnitude variations of the gain patterns of the transmitter and receiver antennas, and no provision is made for accounting for any possible phase variations in the radiation patterns.

In this paper we attempt to derive the second moments of the differential scattering matrix from the statistics of the measured matrix without making any approximation in the radar distortion matrices or using the equivalent differential scattering matrix representation. In random polarimetry, the scattering characteristics of a distributed target usually are represented by its Mueller matrix, which is the averaged Stokes matrix [Ulaby and Elachi, 1990]. The Mueller matrix contains the second moments of the the scattering matrix elements. By the central limit theorem, if the scatterers in the illuminated area are numerous and are of the same type, then the statistics describing the scattering is Gaussian (Rayleigh statistics). In such cases, knowledge of the Mueller matrix is sufficient to describe the scattering statistics of the target [Sarabandi, 1992].

In a manner analogous with the definition of the scattering coefficient as the scattering cross section per unit area, let us define the differential Mueller matrix $\overline{\overline{\mathbf{M}}}^{\circ}$ as the ratio of the the Mueller matrix ($\Delta\overline{\overline{\mathbf{M}}}$) derived from the differential scattering matrix ($\Delta\overline{\overline{\mathbf{S}}}$) to the differential area; i.e.,

$$\overline{\overline{\mathbf{M}}}^{\circ} = \lim_{\Delta A \to 0} \frac{\Delta\overline{\overline{\mathbf{M}}}}{\Delta A}$$

To compute the differential Mueller matrix, the ensemble average of the cross products

of the differential matrix components are needed. Let us define

$$\overline{\overline{\mathbf{W}}}^{\circ} = \begin{bmatrix} < S_{vv}^{\circ *} S_{vv}^{\circ} > & < S_{vh}^{\circ *} S_{vh}^{\circ} > & < S_{vh}^{\circ *} S_{vv}^{\circ} > & < S_{vv}^{\circ *} S_{vh}^{\circ} > \\ < S_{hv}^{\circ *} S_{hv}^{\circ} > & < S_{hh}^{\circ *} S_{hh}^{\circ} > & < S_{hh}^{\circ *} S_{hv}^{\circ} > & < S_{hv}^{\circ *} S_{hh}^{\circ} > \\ < S_{hv}^{\circ *} S_{vv}^{\circ} > & < S_{hh}^{\circ *} S_{vh}^{\circ} > & < S_{hh}^{\circ *} S_{vv}^{\circ} > & < S_{hv}^{\circ *} S_{vh}^{\circ} > \\ < S_{vv}^{\circ *} S_{hv}^{\circ} > & < S_{vh}^{\circ *} S_{hh}^{\circ} > & < S_{vh}^{\circ *} S_{hv}^{\circ} > & < S_{vv}^{\circ *} S_{hh}^{\circ} > \end{bmatrix} \tag{6.5}$$

where

$$< S_{pq}^{\circ *} S_{st}^{\circ} >= \lim_{\Delta A \to 0} \frac{< \Delta S_{pq}^{*} \Delta S_{st} >}{\Delta A}$$

In terms of the correlation matrix $\overline{\overline{\mathbf{W}}}^{\circ}$, the differential Mueller matrix can be computed from

$$\overline{\overline{\mathbf{M}}}^{\circ} = 4\pi\nu\overline{\overline{\mathbf{W}}}^{\circ}\,\nu^{-1} \tag{6.6}$$

where [Ulaby and Elachi, 1990]

$$\nu = \begin{pmatrix} 1 & 0 & 0 & 0 \\ 0 & 1 & 0 & 0 \\ 0 & 0 & 1 & 1 \\ 0 & 0 & -i & i \end{pmatrix}$$

In order to calibrate a radar system so as to measure the differential Mueller matrix, let us represent each 2×2 matrix in (6.4) by a corresponding four-component vector, in which case (6.4) simplifies to

$$\overline{U} = \sum_i \sum_j \frac{e^{2ik_0 r(x_i, y_j)}}{r^2(x_i, y_j)} \overline{\overline{\mathbf{D}}}(x_i, y_j) \overline{\Delta \mathcal{S}}(x_i, y_j) \tag{6.7}$$

where

$$\overline{U} = \begin{bmatrix} U_{vv} \\ U_{vh} \\ U_{hv} \\ U_{hh} \end{bmatrix}, \qquad \overline{\Delta \mathcal{S}}(x_i, y_j) = \begin{bmatrix} \Delta S_{vv}(x_i, y_j) \\ \Delta S_{vh}(x_i, y_j) \\ \Delta S_{hv}(x_i, y_j) \\ \Delta S_{hh}(x_i, y_j) \end{bmatrix}, \tag{6.8}$$

$$\overline{\mathcal{R}}(x_i,y_j)=\begin{bmatrix} R_{vv}(x_i,y_j)\\ R_{vh}(x_i,y_j)\\ R_{hv}(x_i,y_j)\\ R_{hh}(x_i,y_j)\end{bmatrix},\overline{\mathcal{T}}(x_i,y_j)=\begin{bmatrix} T_{vv}(x_i,y_j)\\ T_{vh}(x_i,y_j)\\ T_{hv}(x_i,y_j)\\ T_{hh}(x_i,y_j)\end{bmatrix},$$

and it can be easily shown that

$$\overline{\overline{\mathbf{D}}}(x_i,y_j)=\begin{bmatrix} R_{vv}T_{vv} & R_{vv}T_{vh} & R_{vh}T_{vv} & R_{vh}T_{vh}\\ R_{vv}T_{hv} & R_{vv}T_{hh} & R_{vh}T_{hv} & R_{vh}T_{hh}\\ R_{hv}T_{vv} & R_{hv}T_{vh} & R_{hh}T_{vv} & R_{hh}T_{vh}\\ R_{hv}T_{hv} & R_{hv}T_{hh} & R_{hh}T_{hv} & R_{hh}T_{hh}\end{bmatrix} \tag{6.9}$$

The m^{th} component of the measured target vector ($\overline{\mathcal{U}}_m$) defined by (6.8) can be obtained from (6.7) and is given by

$$\mathcal{U}_m=\sum_i\sum_j\frac{e^{2ik_0r(x_i,y_j)}}{r^2(x_i,y_j)}\left[\sum_{\ell=1}^{4}D_{m\ell}(x_i,y_j)\Delta\mathcal{S}_\ell(x_i,y_j)\right]$$

Thus, the averaged cross products of these components are

$$<\mathcal{U}_m\mathcal{U}_n^*>=\sum_i\sum_j\sum_{i'}\sum_{j'}\frac{e^{2ik_0[r(x_i,y_j)-r(x_{i'},y_{j'})]}}{r^2(x_i,y_j)r^2(x_{i'},y_{j'})}\sum_{\ell=1}^{4}\sum_{p=1}^{4}D_{m\ell}(x_i,y_j)D_{np}^*(x_{i'},y_{j'})$$
$$<\Delta\mathcal{S}_\ell(x_i,y_j)\Delta\mathcal{S}_p^*(x_{i'},y_{j'})> \tag{6.10}$$

If the number of scatterers in each pixel is assumed to be large, or the correlation length of the surface is much smaller than the pixel dimensions, then

$$<\Delta\mathcal{S}_\ell(x_i,y_j)\Delta\mathcal{S}_p^*(x_{i'},y_{j'})>=\begin{cases}0 & i\neq i' \text{ and } j\neq j'\\ <\mathcal{S}_\ell^\circ\mathcal{S}_p^{\circ *}>\Delta A_{ij} & i=i' \text{ and } j=j'\end{cases}$$

It should be mentioned here again that the target is assumed to be statistically homogeneous and the antenna beam is assumed to have a narrow beam. Hence $<\mathcal{S}_\ell^\circ\mathcal{S}_p^{\circ *}>$ is not a function of position within the illuminated area. In the limit as

ΔA approaches zero, (6.10) takes the following form

$$< \mathcal{U}_m \mathcal{U}_n^* >= \sum_{\ell=1}^{4} \sum_{p=1}^{4} \left[\iint_A \frac{1}{r^4(x,y)} D_{m\ell}(x,y) D_{np}^*(x,y) dx dy \right] < \mathcal{S}_\ell^\circ \mathcal{S}_p^{\circ *} > \qquad (6.11)$$

Equation (6.11) is valid for all combinations of m and n and, therefore, it constitutes 16 equations for the 16 correlation unknowns. Let us denote the measured correlations by a 16-component vector $\overline{\mathcal{Y}}$ and the actual correlations by another 16-component vector $\overline{\mathcal{X}}$ so that

$$\mathcal{X}_i =< \mathcal{S}_\ell^\circ \mathcal{S}_p^{\circ *} > \;\; ; \; i = 4(\ell - 1) + p$$

$$\mathcal{Y}_j =< \mathcal{U}_m \mathcal{U}_n^* > \;\; ; \; j = 4(m - 1) + n$$

In this form, (6.11) reduces to the following matrix equation

$$\overline{\mathcal{Y}} = \overline{\overline{\mathbf{B}}} \;\; \overline{\mathcal{X}} \qquad (6.12)$$

where the ij element of $\overline{\overline{\mathbf{B}}}$ is given by

$$b_{ij} = \iint_A \frac{1}{r^4(x,y)} D_{m\ell}(x,y) D_{np}^*(x,y) dx dy \qquad (6.13)$$

and as before,

$$i = 4(\ell - 1) + p \;\; ; \;\; j = 4(m - 1) + n$$

Once the elements of the correlation calibration matrix $\overline{\overline{\mathbf{B}}}$ are found from (6.13), equation (6.12) can be inverted to obtain the correlation vector $\overline{\mathcal{X}}$. The elements of the correlation vector are not arbitrary complex numbers; for example, $\mathcal{X}_2$ and $\mathcal{X}_5$ are complex conjugate of each other and $\mathcal{X}_1$ is a real number; thus, these relationships can be used as a criterion for calibration accuracy. The differential Mueller matrix can be obtained from the correlation matrix $\overline{\overline{\mathbf{W}}}^\circ$ whose entries in terms of the vector

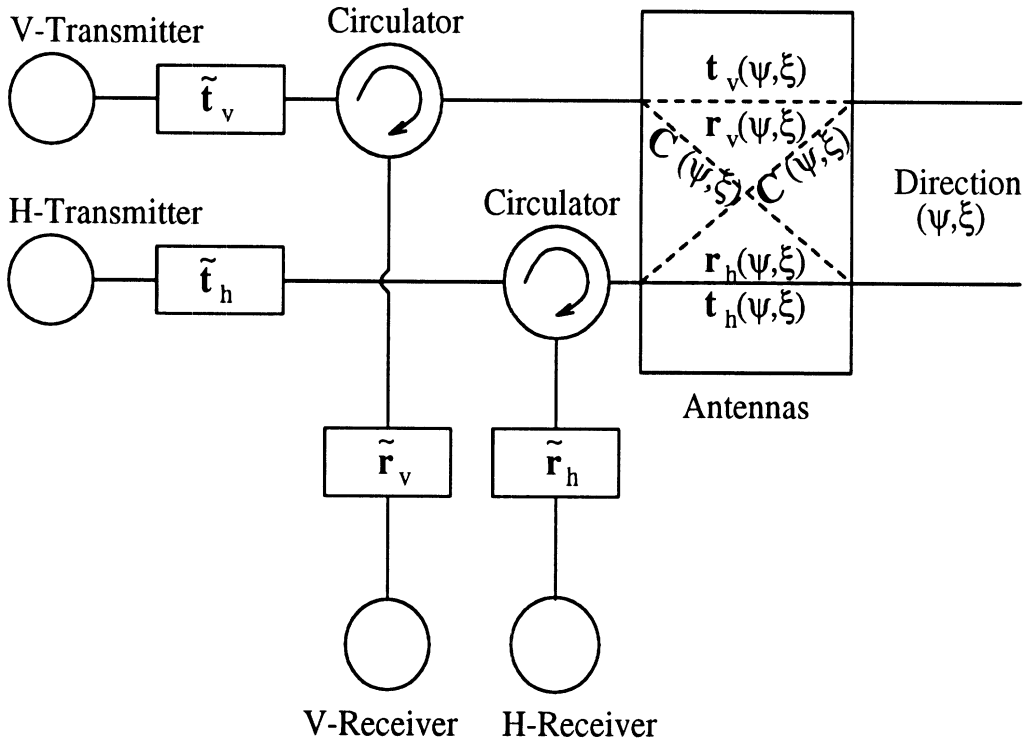

Figure 6.2: Simplified block diagram of a polarimetric radar system.

$\overline{\mathcal{X}}$ are given by

$$\overline{\overline{\mathbf{W}}}^{\circ} = \begin{bmatrix} \mathcal{X}_1 & \mathcal{X}_6 & \mathcal{X}_2 & \mathcal{X}_5 \\ \mathcal{X}_{11} & \mathcal{X}_{16} & \mathcal{X}_{12} & \mathcal{X}_{15} \\ \mathcal{X}_3 & \mathcal{X}_8 & \mathcal{X}_4 & \mathcal{X}_7 \\ \mathcal{X}_9 & \mathcal{X}_{14} & \mathcal{X}_{10} & \mathcal{X}_{13} \end{bmatrix}$$

Evaluation of the elements of $\overline{\overline{\mathbf{B}}}$ requires knowledge of the radar distortion matrices over the main lobe of the antenna system. The distortion matrices of the radar can be found by applying the calibration method presented in the next section.

6.3 Calibration Procedure

As was shown in the previous section, the correlation vector $\overline{\mathcal{X}}$ can be obtained if the calibration matrix $\overline{\overline{\mathbf{D}}}(x, y)$ given by (6.9) is known. A simplified block diagram of

a radar system is shown in Fig. 6.2. The quantities $\tilde{t}_v, \tilde{t}_h, \tilde{r}_v, \tilde{r}_h$ represent fluctuating factors of the channel imbalances caused by the active devices in the radar system. Without loss of generality, it is assumed that the nominal value of these factors is one and their rate of change determines how often the radar must be calibrated. The antenna system also causes some channel distortion due to variations in the antenna pattern and path length differences. The cross-talk contamination occurs in the antenna structure which is also a function of the direction of radiation. It has been shown that the antenna system, together with two orthogonal directions in a plane perpendicular to the direction of propagation, can be represented as a four-port passive network [Sarabandi ana Ulaby, 1990]. Using the reciprocity properties of passive networks, the distortion matrices of the antenna system were shown to be [Sarabandi ana Ulaby, 1990]

$$\overline{\overline{\mathcal{R}}}_a(\psi,\xi) = \begin{bmatrix} r_v(\psi,\xi) & 0 \\ 0 & r_h(\psi,\xi) \end{bmatrix} \begin{bmatrix} 1 & C(\psi,\xi) \\ C(\psi,\xi) & 1 \end{bmatrix} \tag{6.14}$$

$$\overline{\overline{\mathcal{T}}}_a(\psi,\xi) = \begin{bmatrix} 1 & C(\psi,\xi) \\ C(\psi,\xi) & 1 \end{bmatrix} \begin{bmatrix} t_v(\psi,\xi) & 0 \\ 0 & t_h(\psi,\xi) \end{bmatrix} \tag{6.15}$$

where ψ, ξ are some coordinate angles defined with respect to the boresight direction of propagation. The quantity $C(\psi,\xi)$ is the antenna cross-talk factor and $r_v(\psi,\xi)$, $r_h(\psi,\xi)$, $t_v(\psi,\xi)$, $t_h(\psi,\xi)$ are the channel imbalances caused by the antenna system. These quantities are not subject to change due to variations in active devices and once they are determined, they can be used repeatedly.

In order to find the radar distortion parameters at a given point (x,y) on the surface, we first need to specify a convenient coordinate system with respect to the antenna's boresight direction so that the distortions become independent of incidence

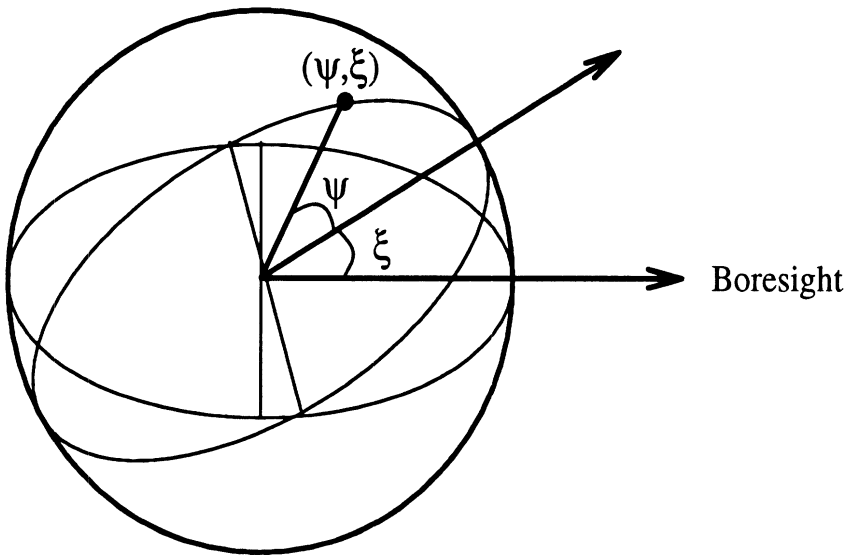

Figure 6.3: Azimuth-over elevation and elevation-over azimuth coordinate systems (ψ, ξ) specifying a point on the surface of a sphere.

angle and range to the target. The azimuth-over-elevation and elevation-over-azimuth coordinate angles (ψ, ξ) provide a coordinate system that is appropriate for antenna pattern measurements. The angle ξ specifies the elevation angle and ψ specifies the azimuth angle in a plane with elevation ξ as shown in Fig. 6.3. The mapping from (ψ, ξ) coordinates to (x, y) coordinates can be obtained by considering a radar at height h with incidence angle θ_0 and the boresight direction in the $y-z$ plane as shown in Figs. 6.4(a) and (b) for azimuth-over-elevation and elevation-over-azimuth coordinate systems, respectively. It is easy to show that constant-ξ curves on surface of a sphere map to constant-y lines and constant-ψ curves map to hyperbolic curves in case of azimuth-over-elevation coordinate system. The mapping functions are given by

$$x = \frac{h \tan \psi}{\cos(\theta_0 + \xi)},$$

(a)

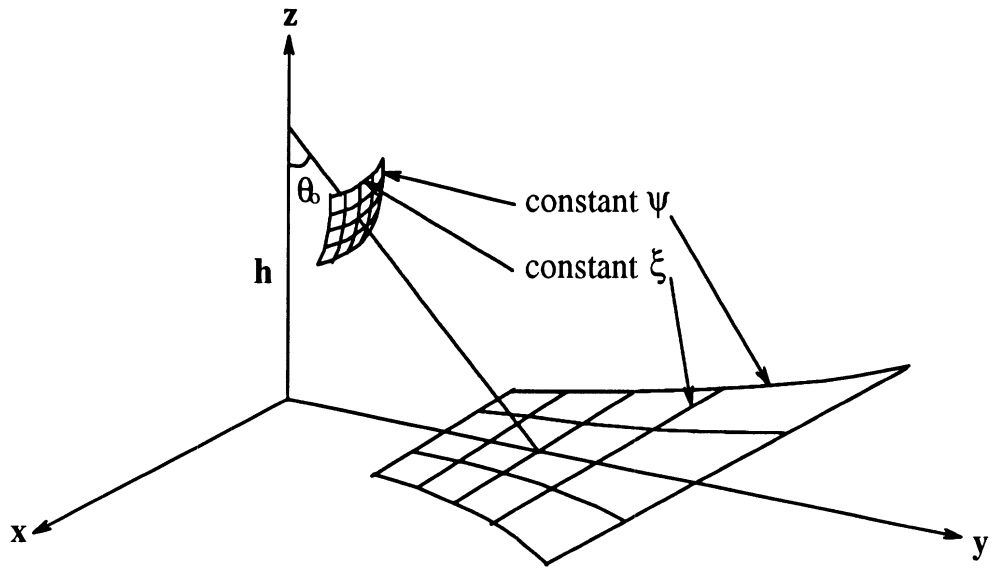

(b)

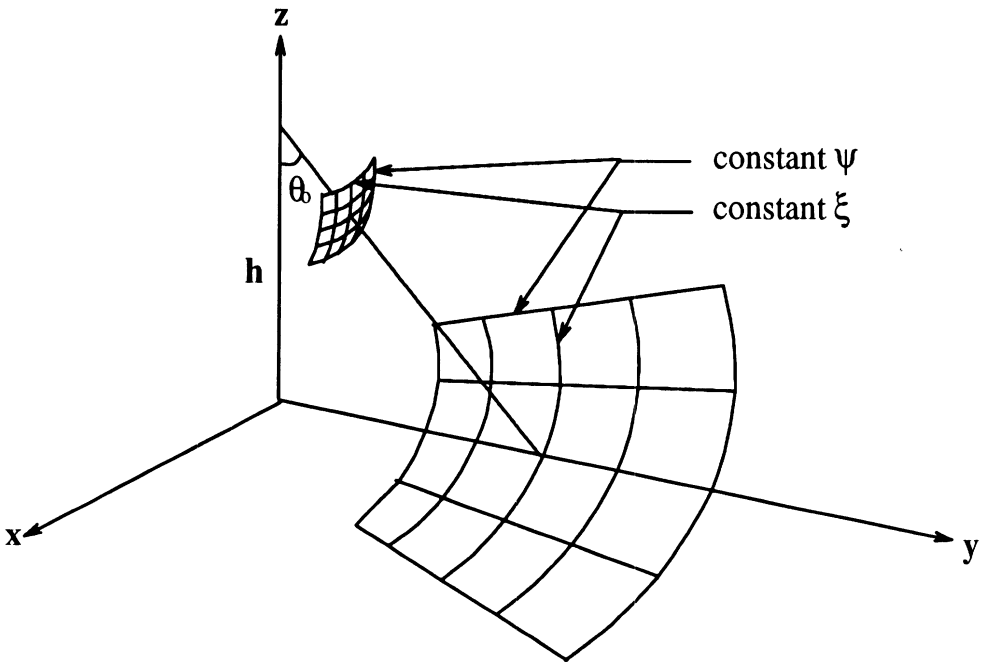

Figure 6.4: Geometry of a radar above x-y plane and transformation to cartesian coordinates from (a) azimuth-over-elevation coordinate and (b) elevation-over-azimuth coordinate .

$$y = h\tan(\theta_0 + \xi)$$

where $\psi = \xi = 0$ represents the boresight direction. For the elevation-over-azimuth coordinate system, constant-ξ curves on surface of a sphere map to elliptic curves and constant-ψ curves map to straight lines emitting from one of focus points of the ellipsoids, and the mapping functions are given by by

$$x = \frac{h\sin\psi}{\cos\theta_0\ \cos\psi\ -\ \sin\theta_0\ \tan\xi)},$$
$$y = \frac{h(\sin\theta_0\ \cos\psi\ +\ \cos\theta_0\ \tan\xi)}{\cos\theta_0\ \cos\psi\ -\ \sin\theta_0\ \tan\xi)}$$

The entries of the calibration matrix $\overline{\overline{\mathbf{D}}}(\psi,\xi)$ as defined by (6.9) should be obtained through a calibration procedure. Following the single target calibration technique given in [Sarabandi and Ulaby, 1990], a single sphere is sufficient to determine the channel imbalances as well as the antenna cross-talk factor for a given direction. Hence, by placing a sphere with radar cross section σ^s at a distance r_0 and a direction (ψ,ξ) with respect to the radar, the receive and transmit distortion parameters can be obtained as follows:

$$\begin{aligned}
R_{vv}T_{vv} &= r_0^2 e^{-2ik_0r_0}\frac{U^s_{vv}}{(1+C^2)\sqrt{\sigma^s/4\pi}} \\
\beta \triangleq \frac{R_{hh}}{R_{vv}} &= \frac{2C}{(1+C^2)}\frac{U^s_{hh}}{U^s_{vh}} = \frac{1+C^2}{2C}\frac{U^s_{hv}}{U^s_{vv}} \\
\alpha \triangleq \frac{T_{hh}}{T_{vv}} &= \frac{1+C^2}{2C}\frac{U^s_{vh}}{U^s_{vv}} \\
C &= \pm\frac{1}{\sqrt{a}}(1-\sqrt{1-a})
\end{aligned} \tag{6.16}$$

where

$$a \triangleq \frac{U^s_{vh}U^s_{hv}}{U^s_{vv}U^s_{hh}}$$

and $\overline{\overline{\mathbf{U}}}^s$ is the measured (uncalibrated) response of the sphere at a specific direction (ψ,ξ). In terms of the known quantities given by (6.16), the calibration matrix $\overline{\overline{\mathbf{D}}}$

can be written as

$$\overline{\overline{\mathbf{D}}}(\psi,\xi) = R_{vv}T_{vv}\begin{bmatrix} 1 & C\alpha & C & C^2\alpha \\ C & \alpha & C^2 & C\alpha \\ C\beta & C^2\alpha\beta & \beta & C\alpha\beta \\ C^2\beta & C\alpha\beta & C\beta & \alpha\beta \end{bmatrix} \tag{6.17}$$

where the dependencies on ψ and ξ of all parameters is understood.

In practice it is impossible to measure the sphere for all values of ψ and ξ within the desired domain; however, by discretizing the domain of ψ and ξ (main lobe) into sufficiently small subdomains over which the antenna characteristics are almost constant, the integral given by (6.13) can be evaluated with good accuracy.

Polarimetric measurement of a sphere over the entire range of ψ and ξ is very time consuming, and under field conditions performing these measurements seems impossible. However this measurement can be performed in an anechoic chamber with the desired resolution $\Delta\psi$ and $\Delta\xi$ only once, and then under field conditions we need to measure the sphere response only at boresight to keep track of variations in the active devices. Without loss of generality, let us assume that $\tilde{r}_v = \tilde{r}_h = \tilde{t}_v = \tilde{t}_h = 1$ for the sphere measurements when performed in the anechoic chamber, and that these quantities can assume other values for the measurements made under field conditions. If the measured distortion parameters at boresight (field condition) are denoted by prime and calculated from (6.16), then the channel imbalances corresponding to the field measurements are

$$\begin{aligned} \tilde{r}_v\tilde{t}_v &= (\frac{r_0'}{r_0})^2 e^{-2ik_0(r_0'-r_0)} \frac{R'_{vv}(0,0)T'_{vv}(0,0)}{R_{vv}(0,0),T_{vv}(0,0)} \\ \frac{\tilde{t}_h}{\tilde{t}_v} &= \frac{T'_{hh}(0,0)}{T'_{vv}(0,0)} \cdot \frac{T_{vv}(0,0)}{T_{hh}(0,0)} \\ \frac{\tilde{r}_h}{\tilde{r}_v} &= \frac{R'_{hh}(0,0)}{R'_{vv}(0,0)} \cdot \frac{R_{vv}(0,0)}{R_{hh}(0,0)}. \end{aligned} \tag{6.18}$$

Now the calibration matrix at any direction ($\overline{\overline{\mathbf{D}}}'(\psi,\xi)$) can be obtained from (6.17) by replacing $R_{vv}T_{vv}, \alpha$, and β by $R'_{vv}T'_{vv}, \alpha'$, and β' where

$$\begin{aligned} R'_{vv}T'_{vv} &= \tilde{r}_v\tilde{t}_v R_{vv}T_{vv} \\ \alpha' &= \frac{\tilde{t}_h}{\tilde{t}_v}\alpha \\ \beta' &= \frac{\tilde{r}_h}{\tilde{r}_v}\beta \ . \end{aligned} \tag{6.19}$$

Having found the calibration matrices for all subdomains, the element ij of the correlation-calibration matrix ($\overline{\overline{\mathbf{B}}}$), as given by (6.13) takes the following form

$$b_{ij} = \iint_{\Omega} D_{m\ell}(\psi,\xi) D^*_{np}(\psi,\xi) \frac{1}{r^4(\psi,\xi)} \left|J(x,y;\psi,\xi)\right| d\psi d\xi, \tag{6.20}$$

where Ω is the solid angle subtented by the illuminated area (main lobe of the antenna) and $J(x,y;\psi,\xi)$ is the Jacobian for the transformation of integral variables. Since $r(\psi,\xi)$ and $|J(x,y;\psi,\xi)|$ in the azimuth-over-elevation coordinate system are computed as, respectively,

$$\begin{aligned} r(\psi,\xi) &= \frac{h}{\cos\psi\cos(\theta_0+\xi)} \\ |J(x,y;\psi,\xi)| &= \frac{h^2}{\cos^2\psi\cos^3(\theta_0+\xi)}, \end{aligned}$$

the ijth element of the matrix $\overline{\overline{\mathbf{B}}}$ in (6.20) in the azimuth-over-elevation coordinate system is given by

$$b_{ij} = \iint_{\Omega} D_{m\ell}(\psi,\xi) D^*_{np}(\psi,\xi) \frac{\cos^2\psi\cos(\theta_0+\xi)}{h^2} d\psi d\xi. \tag{6.21}$$

In the elevation-over-azimuth coordinate system, $r(\psi,\xi)$ and $|J(x,y;\psi,\xi)|$ are computed as, respectively,

$$\begin{aligned} r(\psi,\xi) &= \frac{h}{\cos\xi\left(\cos\theta_0\cos\psi - \sin\theta_0\tan\xi\right)} \\ |J(x,y;\psi,\xi)| &= \frac{h^2}{\cos^2\xi\left|\left(\cos\theta_0\cos\psi - \sin\theta_0\tan\xi\right)^3\right|}, \end{aligned}$$

the ijth element of the matrix $\overline{\overline{\mathbf{B}}}$ in (6.20) in the elevation-over-azimuth coordinate system is given by

$$b_{ij} = \int\int_{\Omega} D_{m\ell}(\psi,\xi) D^{*}_{np}(\psi,\xi) \frac{\cos^2\xi |\cos\theta_0 \cos\psi - \sin\theta_0 \tan\xi)|}{h^2} d\psi d\xi. \qquad (6.22)$$

6.4 Experimental Procedure and Comparison

To demonstrate the performance of the new calibration technique, the polarimetric response of a random rough surface was measured by a truck-mounted L-, C-, and X-band polarimetric scatterometer with center frequencies at 1.25, 5.3 and 9.5 GHz.. Prior to these measurements, each scatterometer was calibrated in an anechoic chamber. The scatterometer was mounted on an azimuth-over-elevation positioner at one end of the chamber and a 36cm metallic sphere was positioned at the antenna boresight at a distance of 12m. Then the polarimetric response of the sphere was measured over the mainlobe of the antenna. The sphere measurements at L-band, which has the widest beam of the three systems, was performed over $(\psi, \zeta) \in [-21°, +21°]$ in steps of 3° and the ranges of (ψ, ζ) for C- and X-band were $\pm 10.5°$ and $\pm 7°$ with steps of 1.5° and 1°, respectively. To improve the signal to noise ratio by removing the background contribution, the chamber in the absence of the sphere was also measured for all values of ψ and ζ.

Figures 6.5(a) and (b) show the co- and cross-polarized responses of the sphere at X-band, and Figs. 6.5(c) and (d) show the co- and cross-polarized phase differences $(\phi_{hh} - \phi_{vv},\ \phi_{hv} - \phi_{vv})$. Similar patterns were obtained for L- and C-band. Using the sphere responses the correlation-calibration matrices were determined as outlined in the previous section.

To evaluate the improvement provided by the new calibration technique, we shall compare results of polarimetric observations of a bare soil surface processed using the

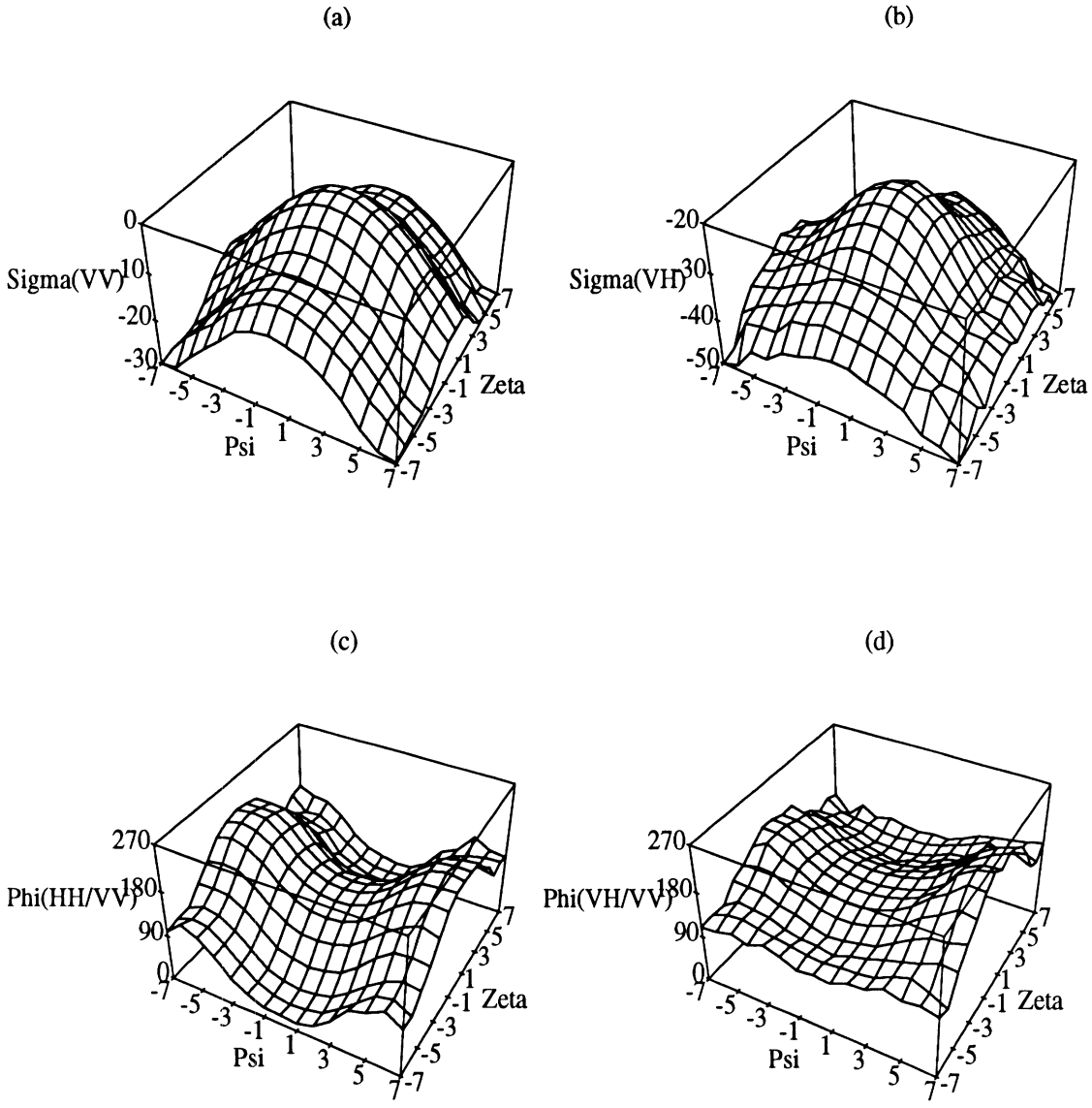

Figure 6.5: Polarimetric response of a metallic sphere over the entire mainlobe of X-band scatterometer; Normalize σ_{vv} (a) corresponds to G_v^2 and normalized σ_{vh} (b) corresponds to $G_v G_h$; Phase difference between co-polarized (c) and cross-polarized (d) components of the sphere response correspond to phase variation of the co- and cross-polarized patterns of the antenna.

new technique with those obtained previously on the basis of the boresight-only calibration technique. The data were acquired from a truck-mounted 17-m high platform for a rough surface with measured rms height of 0.56cm and correlation length of 8cm. The polarimetric backscatter response was measured as a function of incidence angle over the range $20° - 70°$. To reduce the effect of speckle on the measured data, 100 spatially independent samples were measured at each frequency and incidence angle. Also, the response of the sphere at boresight was measured to account for any possible changes in the active devices. The collected backscatter data was calibrated by the new and old methods. The first test of the new accuracy of the calibration algorithm was to make sure that the components of the correlation vector $\overline{\mathcal{X}}$ satisfy their mutual relationships as explained in the previous sections. For all cases, these relationships were found to be valid within $\pm 0.05\%$.

The second step in the evaluation process is the relative comparison of the backscattering coefficients and phase statistics derived from the two techniques. Figures 6.6(a)-(c) show the co- and cross-polarized backscattering coefficients as a function of incidence angle, calibrated by the old and the new methods. The differences in backscattering coefficients, as shown in these figures, are less than 0.75dB. It was found that the difference in backscattering coefficients is less than 1 dB for all frequencies and incidence angles. Although 1dB error in $\sigma°$ may seem negligible, in some cases, such as the variation with soil moisture content for which the total dynamic range of $\sigma°$ is about 5dB, the 1dB error becomes significant. Figure 6.6(d) shows the ratio of two cross-polarized scattering coefficients after calibration by each of the two methods. Theoretically this ratio must be one and independent of incidence angle. In this figure it is shown that the new calibration method more closely agrees with theoretical expectations than the old method.

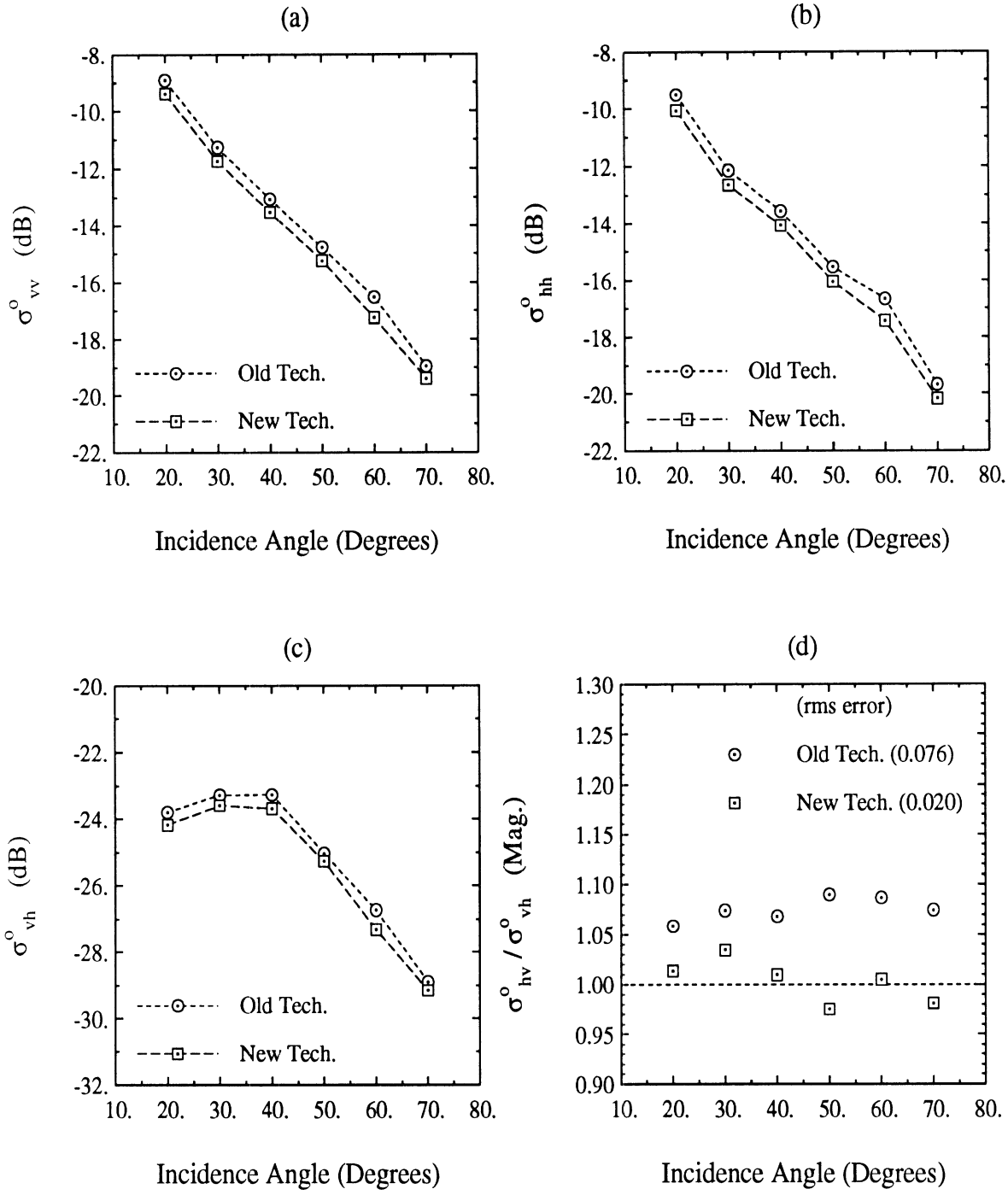

Figure 6.6: Comparison between the new and old calibration techniques applied to the X-band measured backscatter from a bare soil surface; (a), (b), and (c) show the difference in the co- and cross-polarized backscattering coefficients and (d) demonstrates the enhancement in the ratio of the cross-polarized backscattering coefficients obtained by the new method.

(a)

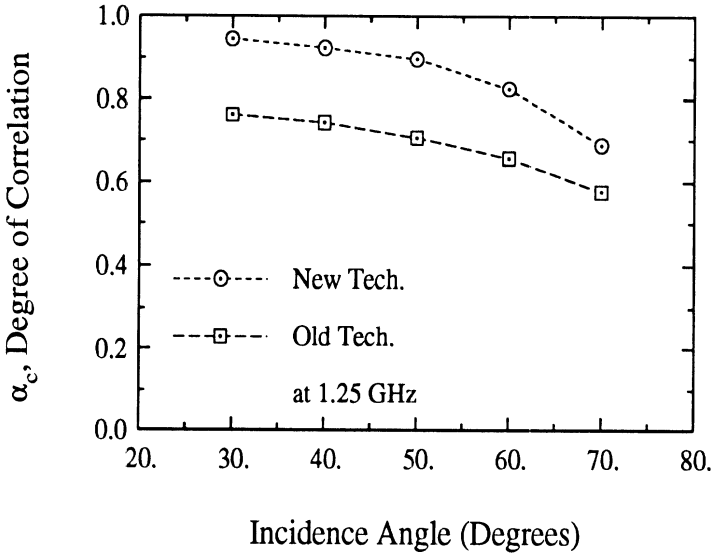
1.0
0.8
0.6
0.4
0.2
0.0
20.
30.
40.
50.
60.
70.
80.
α_c, Degree of Correlation
New Tech.
Old Tech.
at 1.25 GHz
Incidence Angle (Degrees)

(b)

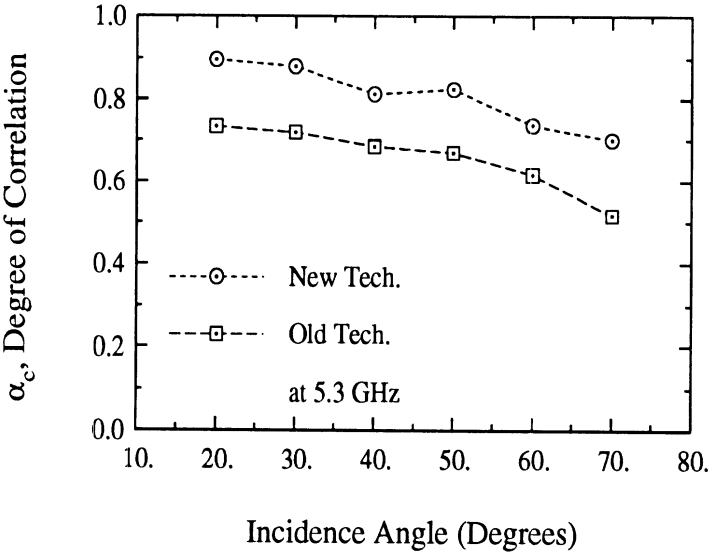
1.0
0.8
0.6
0.4
0.2
0.0
10.
20.
30.
40.
50.
60.
70.
80.
α_c, Degree of Correlation
New Tech.
Old Tech.
at 5.3 GHz
Incidence Angle (Degrees)

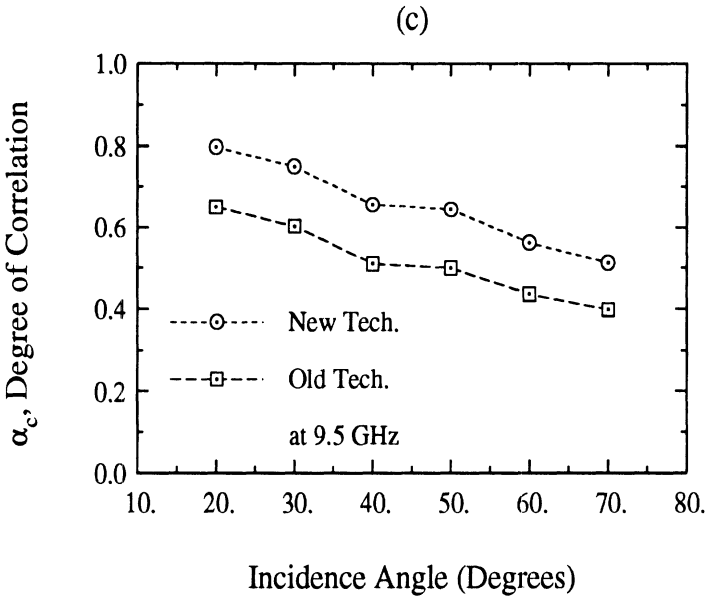

Figure 6.7: Degree of correlation for co-polarized components of the scattering matrix for L-band (a), C-band (b), and X-band (c).

The third step involves a comparison of the phase difference statistics of the distributed target. It has been shown that when the dimensions of the antenna footprint are much larger than the correlation length, the probability density function (pdf) of the phase differences can be expressed in terms of two parameters: the degree of correlation (α) and the polarized-phase-difference (ζ) [Sarabandi, 1992]. The degree of correlation is a measure of the width of the pdf and the polarized-phase-difference represents the phase difference at which the pdf is maximum. These parameters can be computed directly from the components of the Mueller matrix and are given by [Sarabandi, 1992]

$$\alpha = \frac{1}{2}\sqrt{\frac{(\mathcal{M}_{33}+\mathcal{M}_{44})^2+(\mathcal{M}_{34}-\mathcal{M}_{43})^2}{\mathcal{M}_{11}\mathcal{M}_{22}}}$$

$$\zeta = \tan^{-1}\left(\frac{\mathcal{M}_{34}-\mathcal{M}_{43}}{\mathcal{M}_{33}+\mathcal{M}_{44}}\right)$$

Parameter α varies from zero to one, where zero corresponds to a uniform distribution

and one corresponds to a delta-function distribution (fully polarized wave). Parameter ζ varies between $-180°$ and $180°$.

Figures 6.7(a)-(c) show the degree of correlation calculated by the new and old methods for the co-polarized phase difference ($\phi_{hh} - \phi_{vv}$) at L-, C-, and X-band, respectively. There is a significant difference between the two methods in all cases. The partially polarized backscattered Stokes vector obtained by the old calibration method appears more unpolarized than the Stokes vector obtained by the new method. The virtue of this result can be checked in the limiting case if an analytical solution is available. A first-order solution of the small perturbation method for slightly rough surfaces shows that the backscatter signal is fully polarized and, therefore, the pdf of the co-polarized phase difference is a delta function, corresponding to $\alpha = 1$. The roughness parameters of the surface under investigation falls within the validity region of the small perturbation method at L-band. The value of α at L-band derived from the new calibration method is in much closer agreement with theoretical expectations than the value obtained by the old method. Figures 6.8(a)-(c) show plots of the co-polarized phase difference at L-, C-, and X-band, respectively. At L- and X-band the value of ζ obtained by the two methods are positive and not very different from each other. Also, it noted that ζ has a positive slope with incidence angle. However, this is not the case for C-band; the value of ζ obtained by the old method is negative has a negative slope while the behavior of ζ obtained by the new method is very similar to that at the other two frequencies. Figure 6.9 shows the deviation between the PDFs (probability density functions) of co-polarized phase difference of the two methods for C-band at 30°. This deviation shown in Fig. 6.8(b) and Fig. 6.9 is due to the large variation of phase difference between the V- and H-channels of the C-band radar over the illumination area, and since the old method does not account

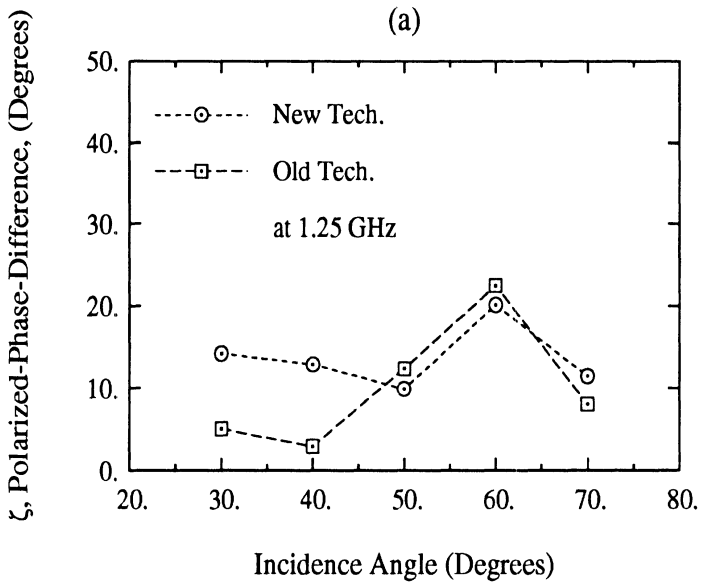
(a)
ζ, Polarized-Phase-Difference, (Degrees)
50.
40.
30.
20.
10.
0.
New Tech.
Old Tech.
at 1.25 GHz
20.
30.
40.
50.
60.
70.
80.
Incidence Angle (Degrees)

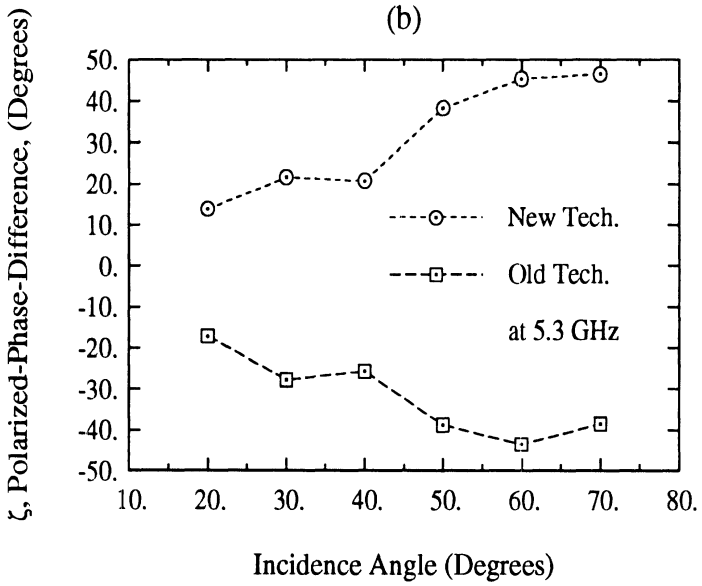
(b)
ζ, Polarized-Phase-Difference, (Degrees)
50.
40.
30.
20.
10.
0.
-10.
-20.
-30.
-40.
-50.
New Tech.
Old Tech.
at 5.3 GHz
10.
20.
30.
40.
50.
60.
70.
80.
Incidence Angle (Degrees)

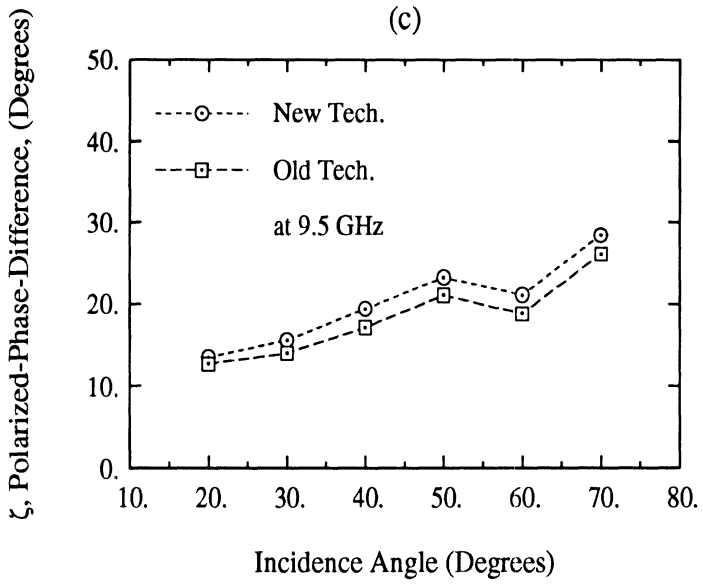

Figure 6.8: Polarized-phase-difference for co-polarized components of the scattering matrix for L-band (a), C-band (b), and X-band (c).

for phase variations, it is incapable of correcting the resulting errors. Similar results were observed for the statistics of the cross-polarized phase difference ($\phi_{hv} - \phi_{vv}$).

6.5 Conclusions

A rigorous method is presented for calibrating polarimetric backscatter measurements of distributed targets. By characterizing the radar distortions over the entire mainlobe of the antenna, the differential Mueller matrix is derived from the measured scattering matrices with a high degree of accuracy. It is shown that the radar distortions can be determined by measuring the polarimetric response of a metallic sphere over the mainlobe of the antenna. The radar distortions are categorized into two groups, namely, distortions caused by the active devices and distortions caused by the antenna structure (passive). Since passive distortions are immune to changes once they are determined, they can be used repeatedly. The active distortions can

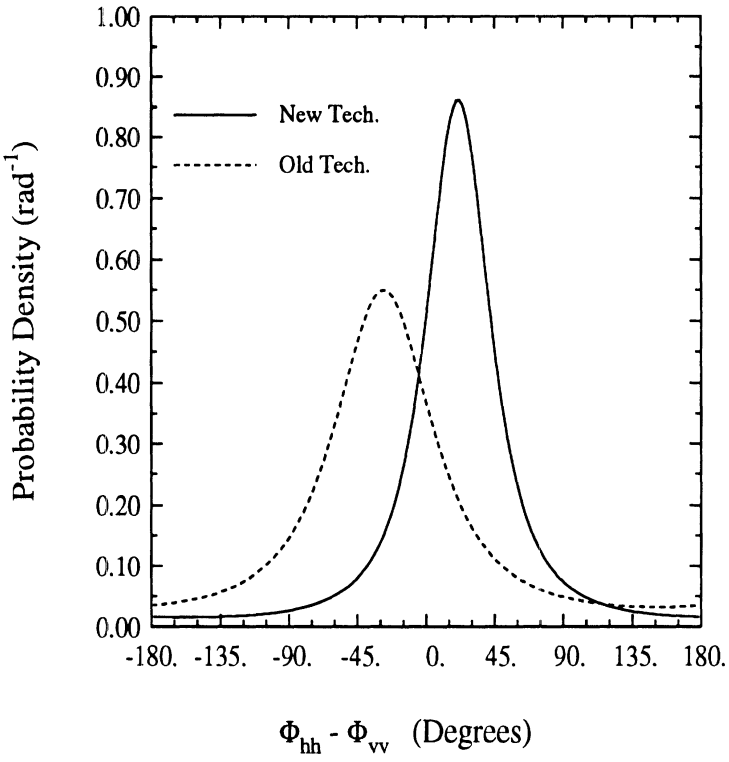

Figure 6.9: Probability density functions (PDF) for co-polarized phase-difference for C-band at 30°.

be obtained by measuring the sphere response only at boresight, thereby reducing the time required for calibration under field conditions. The calibration algorithm was applied to backscatter data collected from a rough surface by L-, C-, and X-band scatterometers. Comparison of results obtained with the new algorithm with the results derived from old calibration method show that the discrepancy between the two methods is less 1dB for the backscattering coefficients. The discrepancy, however, is more drastic for the phase-difference statistics, indicating that removal of the radar distortions from the cross products of the scattering matrix elements (differential Mueller matrix elements) cannot be accomplished with the traditional calibration methods.

CHAPTER VII

MICROWAVE POLARIMETRIC RADAR MEASUREMENTS OF BARE SOIL SURFACES, A SEMI-EMPIRICAL MODEL AND AN INVERSION TECHNIQUE

7.1 INTRODUCTION

Polarimetric radar measurements were conducted for bare soil surfaces under a variety of roughness and moisture conditions at L-, C-, and X-band frequencies at incidence angles ranging from 10° to 70°. Using a laser profile meter and dielectric probes, a complete and accurate set of ground truth data were collected for each surface condition, from which accurate measurements were made of the rms height, correlation length, and dielectric constant. The angular and spectral dependencies of co-polarized ratio ($\sigma^\circ_{vv}/\sigma^\circ_{hh}$) and cross-polarized ratio ($\sigma^\circ_{vh}/\sigma^\circ_{vv}$) for a wide range of roughnesses and moisture conditions are examined. Based on knowledge of the scattering behavior in limiting cases and the experimental observations, an empirical model was developed for σ°_{vv}, σ°_{hh}, and σ°_{hv} in terms of ks (where $k = 2\pi/\lambda$ is the wave number and s is the rms height) and the relative dielectric constant of the soil surface. The model, which was found to yield very good agreement with the backscattering measurements of this study as well as with measurements reported in other investigations, was used to develop an inversion technique for predicting the rms

height of the surface and its moisture content from multipolarized radar observations.

Investigation of the radar backscattering response of natural surfaces is of great importance because of its potential in retrieving the desired physical surface parameters. Soil moisture content and surface roughness are two such parameters.

The problem of electromagnetic wave scattering with random surfaces have long been studied and because of its complexity theoretical solution exist only for limiting cases. When deviation of the surface profile is slightly different from that of a smooth surface, perturbation solutions can be used. In the classic treatment of small perturbation method (SPM) [Rice, 1951; Tsang et al., 1985] it is required that the rms height be much smaller than the wavelength and the rms slope be same order of magnitude as the wavenumber times the rms height. Recently, a perturbation method based on perturbation expansion of phase of the surface field (PPM) was developed which extends the region of validity of SPM to higher rms height but with modest slope and curvature [Wineberner and Ishimaru, 1985]. The other limiting case is when surface irregularities are large compared to the wavelength, namely the radius of curvature at each point on the surface is large. In this limit the solution is known as Kirchhoff approximation (KA) [Beckmann and Spizzichino, 1963; Ulaby et al., 1982]. Various types of modifications and improvements to this model can be found in literature. In these papers the effects of shadowing and multiple scattering are discussed which basically extends the region of KA slightly [Fung and Eom, 1981]. Combined solution of KA and SPM which is applicable for composite surfaces has basically the same regions of validity as the individual models [Brown, 1978].

At microwave frequencies most of natural surfaces do not fall into the validity regions of the theoretical models. Also a complete set of measured data does not exist to characterize the role of influential parameters in the scattering mechanism. Thus

the major goal in this investigation is to find the dependency of the radar backscatter to the roughness parameters and soil moisture condition through extensive backscatter measurement for variety of moisture and roughness conditions and over a wide range of incidence angles and frequencies. Once the dependency of the radar backscatter to these parameters are obtained, the empirical model can be used to retrieve the surface roughness and soil moisture content from measured data.

The radar backscatter of bare soil surfaces under variety of conditions are measured using a truck mounted network analyzer based scatterometer (LCX POLARSCATS) [Tassoudji et al., 1989]. The data are collected polarimetrically at three L-, C-, and X-band frequencies at incidence angles ranging from 10° to 70°. An empirical model is formulated based on a set of measured data and another set of data is used to verify the empirical model. Excellent qualitative and reasonable quantitative agreement is obtained. The polarimetric measurements included recordings of the phase statistics of the backscattered signal, but these will be discusseded in the next chapter.

7.2 EXPERIMENTAL PROCEDURE

Fig. 7.1 shows simple sketches of experimental set-ups for a scatterometer, a profile meter, and a dielectric probe. A description of each of the set-ups is given below briefly.

7.2.1 Scatterometer

The University of Michigan's LCX POLARSCAT [Tassoudji et al., 1989] is designed with the capability to measure the scattering matrix of point or distributed targets at L-, C- and X-band frequencies (1.25, 4.75, and 9.5 GHz of center frequencies, respectively) as shown in Table 7.2.1. The scatterometer consists of an automatic

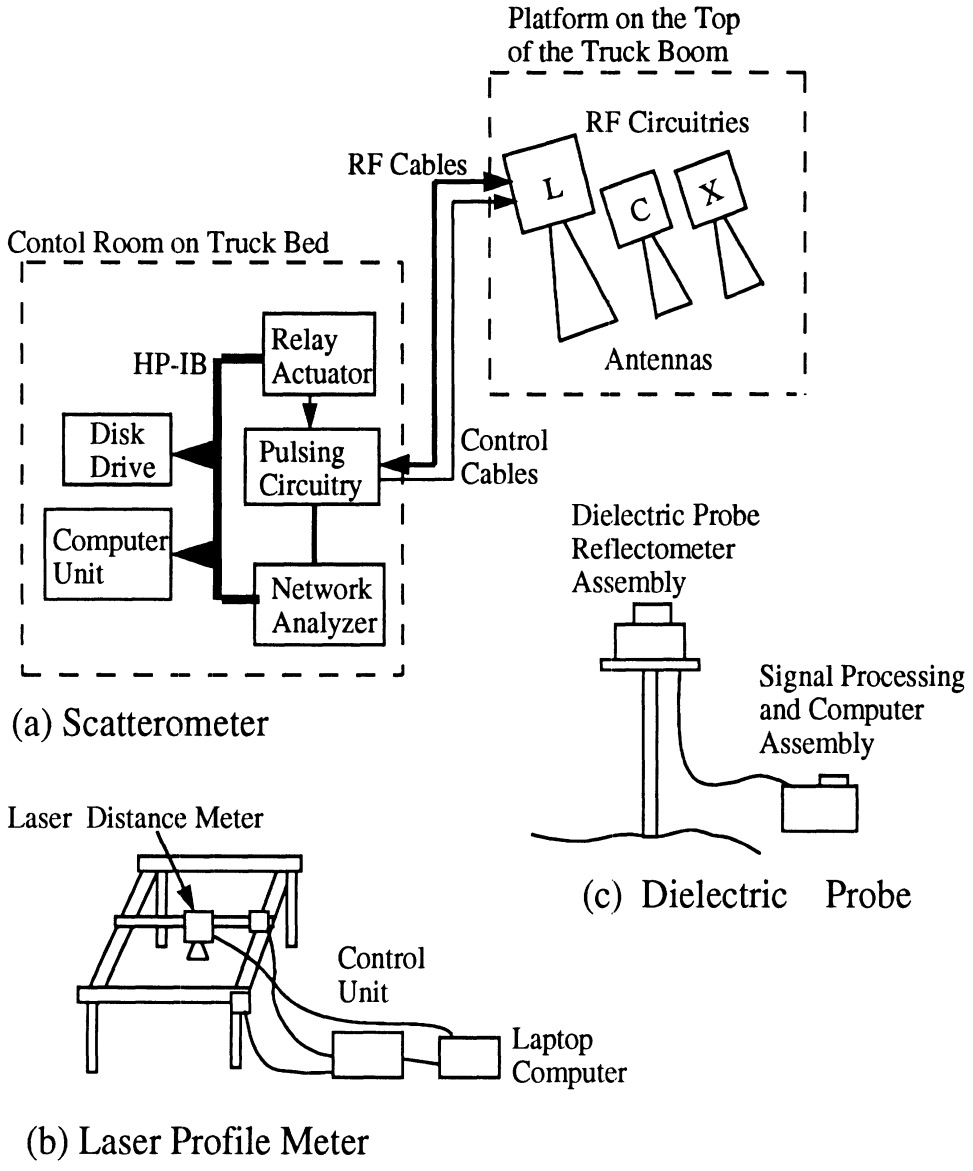

Figure 7.1: Experimental system, (a) a scatterometer block diagram, (b) Laser profile meter, and (c) dielectric probe.

Table 7.1: Polarimetric scatterometer (POLARSCAT) characteristics.

	L	C	X
Center frequency	1.50 GHz	4.75 GHz	9.50 GHz
Frequency bandwidth	0.3 GHz	0.5 GHz	0.5 GHz
Antenna type	Dual polarized pyramidal horn		
Antenna gain	22.1 dB	25.3 dB	29.5 dB
Beam width	12.0°	8.0°	5.4°
Far field ($2d^2/\lambda$)	8.5 m	5.8 m	10.5 m
Platform height	18 m	18 m	18 m
Cross-pol Isolation†	45 dB	45 dB	45 dB
Calibration accuracy	±0.3 dB	±0.3 dB	±0.3 dB
Measurement precision(N>100)	±0.4 dB	±0.4 dB	±0.4 dB
Phase accuracy†	±3°	±3°	±3°

† After polarimetric calibration using STCT [Sarabandi and Ulaby, 1990]

vector network analyzer (HP 8753A), a computer unit, a disk drive for data storage, an amplifying and pulsing circuitry for hardware range gating, a relay actuator, and L-, C-, X-band RF circuitries and antennas as shown in Fig. 7.1. Antennas are dual-polarized with orthogonal mode transducers (OMT) to transmit and receive a set of orthogonal polarizations.

A computer is used to control the network analyzer through HP-IB (interface bus) to acquire the desired data automatically. The computer also controls a relay actuator which energizes the desired frequency and polarization switches. Table 7.2.1 shows a basic characteristics of the scatterometers including specifications of frequencies, antennas, and overall performances.

To achieve good statistical representation of the measured backscatter for distributed targets, a large number of spatially independent samples are required. In this experiment 90 and 60 independent samples were taken at incidence angles of 10°, 20°, 30° and 40°, 50°, 60°, 70°, respectively. To achieve temporal resolution and also to increase the number of independent samples, measurements were performed over 0.3 GHz for L-band and 0.5 GHz for C- and X-band, assuming backscattering coefficient is constant over the mentioned bandwidths. Thus the total number of independent samples including those achieved by these bandwidths, for each incidence angle, is more than 1000.

In addition to the soil backscatter data, the noise background level was measured by pointing the antennas towards the sky. The noise background level was subtracted from the soil backscatter data coherently to improve the signal to noise ratio. The polarimetric response of a conducting sphere was measured to achieve absolute calibration of the radar system [Sarabandi and Ulaby, 1990]. To minimize the time elapsed between the four polarization measurements that completes a polarimetric

set, the soil backscatter data were collected in a raw-data format. The radar data was post-processed to separate the unwanted short-range returns from the target return using the time domain gating capability. The gated target response was then calibrated using the sphere data.

7.2.2 Laser Profile Meter

The height profiles of soil surfaces are measured by the Laser profile meter mounted on a stepper-motor driven XY-table as shown in Fig. 7.1. The Laser profile meter can measure a surface profile with 1 mm horizontal resolution and 2 mm vertical accuracy. A laptop computer is connected to the stepper-motor controllers to position the Laser distance meter with the desired steps in X and Y directions. The heights measured by the Laser distance meter are also collected and stored by the same computer. A minimum of ten one-meter profiles are collected for each surface with steps of 0.25 cm in the horizontal direction. In addition to the surface profiles acquired by the Laser profile meter, a couple of three-meter-profiles were collected using chart paper and spray paint to monitor large scale roughnesses variations. Radar measurements were conducted for four surface-roughness conditions, covering the range from 0.32 cm to 3.02 cm in rms height as shown in Table 7.2.2.

7.2.3 Dielectric Probe

Dielectric constants of the soil fields were measured by a C-band field-portable dielectric probe [Brunfeldt, 1987]. The probe consists of a reflectometer assembly with a coaxial probe tip and a signal processing assembly with a calculator. Dielectric constants were measured at the top and at the depth of 4 cm for more than fifty spots randomly chosen over each surface. The dielectric constants (ϵ_r) were used to

Table 7.2: Summary of roughness parameters.

Surface	s (cm)	l (cm)	m	Freq(GHz)	ks	kl	Denotation
				1.50	0.13	2.6	L1
S-1	0.40	8.4	0.048†	4.75	0.40	8.4	C1
				9.50	0.80	16.7	X1
				1.50	0.10	3.1	L2
S-2	0.32	9.9	0.032†	4.75	0.32	9.8	C2
				9.50	0.64	19.7	X2
				1.50	0.35	2.6	L3
S-3	1.12	8.4	0.133†	4.75	1.11	8.4	C3
				9.50	2.23	16.7	X3
				1.50	0.95	2.8	L4
S-4	3.02	8.8	0.485‡	4.75	3.00	8.8	C4
				9.50	6.01	17.5	X4

† $m = s/l$ assuming exponential autocorrelation function,

‡ $m = \sqrt{2}s/l$ assuming Gaussian autocorrelation function.

Table 7.3: Summary of soil moisture contents.

Surf.	Meas. ϵ_r (4.8 GHz)		Estim. m_v		calculated ϵ_r (ϵ_r', ϵ_r'')		
No.	Top soil	4cm depth	Top	4cm	1.5 GHz	4.75 GHz	9.5 GHz
1 -wet	14.15, 4.62	16.74, 5.94	0.29	0.33	15.57, 3.71	15.42, 2.15	12.31, 3.55
1 -dry	6.58, 1.54	11.05, 3.27	0.14	0.24	7.99, 2.02	8.77, 1.04	5.70, 1.32
2 -wet	14.66, 4.18	14.30, 4.08	0.30	0.29	14.43, 3.47	14.47, 1.99	12.64, 3.69
2 -dry	4.87, 0.83	8.50, 2.15	0.09	0.19	5.85, 1.46	6.66, 0.68	4.26, 0.76
3 -wet	15.20, 5.84	15.10, 5.71	0.31	0.31	15.34, 3.66	15.23, 2.12	13.14, 3.85
3 -dry	7.04, 1.85	10.02, 3.15	0.15	0.22	7.70, 1.95	8.50, 1.00	6.07, 1.46
4 -wet	8.80, 2.38	10.57, 3.27	0.19	0.23	8.92, 2.24	9.64, 1.19	7.57, 1.99
4 -dry	7.28, 1.93	8.84, 2.58	0.16	0.19	7.23, 1.83	8.04, 0.92	6.28, 1.53

estimate the moisture contents (m_v) by inverting a semiempirical model [Hallikainen et al., 1985] which gives ϵ_r in terms of m_v. The real part of ϵ_r is chosen since the error in measuring the imaginary part of ϵ_r by dielectric probe is relatively higher [Jackson, 1990]. The mean value of m_v then was used in the same semiempirical model to obtain an estimate for ϵ_r at L-, C- and X-band frequencies. Table 7.2.3 gives the measured ϵ_r at 4.8 GHz and the estimated values of m_v for the top surface and 4-*cm* deep layers, from which the 0-4 *cm* average dielectric constant was calculated at L-, C-, and X-band. Soil density was determined from soil samples which known volume.

7.3 EXPERIMENTAL OBSERVATIONS AND COMPARISON WITH CLASSICAL SOLUTIONS

In this section we present samples of the measured radar backscatter to demonstrate the spectral, angular, and polarimetric behavior of rough surface backscattering coefficients. Next the theoretical solutions for rough surface backscattering will be compared with experimental data where applicable.

7.3.1 Experimental Observations

Four different fields (S1, S2, S3, and S4) were considered. Each one of four surfaces was measured under two different moisture conditions, relatively wet and relatively dry. The roughness parameters of the surfaces such as rms height s, autocorrelation function $\rho(\xi)$, correlation length l, and rms slope m, are calculated from the measured surface height distributions as given in Table 7.2.2.

The surface height distributions of all four surfaces fit well to Gaussians distribution, where

$$p(z) = \frac{1}{\sqrt{2\pi}s} \exp\left[-\frac{z^2}{2s^2}\right]. \tag{7.1}$$

The autocorrelation functions for surfaces 1, 2, and 3, fit better to exponential functions ($\rho(\xi) = \exp[-|\xi|/l]$) than to Gaussian functions ($\rho(\xi) = \exp[-\xi^2/l^2]$). The Gaussian form provided a better fit for the roughest field, S4. This is illustrated in Fig. 7.2 for fields S1 and S4. The surface rms slopes can be calculated from $m = s\sqrt{|\rho''(0)|}$, where $\rho''(0)$ is the second derivative of $\rho(\xi)$ evaluated at ξ=0.

Measured surface roughness parameters are summerized in Table 7.2.2 and Fig. 7.7. Among the four surfaces, surface S2 is the smoothest (s = 0.32 cm), surface S1 (s = 0.4 cm) is slightly rougher, surface S3 (s = 1.12 cm) represents an intermediate-roughness condition, and surface S4 (s = 3.02 cm) is a very rough surface that was

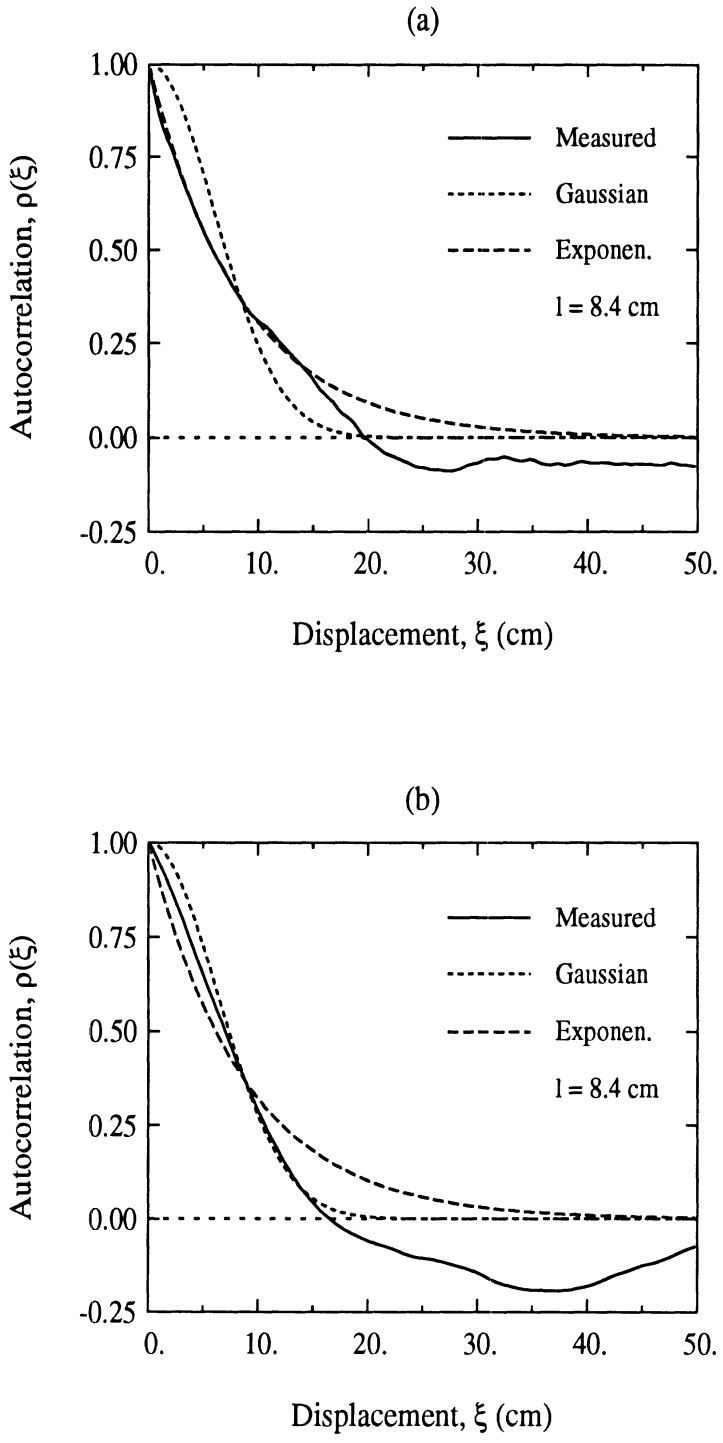

Figure 7.2: Comparison of the measured autocorrelation functions with the Gaussian and exponential functions (a) S1 and (b) S4.

generated by plowing the top 15-cm surface layer. Electromagnetically, these surfaces cover a wide range of roughness conditions, extending from $ks = 0.1$ to $ks = 6.01$ (where $k = 2\pi/\lambda$ is the wave number) and from $kl = 2.6$ to $kl = 19.7$. Surface 1, for example, may be considered smooth at 1.5 GHz ($ks = 0.13$, where k is a wave number), and medium rough at 4.75 GHZ and 9.5 GHz ($ks = 0.42$ and 0.80, respectively). The 12 roughness conditions corresponding to the four surfaces and three wavelengths are identified in $ks - kl$ space in Fig. 7.7, together with the boundaries for the regions of validity of the small perturbation model (SPM) and the physical optics (PO) and geometrical optics (GO) solutions of the Kirchhoff approximation.

Fig. 7.3 shows angular responses of the vv-polarized backscattering coefficient (σ^o_{vv}) for four different bare soil surfaces with rms heights ranging from 0.3 cm to 3.0 cm all at a moderately dry condition ($m_v \simeq 0.15$). The sensitivity of σ^o_{vv} to surface roughness is clearly evident at both 1.5GHz (Fig. 7.3a) and 9.5 GHz (Fig. 7.3b); over the 30° - 70° angular range. At L-band (1.5 GHz) there is a total of 16 dB dynamic range in σ^o_{vv} when surface roughness (s) changes from 0.3 cm to 3 cm at the angles ranging from 30° to 70°. Fig. 7.3(b) shows the angular pattern of the same surfaces at X-band (9.5 GHz). In this case the total dynamic range is reduced to 10 dB and the changes in σ^o_{vv} for $s = 1.1$ cm and $s = 3.0$ cm is negligible. The radar backscatter is very sensitive to surface roughness at lower values of ks ($ks \leq 2.0$), but insensitive at higher values of ks ($ks \geq 2.0$).

Further illustration of the effect of surface roughness on the angular response of σ° is shown in Fig. 7.4 which contains plots of the three principal polarization components for the smoothest case (Fig. 7.4a), corresponding to surface S2 at 1.5 GHz, and for the roughest-surface condition (Fig. 7.4b), corresponding to surface S4 at 9.5 GHz. Based on these and on the data measured for the other surfaces, we

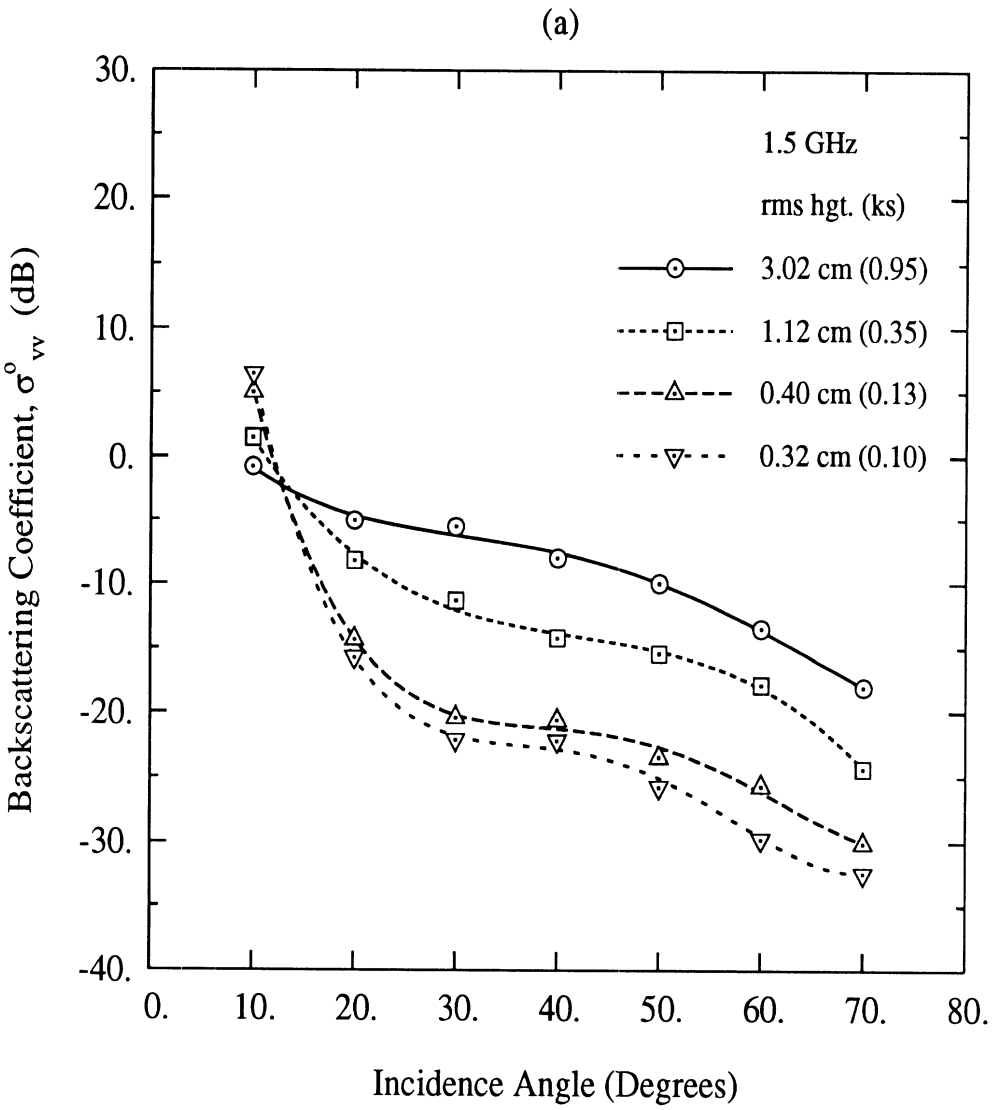
(a)
30.
20.
10.
0.
-10.
-20.
-30.
-40.
0.
10.
20.
30.
40.
50.
60.
70.
80.
1.5 GHz
rms hgt. (ks)
3.02 cm (0.95)
1.12 cm (0.35)
0.40 cm (0.13)
0.32 cm (0.10)
Backscattering Coefficient, σ°vv (dB)
Incidence Angle (Degrees)

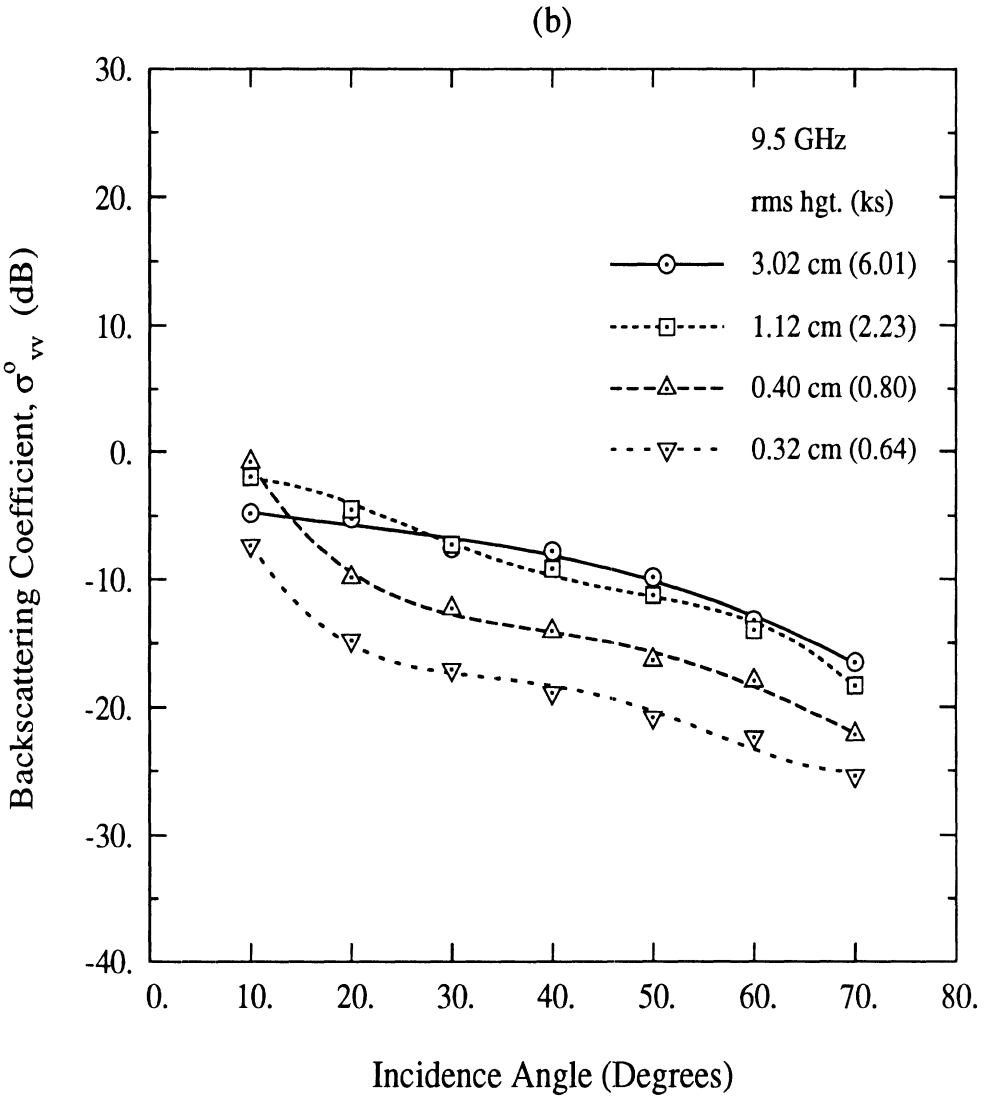

Figure 7.3: Angular response of σ°_{vv} for four different surface roughnesses at moderately dry condition ($m_v \simeq 0.15$), at (a) 1.5 GHz and (b) 9.5 GHz.

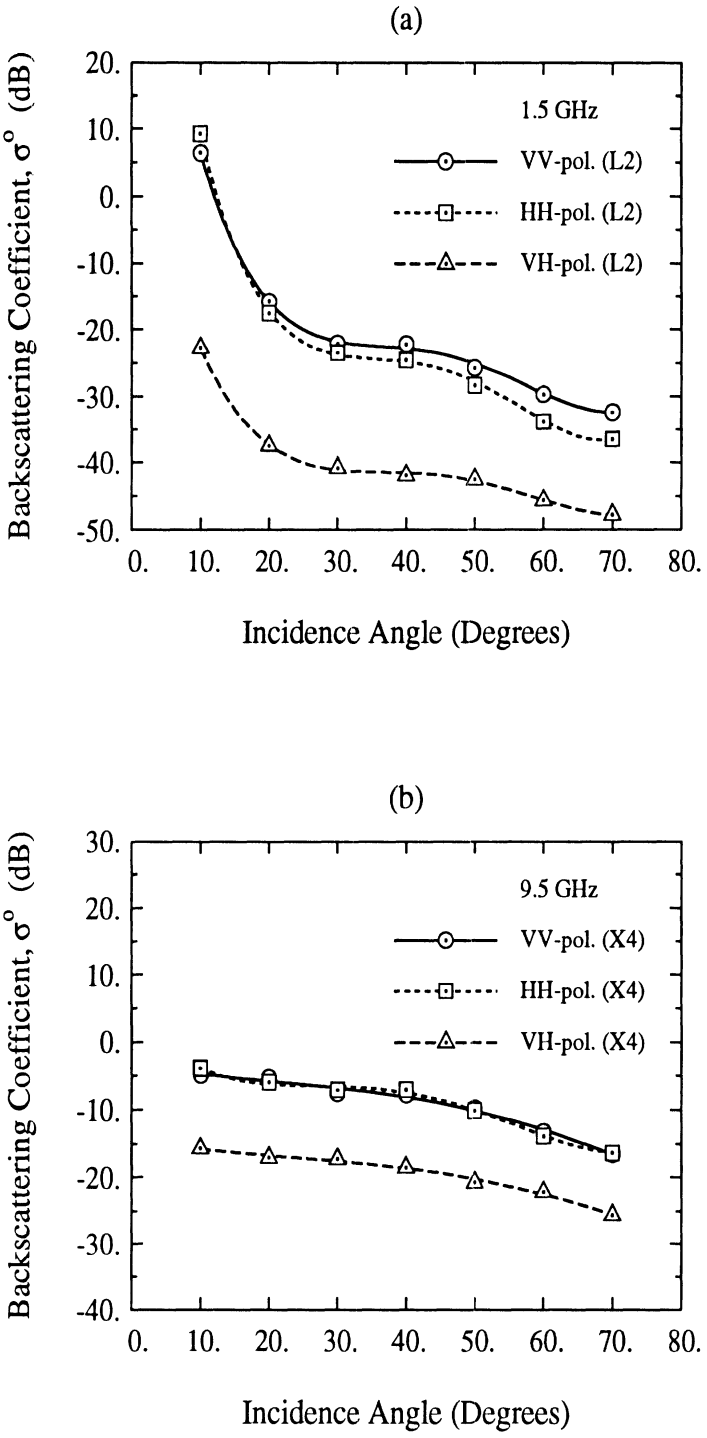

Figure 7.4: Angular responses of σ°_{vv}, σ°_{hh}, and σ°_{hv} for (a) a smooth surface at 1.5 GHz (L2) and (b) a very rough surface at 9.5 GHz (X4).

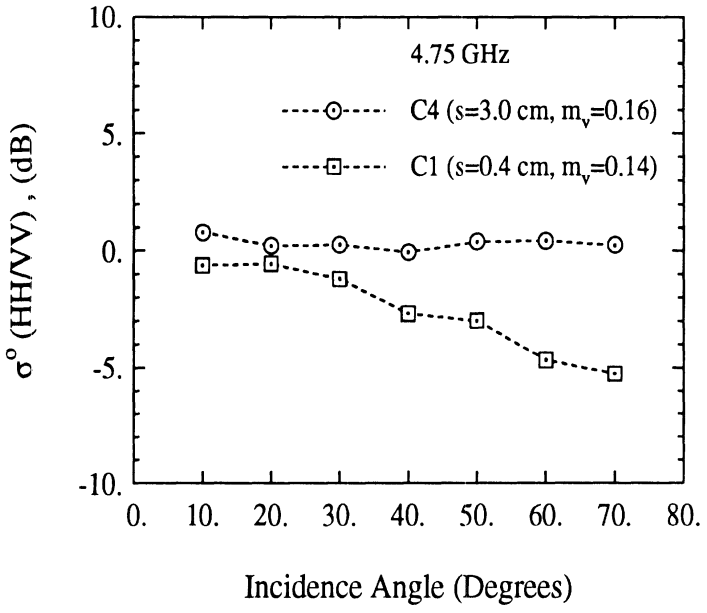

Figure 7.5: Angular dependence of the like-polarized ratio, $\sigma^o_{hh}/\sigma^o_{vv}$, at 4.75 GHz for a smooth surface and a very rough surface.

note that the ratio of σ^o_{hh} to σ^o_{vv}, which will be referred to as the co-polarized ratio, is always smaller than or equal to 1, and it approaches 1 as ks becomes large. Very rough surfaces such as C4 (surface 4 at C-band) and X4 do not show any noticeable differences between σ^o_{vv} and σ^o_{hh}, while smooth surfaces show values of $\sigma^o_{hh}/\sigma^o_{vv}$ smaller than 1. It is also observed that co-polarized ratio is a function of incidence angle for smooth surfaces and increases as the incidence angle increases. The sensitivity of the co-polarized ratio $\sigma^o_{hh}/\sigma^o_{vv}$ to surface roughness and the incidence angle is shown in Fig. 7.5. For very rough surfaces ($ks \geq 2$) $\sigma^o_{hh}/\sigma^o_{vv} \simeq 1$ independent of incidence angle. Another point worth noting is that the shape of the angular pattern of the cross-polarized backscattering coefficient σ^o_{hv}, is similar to that of σ^o_{vv}, but the ratio $\sigma^o_{hv}/\sigma^o_{vv}$, which will be referred to as cross-polarized ratio, increases with ks as shown in Figs. 7.4 (a), (b) (and more explicitly in Fig. 7.11).

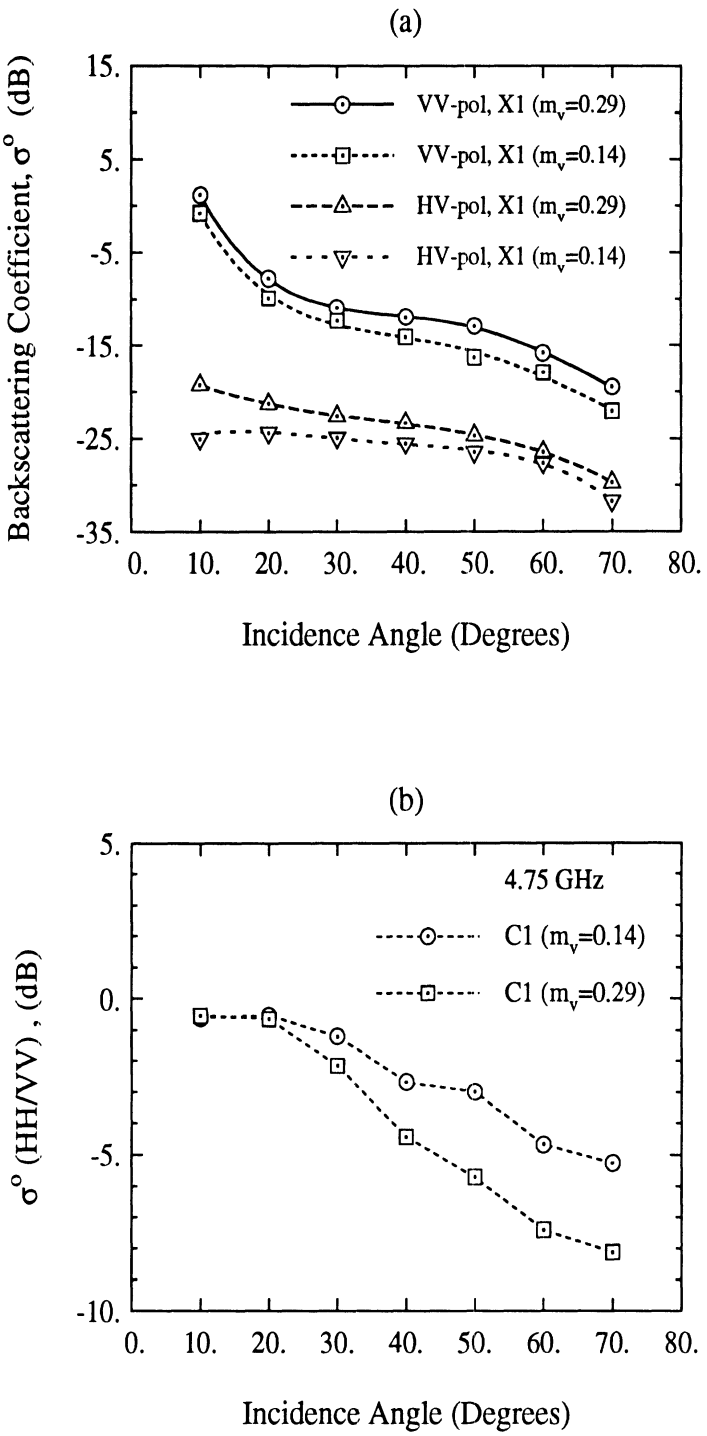

Figure 7.6: Angular plots of (a) σ°_{vv} and σ°_{hv} of surface S1 at X-band for two different moisture conditions and (b) the like-polarized ratio, $\sigma^\circ_{hh}/\sigma^\circ_{hh}$, for the same surface at C-band.

The backscattering coefficients of a surface is a function of moisture content. Figure 7.6(a) shows the backscattering coefficient of surface 1 for two moisture conditions, m_v=0.29 and m_v=0.14. The ratio of σ^o_{vv} (or σ^o_{hv}) of wet soil to σ^o_{vv} (or σ^o_{hv}) of dry soil is about 3 dB at the angles ranging from 20° to 70°. The sensitivity of σ^o to moisture contents (≈3 dB in Fig. 7.5 (a)) is much lower than the sensitivity to surface roughness (≈16 dB in Fig. 7.3 (a)) in this experiment. Figure 7.6 (b) shows the angular response of the co-polarized ratio $\sigma^o_{hh}/\sigma^o_{vv}$ for a fixed roughness at two different moisture contents. The magnitude of the co-polarized ratio is larger for the wet surface (6 dB at 50°) than for the dry surface (3 dB at 50°).

7.3.2 Comparison with Classical Solutions

This section evaluates the applicability of the small perturbation method (SPM), the physical optics (PO) model, and the geometrical optics (GO) model to the measured radar data. Expressions for the backscattering coefficient σ° and the regions of validity of these models are given in Chapter 2. Measured roughnesses for all four surfaces at three frequencies are shown in Fig. 7.7 in terms of ks and kl. Also shown are the regions of validity of the models; SPM, PO, GO models. The lower limit of the ks value of the validity region for GO model given by $ks > \sqrt{2.5}/\cos\theta$ is chosen at the incidence angle θ of 30°, where the lower limit varies from $ks = 1.62$ at $\theta = 10°$ to $ks = 6.32$ at $\theta = 60°$

Small Perturbation Model

SPM is applicable only on L1 (surface 1 at L-band frequencies) according to Fig. 7.7, and the backscattering coefficients computed by SPM are compared with those measured for L1 in Figs. 7.8 (a)-(c). The vv-polarized backscattering coefficients

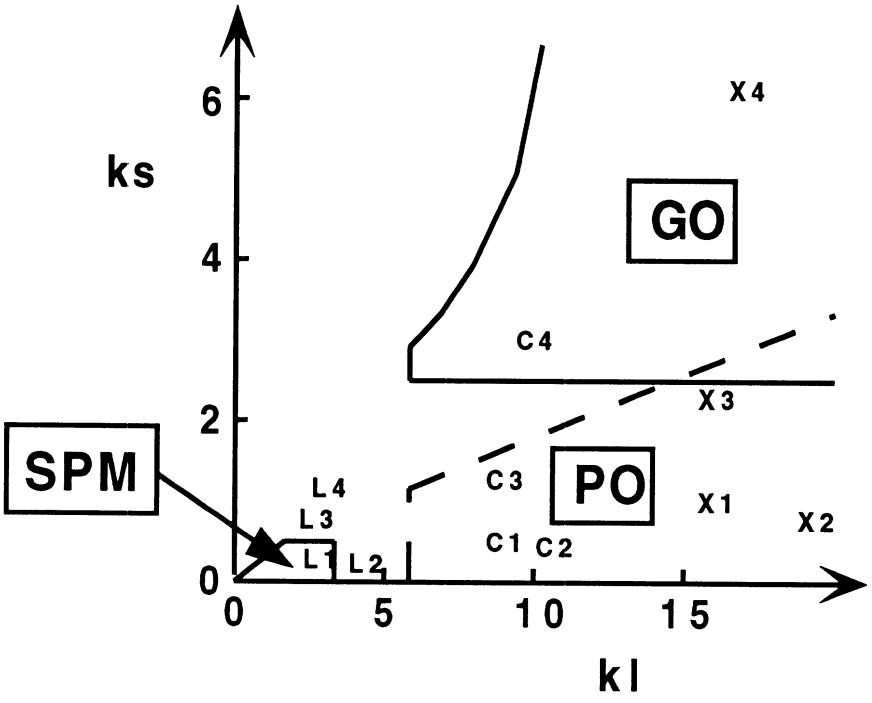

Figure 7.7: Roughness parameters and the region of validity of SPM, PO, and GO models.

σ°_{vv} computed using SPM are compared with measured σ°_{vv} as shown in Fig. 7.7 (a) for three types of autocorrelation functions, namely, a Gaussian, an exponential, and a numerical form of autocorrelation functions. These autocorrelation functions and their Fourier transforms (which are the normalized roughness spectrums) are given in Chapter 2.

The backscattering coefficient σ°_{vv} of SPM with exponential autocorrelation function fits better to the measured σ°_{vv} than those with the other autocorrelation functions, even though there is about 5 dB discrepancies at higher incidence angles. The measured σ°_{hh} agrees quite well with SPM model (within about 1 dB tolerance) when exponential autocorrelation is assumed as shown in Fig. 7.7(b). As mentioned earlier, the measured autocorrelation function of surface 1 fits better to exponential than to Gaussian autocorrelation function, which makes sense to the results in Figs. 7.8 (a) and (b).

The cross-polarized backscattering coefficient for L1 computed using the second-order SPM with exponential autocorrelation function is shown in Fig. 8 (c), and the angular trend of the calculated σ°_{hv} fits well to that of the measured σ°_{hv} while the values of the measured σ°_{hv} are higher than those of the SPM. Fig. 7.7 (c) also shows that the angular pattern of σ°_{hv} calculated by SPM is quite similar to that of σ°_{vv}.

SPM model is applicable to the case of L2 ($ks = 0.10$, $kl = 3.1$) and L3 ($ks = 0.35$, $kl = 2.6$) also. But SPM model failed on the case of L4 ($ks = 0.95$, $kl = 2.8$) as indicated in Table 7.3.2.

Physical Optics Model

Several roughnesses of this experiment, C1, C2, C3, X1, X2, and X3, are in the region of validity of the PO Model. One case of those roughnesses, X1, is closely

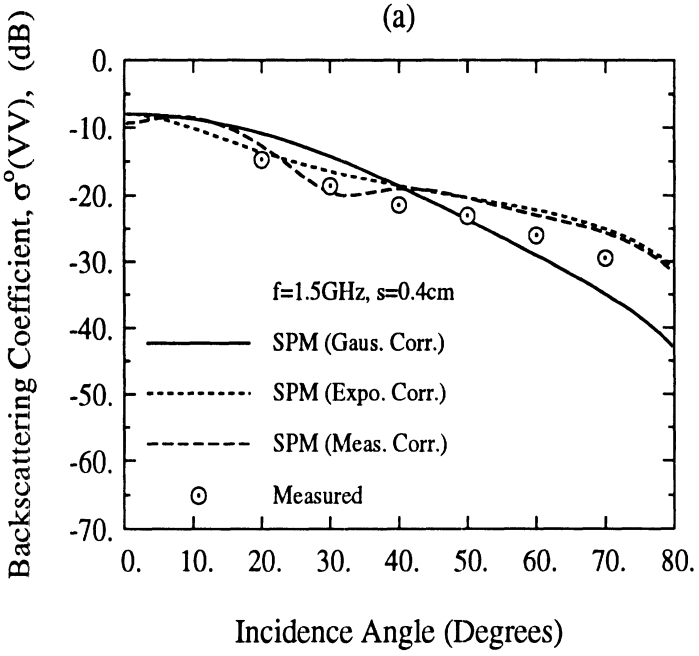
(a)
Backscattering Coefficient, σ°(VV), (dB)
0.
-10.
-20.
-30.
-40.
-50.
-60.
-70.
f=1.5GHz, s=0.4cm
SPM (Gaus. Corr.)
SPM (Expo. Corr.)
SPM (Meas. Corr.)
Measured
0. 10. 20. 30. 40. 50. 60. 70. 80.
Incidence Angle (Degrees)

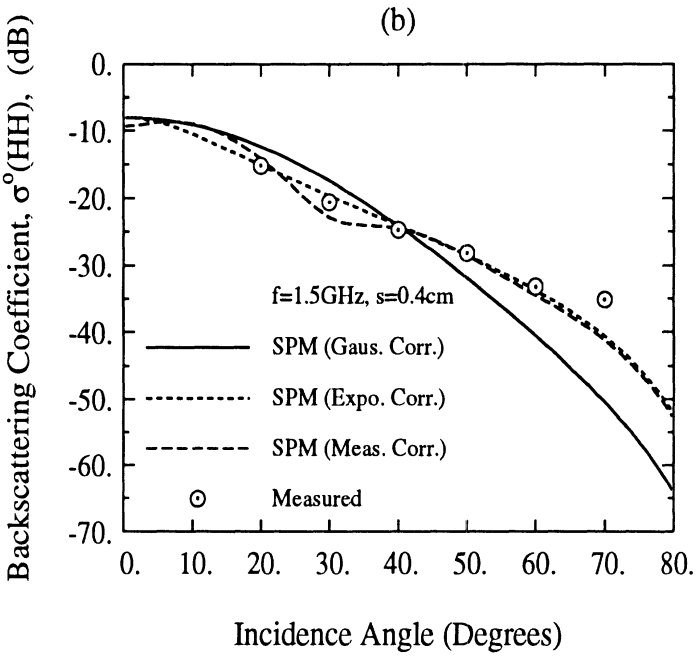
(b)
Backscattering Coefficient, σ°(HH), (dB)
0.
-10.
-20.
-30.
-40.
-50.
-60.
-70.
f=1.5GHz, s=0.4cm
SPM (Gaus. Corr.)
SPM (Expo. Corr.)
SPM (Meas. Corr.)
Measured
0. 10. 20. 30. 40. 50. 60. 70. 80.
Incidence Angle (Degrees)

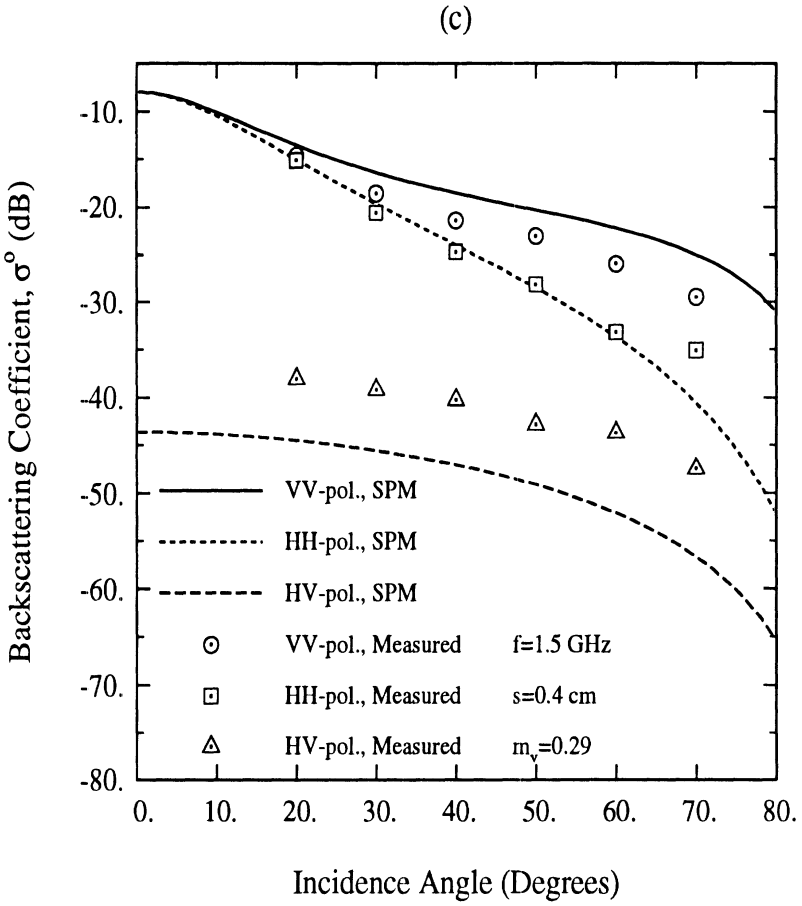

Figure 7.8: SPM model with different autocorrelation functions compared to the measured data of L1 (surface 1 at 1.5 GHz, ks=0.13), (a) VV-polarization, (b) HH-polarization, and (c) VV-, HH-, and HV-polarizations using an exponential autocorrelation function.

Table 7.4: Comparison between σ° of SPM model (with exponential correlation) and the measured data for wet soil surfaces.

Surface	$\sigma^\circ_{spm}/\sigma^\circ_{meas}$ (dB) at 40°		
	VV-pol	HH-pol	HV-pol
L1	2.9	0.7	-6.7
L2	0.5	0.8	-8.7
L3	-0.4	-1.0	-3.8
L4	5.6	1.6	3.4

examined and the results are shown in Figs. 9 (a)-(c). σ°_{vv} modeled by PO with Gaussian autocorrelation function deviates from the measured σ°_{vv} except at small incidence angles, but σ°_{vv} modeled by PO with exponential autocorrelation function agrees to the measured σ°_{vv} quite well over a wide range of angles ($\theta < 40°$) as shown in Fig. 7.9 (a). The comparison between σ°_{hh} of PO model and σ°_{hh} measured for the surface of X1 is shown in Fig. 7.9 (b). The ratios of the backscattering coefficients computed by PO model σ°_{po} to those measured in this experiment (σ°_{meas}) are tabulated in Table 7.3.2 for incidence angles of $20°, 40°$ and $60°$ for wet soil surfaces. The hh-polarized backscattering coefficients σ°_{hh} of the PO model agree, within about 3 dB, to the measured values for the surfaces of C2, c3, and X1 at the angles less than 40°. The vv-polarized backscattering coefficients σ°_{vv} of the PO model, however, deviate much from the measured values for all surfaces. The deviation is very large at large incidence angles ($\theta \geq 50°$) as shown in Fig. 7.9 (a) and Table 7.3.2. PO model failed on the prediction of σ° for the most surfaces which roughness parameters are in the region of validity of the PO model. The cross polarization backscattering coefficient

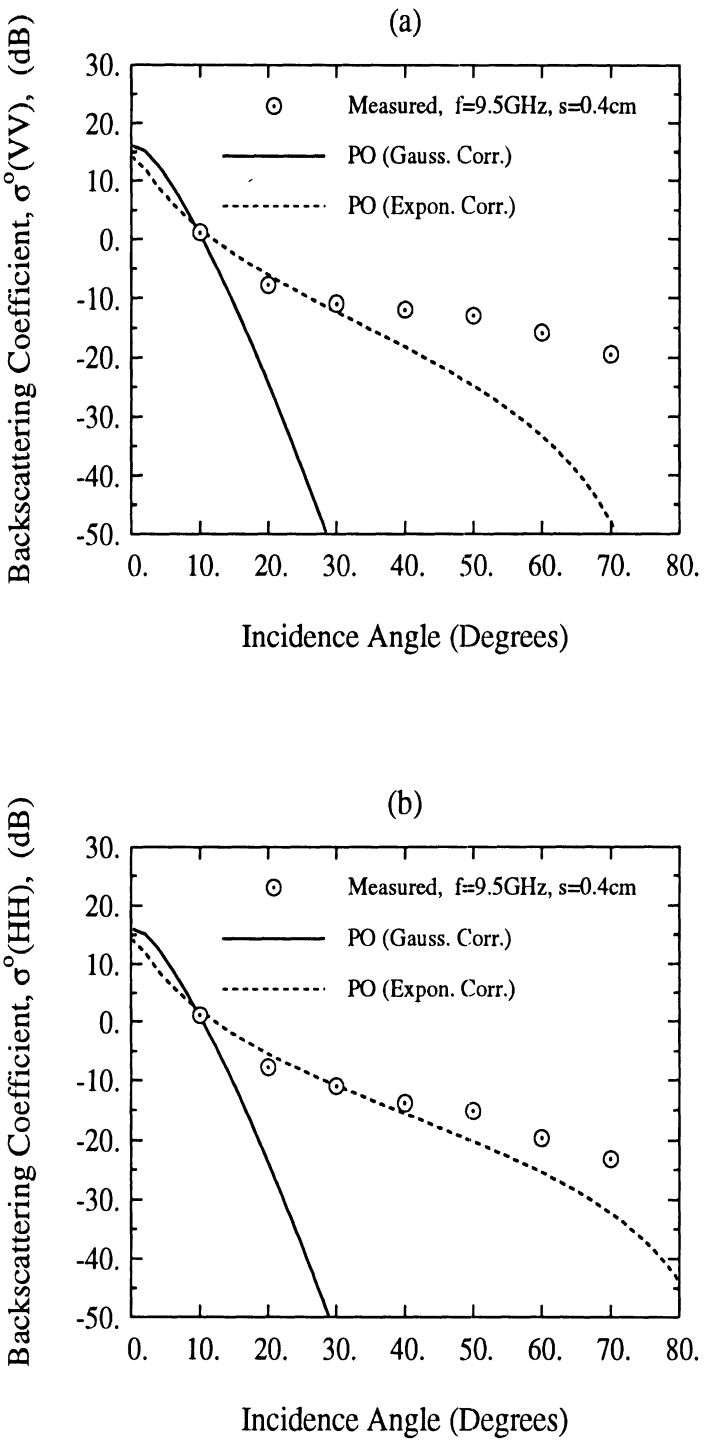

Figure 7.9: PO model with different autocorrelation functions compared to the measured data of X1 (surface 1 at 9.5 GHz, ks=0.80) for (a) VV-polarization and (b) HH-polarization.

Table 7.5: Comparison between σ° of PO model (with exponential correlation) and the measured data for wet soil surfaces.

Surface	$\sigma^\circ_{po}/\sigma^\circ_{meas}$ (dB)					
	VV-pol			HH-pol		
	20°	40°	60°	20°	40°	60°
C1	2.6	-5.8	-17.6	3.7	1.0	-3.0
C2	0.5	-6.7	-20.1	2.2	-0.2	-6.9
C3	-4.7	-5.6	-15.3	-2.8	-1.5	-5.1
X1	1.6	-6.3	-17.5	2.3	-1.8	-5.7
X2	0.8	-5.8	-20.0	3.6	-0.2	-8.5
X3	-7.6	-5.6	-12.8	-6.5	-2.4	-5.4

is not available for PO model. The measured σ°_{vv} is higher than or equal to σ°_{hh} in all cases of roughnesses, moisture contents, and incidence angles, which is contrary to the PO model. This is due to the fact that σ°_{vv} and σ°_{hh} of the PO model are directly proportional to the Fresnel reflectivities.

Geometrical Optics Model

The GO model agrees with the measured σ°_{vv} and σ°_{hh} within 4 dB tolerance for C4 case and within about 2 dB tolerance for X4 for the incidence angles less than or equal to 50°. Figure 7.10 shows the measured backscattering coefficients of X4 case compared with the GO model. The coherent component of the backscattering coefficient is negligibly small for the very rough surfaces like C4 and X4, and the noncoherent component dominates at all angles including normal incidence.

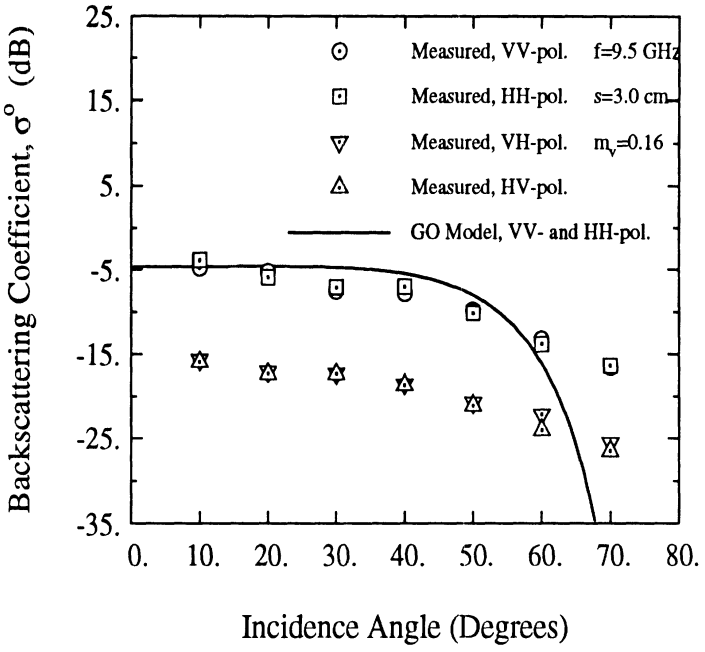

Figure 7.10: GO model compared to the measured data of X4 (surface 4 at 9.5 GHz, ks=6.0).

The GO model like the PO model is incapable of predicting the cross-polarized terms. This model also failed to predict σ°_{vv} (or σ°_{hh}) at larger incidence angle ($\sigma > 60°$) as shown in Fig. reffig:5-10.

The major conclusions we drew from our analysis of the measured radar data when compared with the predictions of the SPM, PO, and GO models are:

1. Some natural surface conditions fall outside the regions of validity of all three models.

2. None of the models provides consistently good agreement with the measured data, particularly at incidence angles greater than 40°.

3. The PO model predicts that $\sigma^\circ_{vv} < \sigma^\circ_{hh}$, contrary to all observations.

Additionally, being first-order solutions, both the PO and GO models cannot be

used for σ°_{hv}. Faced with these inadequacies of the available theoretical scattering models, we decided to develop an empirical model that relates σ°_{vv}, σ°_{hh}, and σ°_{hv} to the roughness (ks) and dielectric constant (ϵ_r) of the surface. This is the subject of the next section.

7.4 SEMI-EMPIRICAL MODEL (SEM)

The failure of existing models to cover roughness conditions that occur more often in nature as described in the previous section, prompts development of semi-empirical backscattering models for random surfaces. Another reason for developing the semi-empirical model is to generate an inversion algorithm to retrieve soil moisture and surface roughness from the measured radar backscatter.

Semi-empirical models of backscattering coefficients, $\sigma^\circ_{vv}, \sigma^\circ_{hh}$ and σ°_{hv}, are developed based on the measured radar backscatter of the eight soil surfaces and knowledge of scattering solutions in the limiting cases. For this set of data, surface roughnesses and the volumetric moisture contents are in the range of $0.1 < ks < 6.0$, $2.6 < kl < 19.7$, and $0.09 < m_v < 0.31$, which is the region of interest at microwave frequencies.

7.4.1 Development

we begin with an examination of the cross-polarized ratio $q = \sigma^\circ_{hv}/\sigma^\circ_{vv}$. The angular pattern of σ°_{hv} follows the pattern of σ°_{vv} and thus the cross-polarized ratio is only a function of roughness and frequency as shown previously. Cross-polarized ratio increases when frequency and/or surface rms height s increases.

Figs. 7.11 (a) and (b) show the variation of $\sigma^\circ_{hv}/\sigma^\circ_{vv}$ as a function of ks which includes both frequency and rms height, for incidence angles of $30°, 40°$ and $50°$. The

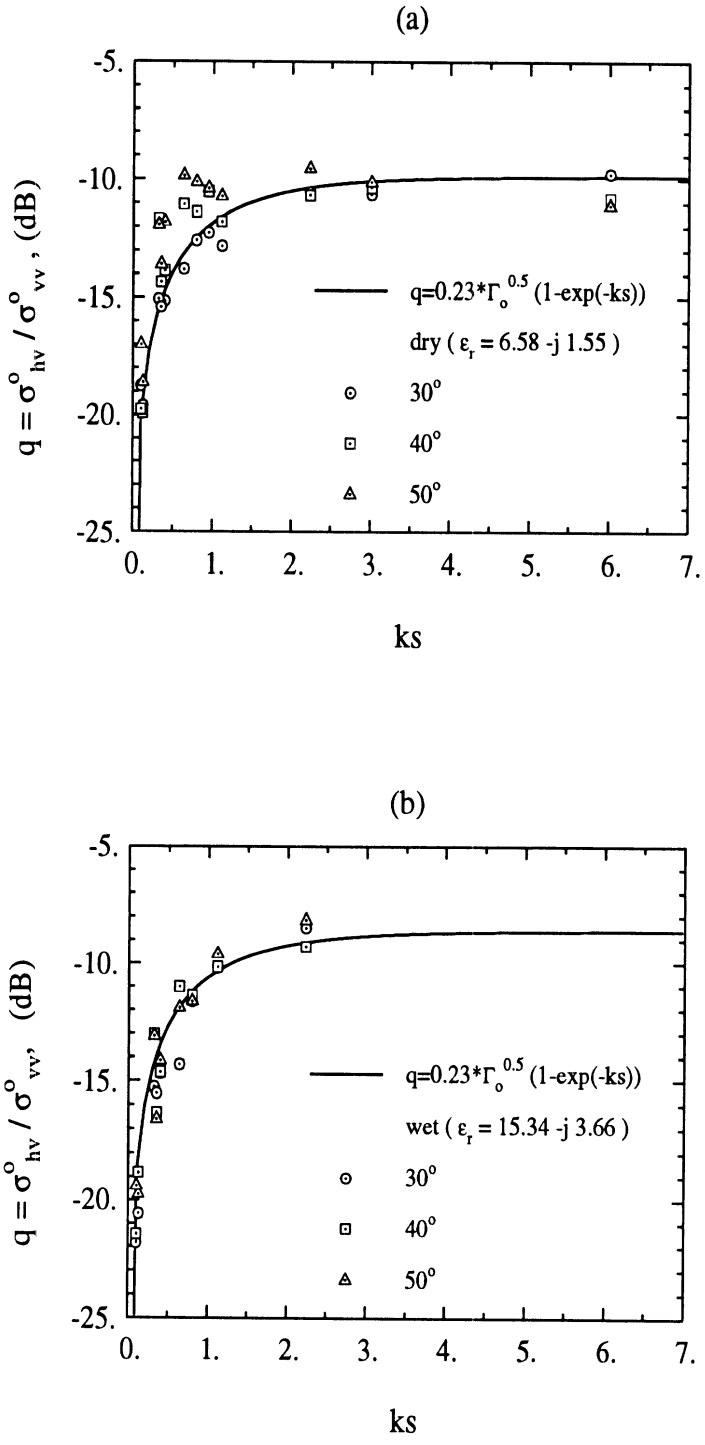

Figure 7.11: The sensitivity of the depolarization ratio, $\sigma^\circ_{hv}/\sigma^\circ_{vv}$, to surface roughness for (a) dry soil and (b) wet soil.

cross-polarized ratio starts from values of about -20 dB for $ks \approx 0.1$ and increases linearly with ks until $\sigma^\circ_{hv}/\sigma^\circ_{vv}$ saturates at values about -10 dB ($ks \geq 2$) as shown in Fig. 7.11 (a). Cross-polarized ratios for the relatively wet surfaces start from smaller values than those for the relatively dry surfaces and increases more rapidly as ks increases, and the ratio saturates at higher values ($\approx$ -9 dB) as shown in Fig. 7.11 (b). An empirical form for the cross-polarized ratio $\sigma^\circ_{hv}/\sigma^\circ_{vv}$ is obtained by curve fitting of the measured data as follows:

$$\mathbf{q} \triangleq \frac{\sigma^\circ_{hv}}{\sigma^\circ_{vv}} = 0.23\sqrt{\Gamma_o}[1 - \exp(-ks)] \tag{7.2}$$

where Γ_o is the Fresnel reflectivity of the surface at nadir,

$$\Gamma_o = \left|\frac{1 - \sqrt{\epsilon_r}}{1 + \sqrt{\epsilon_r}}\right|^2 . \tag{7.3}$$

The empirical function for the cross-polarized ratio is compared with the measured data as shown in Figs. 7.11 (a) and (b).

Next, we shall examine the co-polarized ratio $p = \sigma^\circ_{hh}/\sigma^\circ_{vv}$. The measured values of the co-polarized ratio $\sigma^\circ_{hh}/\sigma^\circ_{vv}$ is a function of surface roughness, soil moisture content, and incidence angle. Figs. 7.12 (a) and (b) show the variation of the ratio $\sigma^\circ_{hh}/\sigma^\circ_{vv}$ with respect to the roughness parameter ks for both of wet and dry conditions at the incidence angles of 40° and 50°, respectively. The co-polarized ratios start from -7.5 dB for wet soil and -4.5 dB for dry soil at 50° incidence, which are much lower than those for 40° incidence. Both Fig. 7.12 (a) and (b) show that the co-polarized ratio $\sigma^\circ_{hh}/\sigma^\circ_{vv}$ of wet soil are lower than those of the dry soil. The curves shown in Fig. 7.12 are based on the empirical expression

$$\sqrt{p} \triangleq \sqrt{\frac{\sigma^\circ_{hh}}{\sigma^\circ_{vv}}} = 1 - \left(\frac{2\theta}{\pi}\right)^{[1/(3.0\Gamma_o)]} \cdot \exp(-ks) \tag{7.4}$$

where θ is the incidence angle in radians.

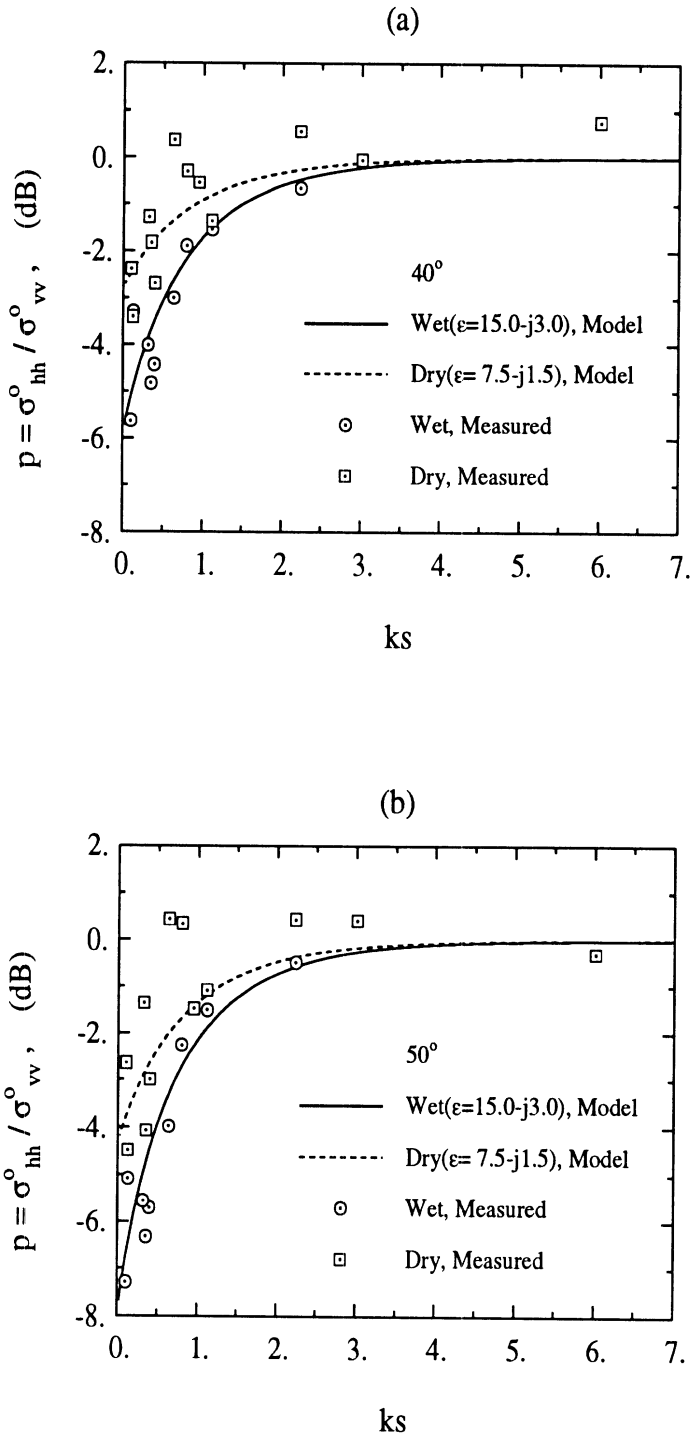

Figure 7.12: The sensitivity of the like-polarized ratio, $\sigma^\circ_{hh}/\sigma^\circ_{vv}$, to surface roughness and soil moisture at (a) 40° and (b) 50°.

Having established empirical formulas for $q = \sigma^\circ_{hv}/\sigma^\circ_{vv}$ and $p = \sigma^\circ_{hh}/\sigma^\circ_{vv}$ that provide reasonable agreement with the measured data, the remaining task is to relate the absolute level of any one of the three linearly polarized backscattering coefficients to the surface parameters. Upon examining the measured data, an empirical formula for the magnitude of the backscattering coefficient σ°_{vv} is found to have the following form:

$$\sigma^\circ_{vv}(\theta, \epsilon_r, ks) = \frac{g \cos^3\theta}{\sqrt{p}} \cdot [\Gamma_v(\theta) + \Gamma_h(\theta)] \tag{7.5}$$

where

$$g = 0.7\left[1 - \exp(-0.65(ks)^{1.8})\right], \tag{7.6}$$

and p is given in (7.4).

The multiplying term of $\Gamma_v(\theta) + \Gamma_h(\theta)$ is included in (7.5) to provide a moisture dependency of σ°_{vv} as shown in Fig. 7.6 (a), which may be a reasonable assumption since all three theoretical models described in previous sections include the Fresnel reflectivity or equivalent forms of the Fresnel reflectivity in their formulae of the backscattering coefficients. The measured angular patterns of the backscattering coefficient σ°_{vv} follow the form of $(\cos\theta)^m$, where m is ranging from 2.0 to 4.0. The angular patterns of backscattering coefficients σ°_{vv} for a very rough surfaces approach the form of $\cos^2\theta$ which is the scattering pattern of a Lambertian surface [Ulaby et al, 1982], and those for the smooth and dry surfaces follow the form of $\cos^4\theta$. To avoid complication of the empirical formula, the term $\cos^3\theta$ was chosen, which can be applicable generally to most surfaces. The roughness dependency of σ°_{vv} is represented by factor g in (7.6) which is found by curve-fitting of the measured data.

Consequently, the backscattering coefficient σ°_{hh} can be obtained from (7.4)-(7.6) and is given by

$$\sigma^\circ_{hh}(\theta, \epsilon_r, ks) = g\sqrt{p}\cos^3\theta\ [\Gamma_v(\theta) + \Gamma_h(\theta)] \tag{7.7}$$

and the backscattering coefficient $\sigma^{\circ}_{hv}(=\sigma^{\circ}_{vh})$ is simply given by

$$\sigma^{\circ}_{hv}(\theta, \epsilon_r, ks) = q\ \sigma^{\circ}_{vv}(\theta, \epsilon_r, ks). \tag{7.8}$$

As we will see next, the semi-empirical model was found to provide a good representation of the measured data at all frequencies and over a wide angular range. The model was evaluated against three data sets: (a) the data measured in this study, (b) another independently measured data set that was not used in the development of this model, which shall be referred to as Independent Data Set II, and (c) a data set that was recently reported by Yamasaki et al. [1991] at 60 GHz.

7.4.2 Comparison With Measured Data

Because of the space limitations, we will present only two typical examples illustrating the behavior of the semi-empirical model, in comparison with the data measured in this study. This is shown in Fig. 7.13 and 7.14 for surface S1 (representing a very smooth surface with $s = 0.40$) and surface S4 (representing a very rough surface with $s = 3.02$). In both cases, very good agreement is observed between the model and the measured data at all three frequencies and across the entire angular range between 20° and 70°. The levels of the measured values of σ°_{vv} and σ°_{hh} at $\theta = 10°$ for surface S1 include a strong contribution due to the coherent backscattering component that exists at angles close to normal incidence. No attempt has been made at this stage to add a coherent component to the empirical, and therefore its range of applicability does not include the angular range below 20° for smooth surface. If the surface is rough, as is the cse for surface S4 (Fig. 7.14), the coherent backscattering coefficient is negligibly small, in which case the empirical model may be used at all angles between 0° and 70°.

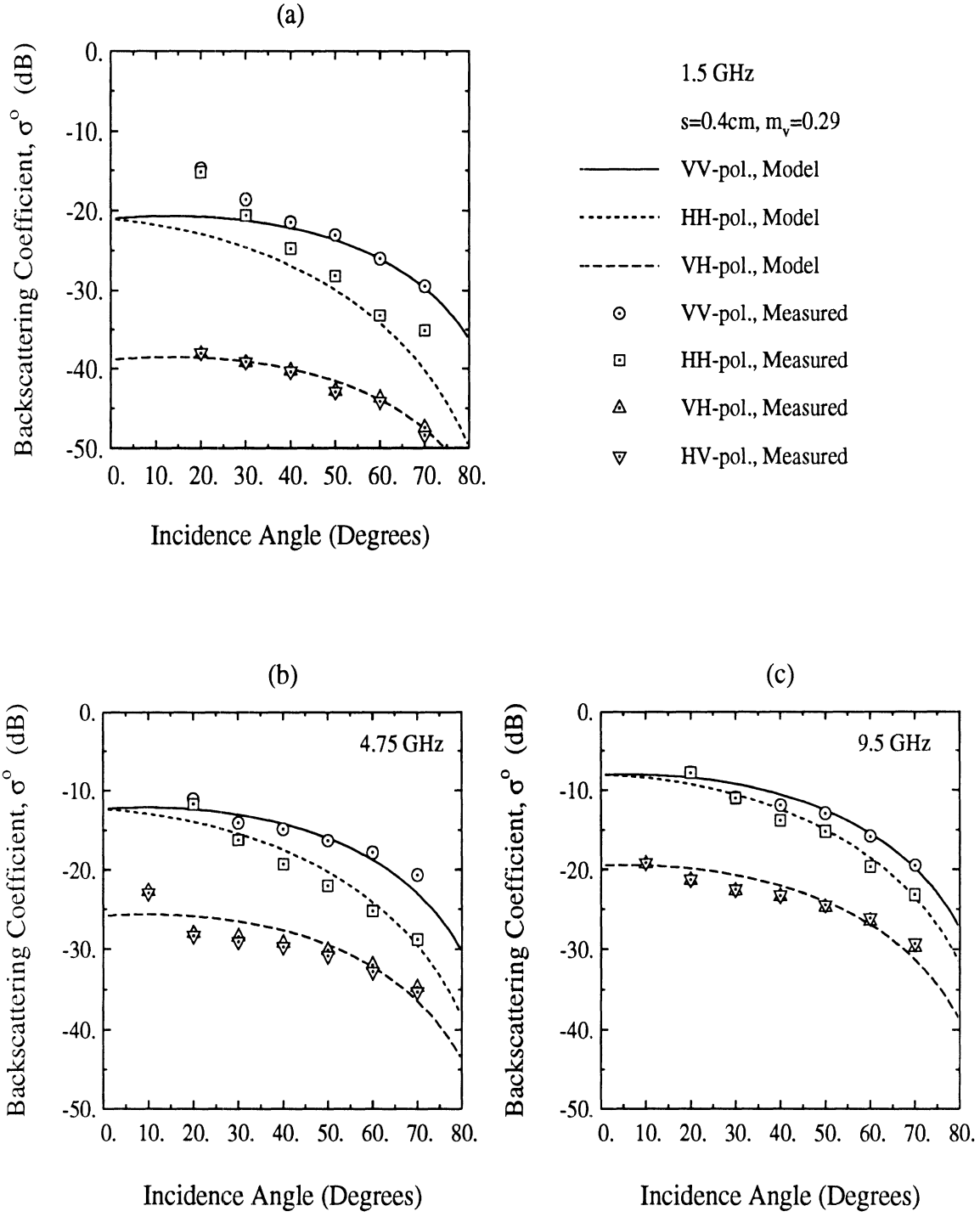

Figure 7.13: Empirical model compared to the measured data of surface 1 for wet soil at (a) 1.5 GHz, (b) 4.75 GHz, and (c) 9.5 GHz.

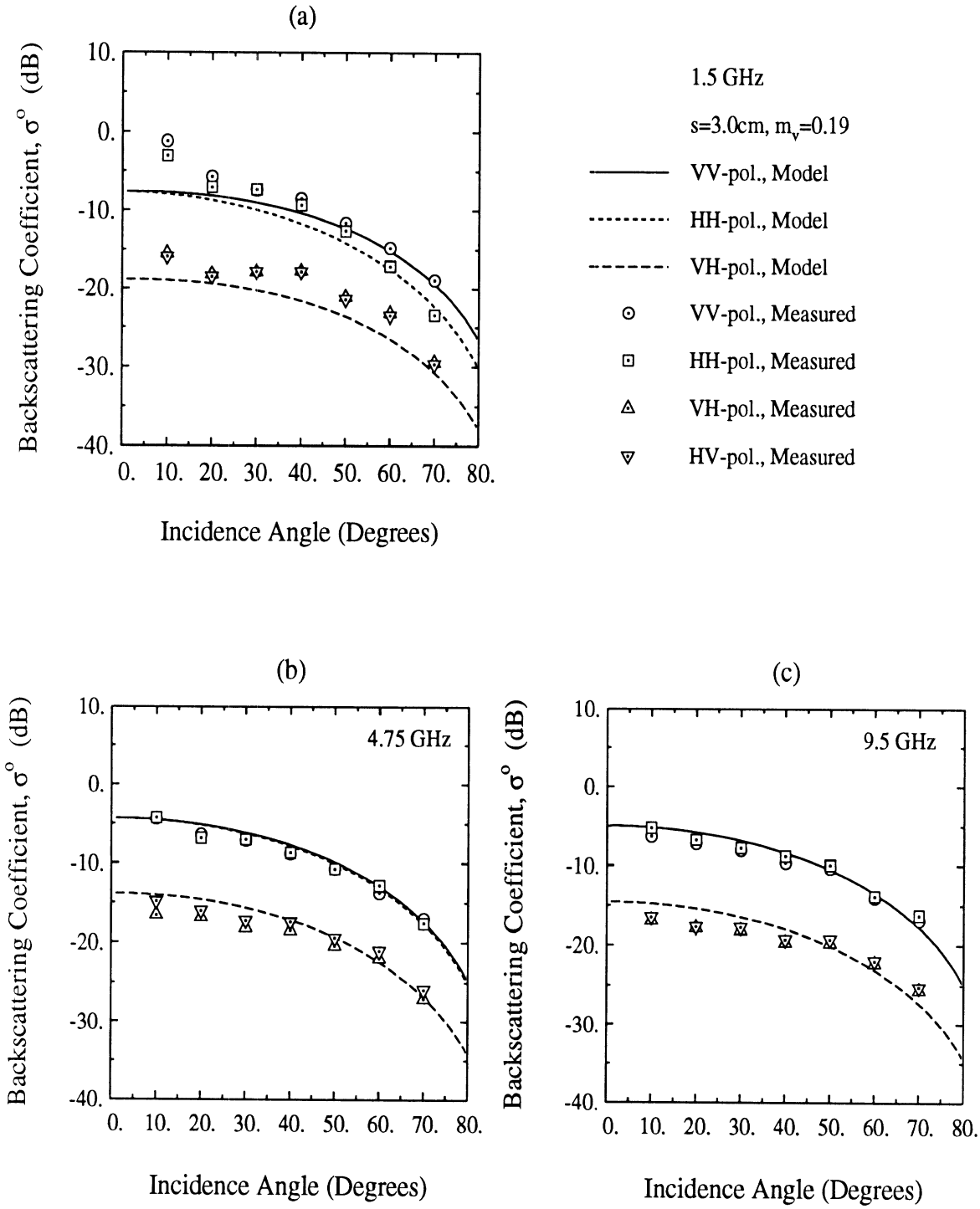

Figure 7.14: Empirical model compared to the measured data of surface 4 for wet soil at (a) 1.5 GHz, (b) 4.75 GHz, and (c) 9.5 GHz.

Table 7.6: Measured surface parameters for the Independent Data Set II.

Surface	Moisture contents, m_v			rms height,	correl.
No	Top soil	3cm depth	6cm depth	s (cm)	length, l (cm)
1	0.11	0.20	0.27	0.46	3.0
2	0.11	0.18	-	1.10	2.9
3	0.08	0.18	-	2.88	4.0

7.4.3 Comparison With Independent Data Set

Prior to conducting the measurements reported in this study, another data set was acquired by the same radar system for three surface roughnesses. The surface profiles were measured by inserting a plate into the surface and spraying it with paint. Such a technique provides an approximate representation of the surface, but it is not as accurate as that obtained using the laser profiler. Hence, our estimate of the values of ks and kl for Independent Data Set are not as accurate as those we obtained with the laser profiler for the surfaces discussed in the preceding sections of this section. Nevertheless, we conducted an evaluation of the semi-empirical model by comparing its prediction with the backscatter data of Independent Data Set II and found the agreement to be very good at all three frequencies, provided we are allowed to modify the values of s measured with the metal plate technique. An example is given in Fig. 7.15 in which the curves were calculated using the empirical model with $s = 0.7$; the value of s estimated from the metal-plate record was 0.46 cm (Table 7.4.3).

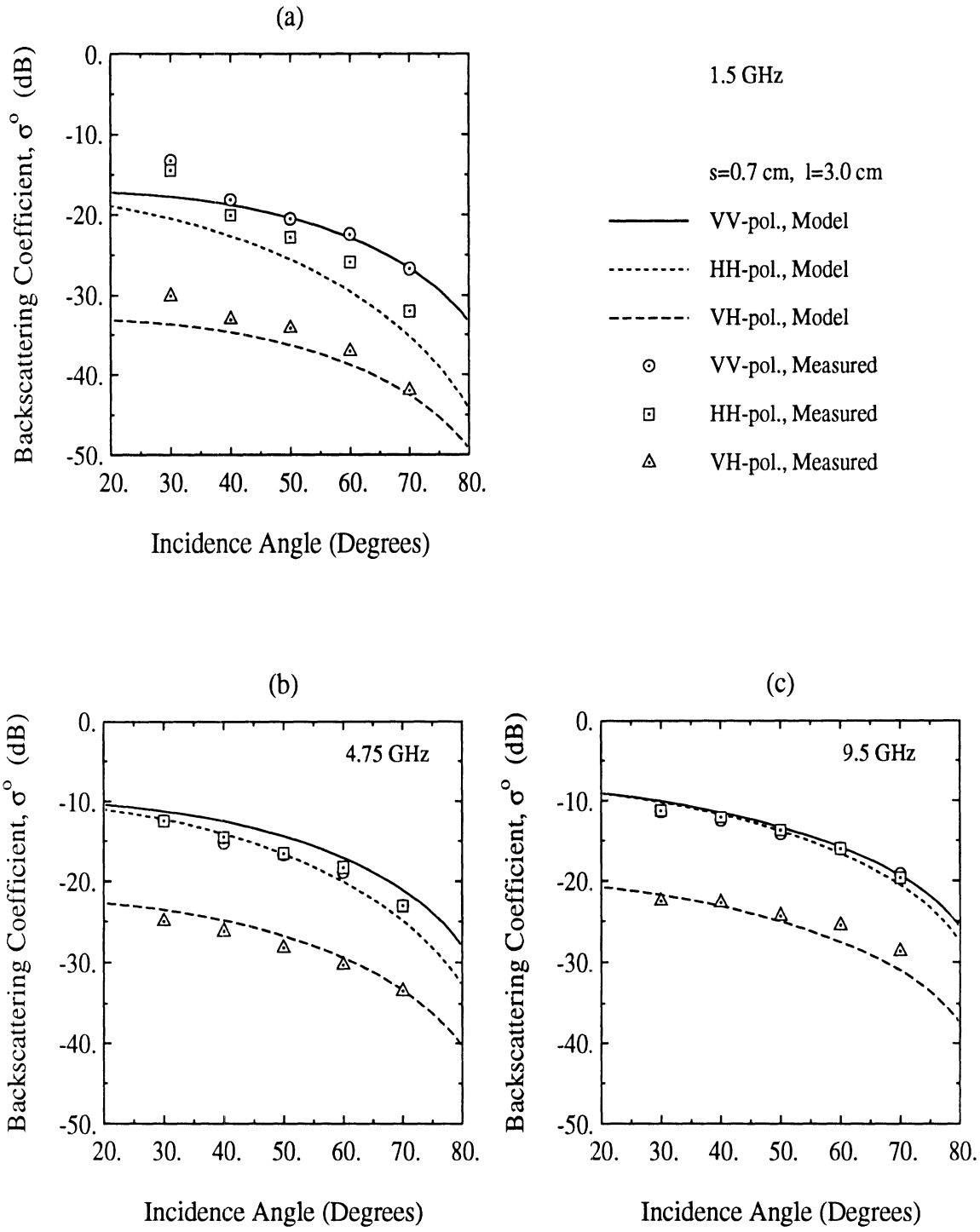

Figure 7.15: Empirical model compared with the data from independent data set II for a surface with $s = 0.7$ *cm* and $l = 3.0$ *cm*, measured at (a) 1.5 GHz, (b) 4.75 GHz, and (c) 9.5 GHz

Table 7.7: Surface parameters for Yamasaki et al.'s measurement.

	Soil-1	Soil-2	Soil-3
Frequency (GHz)	57 - 58		
Soil moisture	30%		
ϵ_r	1.9 -j0.4		
s (cm)	0.013	0.051	0.139
l (cm)	0.055	0.12	0.20
ks	0.16	0.64	1.75
kl	0.69	1.51	2.51

7.4.4 Comparison With 60 GHz Data

Our final comparison is with a 60 GHz data set that was recently reported by Yamasaki et al. 1991. Even though $k = 2\pi/\lambda = 1260$ at 60 GHz, the three surfaces examined in this study were extremely smooth, with rms heights of 0.055 cm, 0.12 cm, and 0.20 cm. The corresponding values of ks are 0.16, 0.64, and 1.75 as summarized in Table 7.4.4. Good overall agreement is observed (Fig. 7.16) between this data and the empirical model, inspite of the fact that the correlation lengths for all three surfaces are smaller than the smallest correlation length of the surfaces on the basis of which the empirical model was developed.

7.5 INVERSION MODEL

Having established in the preceding section that the semi-empirical model (SEM) is a good estimator of σ°_{vv}, σ°_{hh}, and σ°_{vh} over a wide range of ks (0.1 to 6), we shall now invert the model to obtain estimates of s and the moisture content m_v from

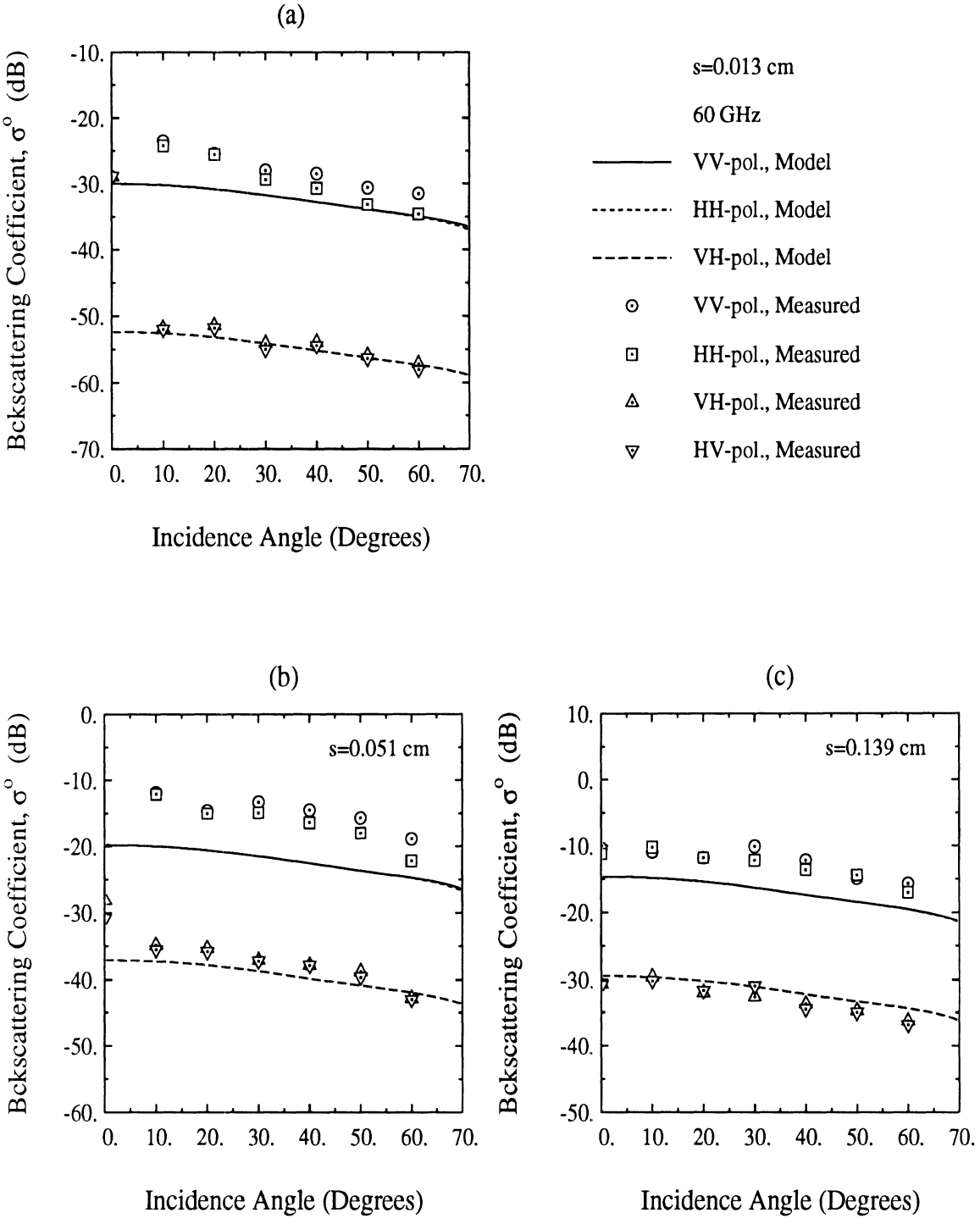

Figure 7.16: Empirical model compared with the data reported by Yamasaki et al. [1991] at 60 GHz for (a) soil-1 (s=0.013 cm, l=0.055 cm), (b) soil-2 (s=0.051 cm, l=0.12 cm), and (c) soil-3 (s=0.139 cm, l=0.20 cm).

observation of σ°_{vv}, σ°_{hh}, and σ°_{vh}. Because the semi-empirical model was developed on the basis of data for surfaces with kl in the range $2.6 < kl < 19.7$, we cannot ascertain its applicability of the inversion model for surfaces with kl outside this range. Suppose we have measurements of σ°_{vv}, σ°_{hh}, and σ°_{vh} for a given surface at a given incidence angle θ and wavelength λ. From these measurements, we compute the co-polarized and cross-polarized ratios $p = \sigma^\circ_{hh}/\sigma^\circ_{vv}$ and $q = \sigma^\circ_{hv}/\sigma^\circ_{vv}$. By eliminating ks from (7.2) and (7.4), we obtain the following nonlinear equation for Γ_o:

$$\left(\frac{2\theta}{\pi}\right)^{1/[3.0\Gamma_o]} \cdot \left[1 - \frac{q}{0.23\sqrt{\Gamma_o}}\right] + \sqrt{p} - 1 = 0 \tag{7.9}$$

where θ is the incidence angles in radians. After solving for Γ_o using an iterative technique, we can calculate the real part of the dielectric constant ϵ'_r from (7.3) by ignoring the imaginary part ϵ''_r, which is a valid approximation for a soil material. Next, the moisture content m_v and the imaginary part of the dielectric constant ϵ''_r can be determined from the model given in [Hallikainen et al., 1985]. Finally, with Γ_o known, the roughness parameter ks can be determined from (7.4).

Because the co-polarized and cross polarized ratios p and q are not sensitive to surface roughness for very rough surfaces ($ks > 3$), this technique cannot estimate ks for such surfaces. Hence, it is preferable to use radar observations at the lowest available frequency for estimating the moisture content and rms height of a bare soil surface. By way of illustrating the capability of the inversion technique, we present in Fig. 7.17(a) the values of ks estimated by the inversion technique plotted against the values measured *in situ*. The data points include the data measured in support of this study for all surface conditions (1990 data) in addition to the data measured independently one year later (1991 data), but exclude the surfaces for which $ks > 3$. Each data point in Fig. 7.17(a) represents the average values for four incidence angles (30° to 60°) and two different moisture conditions (wet and dry). Figure 7.17(b) shows

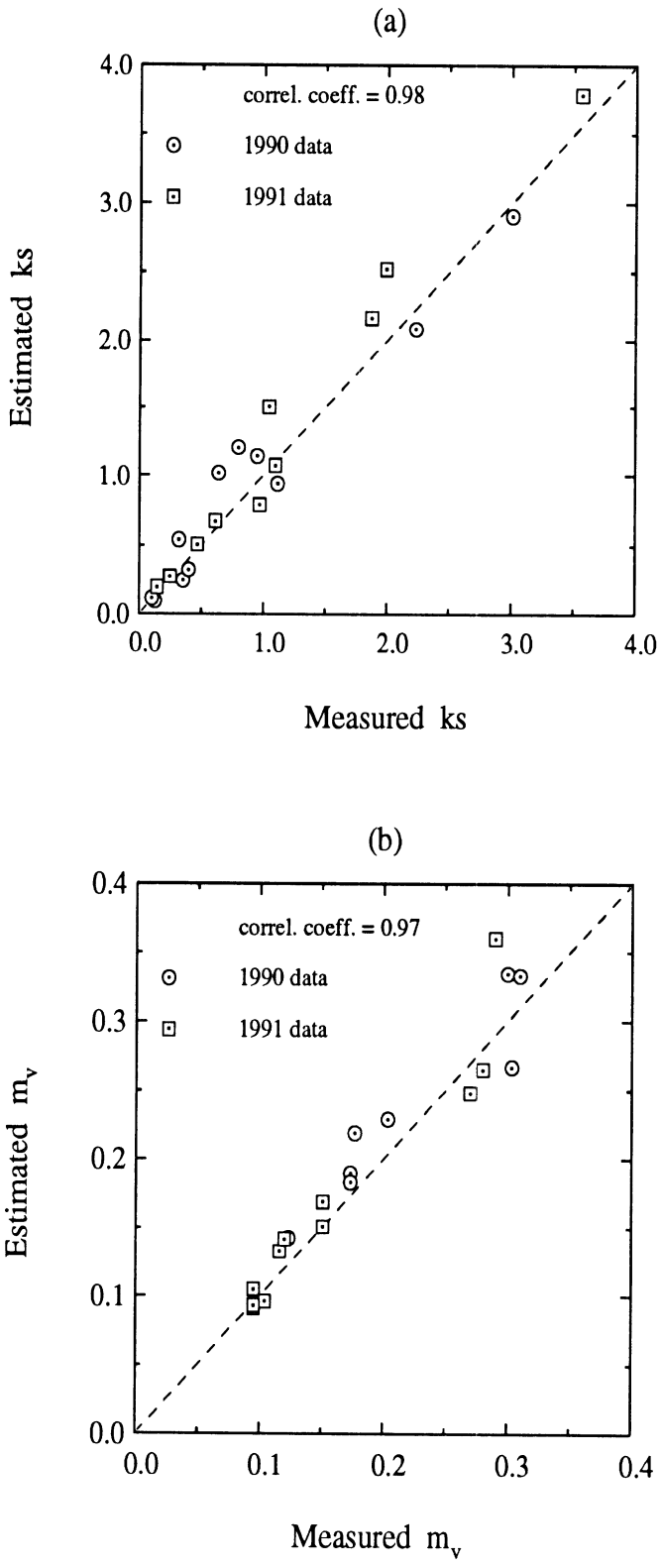

Figure 7.17: Comparison between the values of surface parameters estimated by the inversion technique and those measured *in situ* for (a) ks and (b) the volumetric moisture contents m_v.

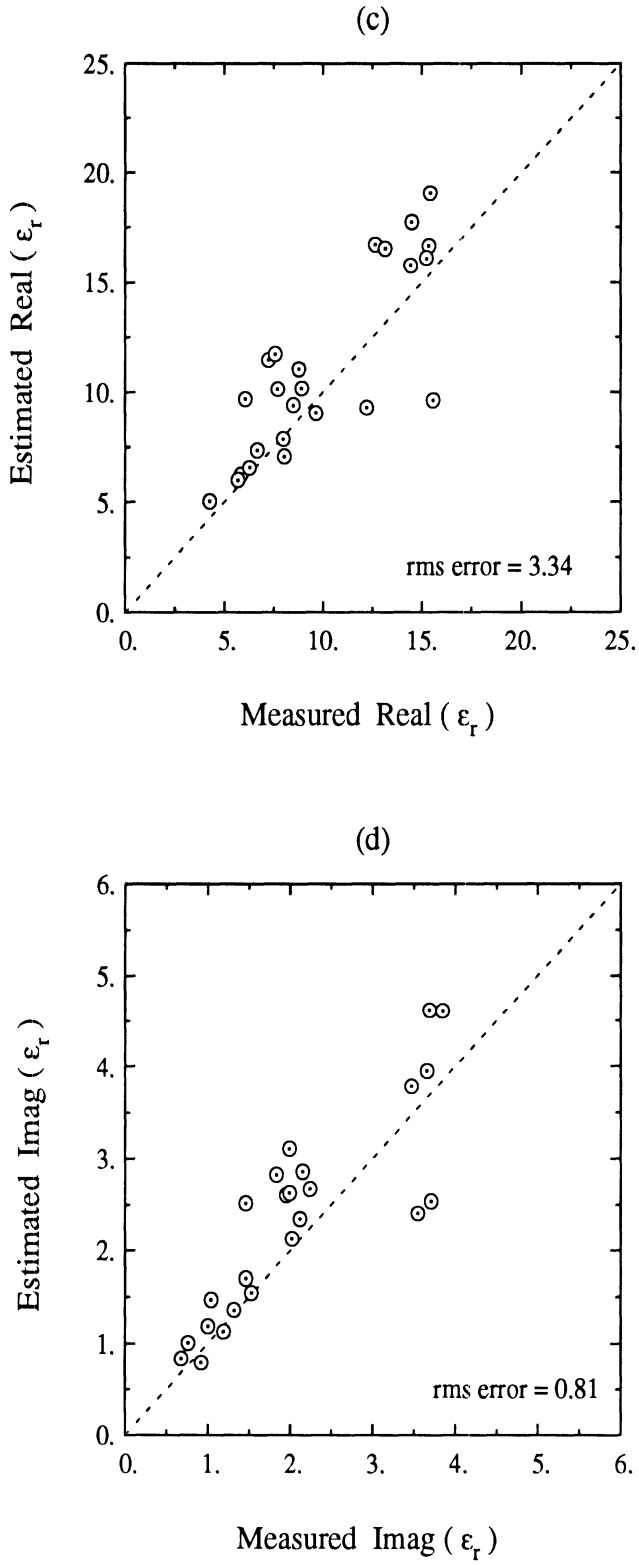

Figure 7.18: Comparison between the values of surface parameters estimated by the inversion technique and those measured *in situ* for (a) the real part of ϵ_r and (b) the imaginary part of ϵ_r.

the results for m_v where each data point presents the average values for four incidence angles (30° to 60°) and three different frequencies (L, C, and X-band). Figures 7.18 (a) and (b) show the results for ϵ_r' and ϵ_r'', respectively, for all surfaces measured in this study (the inversion technique is capable of estimating ϵ_r', ϵ_r'', and m_v for any ks, but it is incapable of estimating ks if $ks > 3$). Note that for each value of m_v, we have three sets of values for ϵ_r' and ϵ_r'', corresponding to the three frequencies used in this study. Inversion diagrams could be generated (see Appendix B) for the frequencies of 1.25 and 5.3 GHz at 20°, 30°, 40°, 50°, and 60° using the semi-empirical scattering model developed in this study. The approximated values of the moisture content m_v and the rms height s can be estimated quickly by looking up the inversion diagrams with known values of co- and cross-polarized ratios.

The results displyed in Figs. 7.17 and 7.18 represent the first demonstration ever reported of a practical algorithm for estimating the roughness, dielectric constant, and moisture content of a bare soil surface from multi-polarized radar observations. Before this technique can be widely applied, however, it is prudent to conduct additional experiments over a wide range of roughness and moisture conditions.

7.6 CONCLUSIONS

The major results of this study are summarized as follows:

1. At microwave frequencies, the available rough-surface scattering models are incapable of predicting the scattering behavior observed for bare-soil surface.

2. The co-polarized ratio $p = \sigma_{hh}^{\circ}/\sigma_{vv}^{\circ} \leq 1$ for all angles, roughness conditions, and moisture contents; for all values of incidence angle, roughness, and moisture contents. The ratio p increases rapidly with increasing ks up to $ks \simeq 1$, then it increases at a slower rate, reaching the value 1 for $ks > 3$. For $ks < 3$, p

decreases with increasing incidence angle and with increasing moisture content.

3. The cross-polarized ratio $q = \sigma^{\circ}_{vh}/\sigma^{\circ}_{vv}$ exhibits a strong dependence on ks and a relatively weak dependence on moisture content. The ratio q increases rapidly with increasing ks up to $ks \simeq 1$, then it increases at a slower rate, reaching the value (that depends on the moisture content) for $ks > 3$.

4. The proposed scattering model (SEM) provides very good agreement with experimental observations made over the ranges $0.1 \leq ks \leq 6.0$, $2.5 \leq kl \leq 20.0$, and $0.09 \leq m_v \leq 0.31$. The model was found to be equally applicable when tested against radar data measured for surfaces with parameters outside the above ranges. re outside of the above ranges.

5. Soil moisture content (m_v) and surface roughness (ks) can be retrieved from multipolarized radar observations by applying the model-driven inversion technique developed in this chapter.

CHAPTER VIII

CONCLUSIONS AND RECOMMENDATIONS

8.1 Summary

The major contributions of this thesis have been the developments of a semi-empirical model (SEM) for microwave backscattering from bare soil surfaces and an inversion algorithm for retrieving soil moisture and surface roughness from the polarimetric radar backscatter. Besides these major accomplishments, the classical scattering models were evaluated using exact numerical solutions and extensive experimental observations. Also, an accurate calibration technique for the measurement of polarimetric backscatter from distributed targets was developed.

In Chapter 2, classical scattering models for radar backscattering from dielectric random surfaces were reviewed. In specific, the small perturbation method and the Kirchhoff approximation (the physical optics and geometrical optics models) were considered.

In Chapter 3, a Monte Carlo method in conjunction with the method of moments was developed to solve scattering from a one-dimensional conducting random surface. In order to make the numerical simulation of the random surface scattering tractable, the random surface sample of finite length must be considered. Since the edges of the finite sample perturb the scattering solution, the edge contribution should be

suppressed. This is done by adding a resistive sheet at each end of the illuminated surface sample. This numerical technique was used to examine existing scattering models and to compute the phase-difference statistics as well as the backscattering coefficients.

In Chapter 4, an improved high frequency scattering solution was formulated and evaluated numerically for a one-dimensional random surface. This solution showed an excellent agreement with the numerical solution developed in chapter 3. Using this formulation, the zeroth- and the first-order classical physical optics approximations were examined.

In Chapter 5, the effect of dielectric inhomogeneity in a soil medium was considered by developing an efficient numerical technique for one-dimensional inhomogeneous dielectric rough surfaces.

In Chapter 6, an accurate technique for measurement of polarimetric backscatter from distributed targets was introduced. In this technique the polarization distortion matrix of a radar system was completely characterized from the polarimetric response of a sphere over the entire main lobe of the antenna.

In Chapter 7, the experimental procedure and the backscattered data collected from bare soil surfaces with many different roughness and moisture conditions at microwave frequencies were explained. These data were analyzed and compared with the results from the theoretical scattering models. Also they were used to find the dependency of the backscattering coefficients on the radar and the surface parameters. Using the co-polarized and the cross-polarized ratios ($\sigma^{\circ}_{hh}/\sigma^{\circ}_{vv}$, $\sigma^{\circ}_{hv}/\sigma^{\circ}_{vv}$), a semi-empirical scattering model was developed. It was shown that the semi-empirical scattering model provided a very good agreement with independent experimental observations. In this chapter an inversion algorithm for the empirical model was also

developed, and its performance in estimation of the soil moisture and surface roughness parameters was tested.

8.2 Recommendations for Future Work

Numerical solution of electromagnetic wave scattering from randomly rough surface exists at present for only one-dimensional surfaces. Since the numerical solution of a one-dimensional random surface doesn't predict the cross-polarized scattering coefficient and moreover gives anisotropic results, development of a numerical code for scattering from a two-dimensional random surface would be extremely useful because it can be used for verification of not only the existing scattering models but also experimental observations for the co- and cross-polarized backscattering coefficients and the phase difference statistics. One way may be to start by solving a scatter problem of a three-dimensional dielectric hump above an impedance surface. Then, scattering from two-dimensional random surface could be solved similarly as the Monte Carlo method presented in Chapter 5. In order to achieve this work, either a powerful computer may be used, or the problem itself might be simplified with an efficient numerical technique.

Existing scattering models for rough surfaces, including the semi-empirical model developed in this study, have ignored the information contained in the phase difference statistics. However, it have been shown that the phase difference statistics measured from bare soil surfaces by a polarimetric radar depends on radar parameters (frequency, incidence angle, and polarization) and target parameters (soil moisture and surface roughness). The preliminary results show that the co-polarized phase difference distribution has a strong dependency on the target and radar parameters, while the cross-polarized phase difference distribution doesn't have any dependency

on the target and radar parameters. In order to utilize the phase difference information, it seems necessary to extend the scattering models to relate the co-polarized phase difference distribution to surface roughness and soil moisture.

The semi-empirical model is based on radar measurements of a limited number of soil surfaces. In order to increase the validity of the model, it would be recommended to conduct additional experiments over a wide range of roughnesses and soil types. Since the backscattering coefficients of soil surface show strong dependencies on soil moisture and rms height, the semi-empirical model was given as a function of those parameters. However, the backscattering coefficients was also affected by other parameters such as the correlation length and soil type of the surface even though the dependencies are relatively weak as shown in Fig. 8.1. I believe the validity of the semi-empirical model can be extended by finding more functional relationships and using more target parameters with additional extensive experiments.

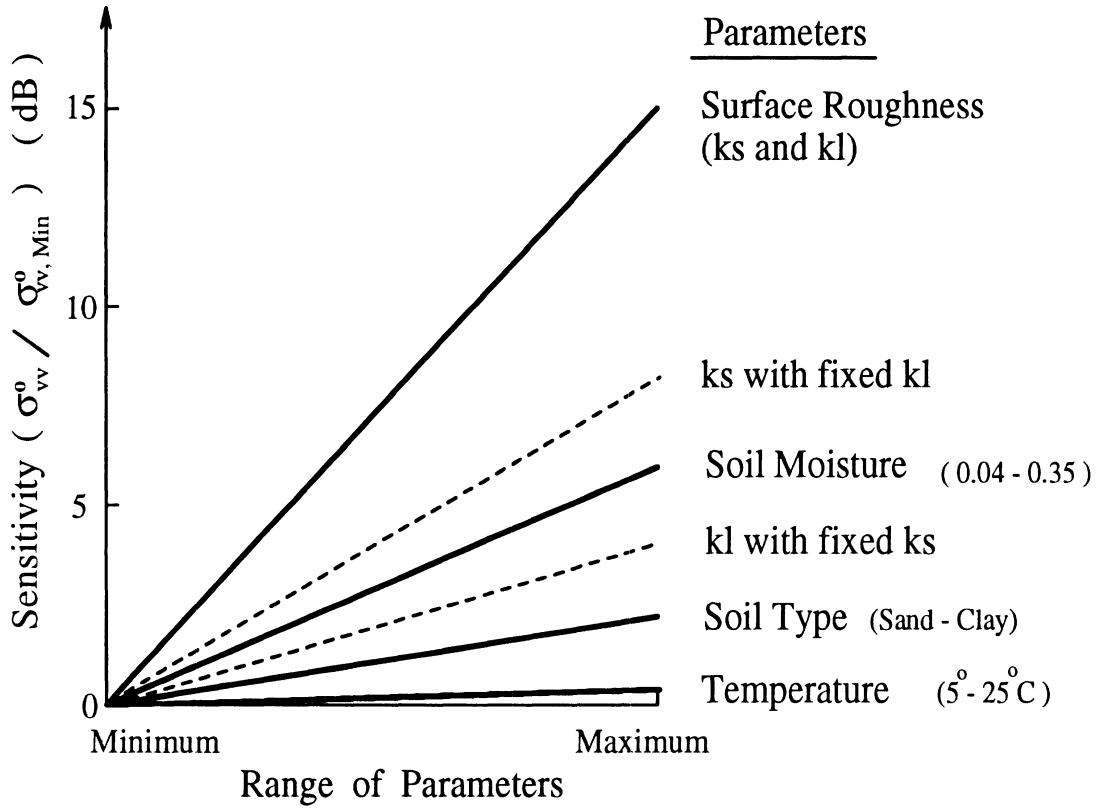

Figure 8.1: Sensitivity of σ°_{vv} on surface parameters at 40°.

APPENDICES

APPENDIX A

CHARACTERISTIC FUNCTION FOR A GAUSSIAN RANDOM VECTOR

The characteristic function is defined as;

$$\Phi_{\overline{X}}(\overline{\omega}) \triangleq \left\langle e^{i\overline{\omega}^T\overline{x}} \right\rangle = \int_{-\infty}^{\infty} P_{\overline{X}}(\overline{x})\, e^{i\overline{\omega}^T\overline{x}}\, d\overline{x} \tag{A.1}$$

where $\overline{x} = (x_1, \cdots, x_n)^T$ is a real n-component random vector, $\overline{\omega} = (\omega_1, \cdots, \omega_n)^T$ is a real n-component parameter vector. The probability density function (PDF) $P_{\overline{X}}(\overline{x})$ for a Gaussian random vector can be written compactly as;

$$P_{\overline{X}}(\overline{x}) = \frac{1}{(2\pi)^{n/2}[det(\overline{\overline{K}})]^{1/2}} \exp\left[-\frac{1}{2}(\overline{x}-\overline{\mu})^T\ \overline{\overline{K}}^{-1}\ (\overline{x}-\overline{\mu})\right] \tag{A.2}$$

where $\overline{\mu} = (\mu_1, \cdots, \mu_n)^T$ is a n-component mean vector and $\overline{\overline{K}}$ is the covariance matrix defined as the average value of the outer vector product $(\overline{x}-\overline{\mu}) \cdot (\overline{x}-\overline{\mu})^T$, *i.e.*,

$$\overline{\overline{K}} \triangleq \left\langle (\overline{x}-\overline{\mu})(\overline{x}-\overline{\mu})^T \right\rangle. \tag{A.3}$$

Substituting (A.3) into (A.1), the characteristic function for a Gaussian random vector can be obtained. When we assume a Gaussian random vector has zero mean, the

covariance matrix becomes a correlation matrix $\overline{\overline{R}}$,

$$\overline{\overline{R}} \triangleq \left\langle \overline{x}\,\overline{x}^T \right\rangle = \begin{bmatrix} < x_1\,x_1 > & < x_1\,x_2 > & \cdots & < x_1\,x_n > \\ \cdot & \cdot & \cdot & \cdot \\ \cdot & \cdot & \cdot & \cdot \\ < x_n\,x_1 > & < x_n\,x_2 > & \cdots & < x_n\,x_n > \end{bmatrix}, \tag{A.4}$$

which is a real symmetric matrix, and the corresponding characteristic function is given [Stark and Woods; 1986] as;

$$\Phi_{\overline{X}}(\overline{\omega}) = \exp\left[-\frac{1}{2}\overline{\omega}^T\overline{\overline{R}}\overline{\omega}\right] = \exp\left[-\frac{1}{2}\sum_{m=1}^{n}\sum_{n=1}^{n}\omega_m\omega_n\left\langle x_m x_n\right\rangle\right]. \tag{A.5}$$

In order to get the characteristic function for a two-dimensional random surface having a Gaussian height distribution with the random vector $\overline{x} = [Z_{x_1},\ Z_{x_2}, Z_{y_1},\ Z_{y_2}, z_d]^T$ and the parameter vector $\overline{\omega} = [-\alpha_{x_1},\ \alpha_{x_2}, -\alpha_{y_1},\ \alpha_{y_2}, k_{dz}]^T$ (Ch. 3), at first the correlation matrix is written explicitly as;

$$\begin{aligned} \overline{\overline{R}} &\triangleq \left\langle \overline{x}\,\overline{x}^T \right\rangle \\ &= \begin{bmatrix} < Z_{x_1}^2 > & < Z_{x_1}Z_{x_2} > & < Z_{x_1}Z_{y_1} > & < Z_{x_1}Z_{y_2} > & < Z_{x_1}z_d > \\ < Z_{x_1}Z_{x_2} > & < Z_{x_2}^2 > & < Z_{x_2}Z_{y_1} > & < Z_{x_2}Z_{y_2} > & < Z_{x_2}z_d > \\ < Z_{x_1}Z_{y_1} > & < Z_{x_2}Z_{y_1} > & < Z_{y_1}^2 > & < Z_{y_1}Z_{y_2} > & < Z_{y_1}z_d > \\ < Z_{x_1}Z_{y_2} > & < Z_{x_2}Z_{y_2} > & < Z_{y_1}Z_{y_2} > & < Z_{y_2}^2 > & < Z_{y_2}z_d > \\ < Z_{x_1}z_d > & < Z_{x_2}z_d > & < Z_{y_1}z_d > & < Z_{y_2}z_d > & < z_d^2 > \end{bmatrix}. \end{aligned} \tag{A.6}$$

When we consider the random process of zero mean, $\mu = \langle z(x,y)\rangle = 0$, the variance is defined as $\sigma^2 \triangleq \langle z^2(x,y)\rangle$. Since we assume the random process $\{z(x,y)\}$ is stationary in the wider sense, the correlation of $z(x_1,y_1)$ and $z(x_2,y_2)$ can be computed as;

$$C(u,v) = C(x_1 - x_2, y_1 - y_2) \triangleq \langle z(x_1,y_1)z(x_2,y_2)\rangle = \sigma^2\rho(u,v) \tag{A.7}$$

where the correlation coefficient $\rho(u,v)$ is defined by

$$\rho(u,v) \triangleq \frac{\langle z(x_1,y_1)z(x_2,y_2)\rangle}{\sqrt{\langle z^2(x_1,y_1)\rangle}\sqrt{\langle z^2(x_2,y_2)\rangle}} \tag{A.8}$$

and $\langle z^2(x_1,y_1)\rangle = \langle z^2(x_2,y_2)\rangle = \sigma^2$. Quadratic-mean derivative of a random process $\{z(x)\}$ at a point x is defined [Wong and Hajek, 1985] as

$$Z_x \triangleq \frac{\partial z(x)}{\partial x} \triangleq \lim_{\Delta x \to 0} \frac{z(x+\Delta x) - z(x)}{\Delta x}, \tag{A.9}$$

when the following conditions are satisfied;

$$\lim_{\Delta x, \Delta x' \to 0} \left\langle \left| \frac{z(x+\Delta x) - z(x)}{\Delta x} - \frac{z(x+\Delta x') - z(x)}{\Delta x'} \right|^2 \right\rangle = 0.$$

One element $< Z_{x_1}^2 >$ of the correlation matrix $\overline{\overline{R}}$ can be computed using (A.9) and the linearity of expectation as

$$\left\langle Z_{x_1}^2 \right\rangle = \lim_{\Delta u \to 0} \frac{1}{(\Delta u)^2} \left\langle z^2(x_1+\Delta u, y_1) + z^2(x_1,y_1) - 2z(x_1+\Delta u, y_1)\, z(x_1,y_1) \right\rangle$$

$$= \lim_{\Delta u \to 0} \frac{1}{(\Delta u)^2} 2\sigma^2 \left[1 - \rho(\Delta u, 0)\right]. \tag{A.10}$$

When we expand the correlation coefficient $\rho(u,v)$ in a Taylor's series for a function of two variables,

$$\rho(a+h, b+k) = \rho(a,b) + \left(h\frac{\partial \rho(u,v)}{\partial u} + k\frac{\partial \rho(u,v)}{\partial v} \right)\Bigg|_{\substack{u=a \\ v=b}}$$

$$+ \frac{1}{2!}\left(h^2\frac{\partial^2 \rho(u,v)}{\partial u^2} + 2hk\frac{\partial^2 \rho(u,v)}{\partial u \partial v} + k^2\frac{\partial^2 \rho(u,v)}{\partial v^2} \right)\Bigg|_{\substack{u=a \\ v=b}} + \cdots. \tag{A.11}$$

Since the correlation coefficient $\rho(u,v)$ is an even function having a maximum of 1 at $u = v = 0$, (A.11) can be rewritten substituting $h = \Delta u$, $k = 0$, and $a = b = 0$ as,

$$\rho(\Delta u, 0) = 1 + \frac{(\Delta u)^2}{2!}\frac{\partial^2 \rho(u,v)}{\partial u^2}\Bigg|_{\substack{u=0 \\ v=0}} + \frac{(\Delta u)^4}{4!}\frac{\partial^4 \rho(u,v)}{\partial u^4}\Bigg|_{\substack{u=0 \\ v=0}} + \cdots. \tag{A.12}$$

Therefore, substituting (A.12) into (A.10, $< Z_{x_1}^2 >$ can be computed as

$$\left\langle Z_{x_1}^2 \right\rangle = 2\sigma^2 \lim_{\Delta u \to 0} \left[-\frac{1}{2} \left. \frac{\partial^2 \rho(u,v)}{\partial u^2} \right|_{\substack{u=0 \\ v=0}} + \frac{(\Delta u)^2}{4!} \left. \frac{\partial^4 \rho(u,v)}{\partial u^4} \right|_{\substack{u=0 \\ v=0}} + \cdots \right]$$

$$= -\sigma^2 \left. \frac{\partial^2 \rho(u,v)}{\partial u^2} \right|_{\substack{u=0 \\ v=0}}. \tag{A.13}$$

In order to avoid complicity in writing, new notations are defined for convenience as follows;

$$\left. \frac{\partial \rho(u,v)}{\partial u} \right|_{\substack{u=a \\ v=b}} \triangleq \rho_u(a,b), \quad \left. \frac{\partial \rho(u,v)}{\partial v} \right|_{\substack{u=a \\ v=b}} \triangleq \rho_v(a,b), \quad \left. \frac{\partial^2 \rho(u,v)}{\partial u^2} \right|_{\substack{u=a \\ v=b}} \triangleq \rho_{uu}(a,b)$$

$$\left. \frac{\partial^2 \rho(u,v)}{\partial v^2} \right|_{\substack{u=a \\ v=b}} \triangleq \rho_{vv}(a,b), \quad \left. \frac{\partial^2 \rho(u,v)}{\partial u \, \partial v} \right|_{\substack{u=a \\ v=b}} \triangleq \rho_{uv}(a,b), \quad etc. \tag{A.14}$$

Using stationary characteristics and new notations, the diagonal elements of the correlation matrix can be computed as;

$$\left\langle Z_{x_1}^2 \right\rangle = \left\langle Z_{x_2}^2 \right\rangle = -\sigma^2 \rho_{uu}(0,0), \tag{A.15}$$

$$\left\langle Z_{y_1}^2 \right\rangle = \left\langle Z_{y_2}^2 \right\rangle = -\sigma^2 \rho_{vv}(0,0), \tag{A.16}$$

$$\left\langle z_d^2 \right\rangle = \left\langle z^2(x_1,y_1) + z^2(x_2,y_2) - 2z(x_1,y_1)\, z(x_2,y_2) \right\rangle = 2\sigma^2 \left[1 - \rho(u,v)\right]. \tag{A.17}$$

The off-diagonal elements of the correlation matrix can also be computed using the quadratic-mean derivatives (A.9) and the the Taylor's series expansion (A.11).

$$\langle Z_{x_1}\, Z_{x_2} \rangle = \lim_{\Delta u \to 0} \frac{1}{(\Delta u)^2} \langle z(x_1 + \Delta u, y_1)\, z(x_2 + \Delta u, y_2) + z(x_1,y_1)\, z(x_2,y_2)$$

$$- z(x_1 + \Delta u, y_1)\, z(x_2,y_2) - z(x_1,y_1)\, z(x_2 + \Delta u, y_2) \rangle \tag{A.18}$$

$$= \lim_{\Delta u \to 0} \frac{1}{(\Delta u)^2} \sigma^2 \left[2\rho(u,v) - \rho(u + \Delta u, v) - \rho(u - \Delta u, v)\right]. \tag{A.19}$$

The correlation coefficients, $\rho(u+\Delta u, v)$ and $\rho(u-\Delta u, v)$ can be obtained from (A.11) with $h = \Delta u$, $k = 0$, $a = u$, and $b = v$ as,

$$\rho(u + \Delta u, v) = \rho(u,v) + \Delta u \rho_u(u,v) + \frac{(\Delta u)^2}{2!} \rho_{uu}(u,v) + \cdots, \tag{A.20}$$

$$\rho(u - \Delta u, v) = \rho(u,v) - \Delta u \rho_u(u,v) + \frac{(\Delta u)^2}{2!} \rho_{uu}(u,v) - \cdots. \tag{A.21}$$

Substituting (A.20) and (A.21) into (A.19),

$$\langle Z_{x_1}\ Z_{x_2}\rangle = -\sigma^2\rho_{uu}(u,v). \tag{A.22}$$

Similarly,

$$\langle Z_{y_1}\ Z_{y_2}\rangle = -\sigma^2\rho_{vv}(u,v). \tag{A.23}$$

Other components of the correlation matrix can be computed in similar manners as follows;

$$\begin{aligned}\langle Z_{x_1}\ Z_{y_1}\rangle &= \lim_{\Delta u\to 0}\frac{1}{(\Delta u)^2}\Big\langle z(x_1+\Delta u,y_1)\ z(x_1,y_1+\Delta u)+z^2(x_1,y_1)\\ &\qquad -z(x_1+\Delta u,y_1)\ z(x_1,y_1)-z(x_1,y_1+\Delta u)\ z(x_1,y_1)\Big\rangle\\ &= \lim_{\Delta u\to 0}\frac{\sigma^2}{(\Delta u)^2}\left[\rho(\Delta u,\Delta u)+1-\rho(\Delta u,0)-\rho(0,\Delta u)\right].\end{aligned} \tag{A.24}$$

where

$$\begin{aligned}\rho(\Delta u,\Delta u) &= \rho(0,0)+\Delta u\left[\rho_u(0,0)+\rho_v(0,0)\right]\\ &\qquad +\frac{(\Delta u)^2}{2!}\left[\rho_{uu}(0,0)+2\rho_{uv}(0,0)+\rho_{uu}(0,0)\right]+\cdots\\ &= 1+\frac{(\Delta u)^2}{2}\left[\rho_{uu}(0,0)+\rho_{uu}(0,0)\right]+\cdots\end{aligned} \tag{A.25}$$

$$\rho(\Delta u,0) = 1+\frac{(\Delta u)^2}{2}\rho_{uu}(0,0)+\cdots \tag{A.26}$$

$$\rho(0,\Delta u) = 1+\frac{(\Delta u)^2}{2}\rho_{vv}(0,0)+\cdots. \tag{A.27}$$

Substituting (A.25)-(A.27) into (A.24),

$$\langle Z_{x_1}\ Z_{y_1}\rangle = \langle Z_{x_2}\ Z_{y_2}\rangle = 0. \tag{A.28}$$

In a similar manner, other components are obtained as;

$$\langle Z_{x_1}\ Z_{y_2}\rangle = \langle Z_{x_2}\ Z_{y_1}\rangle = -\sigma^2\rho_{uv}(u,v), \tag{A.29}$$

$$\langle Z_{x_1}\ z_d\rangle = \langle Z_{x_2}\ z_d\rangle = -\sigma^2\rho_u(u,v), \tag{A.30}$$

$$\langle Z_{y_1}\ z_d\rangle = \langle Z_{y_2}\ z_d\rangle = -\sigma^2\rho_v(u,v). \tag{A.31}$$

Finally, the correlation matrix can be written with the correlation coefficient and its derivatives, assuming an isotropic random surface such that $\rho_{uu}(0,0) = \rho_{vv}(0,0)$,

$$\overline{\overline{R}} = -\sigma^2 \begin{bmatrix} \rho_{uu}(0,0) & \rho_{uu}(u,v) & 0 & \rho_{uv}(u,v) & \rho_u(u,v) \\ \rho_{uu}(u,v) & \rho_{uu}(0,0) & \rho_{uv}(u,v) & 0 & \rho_u(u,v) \\ 0 & \rho_{uv}(u,v) & \rho_{uv}(0,0) & \rho_{uu}(u,v) & \rho_u(u,v) \\ \rho_{uv}(u,v) & 0 & \rho_{uu}(u,v) & \rho_{uu}(0,0) & \rho_u(u,v) \\ \rho_u(u,v) & \rho_u(u,v) & \rho_u(u,v) & \rho_u(u,v) & -2\left[1-\rho(u,v)\right] \end{bmatrix}. \quad \text{(A.32)}$$

Therefore, the characteristic function for a the Gaussian random vector, $\overline{x} = [Z_{x_1}, Z_{x_2}, Z_{y_1}, Z_{y_2}, z_d]^T$, can be computed using the components of the correlation matrix, $\overline{\overline{R}}$, and the parameter vector, $\overline{\omega} = [-\alpha_{x_1}, \alpha_{x_2}, -\alpha_{y_1}, \alpha_{y_2}, k_{dz}]^T$. After algebraic computations, the final form of the characteristic function is given by

$$\begin{aligned} \left\langle e^{i\overline{\omega}^T\overline{x}} \right\rangle &= \exp\left[-\frac{1}{2}\overline{\omega}^T\overline{\overline{R}}\overline{\omega}\right] = \\ &= \exp\left[\frac{\sigma^2}{2}\rho_{uu}(0,0)\left\{\alpha_{x_1}^2 + \alpha_{x_2}^2 + \alpha_{y_1}^2 + \alpha_{y_2}^2\right\} - \sigma^2 k_{dz}^2\left\{1-\rho(u,v)\right\}\right. \\ &\quad -\sigma^2\left\{\alpha_{x_1}\alpha_{x_2}\rho_{uu}(u,v) + \alpha_{y_1}\alpha_{y_2}\rho_{uv}(u,v) + \left(\alpha_{x_1}\alpha_{y_2} + \alpha_{x_2}\alpha_{y_1}\right)\rho_{vv}(u,v)\right\} \\ &\quad \left. -\sigma^2 k_{dz}\left\{\left(\alpha_{x_1} - \alpha_{x_2}\right)\rho_u(u,v) + \left(\alpha_{y_1} - \alpha_{y_2}\right)\rho_v(u,v)\right\}\right]. \end{aligned} \quad \text{(A.33)}$$

For a one-dimensional random surface, the correlation matrix for a random vector of $\overline{x} = [Z_{x_1}, Z_{x_2}, z_d]^T$ can be computed similarly with the two-dimensional surface case. Using the quadratic-mean derivative and the Taylor's series expansion, the correlation matrix $\overline{\overline{R}}_1$ is obtained as

$$\overline{\overline{R}}_1 = -\sigma^2 \begin{bmatrix} \rho_{uu}(0) & \rho_{uu}(u) & \rho_u(u) \\ \rho_{uu}(u) & \rho_{uu}(0) & \rho_u(u) \\ \rho_u(u) & \rho_u(u) & -2\left[1-\rho(u)\right] \end{bmatrix}. \quad \text{(A.34)}$$

The characteristic function for a one-dimensional surface having a Gaussian height distribution can be computed using the components of the correlation matrix $\overline{\overline{R}}_1$ and

the parameter vector $\overline{\omega}_1 = [-\alpha_1,\, \alpha_2,\, k_{dz}]^T$ as

$$\left\langle e^{-i\alpha_1 Z_{x_1} + i\alpha_2 Z_{x_2} + ik_{dz} z_d} \right\rangle = \left\langle e^{i\overline{\omega}_1^T \overline{x}} \right\rangle = \exp\left[-\frac{1}{2}\overline{\omega}_1^T \overline{\overline{R}}_1 \overline{\omega}_1\right] =$$

$$= \exp\left[\frac{\sigma^2}{2}\rho_{uu}(0)\left\{\alpha_1^2 + \alpha_2^2\right\} - \sigma^2 k_{dz}^2 \left\{1 - \rho(u)\right\}\right.$$

$$\left. -\sigma^2 \rho_{uu}(u)\alpha_1\alpha_2 - \sigma^2 \rho_u(u) k_{dz}\left(\alpha_1 - \alpha_2\right)\right]. \qquad \text{(A.35)}$$

APPENDIX B

INVERSION DIAGRAMS

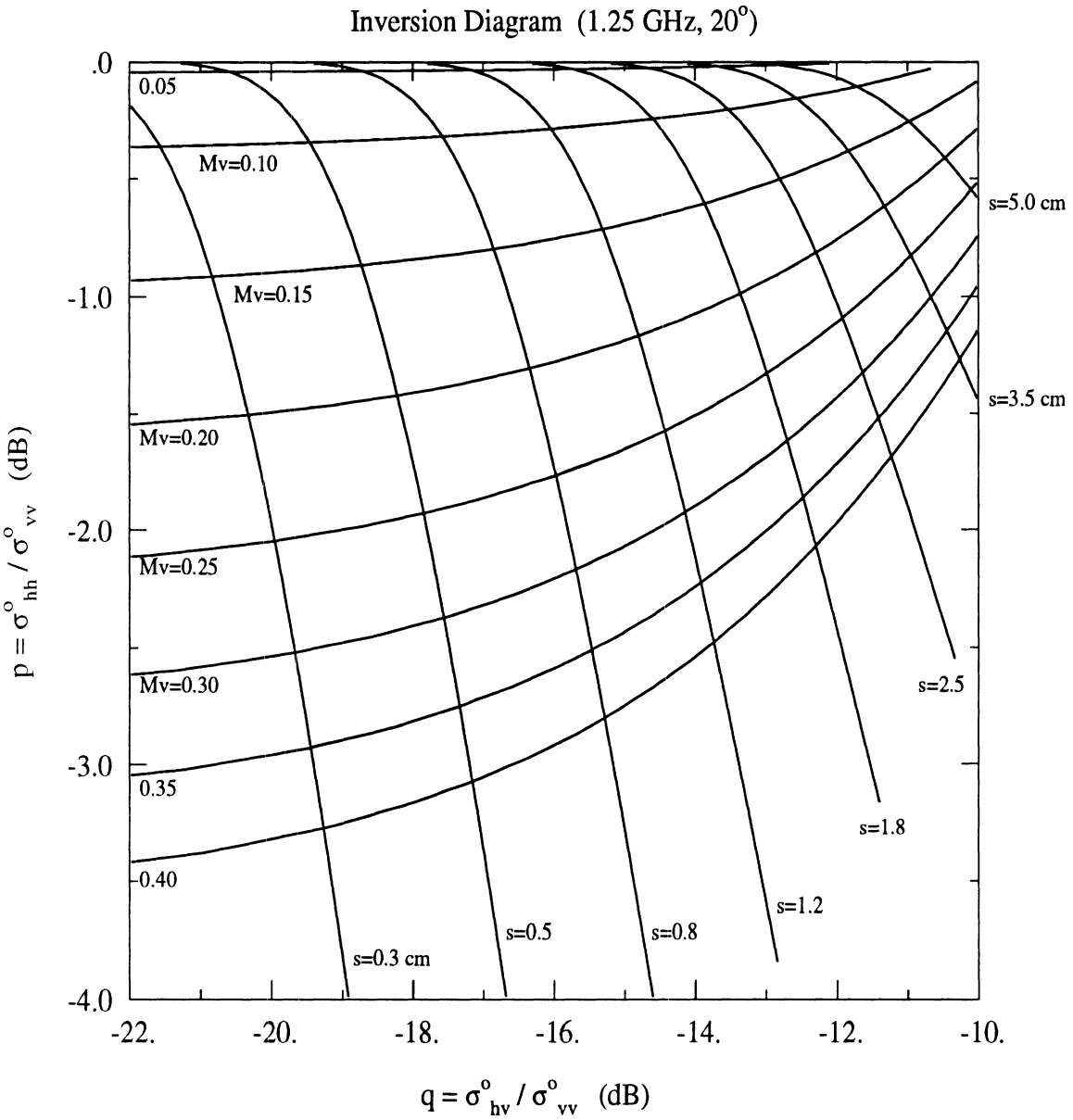

Figure B.1: Inversion diagram for 1.25 GHz at 20°

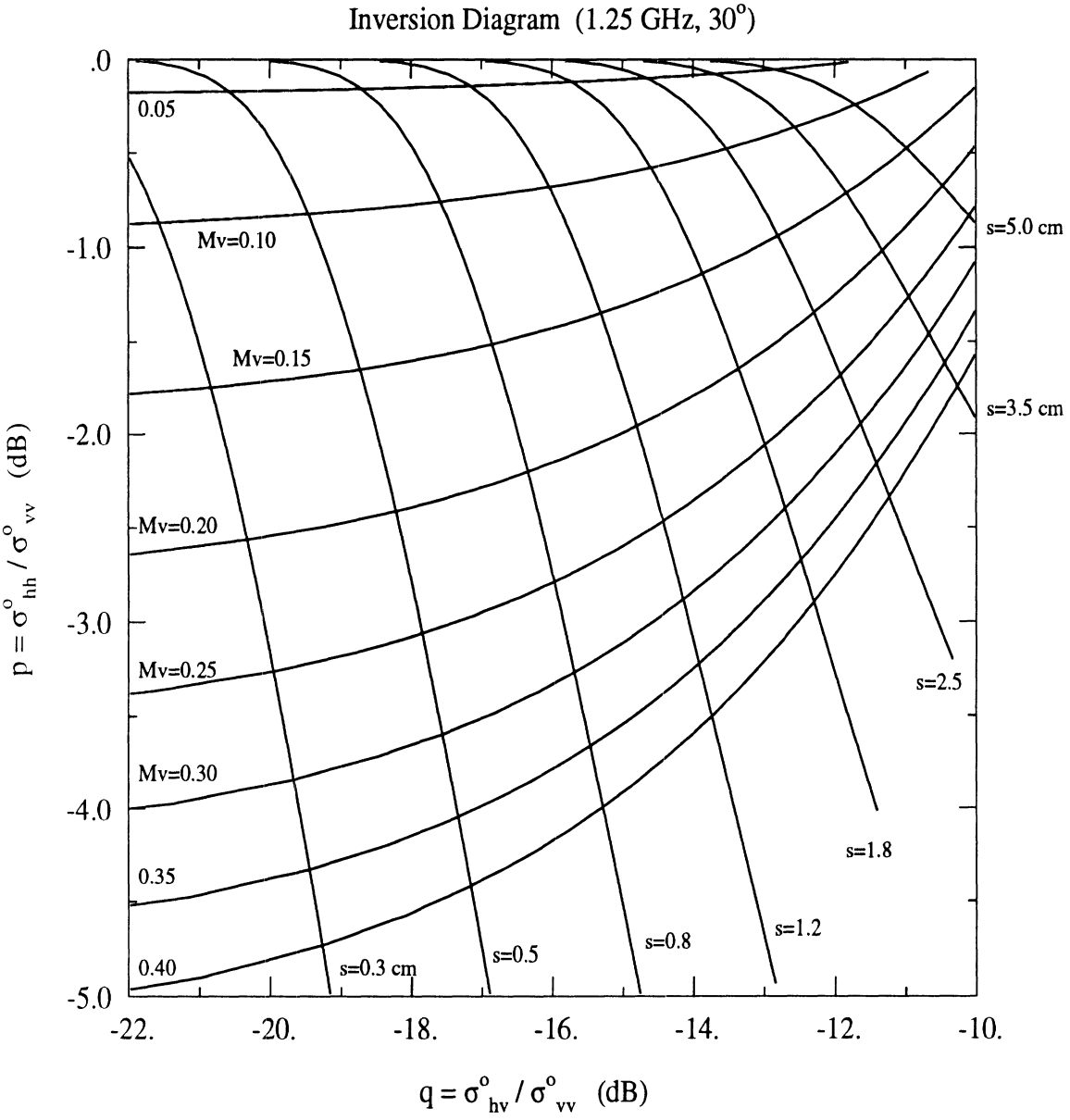

Figure B.2: Inversion diagram for 1.25 GHz at 30°

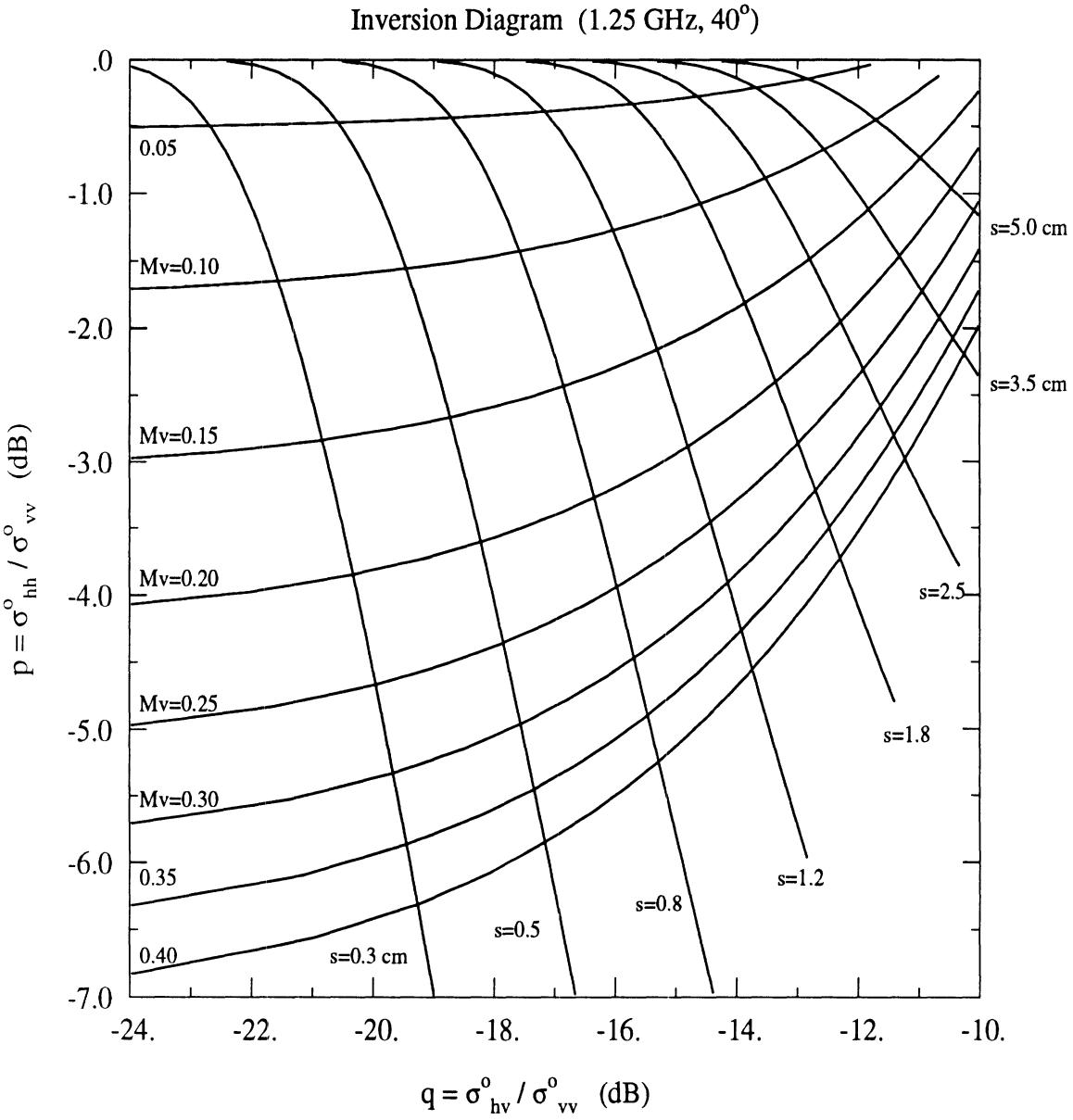

Figure B.3: Inversion diagram for 1.25 GHz at 40°

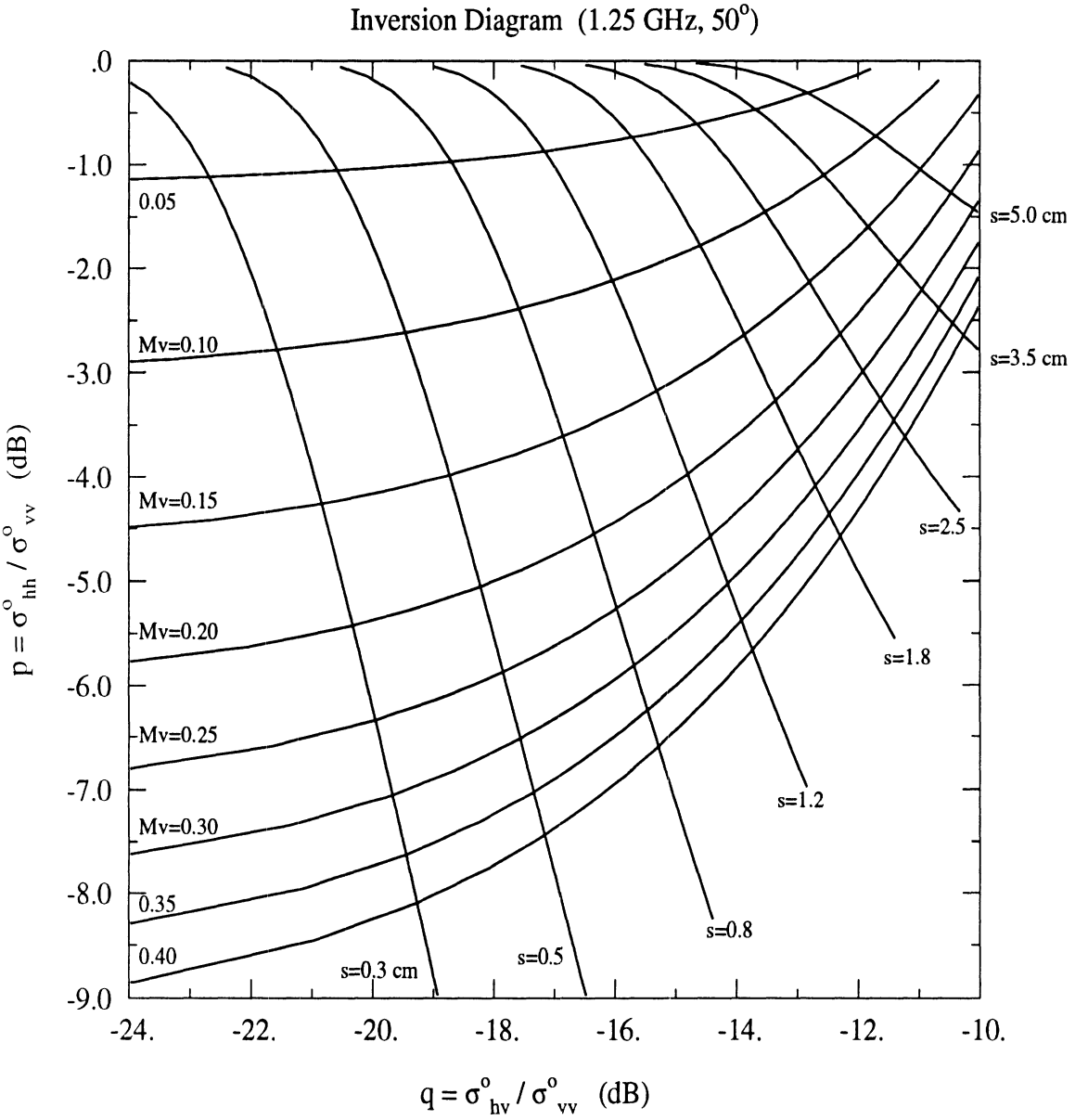

Figure B.4: Inversion diagram for 1.25 GHz at 50°

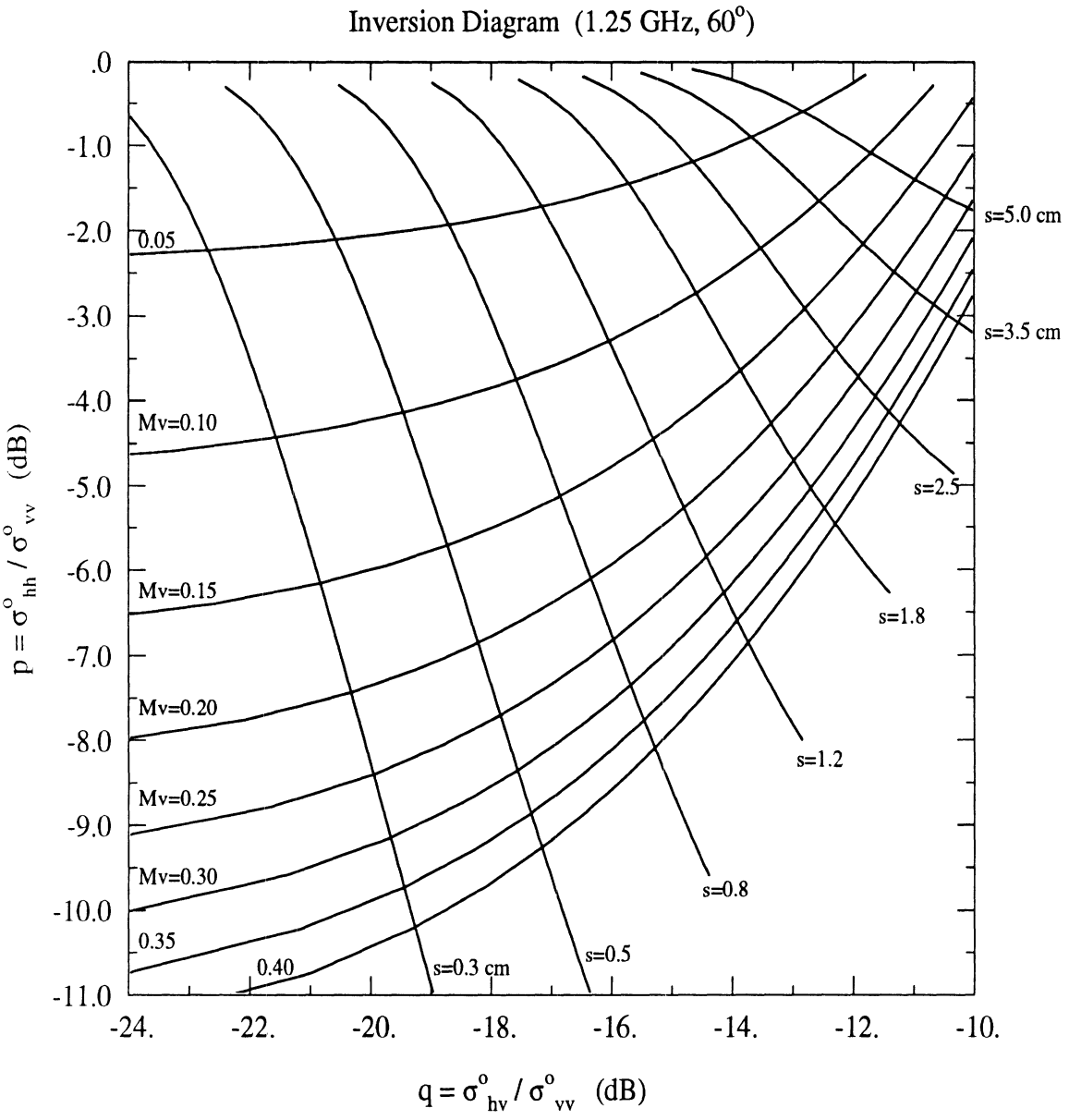

Figure B.5: Inversion diagram for 1.25 GHz at 60°

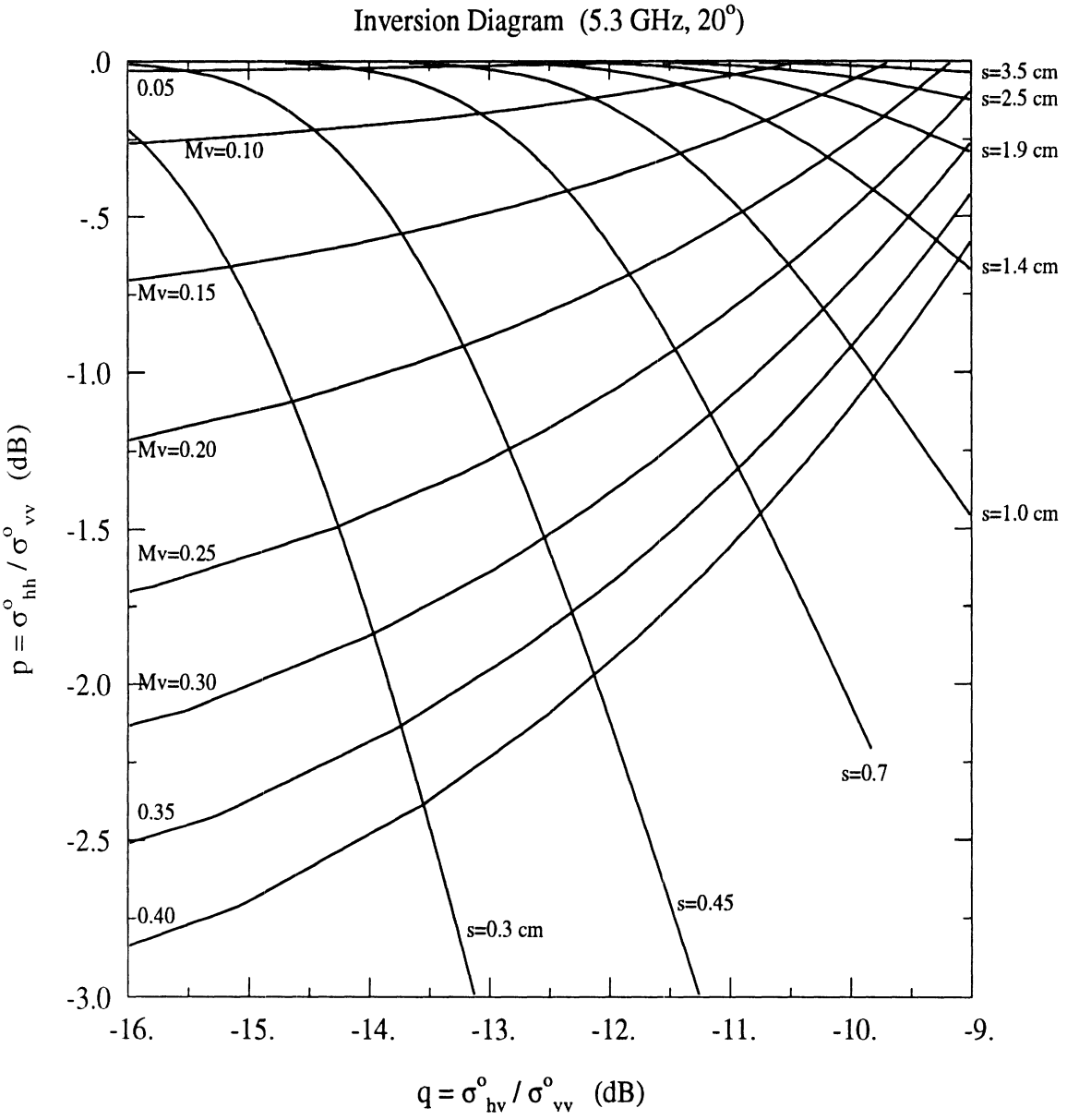

Figure B.6: Inversion diagram for 5.3 GHz at 20°

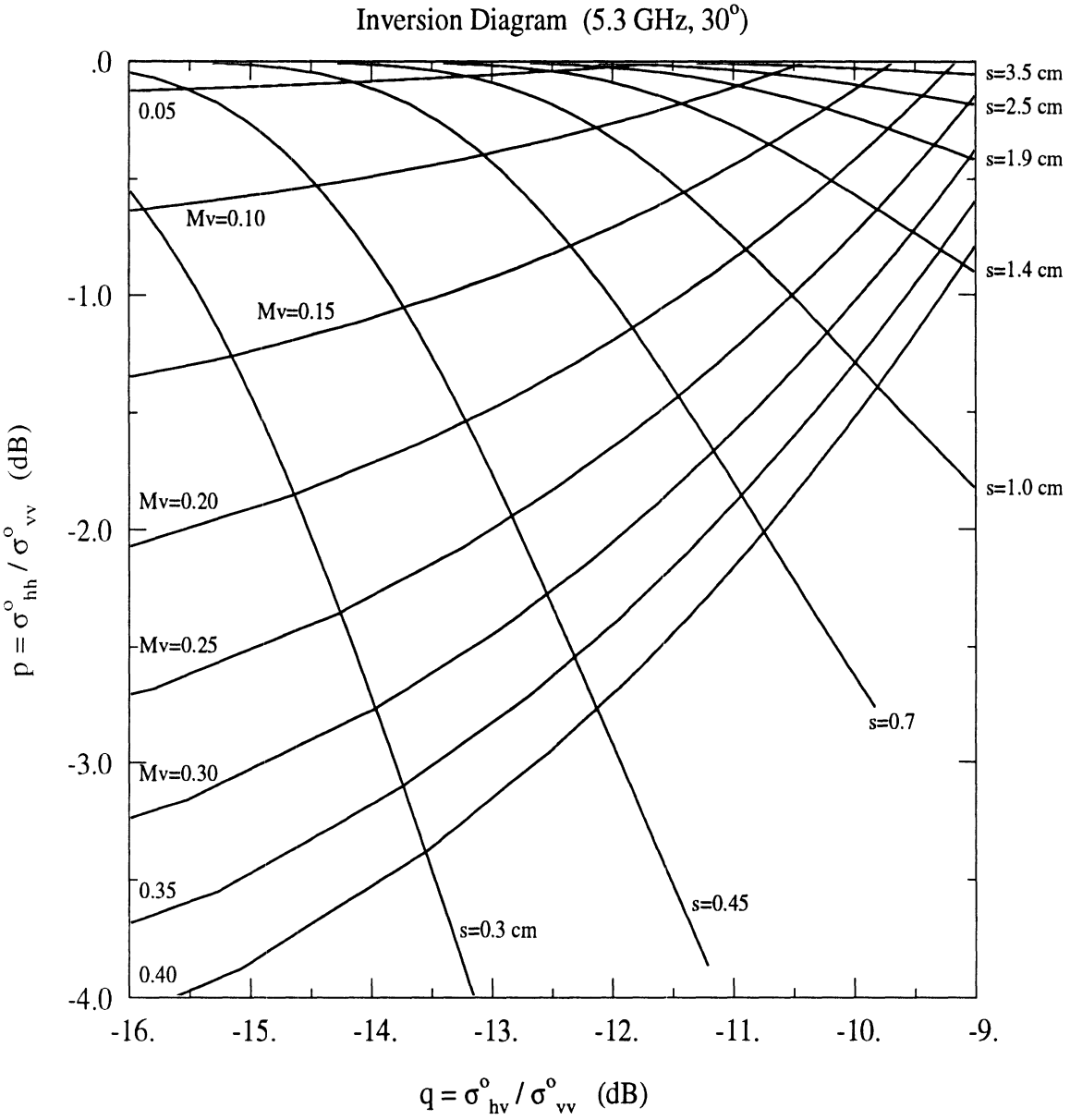

Figure B.7: Inversion diagram for 5.3 GHz at 30°

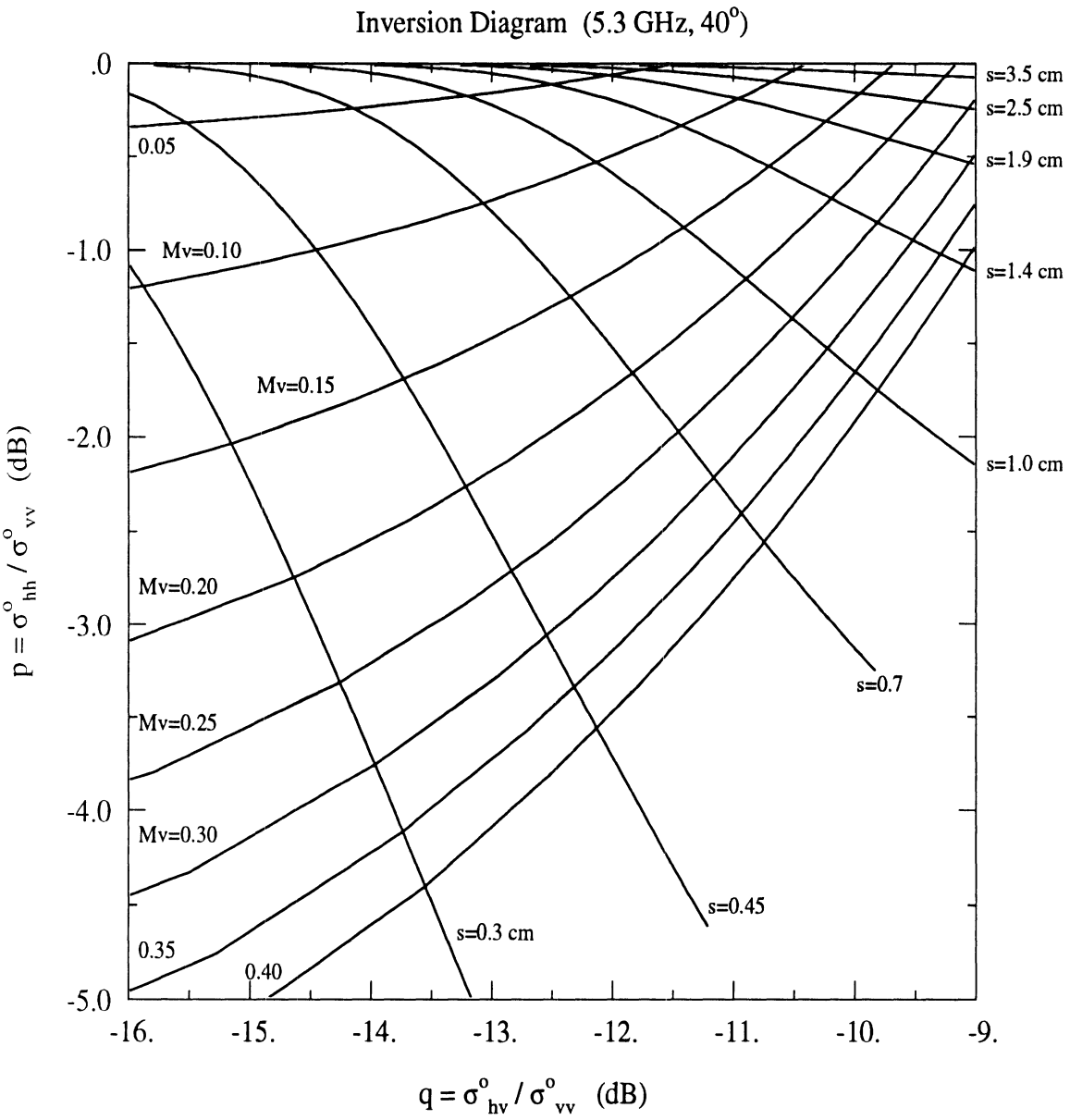

Figure B.8: Inversion diagram for 5.3 GHz at 40°

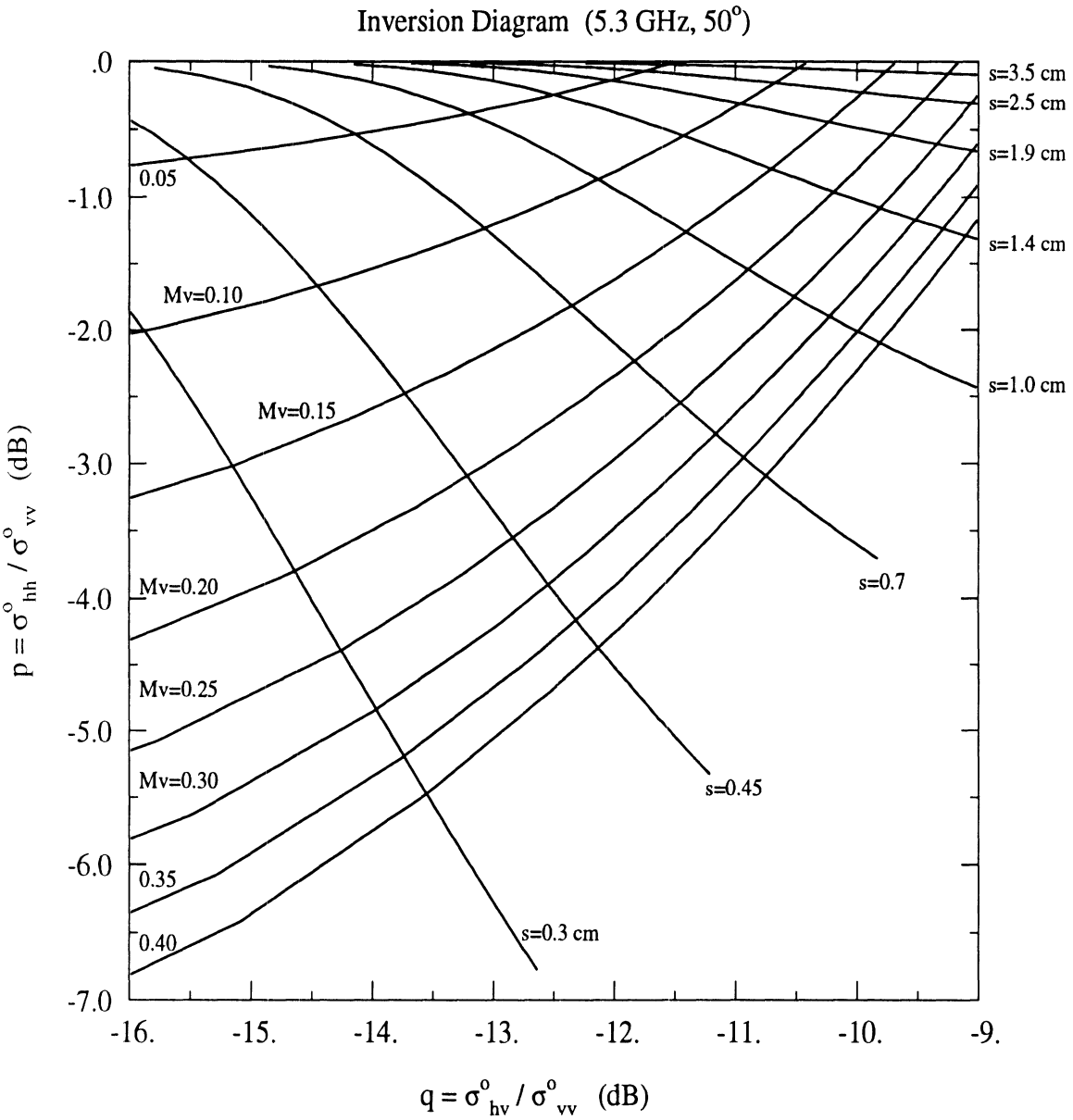

Figure B.9: Inversion diagram for 5.3 GHz at 50°

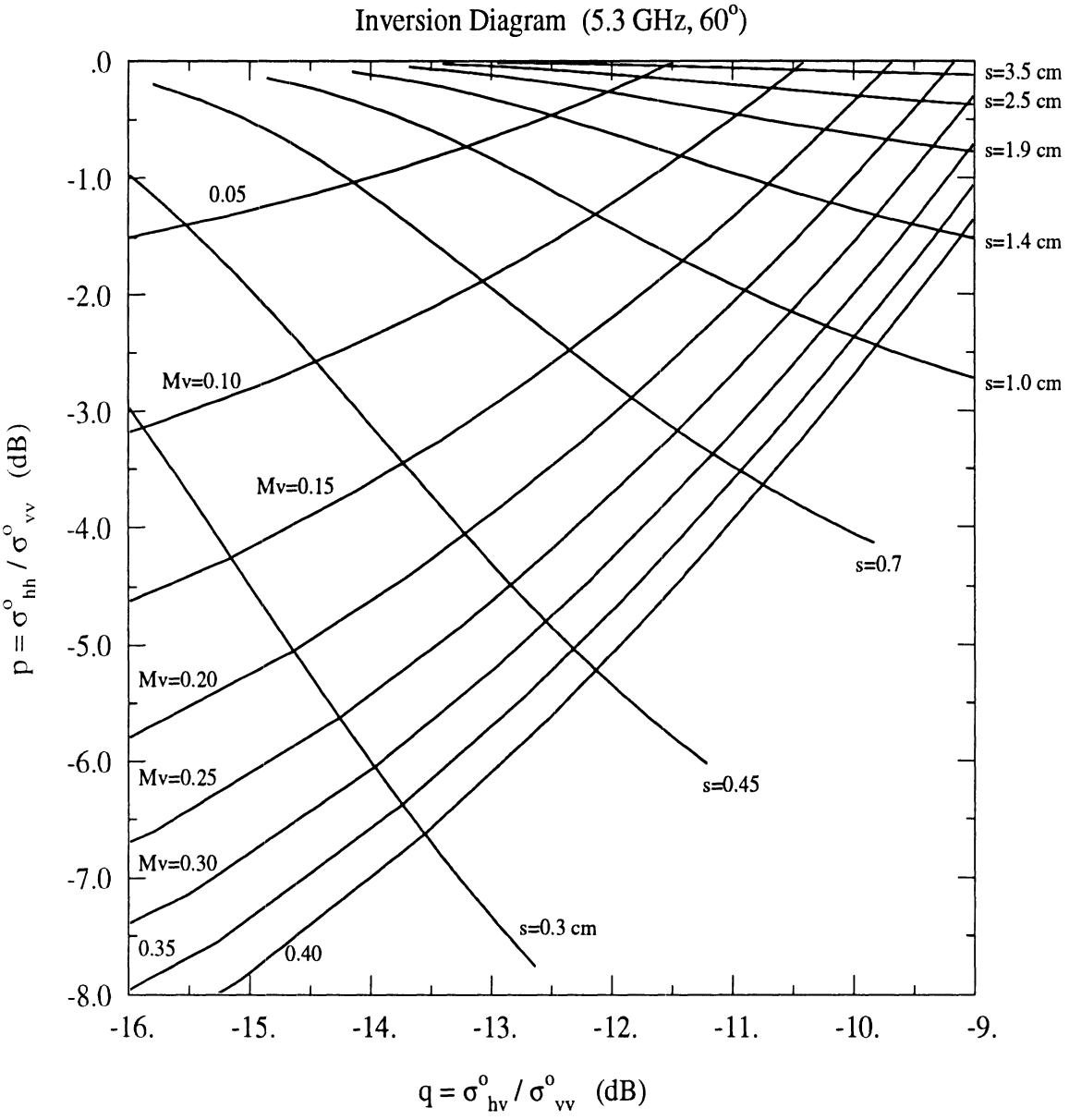

Figure B.10: Inversion diagram for 5.3 GHz at 60°

BIBLIOGRAPHY

BIBLIOGRAPHY

[1] Abramowitz, M. and I. A. Stegun, **Handbook of Mathematical Functions**, Dover Publication, Inc., New York, 1972.

[2] Axline, R. M. and A. K. Fung, "Numerical computation of scattering from a perfectly conducting random surface," *IEEE Trans. Antennas Propagat.*, vol. AP-26, pp. 482-488, May 1978.

[3] Bahar, E., "Full-wave solutions for the depolarization of the scattered radiation fields by rough surfaces of arbitrary slope," *IEEE Trans. Antennas Propagat.*, vol. AP-29, pp. 443-454, May 1981.

[4] Bahar, E. (1991a), "Examination of full-wave solutions and "Exact numerical results" for one-dimensional slightly rough surfaces", *J. Geophys. Res.*, vol. 96, pp. 17123-17131, Sep. 1991.

[5] Bahar, E. (1991b), "Full wave analysis for rough surface diffuse, incoherent radar cross sections with height-slope correlations included", *IEEE Trans. Antennas Propagat.*, vol. 39, pp. 1293-1304, Sep. 1991.

[6] Barnes, R.M., "Polarimetric calibration using in-scene reflectors," Rep. TT.65, MIT, Lincoln Laboratory, Lexington, MA, Sept. 1986.

[7] Bartlivala, P. P. and F. T. Ulaby "Feasibility of monitoring soil moisture using active microwave remote sensing", University of Kansas Center for Research Inc., Lawrence, KS, RSL Technical Report 264-12, Jan. 1977.

[8] Bass, F. G. and I. M. Fuks, **Wave Scattering from Statistically Rough Surfaces**, Pergamon Press, New York, 1979.

[9] Beckmann, P. and A. Spizzichino, **The Scattering of Electromagnetic Waves from Rough Surfaces**, Artech House, MA, 1987.

[10] Broschat, S. L., L. Tsang, A. Ishimaru, and E. I. Thoros, "A numerical Comparison of the Phase Perturbation Technique with the Classical Field Perturbation and Kirchhoff Approximations for Random Rough Surfaces Scattering", *J. Electromagn. Waves Appl.*, vol. 2, No. 1, pp. 55-102, 1987.

[11] Brown, G. S. "Backscattering from a Gaussian Distributed Perfectly Conducting Rough Surface", *IEEE Trans. Antennas Propagat.*, vol. AP-26, pp. 472-482, May 1978.

[12] Brunfeldt, D.R., "Theory and Design of a Field-Portable Dielectric Measurement System", *IEEE International Geoscience and Remote Sensing Symposium (IGARSS) Digest* vol. 1, pp 559-563, 1987.

[13] Chen, K. S. and A. K. Fung, "A Comparison Between Backscattering Models for Rough Surfaces", *IEEE International Geoscience and Remote Sensing Symposium (IGARSS) Digest* vol. 2, pp. 907-909, 1992.

[14] Chen, M. F. and A. K. Fung, "A numerical Study of Validity of the Kirchhoff and Small-Perturbation Rough Surface Scattering Models", *Radio Science*, vol. 23, pp. 163-170, Mar. 1988.

[15] Dobson, M. C. and F. T. Ulaby (1986a), "Active microwave soil moisture research," *IEEE Trans. Geosci. Remote Sensing*, vol. GE-24, pp. 23-36, Jan. 1986.

[16] Dobson, M. C. and F. T. Ulaby (1986b), "preliminary evaluation of the SIR-B response to soil moisture, surface roughness, and crop canopy cover," *IEEE Trans. Geosci. Remote Sensing*, vol. GE-24, pp. 517-526, July 1986.

[17] Durden,S. L. and J. F. Vesecky, "A numerical study of the separation wavenumber in the two-scale scattering approximation", *IEEE Trans. Geosci. Remote Sensing*, vol. 28, pp. 271-272, Mar. 1990.

[18] Eftimiu, C. and G. W. Pan, "First-order Wiener-Hermite expansion in the electromagnetic scattering by dielectric rough surfaces", *Radio Science*, vol. 25, pp. 1-8, Jan.-Feb. 1990.

[19] Engman, E. T., and J. R. Wang, "Evaluating roughness models of radar backscatter," *IEEE Trans. Geosci. Remote Sensing*, vol. GE-25, pp. 709-713, Nov. 1987.

[20] Eom, H.J., and W.M. Boerner, "Rough surface incoherent backscattering of spherical wave," *IEICE Transactions,* vol. E 74, no. 1, Jan. 1991.

[21] Fung, A. K. and H. J. Eom, "Multiple Scattering and Depolarization by a Randomly Rough Kirchhoff Surfaces", *IEEE Trans. Antennas Propagat.*, vol. AP-29, pp. 463-471, May 1981.

[22] Fung, A.K., and H.J. Eom, "Coherent scattering of spherical wave from an irregular surface," *IEEE Trans. Antennas Propagat.*, vol. 31, pp.68-72, Jan. 1983.

[23] Fung, A.K., and M. F. Chen, "Numerical Simulation of Scattering from Simple and Composite Random Surfaces", *J. Opt. Soc. Am. A*, vol. 2, no. 12, pp. 2274-2284, Dec. 1985.

[24] Fung, A.K., and G. W. Pan, "A Scattering Model for Perfectly Conducting Random Surfaces: I. Model Development. II. Range of Validity", *Int. J. Remote Sensing*, vol. 8, no. 11, pp. 1579-1605, 1987.

[25] Fung, A. K. Z. Li and K. S. Chen, "Backscattering from a Randomly Rough Dielectric Surface", *IEEE Trans. Geosci. Remote Sensing*, vol. 30, pp. 356-369, Mar. 1992.

[26] Fung, A.K., and K. S. Chen, "Dependence of the surface backscattering coefficients on roughness, frequency and polarization states," *Int. J. Remote Sensing*, vol. 9, no. 9, pp. 1663-1680, 1992.

[27] Gradshteyn I. S. and I. M. Ryzhik, **Table of Integrals, Series, and Products,** Academic Press, San Diego, CA, 1980.

[28] Hallikainen, M.T., F.T. Ulaby, M.C. Dobson, M.A. El-Rayes, and L. Wu, "Microwave Dielectric Behavior of Wet Soil -Part I: Empirical Models and Experimental Observations", *IEEE Trans. Geosci. Remote Sensing*, vol. GE-23, pp 25-34, 1985.

[29] Harrington, R. F., **Time-Harmonic Electromagnetic Fields**, McGraw-Hill, New York, 1961.

[30] Harrington, R. F., **Field Computation By Moment Methods**, Macmillan, New York, 1968.

[31] Henry S. and J. W. Woods, **Probability, Random Processes, and Estimation Theory for Engineers**, Prentice Hall, Englewood Cliffs, N.J., 1986.

[32] Holzer, J. A. and C. C. Sung, "Scattering of Electromagnetic Waves from a Rough Surfaces. II", *J. Appl. Phys.*, vol. 39, pp. 1002-1011, Mar. 1978.

[33] Ishimaru, A, **Wave Propagation and Scattering in Random Media**, Vol. 1 and 2 Acadimic Press, New York, 1978.

[34] Ivanova, K., M. A. Mich alev, and O. I. Yordanov, "Study of the Phase Perturbation Technique for Scattering of Waves by Rough Surfaces at Intermediate and Large Values of the Roughness Parameter", *J. Electromagn. Waves Appl.*, vol. 4, No. 5, pp. 401-412, 1990.

[35] Jackson, T. J., A. Chang, and T. J. Schmugge, "Aircraft active microwave measurements for estimating soil moisture," *Photogrammetr. Eng. Remote Sensing*, vol. 47, pp 801-805, June 1981.

[36] Jackson, T. J., "Laboratory Evaluation of a Field-Portable Dielectric/Soil-Moisture Probe", *IEEE Trans. Geosci. Remote Sensing*, vol. 28, pp 241-245, Mar. 1990.

[37] Kong, J. A. **Electromagnetic Wave Theory**, John Wiley and Sons, New York, 1990.

[38] Lentz, R. R., "A numerical study of electromagnetic scattering from ocean-like surfaces," *Radio Science*, vol. 9, pp.1139-1146, December 1974.

[39] Leo, C. Kempel, J.L. Volakis, and T.B. A. Senior, "Transverse magnetic diffraction from tapered resistive junctions," *Radio Science*, vol. 28, pp.129-138, March-April 1993.

[40] Lindell, I.V., E. Alanen, "Exact image theory for the Sommerfeld half-space problem, Part III: General formulation," *IEEE Trans. Antennas Propagat.*, vol. 32, no. 10, pp. 1027-1032, 1984.

[41] Lou, S.H., L. Tsang, C.H. Chan, and A. Ishimaru, "Application of the finite element method to Monte Carlo simulations of scattering of waves by random rough surfaces with the periodic boundary condition", *J. Electromagn. Waves Appl.*, vol. 5, No. 8, pp. 835-855, 1991.

[42] Millar, R. F., "The Rayleigh hypothesis and a related least-squares solution to scattering problems for periodic surfaces and other scatterers", *Radio Science*, vol. 8, pp. 785-796, Aug.-Sept., 1973.

[43] Mo, T., J. R. Wang, T. J. Schmugge, "Estimation of surface roughness parameters from dual-frequency measurements of radar backscattering coefficients," *IEEE Trans. Geosci. Remote Sensing*, vol. 26, pp. 574-579, Sep. 1988.

[44] Nieto-Vesperinas, M. and J. M. Soto-Crespo, "Monte Carlo simulations for scattering of electromagnetic waves from perfectly conductive random rough surfaces", *Optics Lett.*, vol. 12, pp. 979-981, 1987.

[45] Oh, Y., K. Sarabandi, and F.T. Ulaby, "An Empirical Model and an Inversion Technique for Radar Scattering from Bare Soil Surfaces", *IEEE Trans. Geosci. Remote Sensing*, vol. 30, pp. 370-382, Mar. 1992.

[46] Oh, Y., K. Sarabandi, and F.T. Ulaby, "An empirical model for phase-difference statistics of rough surfaces", *Intern. Geosc. Remote Sensing Symp. (IGARSS'93)*, Tokyo, Japan, Aug. 1993.

[47] Press, W. H., B. P. Flannery, S. A. Teukolsky, and W. T. Vetterling, **Numerical Recipes: The Art of Scientic Computing,** University Press, Cambridge, Massachusetts, 1986.

[48] Rice, S. O., "Reflection of Electromagnetic Waves by Slightly Rough Surfaces", *Communication in Pure and Applied Mathematics*, vol. 4, pp. 351-378, 1951.

[49] Richmond, J. H., "Scattering by a Dielectric Cylinder of Arbitrary Cross Section Shape", *IEEE Trans. Antennas Propagat.*, vol. AP-13, pp. 334-341, May 1965.

[50] Richmond, J. H., "TE-Wave Scattering by a Dielectric Cylinder of Arbitrary Cross-Section Shape", *IEEE Trans. Antennas Propagat.*, vol. AP-14, pp. 460-464, July 1966.

[51] Rochier, J. D., A. J. Blanchard, and M. F. Chen, "The generation of surface targets with specified surface statistics," *Int. J. Remote Sensing,* vol. 10, no. 7, pp. 1155-1174, 1989.

[52] Rodriguez, E., Y. Kim, and S. L. Durden "A numerical assessment of rough surface scattering theories: I. Horizontal polarization, II. Vertical polarization," *Radio Science*, vol. 27, pp.497-527, July-Aug. 1992.

[53] Sanchez-Gil, J. A. and M. Nieto-Vesperinas, "Lighting scattering from random rough dielectric surfaces", *J. Opt. Soc. Am. A*, vol. 8, pp. 1270-1286, Aug. 1991.

[54] Sarabandi, K., F.T. Ulaby, and M.A. Tassoudji, "Calibration of polarimetric radar systems with good polarization isolation", *IEEE Trans. Geosci. Remote Sensing*, vol. 28, no. 1, pp. 70-75, Jan. 1990.

[55] Sarabandi, K., and F.T. Ulaby, "A convenient technique for polarimetric calibration of radar systems", *IEEE Trans. Geosci. Remote Sensing*, vol. 28, pp. 1022-1033, 1990.

[56] Sarabandi, K., "Scattering from Variable Resistive and Impedance Sheets", *J. Electromagn. Waves Appl.*, vol. 4, No. 9, pp. 865-891, 1990.

[57] Sarabandi, K., Y. Oh and F.T. Ulaby, "Polarimetric Radar Measurement of Bare Soil Surfaces at Microwave Frequencies", in *Proc. IEEE Geosci. Remote Sensing Symp.*, Espoo, June 1991, pp. 387-390.

[58] Sarabandi, K., "Scattering from Dielectric Structures Above Impedance Surfaces and Resistive Sheets", *IEEE Trans. Antennas Propagat.*, vol. 40, pp. 67-78, Jan. 1992.

[59] Sarabandi, K., "Derivation of phase statistics of distributed targets from the Mueller matrix," *Radio Sci.,* vol. 27, pp. 553-560, Sep.-Oct. 1992.

[60] Sarabandi K., Y. Oh, and F.T. Ulaby, "Measurement and Calibration of Differential Mueller Matrix of Distributed Targets," *IEEE Trans. Antennas Propagat.*, vol. 40, pp.1524-1532, Dec. 1992.

[61] Schmugge, T., P. E. O'Neill, and J. R. Wang, "Passive microwave soil moisture research", *IEEE Trans. Geosci. Remote Sensing*, vol. 24, no. 1, pp. 12-22, Jan. 1986.

[62] Stark, H. and J. W. Woods, **Probability, Random Processes and Estimation Theory for Engineers**, Prentice-Hall, Englewood Cliffs, New Jersey, 1986.

[63] Stratton, J. A., **Electromagnetic Theory**, New York: McGraw-Hill, 1941.

[64] Sung, C. C. and W. D. Eberhardt, "Scattering of an Electromagnetic Wave from a Very Rough Semi-Infinite Dielectric Plane (Exact Treatment of The Boundary Conditions)", *J. Appl. Phys.*, vol. 39, pp. 994-1001, Mar. 1978.

[65] Tassoudji, M.A., K. Sarabandi, and F.T. Ulaby, "Design consideration and implementation of the LCX polarimetric scatterometer (POLARSCAT)", *Radiation Laboratory Report No. 022486-T-2*, The University of Michigan, June 1989.

[66] Thorsos, E. I. "The validity of the Kirchhoff approximation for rough surface scattering using a Gaussian roughness spectrum," *J. Acoust. Soc. Am.*, vol. 83, pp. 78-92, Jan. 1988.

[67] Thorsos, E. I. and D. R. Jackson, "The validity of the perturbation approximation for rough surface scattering using Gaussian roughness spectrum," *J. Acoust. Soc. Am.*, vol. 86, pp. 261-277, July 1989.

[68] Thorsos, E. I. and D. P. Winebrenner, "An Examination of the "Full-Wave" Method for Rough Surface Scattering in the Case of Small Roughness", *J. Geophys. Res.*, vol. 96, pp. 17107-17121, Sep. 1991.

[69] Tsang, L., J. A. Kong, and R. T. Shin, **Theory of Microwave Remote Sensing**, John Wiley and Sons, New York, 1985.

[70] Ulaby, F. T., "Radar measurements of soil moisture content," *IEEE Trans. Antennas Propagat.*, vol. AP-22, pp. 257-265, March 1974.

[71] Ulaby, F. T., J. Cihlar, and R. K. Moore, "Active microwave measurement of soil water content," *Remote Sensing Environment*, vol. 3, pp. 185-203, 1974.

[72] Ulaby, F. T., P. P. Bartlivala, and M. C. Dobson, "Microwave Backscatter Dependence on Surface Roughness, Soil Moisture, and Soil Texture: Part I - Bare Soil", *IEEE Trans. Geosci. Electron.*, vol. GE-16, pp. 286-295, Oct., 1978.

[73] Ulaby, F. T., M. K. Moore, and A. K. Fung, **Microwave Remote Sensing, Active and Passive**, vol. 2 , Artech House, Norwood, MA, 1982.

[74] Ulaby, F. T., M. K. Moore, and A. K. Fung, **Microwave Remote Sensing, Active and Passive**, vol. 3 , Artech House, Norwood, MA, 1986.

[75] Ulaby, F. T. and M. C. Dobson, **Handbook of radar scattering statistics for terrain** Artech House, Norwood, MA, 1989.

[76] Ulaby, F. T. and C. Elachi, **Radar Polarimetry for Geoscience Applications**, Artech House, Norwood, MA, 1990.

[77] Ulaby, F. T.,M. W. Whitt, and K. Sarabandi, "AVNA-based polarimetric scatterometers," *IEEE Antennas. Propag. Magazine*, vol. 32, pp. 6-17, Oct. 1990.

[78] Ulaby, F. T., K. Sarabandi, and A. Nashashibi, "Statistical properties of the Mueller matrix of distributed targets," *IEE Proc.-F*, vol. 139, pp. 136-146, April 1992.

[79] Valenzuela, G. R., "Depolarization of EM waves by slightly rough surfaces", *IEEE Trans. Antennas Propagat.*, vol. AP-15, pp. 552-557, July 1967.

[80] Wang, J. R, E. T. Engman, J. C. Shiue, M. Rusek, and C. Steinmeier, "The SIR-B observations of microwave backscatter dependence on soil moisture, surface roughness, and vegitation covers," *IEEE Trans. Geosci. Remote Sensing*, vol. GE-24, pp. 510-516, July 1986.

[81] Whitt, M.W., F.T. Ulaby, P. Polatin, and V.V. Liepa, "A general polarimetric radar calibration technique," *IEEE Trans. Antennas Propagat.*, vol. 39, no. 1, Jan. 1991.

[82] Wineberner, D. and A. Ishimaru (1985a), "Investigation of a Surface Field Phase Perturbation Technique for Scattering from Rough Surfaces", *Radio Science*, vol. 20, pp. 161-170, Mar. 1985.

[83] Wineberner, D. and A. Ishimaru (1985b), "Application of the Phase Perturbation Technique to Random Rough Surfaces", *J. Opt. Soc. Am. A*, vol. 2, No.12, pp. 2285-2294, Dec. 1985.

[84] Wong, E. and B. Hajeck, **Stochastic Processes in Engineering Systems**, Springer-Verlag, New York, 1985.

[85] Yamasaki, H., J. Awaka, A. Takahashi, K. Okamoto, and T. Ihara, "Measurements of Soil Backscatter with a 60 GHz Scatterometer", *IEEE International Geosci. Remote Sensing Symposium (IGARSS '91) Digest*, vol. 2, pp 403-406, 1991.